Copyright

by

Trevor James Watt

2011

The Dissertation Committee for Trevor James Watt certifies that this is the approved version of the following dissertation:

The Onset of Gouging in High-Speed Sliding Contacts

Committee:

David L. Bourell, Supervisor

Michael D. Bryant

Mark T. Crawford

Krishnaswamy Ravi-Chandar

Eric M. Taleff

The Onset of Gouging in High-Speed Sliding Contacts

by

Trevor James Watt, B.S.M.E., M.S.E.

Dissertation

Presented to the Faculty of the Graduate School of

The University of Texas at Austin

in Partial Fulfillment

of the Requirements

for the Degree of

Doctor of Philosophy

The University of Texas at Austin

August, 2011

“Everything should be made as simple as possible, but not simpler.”

- Albert Einstein

Acknowledgements

This work would not have been possible without the help of numerous colleagues, mentors, and friends. Over 20 medium-caliber railgun experiments were performed at the Institute for Advanced Technology (IAT). The success of these experiments was in large part due to the efforts of Steve Ferraro, James Hudson, Bobby Hummel, Paul Snowden, James Stewart, and John Tagle. Martha Simmons and Jose Galvan-Pasada were indispensible in helping prepare and analyze the many metallographic samples. I would also like to thank Akash Gandhi for his assistance in the slider experiments, and Philip Bassett and Charys Clay for their help with the indented rail experiments.

I have had the privilege of working with several researchers responsible for much of the fundamental work on gouging in railguns. I must thank Francis Stefani, Jerry Parker, Sikhanda Satapathy, and Chadee Persad for their invaluable experience, advice, and thoughtful conversations on gouging, metallurgy, and research in general. They are in no small part responsible for me deciding to pursue this degree. I must thank Hans Mark for his assistance in analyzing the slider experiments, and for many illuminating conversations. Without the help and support of my supervisor at IAT and committee member, Mark Crawford, none of this would have been possible.

I would like to express my deep gratitude to David Bourell for being my advisor during this process, and for his steadfast support, encouragement, and insight. I would also like to thank Michael Bryant, Eric Taleff, and K. Ravi-Chandar for their valuable advice and patience as my committee members.

Special thanks go to Doyle and Amanda Motes for their help in editing this document. Their assistance in the last few months has been vital. I must further thank Doyle for his extensive help in the experiments, modeling, and for checking the calculations. I would finally like to thank my family for their unwavering support and encouragement.

Funding for the experiments was provided from both the U.S. Army Research Laboratory (ARL) under contract W911QX-07-D-0002, and the Office of Naval Research (ONR) under MURI award N00014-04-1-0599. The views and conclusions contained in this document are those of the author and should not be interpreted as presenting the official policies or position, either expressed or implied, of the U.S. Army Research Laboratory, the Office of Naval Research, or the U.S. Government unless so designated by other authorized documents. Citation of manufacturers or trade names does not constitute an official endorsement or approval of the use thereof.

The Onset of Gouging in High-Speed Sliding Contacts

Trevor James Watt, Ph.D.

The University of Texas at Austin, 2011

Supervisor: David L. Bourell

Hypervelocity gouging occurs in high speed sliding systems such as rocket sled test tracks, light gas guns, and railguns. Gouging takes the form of teardrop-shaped craters on the rail surface, and usually only occurs above a threshold speed which is dependent on the slider and rail material properties. In this dissertation, the onset of gouging was studied from three perspectives: application of existing modeling techniques developed for gouging and related fields of research, performing new high-speed experiments using a medium-caliber railgun, and analyzing rail microstructural evolution during gouge onset.

A previous gouging model based on shock mechanics was extended, while other models based on mechanisms such as Rayleigh waves, bending waves, and shear band formation were ruled out. An effective Reynolds number approach from explosive welding research was applied to gouging with encouraging results. Based on similarities between gouging, explosive welding, and Kelvin-Helmholtz waves, a linear instability analysis was also performed.

A total of 22 railgun experiments were performed to explore different aspects of gouging. Through these experiments, the effect of new slider materials, thin aluminum coatings, and macroscopic rail indentations on the gouging of copper alloy rails were examined. Results using new materials matched the existing models well, though galling damage to copper rails was often as severe as gouging. Gouging was delayed using electroplated aluminum coatings as thin as 2 μm, though this is not necessarily a robust

solution. Macroscopic indentations were found to have negligible effect on the threshold velocity for gouging onset, though the morphology of the gouges was strongly affected.

Both galling and gouging craters were shown to initiate at existing defects. This applied to both microscopic and macroscopic features. A consistent microscopic feature observed prior to galling and gouging were deformation bands that resembled persistent slip bands on the rail surface. Another consistent feature was the transfer of slider material to the rail prior to galling and gouging. This suggests that gouging may not be triggered by micro-impact events, but by instabilities associated with high-speed thermoplastic shear.

Table of Contents

List of Tables

List of Figures

CHAPTER 1. INTRODUCTION

Hypervelocity gouging occurs in systems with high sliding speeds such as rocket sled test tracks, light gas guns, and railguns. Gouging takes the form of teardrop-shaped craters on the rail surface (see Figure 1.1), and usually occurs above a threshold speed which is dependent on the slider and rail material properties [1]. Gouge craters normally begin at a point and propagate outward until the free surfaces of the slider or rail are reached. Gouging is a problem for two reasons: first, the gouging process generates very large dynamic stresses which can result in failure of both slider and rail hardware. Second, existing rail gouges on subsequent experiments can generate large balloting loads which can result in projectile failure.

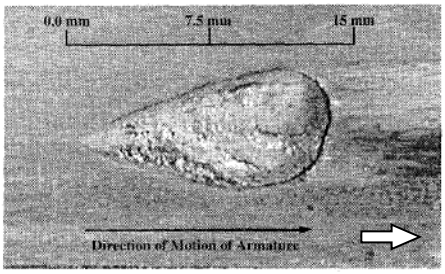

Figure 1.1. Gouge on copper rail [1]. White arrow indicates the direction of motion (© 1997 IEEE)

1.1 Background

1.1.1 HIGH-SPEED SLIDING

In high-speed sliding systems, materials can experience high strains, strain rates, and frictional heating. Sliding wear typically results in plastic deformation, microscopic fracture, and heat treatment of the surface layers. In dry (unlubricated) sliding metals the wear rates can be severe, resulting from adhesive/abrasive wear of the slider and rail surfaces as well as erosive wear, delamination, fretting, and galling [2,3]. An example of different wear mechanisms is shown in Figure 1.2.

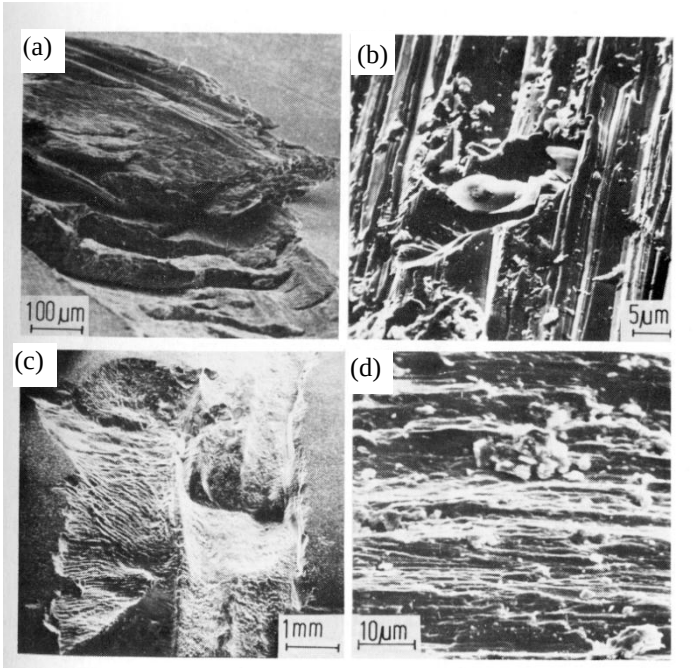

Figure 1.2. SEM images of wear modes: (a) adhesion, (b) abrasion, (c) fretting, (d) corrosive[1]

In general, "mild" and "severe" wear can be delineated by the presence of oxide films which act to reduce the adhesive forces between sliding surfaces [4]. Removal of

[1] Reprinted from K.-H. Z. Gahr, "Microstructure and Wear of Materials," Tribology Series 10, Elsevier Science Publishers B.V., Copyright 1987, with permission from Elsevier

the respective oxide layers can result in strong metallic bonding between metals, one of the principles of friction welding. This is also responsible for galling damage in metals, where the metallic bond between two materials results in a piece getting torn out of the weaker material.

Adhesive wear and galling depend primarily on how strongly the slider and rail materials bond with each other. The degree of bonding depends on the adhesion energy and crystal structure as studied by Akagaki [5], or more generally on the degree of "compatibility" as suggested by Rabinowicz [6]. A chart developed by Rabinowicz for the compatibility of different metals is shown in Figure 1.3. This is primarily based on inspecting the binary alloy phase diagrams for the relevant material pair. Binary alloy systems with a high degree of liquid and solid solubility exhibit a high degree of compatibility, and tend to suffer from greater adhesive wear and galling.

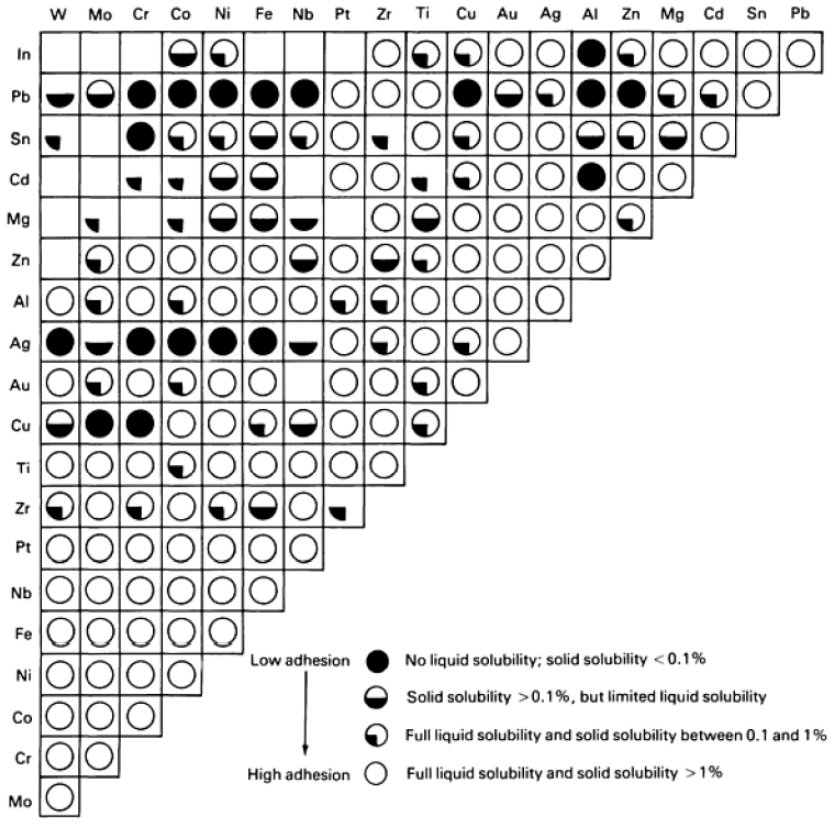

Figure 1.3. Metal compatibility chart from Rabinowicz [6]

For adhesive wear, the resistance to damage is also proportional to the hardness of the softer material [7]. Resistance to galling damage corresponds to low stacking fault energy, and a high stacking fault density. These materials tend to strain-harden rapidly, and show the highest resistance to galling [8]. At high enough contact pressures seizure can occur, especially for materials with low galling resistance. Seizure occurs when contact asperities form metallic bonds and then increase in size as the asperities plastically deform [9]. When the real contact area becomes large enough, the surfaces seize.

Wear theory typically relates the volume of material lost to the pressure divided by hardness of the material. The well-known Archard-Holm wear law for adhesive/ abrasive wear is given in Equation (1.1), where V is the volume of removed slider material (m^3), W is applied load (N), H is the hardness of the slider (Pa), L is the sliding length (m), and K_W is a dimensionless wear coefficient that is material-pair dependent [10]. For metal/metal systems the wear coefficient can vary widely but is on the order of 10^{-4} to 10^{-3}. A similar equation exists for erosive wear, where abrasive particles are suspended in a high-speed fluid impinging on a surface Equation (1.2). Here, m is the mass of the abrasive particle and u_p is its velocity. In this case, the volume lost is proportional to the ratio of particle impact energy to hardness [11]. In both cases, wear is a linear function of the applied load divided by the hardness of the material.

$$V(\text{adhesive/abrasive}) = K_W \frac{W}{H} L \tag{1.1}$$

$$\text{V(erosive)} = K_E \frac{m {u_p}^2}{H} \tag{1.2}$$

The above equations relate the total volume lost from a macroscopic sliding surface as a function of sliding distance, and the appropriate coefficients are usually determined from pin-on-disk or similar experiments with hundreds or thousands of

cycles. The effective depth of material lost on a given cycle is often a few micrometers. In contrast, the focus of this research is on high-speed, high-pressure, single-cycle "catastrophic" wear that is not encountered in most other applications. Nevertheless, the general form of Equations (1.1) and (1.2) may be extended to this regime if appropriate care is taken.

All engineering surfaces have some characteristic roughness as a result of fabrication and handling processes. Contacting bodies therefore only touch in local regions known as asperities that are the respective mountains of the two surfaces. When a load is applied to a surface, that load is transferred through a collection of asperities that determines the *real* contact area. The *apparent* contact area is the macroscopic area of contact as observed with the naked eye. The *real* contact area can be calculated as $A \approx W/H$, where W is the load and H is the hardness of the weaker contact material [12].

At high sliding speeds (>100 m/s), the interactions between surface asperities can become strongly influenced by inertial forces, the wave nature of stress propagation, and local impact stresses. Materials typically have wave propagation speeds on the order of 10^3 m/s which are in the velocity regime of high-speed sliding systems like light gas guns, and railguns. Sliding impacts at these high speeds can generate pressures well in excess of the yield strength of materials. At high enough pressures, the materials behave essentially like viscous fluids.

There is a relative lack of data on friction and wear at these high speeds. What data exists is primarily from inclined plate impact experiments [13] and a small set of railgun tests [14]. The inclined plate experiments were performed at low sliding speeds (100 m/s) and very high contact pressures (1-2 GPa) between aluminum and steel alloys. The railgun experiments were done with aluminum sliders on copper rails at speeds up to 2.3 km/s and contact pressures of 50-150 MPa. In both cases, the interface between metals became molten, resulting in a low coefficient of friction and high wear rate.

Gouging occurs even under high-speed sliding conditions that result in a molten slider interface, such as the case of aluminum armatures sliding on copper rails. This is likely because such interfaces are not fully molten, either because the interface is a

mixed-mode lubrication mechanism where the contact forces are supported by both viscous fluid stresses as well as asperity hardness, or because the very leading edge of the contact is still solid.

1.1.2 ROCKET SLED GOUGING

Gouging was first reported by Graff for results at the Holloman High Speed Test Track (HHSTT) facility at Holloman Air Force Base, New Mexico in 1969 [15]. These tests used rockets attached to sleds with steel "slippers" that slid against steel tracks for several miles. Gouges were observed on the steel rails starting around 1.7 km/s, and were 2-4" long, ~1" wide, and about 0.06" deep. Over the course of many experiments, it was found that speed was the dominant factor in gouge onset. The gouges had a rippled, discolored crater described as a fluid-like mixing of material, occasional longitudinal scraping prior to the main crater formation, and evidence of metallic spray downstream of the gouge crater. Since the rails were 1080 steel, martensitic bands were also observed in the gouge craters [16]. Images of the rocket sled hardware, slippers, and damaged rails are shown in Figure 1.4 through Figure 1.6.

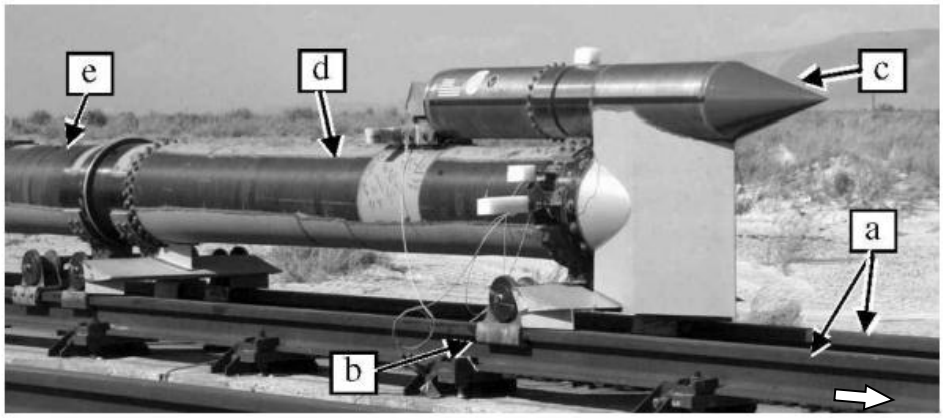

Figure 1.4. Holloman High-Speed Test Track (HHSTT) with Rocket Sled: (a) rail guides, (b) rocket sled slippers, (c) payload, (d-e) rocket motors [20].

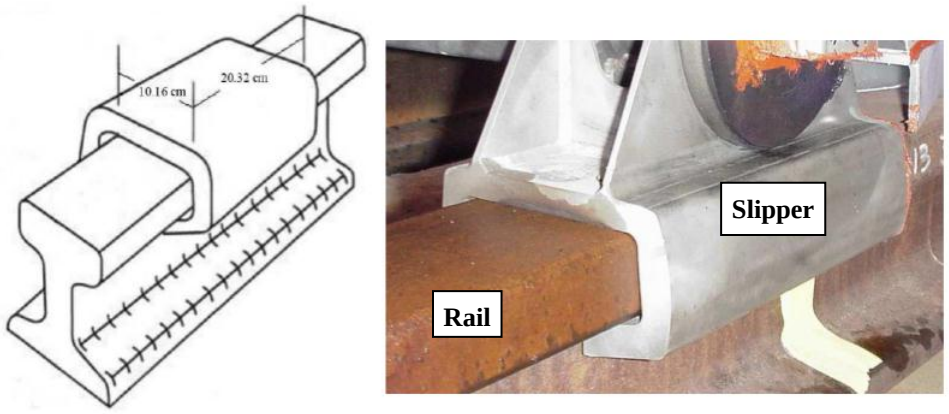

Figure 1.5. HHSTT rail and slipper configuration [17]

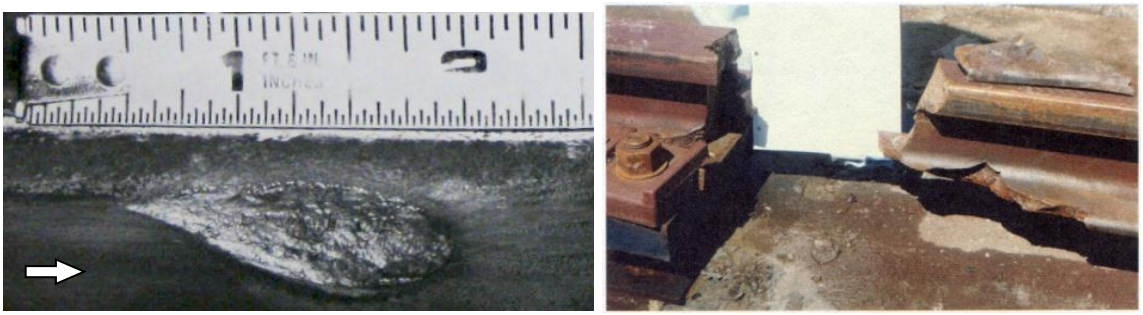

Figure 1.6. Rocket sled gouge crater (left) and track damage (right) from gouging[2]

Most of the research on rocket sled gouging has involved computer modeling since using rocket sleds is impractical (expensive) for conducting gouging experiments [20,17]. Attempts were also made to incorporate a scaling theory of gouging, though scaling cannot properly account for the high strain-rate sensitivity of materials required to accurately model gouge crater formation [18].

Principal findings of the rocket sled experiments and related hydrocode analyses were that gouges could be considered the result of impact-generated material jets where the dynamic pressure of the jet exceeds the flow stress of both materials [19]. Gouges occur simultaneously on the slider and rail material, and for identical material pairs the gouges should be anti-symmetric. It was suggested by Laird and others that both

[2] Reprinted from K.F. Graff and B.B. Dettloff, "The gouging phenomenon between metal surfaces at very high sliding speeds," Wear, Vol. 14, pp. 87-97, Copyright 1969, with permission from Elsevier

materials must be susceptible to gouging for gouging to occur [20], a recurring theme throughout the various gouging theories. Because gouging is based on simultaneous material failure, only one of the materials needs to have a high yield strength to prevent gouging. That is, the threshold for gouging should be determined by the hardness of the harder material.

Lastly, coatings such as iron oxide and epoxy were found to be successful in significantly delaying the onset of gouges (this shall be further addressed in later pages). A comprehensive monograph for rocket sled gouging has recently been written by Cinnamon [21].

1.1.3 RAILGUN GOUGING

In the field of railguns, gouging emerged as a significant problem during the development of solid-armature launchers in the early 1980s. Barber [22] first reported on gouging in railguns for aluminum armatures sliding on copper rails. Gouging was thought to be due to oblique shocks generated by asperities, with the threshold speed set by the ultimate strength of the materials. In addition to metal/metal gouging, gouges were also observed by Barker [23] for polycarbonate projectiles sliding against ETP (electrolytic tough-pitch) copper at speeds between 1.5-2.5 km/s. Gouges for AA7075 on C11000 were found at 1.35 km/s, with severe mechanical deformation of the copper rail including strain hardening and twinning, which is typical of impact damage [1]. Railgun gouges have also been observed with very small contact sizes in Cu-Cd brush armatures on chrome-copper rails [24], and occur at the same speed for a given material pair regardless of slider or rail geometry.

The first systematic study of gouging for a diverse set of metals was undertaken by Stefani and Parker in 1999 [25]. They proposed that gouging was governed by the strength (hardness) of the harder material and acoustic impedance (density and sound speed) of both materials. Experiments were performed up to 2.2 km/s on C11000 rails with electrically-isolated sliders, shown in Figure 1.7. These experiments are discussed in greater detail in later sections.

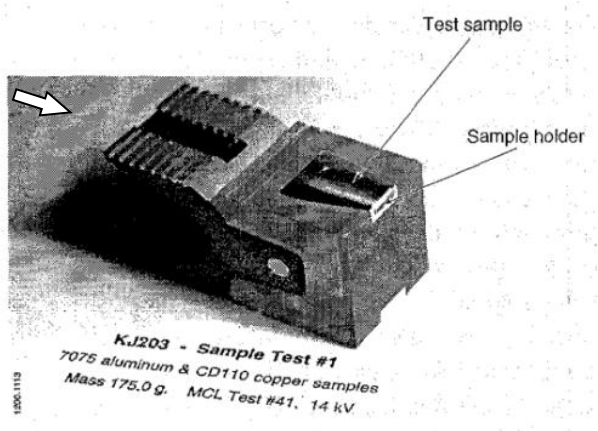

Figure 1.7. Railgun gouging projectile with sliders (© 1999 IEEE) [25]

1.1.4 OTHER GOUGING OBSERVATIONS

Additional experiments have been performed to investigate the behavior of gouging in more controlled environments. Numerous subscale experiments were performed at Holloman AFB using a powder gun and a curved impact track [15,26]. It was found that small (curved track) gouges were similar to large (rocket sled) gouges, and that small track curvature was not able to generate gouges, presumably due to insufficient contact pressure. While the speeds of the rocket sled (3+ km/s) were not attainable using the powder gun, the speeds (~2.2 km/s) were nevertheless able to produce gouges for steel/steel material combinations which occur around 1.8 km/s [27].

Tarcza performed experiments with lead projectiles shot against curved lead tracks in order to produce a relatively low gouging speed of around 250 m/s [28]. Similar to the scaling arguments made by rocket sled researchers, Tarcza stated that gouging is not a scaling phenomenon but is a "materials phenomenon" [29]. He found that gouge size generally increased with sliding speed and that a "sufficient" normal force was required for gouging to occur (found similarly by rocket sled researchers). He also suggested that an upper gouging speed may be governed by the full melting of the slider

surface caused by viscous melt lubrication, though this has yet to be shown experimentally.

Satapathy observed gouging in reverse ballistics tests with tungsten alloy (W-X27X) rods penetrating RHA steel targets [30]. He concluded that gouging correlated with the threshold criteria derived by Stefani and Parker [25]. He also noted that gouge craters could serve as fracture initiation sites which would reduce the effectiveness of the penetrator.

1.1.5 THE USE OF COATINGS TO ELIMINATE GOUGING

In general, gouging can be delayed by using slider and rail materials with low acoustic impedance (low density) and a high hardness. Another approach to prevent gouging is the use of rail coatings. The only presumed requirement is that gouging should not occur on the coating itself. This can be accomplished by using either a very hard or low density coating. Rocket sled experiments have employed refractory coatings such as Ta, Ni-Al, ZrO_2, and W as well as "ablative" layers such as Teflon, carbon-carbon, and carbon-phenolics [31]. Success has been obtained using both epoxy (low density) and iron oxide (hard) coatings on the rail surface to prevent gouging [26]. Computational models were performed by Szmerekovsky that showed that epoxy reduced the impact stress and served as a physical barrier between the rail and slider [32]. Epoxy coatings in this case were applied to AISI 1080 steel rail surfaces in thicknesses of ≥150 μm. While gouging was delayed in these experiments, it was not prevented outright.

In railguns, gouging has been delayed by "pre-coating" the rails. This is accomplished by launching several armatures at speeds below the gouging speed of the armature/rail pair. The high speed wear of the armatures lays down a 10-20 μm layer of aluminum deposits on the rail surface [33,34]. The deposits are irregular, porous and consist of aluminum, aluminum oxides, and Al-Cu inter-metallic compounds [35]. It is not clear whether gouging is prevented because the coating has a low acoustic impedance, hard inter-metallic and oxide phases, or some other property intrinsic to thin

layers. This aspect is addressed in one of the experimental series discussed in Chapter Three.

1.1.6 SUMMARY OF MEASURED GOUGING THRESHOLDS

A summary of the experimentally observed gouging threshold speeds for rocket sled and railgun experiments is provided in Table 1.1. Additional experiments were performed in support of this dissertation, and are added to this table in the Discussion section. These new experiments are detailed in Chapter Three and Four, where the effects of new material combinations, thin surface coatings, and macroscopic rail indentations are examined.

Table 1.1. Measured gouging speeds for different material pairs*

Slider	Rail	Slider Hardness	Rail Hardness	V_{gouge}	Source
		HV	*HV*	*m/s*	
AISI 304	AISI 1080	(129 ± 6)	(309 ± 15)	1,585 ± 79	Rocket Sled [28]
AISI 4340	AISI 1080	(228 ± 11)	(309 ± 15)	1,610 ± 81	"
Vascomax 300	AISI 1080	(545 ± 27)	(309 ± 15)	2,438 ± 122	"
Pb	Pb	(10 ± 1)	(10 ± 1)	245 ± 12	Powder gun [28]
C11000	C11000	109 ± 3	50 ± 3	600 ± 30	Railgun [25]
AA7075-T6	C11000	175 ± 9	88 ± 4	1,400 ± 70	"
C11000	C11000	88 ± 4	88 ± 2	746 ± 50	"
AA7075-T6	C11000	(208 ± 17)	(88 ± 2)	1,300 ± 65	"
Au80-Cu20	C11000	340 ± 13	88 ± 2	1,346 ± 75	"
AISI 1015	C11000	143 ± 8	88 ± 2	977 ± 110	"
Ag	C11000	75 ± 2	88 ± 2	770 ± 90	"
Mo	C11000	296 ± 17	88 ± 2	1,268 ± 30	"
Ni	C11000	207 ± 11	88 ± 2	996 ± 70	"
W	C11000	581 ± 47	88 ± 2	1,474 ± 45	"
Ti	C11000	218 ± 17	88 ± 2	1,420 ± 55	"
AISI 4340	C11000	541 ± 27	88 ± 2	1,878 ± 90	"

* Values in parentheses are estimates based on handbook values
An error value of 5% is assumed, when not provided

1.2 Gouging Models and Predictions

The principal approaches to modeling gouging have taken the form of semi-empirical relationships and hydro-code models. The conceptual model proposed by Barber described gouging as a process where surface asperities interacting at high sliding speeds generate oblique shock waves in the rail material [22]. The threshold speed was related to exceeding the ultimate strength of the materials, but a good correlation between theory and experiment was elusive. “Oblique shocks” in this context is a misnomer, as they should only be generated when the sliding speed exceeds the sound speed in the material. This is on the order of 4-6 km/s for most metals, which is well in excess of all reported gouging speeds (1-2 km/s). Several other theories predict that gouging cannot take place when the sliding speed exceeds the dilatational sound speed. In that regard, oblique shocks may actually prevent gouging.

There are numerous phenomena that have been proposed for gouging over the last few decades [15,22,25,47]. Several theories involve the slider running over surface or bending waves in the rail [47,49,51]. Another theory is that gouging is the result of adiabatic shear (thermo-plastic shear instability) in the rail [21]. A significant amount of effort has been put into modeling the formation of gouge craters using hydrocodes such as CTH [27,31]. However, using these codes to predict the onset of gouging usually requires an assumption about rail defects or incident velocities. The most productive methods of predicting threshold speeds are based on the assumption that micro-impact events generate high shock pressures which subsequently fail both materials [25].

1.2.1 SHEAR & RAYLEIGH WAVES

The propagation of waves in solids is dependent on the stress-strain behavior, density, and the equation of state of the material. At low strains the stress waves are elastic where the wave speed depends on the elastic constants. At higher strains the material plastically deforms, resulting in plastic waves that travel at speeds governed by

the plastic stress/strain behavior. At even higher strains the material compresses adiabatically and shock waves can form [36].

Bulk elastic waves can be divided into two categories, depending on how atoms move across the wave front. The fastest waves are *longitudinal* or *dilatational* waves, also known as pressure or *P-waves*, where the atoms are compressed in the direction of wave propagation. Behind this wave is a *shear* or *distortional* wave (*S-wave*) which propagates at a slower speed. As implied by the name, the atoms across the shear wave front undergo motion orthogonal to the direction of wave propagation. An illustration of the different waves in a material is shown in Figure 1.8.

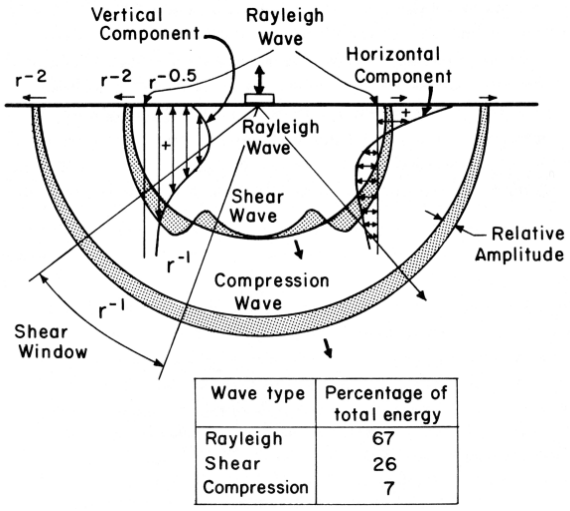

Figure 1.8. Illustration of elastic waves in a material[3]

On the free surface of a material, the interaction of the shear and dilatational waves creates a third wave known as the *surface* or *Rayleigh* wave (*R-wave*). Rayleigh waves travel at speeds slower than distortional waves, but carry the most energy. At the interface between two materials *generalized Rayleigh* waves (sliding interfaces) or *Stonely* waves (bonded interfaces) can exist, which are discussed in the next section.

[3] Reprinted from M.A. Meyers, "Dynamic Behavior of Materials," John Wiley & Sons, Inc., New York, NY, 1994, with permission from John Wiley & Sons, Inc.

One of the early theories for gouging was that the slider was catching up to Rayleigh waves on the rail surface, resulting in severe contact stresses and damage to the slider and rail material. There are several problems with the theory. First, Rayleigh waves are only a function of the rail material properties, and thus the role of slider properties should be irrelevant (known to be otherwise). Second, the Rayleigh wave speed is typically well above observed gouging threshold speeds.

For isotropic elastic materials with a Poisson ratio of 0 to 0.5, the Rayleigh wave speed can be estimated using Viktorov's approximation [37], given by Equation (1.3). In this equation C_R is the Rayleigh wave speed, C_S is the shear wave speed, and ν is Poisson's ratio. C_D is the dilatational wave speed. The dilatational and shear wave speeds are given by Equations (1.4) and (1.5), respectively. In these equations ρ is the mass density, and λ and G are the 1st and 2nd Lamé constants, respectively. Both Lamé constants can be written in terms of the Young's modulus E and Poisson's ratio ν as shown in Equations (1.6) and (1.7). The Lamé constant G is more commonly referred to as the shear modulus (G). The result of these calculations is provided in Table 1.2, which shows that gouging speeds are below all elastic wave speeds for the observed rail materials.

$$C_R = \frac{0.862 + 1.14\nu}{1 + \nu} C_S \tag{1.3}$$

$$C_D = \sqrt{\frac{(\lambda + 2\mathrm{G})}{\rho}} \tag{1.4}$$

$$C_S = \sqrt{\frac{G}{\rho}} \tag{1.5}$$

$$\lambda = \frac{E\nu}{(1 + \nu)(1 - 2\nu)} \tag{1.6}$$

$$G = \frac{E}{2(1+\nu)} \tag{1.7}$$

Table 1.2. Comparison of gouging speeds to rail elastic wave speeds

Slider	Rail	V_{gouge}	C_D	C_S	C_R
		m/s	*m/s*	*m/s*	*m/s*
AISI 304	AISI 1080	1,585 ± 79	5,712	3,206	2,953
AISI 4340	AISI 1080	1,610 ± 81	5,712	3,206	2,953
Vascomax 300	AISI 1080	2,438 ± 122	5,712	3,206	2,953
Pb	Pb	245 ± 12	1,775	659	623
C11000	C11000	600 ± 30	4,378	2,205	2,053
AA7075-T6	C11000	1,400 ± 70	4,378	2,205	2,053
C11000	C11000	746 ± 50	4,378	2,205	2,053
AA7075-T6	C11000	1,300 ± 65	4,378	2,205	2,053
Au80-Cu20	C11000	1,346 ± 75	4,378	2,205	2,053
AISI 1015 (A)	C11000	977 ± 110	4,378	2,205	2,053
Ag	C11000	770 ± 90	4,378	2,205	2,053
Mo	C11000	1,268 ± 30	4,378	2,205	2,053
Ni	C11000	996 ± 70	4,378	2,205	2,053
W	C11000	1,474 ± 45	4,378	2,205	2,053
Ti	C11000	1,420 ± 55	4,378	2,205	2,053
AISI 4340	C11000	1,878 ± 90	4,378	2,205	2,053

1.2.2 SLIP (GENERALIZED RAYLEIGH) WAVES

At the interface between two materials there are two types of waves that can be transmitted. The first are for the case where the two materials are bonded together, and are known as *Stonely waves*. The second are for sliding interfaces and are known as *generalized Rayleigh waves* or *slip waves*. Disturbances in bonded systems can propagate up to the shear wave speed of the materials [38], while slip waves are generally slower.

In the case of sliding interfaces without any interfacial shear stress (friction), the primary slip wave occurs between the Rayleigh wave speeds of the two materials, as calculated by Barnett *et al.* [39]. For identical materials the slip wave speed is identical to the Rayleigh wave speed. Ranjith *et al.* [40] found that if Coulomb friction is included, slip waves are unstable for all friction values. This is corrected if the coefficient of

friction is given a memory-dependence or "averaged out" instead of using an instantaneous dependence on interfacial normal stress. Wang *et al.* [41] later calculated that slip waves could not exist for initially steady sliding if separation between the surfaces was ignored, and further proposed that the stick-slip phenomenon observed in tribology was the result of slip waves. Separating surfaces can admit slip waves when the sliding speed is greater than the generalized Rayleigh wave speed, though they are expected to be limited by the dilatational sound speed [42].

Dunham analyzed 3D perturbation waves in frictional sliding interfaces and calculated that such slip waves were stable for identical materials, which reduced to a pair of Rayleigh waves [43]. Afferrante *et al.* calculated that if thermal expansion and diffusion are considered the problem became a *thermoelastodynamic* one, which resulted in unstable sliding at all speeds [44]. This was due to the coupling between simultaneous elastic and thermal instabilities and was proposed to explain the vibration observed in many forms of frictional sliding. Vibrations have been observed in select high-speed railgun experiments, but are not observed in general [45].

For slip waves, the sliding speed needs to be at or above the lowest Rayleigh wave speed in order for the interface to admit a stable slip wave. Furthermore, the above models are either always unstable, or never unstable, and admit no threshold dependence. As such, they do not appear to be a likely explanation for the onset of gouging.

1.2.3 BENDING / FLEXURAL WAVES

The last category of elastic waves that have been proposed to explain gouging (and other high-speed sliding phenomena) is bending or flexural waves. This was first proposed for railguns by Tzeng in 2003 [46], but has been explored for conventional gun barrels since the 1960s. The general approach is that a launcher has a critical (resonance) wave speed, which is a function of barrel geometry and materials. If the projectile exceeds this speed then dynamic strain amplification occurs which can result in damage.

Johnson *et al.* used this approach to calculate the critical speed for the railgun used to obtain the gouging data shown in Table 1.1 [47]. The approach was based on the

armature exceeding the Bernoulli-Euler speed given by Equation (1.8), where *B* is the rail width, *J* is the rail's cross-sectional moment of inertia, *A* is the cross-sectional rail area, and k_0 is the foundation stiffness. V_{crit} is then the minimum phase speed for an un-attenuated wave on a beam on an elastic foundation. The critical speed for the launcher used in those experiments, the medium caliber launcher (MCL), was calculated to be 1,486 m/s. The calculated dynamic pressures for the armature exceeding this speed were ~1 GPa, while the corresponding amplitudes and wavelengths were 10-50 μm and ~20 mm, respectively.

$$V_{crit} = \left(\frac{4k_0 BEJ}{\rho^2 A^2}\right)^{1/4} \tag{1.8}$$

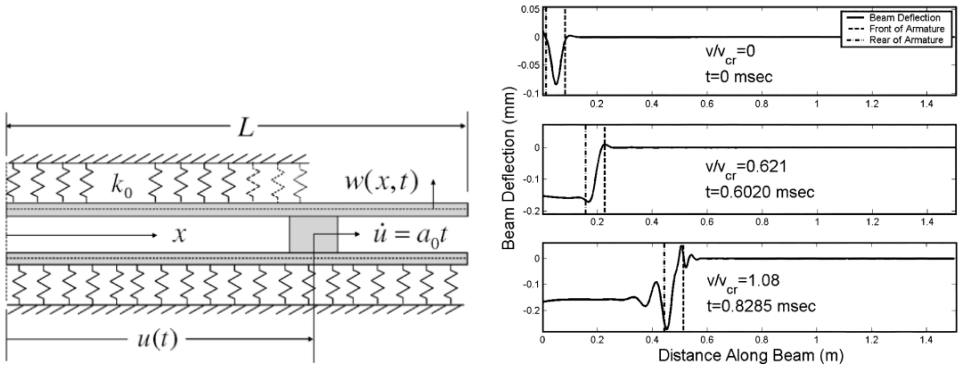

Figure 1.9. Beam-on-elastic foundation model (left) and calculated deflections for a railgun launch (right), © 2006 IEEE [47]

Johnson *et al.* also performed dynamic strain measurements on an electromagnetic launcher at Georgia Tech University [48]. Strain amplification was observed above a critical speed around 1 km/s, which was below the predicted Bernoulli-Euler speed of 1.4 km/s. Johnson proposed that this could be because of the "nonlinear load-deflection curve and the effective mass and rigidity of the foundation." It is reasonable to assume that the critical speed for the MCL could also be reduced.

Similar predictions were undertaken by a variety of researchers using different formulations of the beam on elastic foundation, involving both analytic as well as finite

element formulations [49-52]. In all critical bending speed scenarios, the critical speed is some function of rail shape and is not dependent on the slider material. The calculated critical wave speeds are also typically smaller than observed gouging speeds. Since gouging is highly dependent on slider material, and has no apparent dependence on rail shape, it is unlikely that bending waves are directly responsible for the formation of gouges. However, it is possible that dynamic wave amplification could generate wave perturbations on the rail surface that make it easier for gouges to form once above the critical speed.

1.2.4 SHEAR LOCALIZATION

When gouges were first observed in rocket sled experiments, the gouge craters were found to have a rippled surface with a tempered grain structure, micro-cracks, and significant thermo-plastic deformation. This was believed to partly be a result of "adiabatic slip" [53]. Adiabatic slip (also known as shear banding, "catastrophic" thermoplastic shear, and shear localization) is a localized band of extreme plastic strain that occurs when the rate of thermal softening exceeds the rate of work hardening in a material [36]. An example of shear bands during a micro-cutting operation is shown in Figure 1.10 [54].

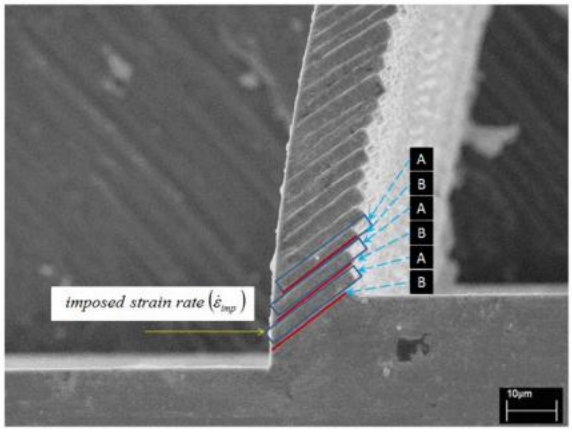

Figure 1.10. Shear band formation during micro-cutting of brass[4]

An excellent text on shear localization is by Bai and Dodd [55]. Bai and Dodd note that adiabatic shear bands (ASBs) occur in metals, polymers, and rocks but have not been observed in glasses or ceramics. Local shear strains can be as high as 100, with strain rates as high as 10^7 s^{-1}. ASB widths are typically on the order of 10-100 μm, with harder materials resulting in thinner shear bands. Under shock wave conditions the shear bands can be 0.1-0.3 μm wide, with a band spacing of ~10 μm. Shear bands usually have a much higher hardness than surrounding material due to rapid quench rates and small grain sizes. In steel, shear bands are usually martensitic, and often serve as crack-initiation sites.

Shear bands usually nucleate at existing stress discontinuities. Initiation is essentially a function of sufficiently high strain rate and sufficiently low thermal conductivity [55]. Pre-hardened materials tend to be more susceptible to shear banding than their annealed counterparts. This is a trend that is opposite to what is observed in gouging. Steel has a low resistance to ASB while copper has a high resistance to ASB [36], which is attributed to greater relative strain hardening in copper than in steel. The critical strain required for ASB is also a function of strain rate. At low strain rates heat

[4] Reprinted from W. Wang, S. To, C.Y. Chan, C.F. Cheung, W.B. Lee, "Elastic strain induced shear bands in the microcutting process," International Journal of Machine Tools & Manufacture, Vol. 50, pp. 9-18, Copyright 2010, with permission from Elsevier

conduction retards localization. At high strain rates, inertial effects (phonon drag) retard localization [56]. Approximate critical strains required for shear band formation are 0.2 for tungsten, 0.5 for tool steel and aluminum, 3.0 for brass, and 6.0 for copper [36].

Gerstle proposed that ASBs occurred during gouge formation, based on the presence of thin martensitic bands observed in AISI 1080 steel rail gouges [53]. There was also speculation by Cinnamon that gouging could be triggered by adiabatic shear band formation [16,21]. There is no doubt that ASBs can occur once a gouge is started, but they do not appear to be a strong factor in gouge onset since they have a dependence on hardness that is opposite that of gouging.

1.2.5 HYDROCODE MODELING

The bulk of computer modeling done on gouging has been performed using hydrocodes such as CTH, LS-DYNA, EPIC, and ABAQUS [26,57,58]. Hydrocodes are finite difference or finite element programs that model the propagation of stress waves in materials, using tabular equations of state and constitutive models to describe material behavior under complex dynamic loading. The program that has seen the greatest use for gouging is CTH [27,59,60]. CTH is an Eulerian-based shock physics code written at Sandia National Laboratories (SNL) that is capable of modeling materials under very large deformations and high strain rates. Details on CTH and its application to gouging can be found in [20] and [61].

CTH gouging calculations are usually carried out in 2D rectilinear coordinates and typically incorporate a surface perturbation to trigger gouging onset. In these models, a sliding body impacts a surface and causes a “hump” to form at the slider/rail interface. This hump is then over-run by the slider, creating a high-pressure core, severe plastic deformation, melting, and a counter-flowing material jet. This results in the mixing of the slider and rail materials [20,62]. Examples of gouging in CTH are shown in Figure 1.11.

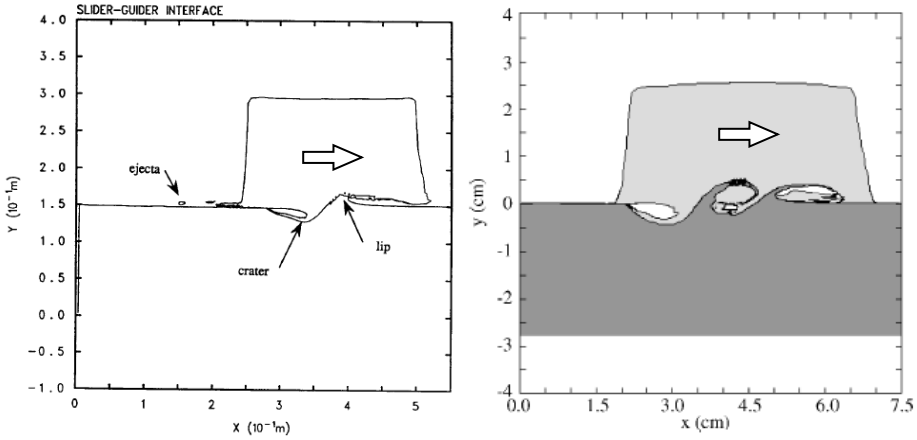

Figure 1.11. CTH hydrocode models of gouging[5]

An alternative to imposing an existing surface perturbation is to define a normal impact speed. Tachau proposed in 1991 that slider vibrations could result in an oblique impact during launch, and analyzed slider/rail gouging using an incident normal slider speed in CTH [63]. His conclusions were that an increasing "high pressure core" was the source of gouge formation, that no gouging was predicted for sliding speeds above 8 km/s, and that the rail surface can reach the melting temperature both with and without gouging.

In recent years, rocket sled research has focused on determining the constants for constitutive material models that incorporate temperature, strain, and strain-rate effects for use in gouging calculations [64,65]. The most common constitutive models are the Johnson-Cook (J-C) and Zerilli-Armstrong (Z-A) models. Both models perform well in capturing the overall effects of strain and strain-rate hardening, though the Z-A model generates better agreement between predicted and observed gouging morphologies [65,66]. Experiments at HHSTT were supplemented by Split Hopkinson bar and Taylor impact tests as well as impact flyer plate experiments using the slider and track materials of VascoMax 300 and AISI 1080 steel, respectively [21]. The predicted gouge shapes using the updated Z-A properties compared very well with experiments, with the CTH

[5] Reprinted from R.D.M. Tachau, C.H. Yew, T.G. Trucano, "Gouge Initiation in High-Velocity Rocket Sled Testing," Int. J. Impact Eng., Vol. 17, pp. 825-836, Copyright 1995, with permission from Elsevier

model calculating strain rates from 10^4-10^6 s^{-1}, pressures of 50-70 GPa, and temperature rises around 1,000 K.

1.2.6 STEFANI-PARKER MODEL

Stefani and Parker proposed that gouging was governed by the hardness of the harder material, the densities of the materials, and their sounds speeds [25]. A set of railgun experiments was conducted using copper rails and different slider materials, and a linear correlation was found between the hardness of the harder material (HV = Vickers microhardness in kg/mm^2) and the normal shock pressure P (GPa) that would be generated for the same material pair at the measured gouging speed. This empirical correlation can be expressed as Equation (1.9).

$$P = 0.073(HV) + 9.343 \tag{1.9}$$

The shock pressure estimate was performed by calculating the normal planar impact pressure using the Rankine-Hugoniot jump conditions and the slider and rail materials' Hugoniot data [67]. The Hugoniot data relates the pressure in a material to its particle speed behind a shock front. The Hugoniot curves for the two materials can then be used with the observed threshold gouging speed to calculate the effective normal planar impact pressure at that speed. This pressure is then plotted against the hardness of the harder material, with the results shown in Figure 1.12.

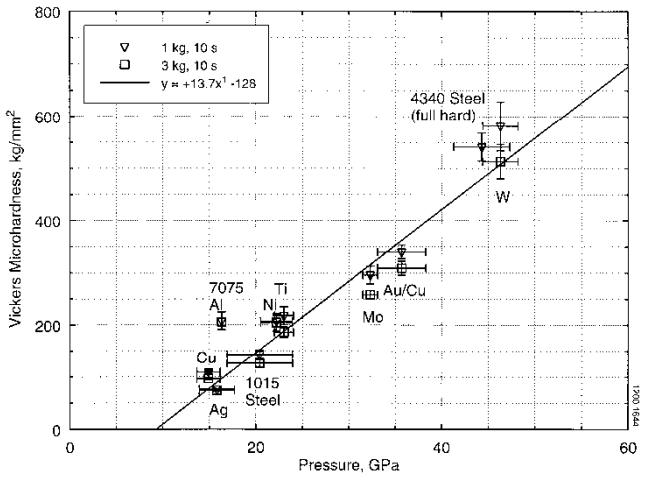

Figure 1.12. Stefani-Parker hardness/shock-pressure correlation (© 1999 IEEE) [25]

To estimate the critical sliding speed V_{crit} for a given material pair, the R-H equations are written with impact speed as a function of shock pressure, as shown in Equation (1.10) [30]. The subscripts *s* and *r* refer to the slider and rail materials, respectively.

$$\mathrm{V}_{crit} = \frac{-C_s}{2s_s} + \frac{1}{2}\sqrt{\left(\frac{C_s}{s_s}\right)^2 + \frac{4P}{\rho_s s_s}} + \frac{-C_r}{2s_r} + \frac{1}{2}\sqrt{\left(\frac{C_r}{s_r}\right)^2 + \frac{4P}{\rho_r s_r}} \qquad (1.10)$$

Using the pressure/hardness curve fit from Figure 1.12, a pressure is defined for a given material pair. This pressure then determines a critical sliding speed based on the Hugoniot curves. This procedure is shown schematically in Figure 1.13. The Stefani-Parker shock pressure method works well for most of the materials tested, but it over-predicts the shock pressure for the lead/lead system which gouges at low speeds (~250 m/s) [28]. Furthermore, Hugoniot curves do not exist for many engineering alloys, though the curve fitting constants can reasonably be substituted from similar materials, or estimated using a rule of mixtures approach [68]. Another potential shortcoming of this approach is that it does not explicitly incorporate strain-rate hardening. Dynamic hardness measurements (DHV) show a consistently higher value than the static hardness

(HV), but the relative increase varies by crystal structure [69,70]. However, Tabor's relationship that relates hardness to yield strength is still correct to first order for these dynamic hardness measurements.

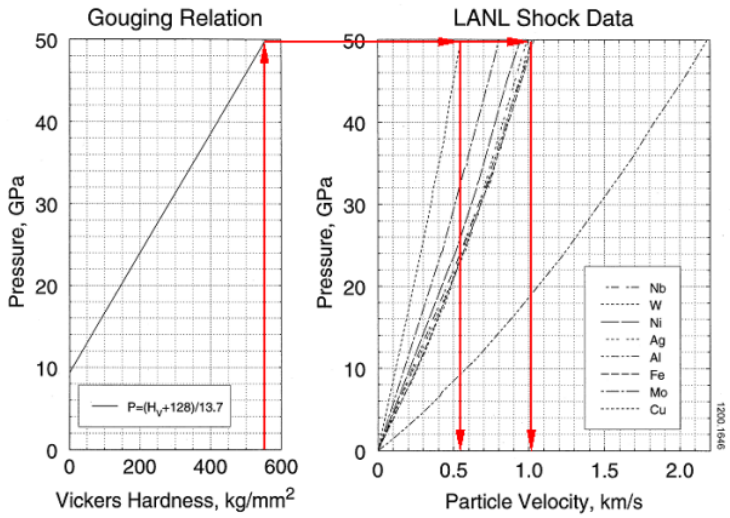

Figure 1.13. Stefani-Parker method for estimating gouging threshold speed[6]

[6] Illustration provided by Francis Stefani, The University of Texas at Austin.

1.3 Related Fields of Study

While a significant amount of research has been performed on understanding the evolution of gouging, there is a relative lack of work done to explore its causes. It is useful in this light to explore other fields of research which are related to gouging, indicated by similar morphology or operating conditions. Two such fields are discussed here: geologic shear folds, and explosive welding.

1.3.1 SHEAR FOLDS

In geology, shear folds occur when a region of layered materials is under compression or shear and develops "folds" whereby one layer becomes disturbed and flows into the surrounding layers. This has been addressed both as a form of buckling instability, and shear instability [71]. Folds are usually the result of multiple layers of "competent" (strong) and "less competent" materials under compressive loads [72]. The more competent layers tend to experience buckling failure, which requires initial curvature, inhomogeneous/anisotropic properties, or asymmetric loading [73-75]. Most shear folds involve rotational or "non-coaxial" shear, illustrated in Figure 1.14 [76].

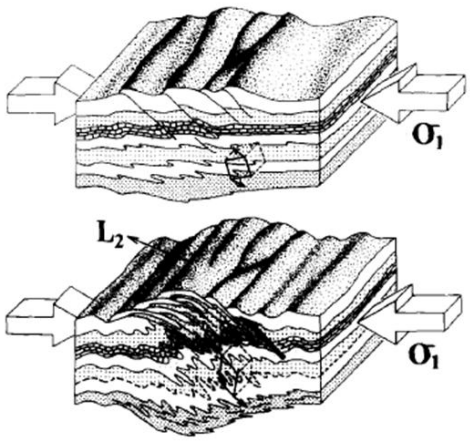

Figure 1.14. Illustration of geologic shear folding[7]

[7] Reprinted from B. Goscombe, "Intense non-coaxial shear and the development of mega-scale sheath folds in the Arunta Block, Central Australia," Journal of Structural Geology, Vol. 13, No. 3, pp. 299-318, Copyright 1991, with permission from Elsevier

Analysis of shear folds has largely been done by treating the materials as viscous Newtonian fluids and performing linear perturbation analyses [77-79]. In these analyses, buckling is primarily a function of viscosity difference between layers [80,81]. While buckling is the primary mechanism suggested for folds, analysis using simple shear shows that "passive" folds can be caused by amplification of perturbations, illustrated in Figure 1.15 [82,83]. This behavior is essentially a form of Kelvin-Helmholtz instability [84]. In addition to inter-layer property variations, shear folds are also greatly influenced by the presence of rigid inclusions and faults [85,86]. The intense shear around shear folds also results in the formation of shear bands [87,88]. Shear folds are themselves sometimes misinterpreted as shear bands [89].

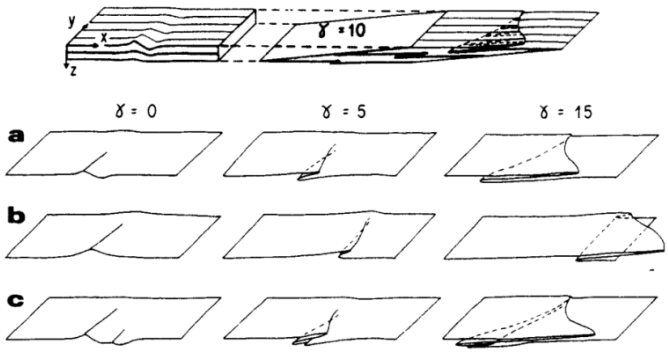

Figure 1.15. Evolution of shear folds triggered by a perturbation[8]

1.3.2 EXPLOSIVE WELDING WAVES

Explosive welding (EW) was developed as a material bonding technology in the 1960s. In explosive welding, a charge is detonated behind a flyer plate which then impacts a target plate a short distance away (Figure 1.16). Impact speeds can exceed 3 km/s, while the impact angle is controlled by the amount of explosive and geometry of

[8] Reprinted from P.R. Cobbold, H. Quinquis, "Development of sheath folds in shear regimes," Journal of Structural Geology, Vol. 2, pp. 119-126, Copyright 1980, with permission from Elsevier

the flyer and target plates. When the flyer plate impacts the target, the oxide layers on the two surfaces are removed via intense heating and shear loading, creating a strong metallic bond between the two substrates. The requirement for the critical impact angle for successful welding is given by an empirical relationship relating hardness of the softer material to the dynamic pressure [90-92], shown in Equation (1.11).

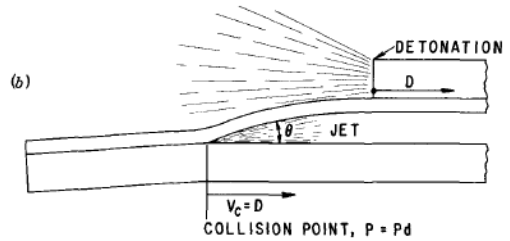

Figure 1.16. Explosive welding process illustration[9]

$$\theta_{crit} = 1.14\sqrt{\frac{H}{\rho V^2}} \tag{1.11}$$

The published work on explosive welding has largely been experimental, with some analytical derivations based on perturbation theory [93]. There has also been some modeling work using hydrocodes, though most of these assume an initial surface perturbation to trigger wave formation [94,95,97].

A proposed requirement for explosive welding is the formation of a re-entrant jet, illustrated in Figure 1.18. This thin counter-flowing metal is believed to remove the oxide layer from the incoming material which allows the strong metallic bond to form between the two substrates [96]. Inspection of EW microstructures has shown fine (~10 nm) grains, which suggests superheating for a few microseconds followed by rapid cooling [97]. The plastic deformation band surrounding the weld zone has significant strain

[9] With kind permission from Springer Science+Business Media: G.R. Cowan, O.R. Bergnrann and A.H. Holtzman, "Mechanism of bond zone wave formation in explosive – clad metals," Metallurgical Transactions, Vol. 2, No. 11, pp. 3145 -3155, 1971, Figure 1.

hardening, with an estimated strain rate on the order of 10^6 s^{-1} [98,99]. Shear bands were also found in the weld zone of explosively welded materials, and were thought to be partly responsible for the welding process [100,101].

As the impact speed increases the bond zone changes from a thin bonded layer, to a wavy interface (Figure 1.17 and Figure 1.18). The onset of EW waves was found to be dominated by the sliding speed, while wave amplitude and wavelength were largely a function of impact angle [102]. The behavior of EW waves led to a collective interpretation that they were a manifestation of fluid instabilities such as Kelvin-Helmholtz (K-H) waves or von Karman (VK) vortex streets [103].

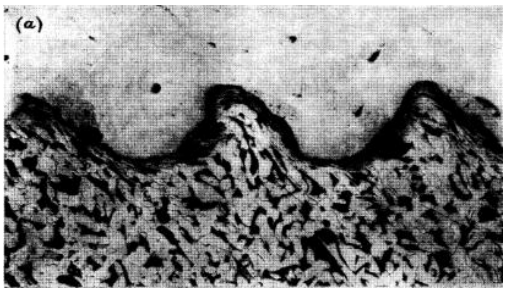

Figure 1.17. Explosive welding waves for brass on steel (cross-section view)[10]

The formation of K-H waves has been well described by Gerwin [104]: For inviscid fluids, the medium is unstable for all perturbation sizes. Liquids with higher viscosities stabilize longer perturbation wavelengths, and are thus less susceptible to instabilities. VK waves or "vortex streets" have been another explanation for EW waves.

[10] Reprinted from A.S.Bahrani, T.J.Black and B.Crossland, "The mechanics of wave formation in explosive welding," Proc. Roy. Soc. A, Vol. 296, pp. 123-136, 1966, with permission from The Royal Society

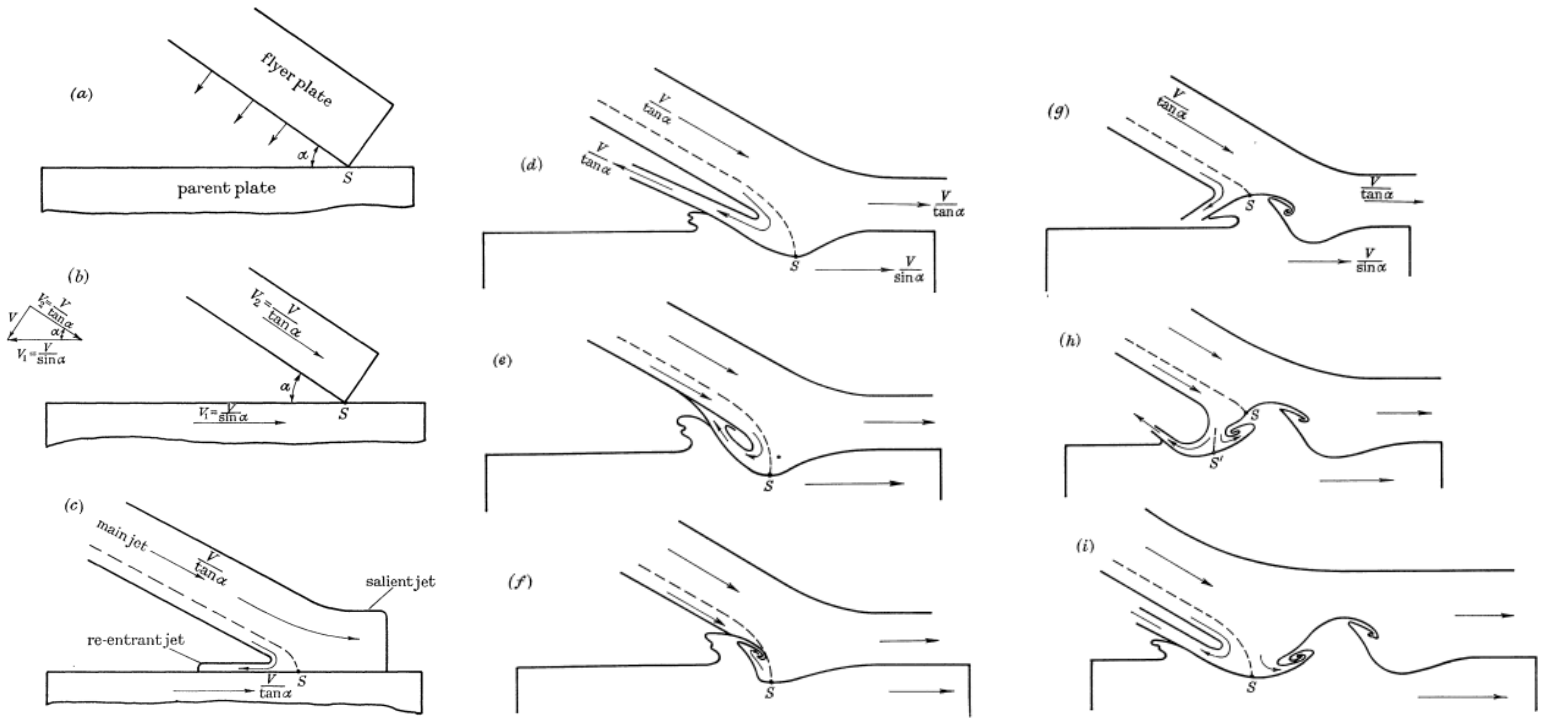

Figure 1.18. Illustration for re-entrant jet in explosive welding (left), and formation of welding waves (center, right)[11]

[11] Reprinted from A.S.Bahrani, T.J.Black and B.Crossland, "The mechanics of wave formation in explosive welding," Proc. Roy. Soc. A, Vol. 296, pp. 123-136, 1966, with permission from The Royal Society

Experiments by Cowan showed that the formation of EW waves were largely a function of exceeding a material-pair-dependent critical speed, with the resulting welding waves exhibiting a striking similarity to VK streets [105]. A particularly illustrative figure showing the evolution of EW waves with increasing speed is shown in Figure 1.19, comparing them to fluid vortices behind an obstacle.

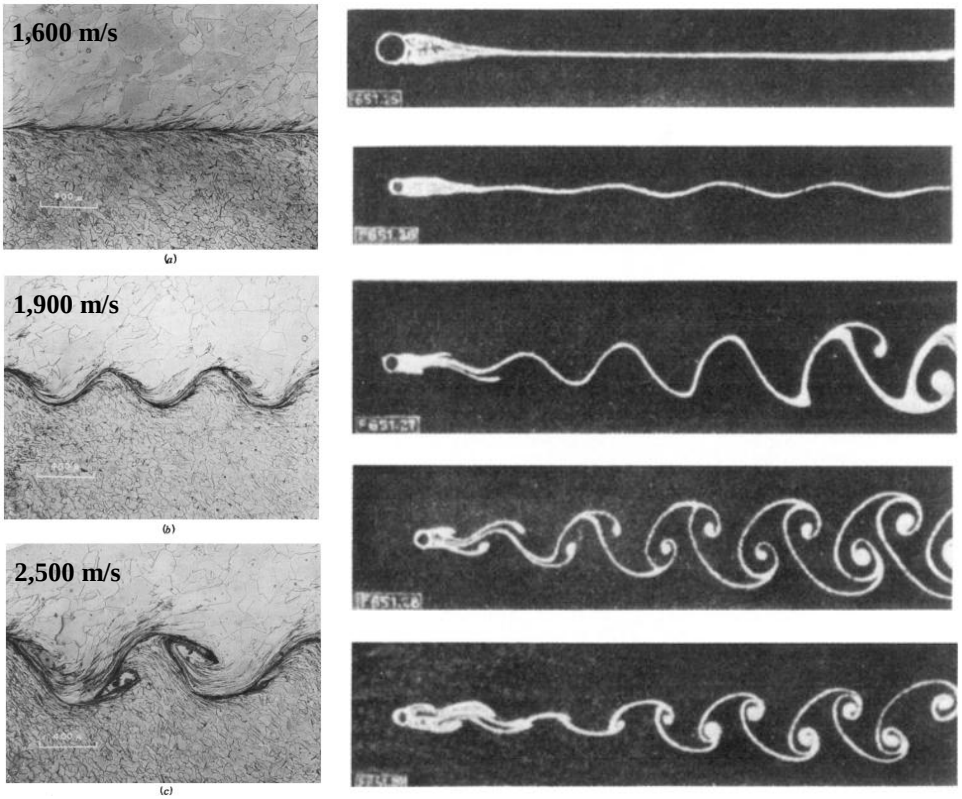

Figure 1.19. Comparison of explosive welding waves and von-Karman vortex streets [105]
Left: EW waves for Ni on 1008 steel, right: Flow of oil past a circular cylinder at increasing speeds[12]

Published critical speeds for EW waves are provided in Table 1.3. Cowan proposed an effective Reynolds number for the known material pairs and their critical speeds [105]. This effective Reynolds number is derived according to Equation (1.12),

[12] With kind permission from Springer Science+Business Media: G.R. Cowan, O.R. Bergnrann and A.H. Holtzman, "Mechanism of bond zone wave formation in explosive – clad metals," Metallurgical Transactions, Vol. 2, No. 11, pp. 3145 -3155, 1971, Figures 6,8.

where *Re* is the effective Reynolds number, *HV* is Vickers microhardness (kg/mm^2), ρ is mass density (kg/m^3), and *U* is velocity (m/s). Hardness is used as the threshold for determining deformation, as it is easily measured and partly contains strain-hardening information for the material. Assuming a known Reynolds number, the critical speed can be determined for a given material pair. The Reynolds number for each material pair is provided in the last column of Table 1.3. Note that the values are very high since the hardness was not first converted to Pascals.

$$Re = \frac{(\rho_A + \rho_B)U^2}{2(HV_A + HV_B)} \tag{1.12}$$

Table 1.3. Measured EW wave speeds for different material pairs [105]

Slider Material	**Rail Material**	**Slider Hardness** *HV*	**Rail Hardness** *HV*	**Wave Speed** *(m/s)*	$\mathbf{R_{eff} \times 10^7}$
DLP Cu	Al 1100	67	49	1,600	13.1
Ni "A"	Ni "A"	133	133	1,600	8.7
Ti 35A	AISI 1008	120	101	1,750	8.7
Ni "A"	AISI 1008	133	101	1,750	10.5
AISI 1008	AISI 1008	101	101	1,800	12.8
Al 1100	Al 1100	49	49	1,900	10.1
A-212	A-212	118	118	1,960	13.0
Ti 35A	Al 5051-T6	120	82	2,100	8.1
Al 6061-T6	Al 6061-T6	82	82	2,300	8.9
Ti 35A	Ti 35A	120	120	2,390	11.0
Mg ZE10A	Mg ZE10A	46	46	2,500	12.0

The welding wave model, based on fluid instability theory, predicts stable wave formation above a critical effective Reynolds number (Re_{cr}). Above Re_{cr} any perturbation size or asymmetry in flow results in unstable flow and the continuous formation of waves. Below Re_{cr} there is a regime where wave formation could depend on the size of

the perturbation if the flow is *metastable*, with lower Reynolds numbers requiring larger perturbations.

If the flow is metastable then there is then a lower critical Reynolds number (Re_{cr}*) below which no perturbation size results in wave formation. This range of instability thresholds (Re_{cr}*<Re<Re_{cr}) and its effect on welding waves has been described by Pai [106] and is shown in Figure 1.20. The collision at 0.9 km/s (Figure 1.20, left) indicates a sub-critical Reynolds number with immediate damping of the perturbation. The collision at 1.3 km/s (Figure 1.20, right) is in the middle regime where the perturbation is sufficient to cause stable wave formation.

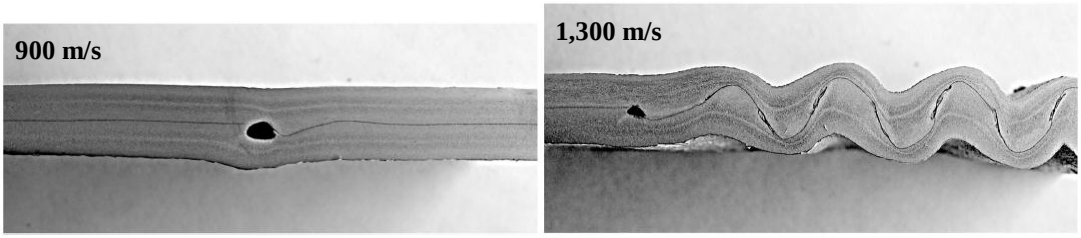

Figure 1.20. Effect of perturbation on EW for Al-Mn alloy at increasing speeds[13]

Chemin proposed that the viscous fluid model (VK waves) was not valid since geometric similarity tests were unsuccessful in producing welding waves [107]. This is an inherent limitation to using the effective Reynolds number, since the Reynolds number as defined for Newtonian fluids has a characteristic length-scale associated with it, while explosive welding does not.

Drennov performed experiments at impact speeds exceeding the sound speed (5-6 km/s), and observed wave formation despite speculation that oblique shocks would prevent this [108]. He found that as speed increased the wave amplitude peaked around Mach 1.5 before decreasing towards zero around Mach 2.0, with the microstructure

[13] With kind permission from Springer Science+Business Media: V.V. Pai, Ya.L. Luk'yanov, G.E. Kuz'min, I.V. Yakovlev, "Wave Formation in a High-Velocity Symmetric Impact of Metal Plates," Combustion, Explosion, and Shock Waves, Vol. 42, No. 5, pp. 611-616, 2006, Figures 4-5.

changing from solitary waves to turbulent mixing as speed increased [109]. Drennov also found that coatings with high dynamic strength and melting temperatures could prevent the onset of welding waves [110].

1.4 Scope of Dissertation

The goals of this effort were to (1) develop a new or revised predictive model for gouging, (2) expand on previous hypervelocity gouging work by testing new material combinations and test conditions using a railgun, and (3) investigate the microstructural evolution of rail material during gouge initiation. The experiments were performed over the course of several years with funding from both the Army Research Laboratory (ARL) and the Office of Naval Research (ONR). The results of the experiments are organized according to content, as opposed to being presented chronologically.

The remainder of this document is outlined as follows: Existing modeling approaches to gouging are discussed in Chapter Two, along with the application of models from other fields of research. The experimental methods are discussed in Chapter Three, with the results provided in Chapter Four. The interpretation and significance of the results are discussed in Chapter Five, with the conclusions provided in Chapter Six.

CHAPTER 2. MODELING

This chapter is focused on the application of existing models for gouging, as well as exploring models developed for explosive welding and fluid instability analyses. The Stefani-Parker (S-P) impact model for gouging will first be addressed, and extended to a simple acoustic impedance method. The effective Reynolds number approach used for explosive welding will then be applied to gouging. This approaches the problem from a fluid instability perspective, though strictly speaking it does not involve liquid metal properties.

The linear instability method suggested by numerous researchers over the last few decades, inspired by comparisons with the Kelvin-Helmholtz (K-H) instability, will then be applied to the problem of gouging. A numerical method based on spectral collocation is used. Lastly, the dynamic behavior of metals is addressed. Advanced constitutive models are applied to the previous gouging models in an effort to understand disagreements between predictions and experiments.

The intent here is to apply existing modeling techniques to the problem of gouging. The linear instability analysis which constitutes the bulk of this chapter lays out a general framework for solving stratified flow problems, but is limited to the problem of viscous incompressible flow which is relevant to the K-H instability. This approach could be extended to problems of compressible flow, elasticity, heat transfer, variable material properties, and so on. However, this is beyond the scope of this dissertation and is best left for future work.

2.1 Asperity Impact / Acoustic Impedance Models

The first successful model to predict the onset of gouging was developed by Stefani and Parker [25]. This approach essentially stated that gouging would occur if both materials failed due to the impact stresses generated by contacting asperities. A graphical depiction for gouge initiation by asperity impact is shown in Figure 2.1 [22]. In this scenario two asperities suddenly contact each other at high speeds which results in an impact stress. The S-P approach is to approximate this is as planar impact problem. In reality, impacting asperities have leading edges with some angle which will decouple the sliding velocity into a horizontal and vertical component.

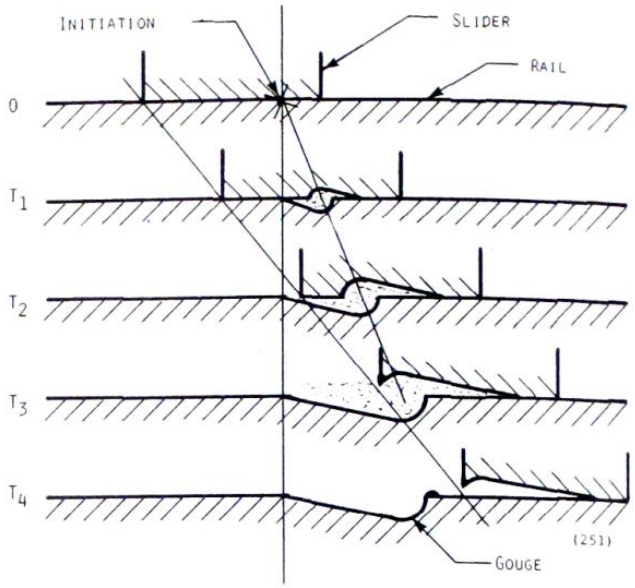

Figure 2.1. Illustration for a gouge initiated by impacting asperities[14]

The method was semi-empirical, and related the measured threshold sliding velocity for gouging to the normal shock pressure that would be generated by the same materials under planar impact at that velocity. Their approach used the Hugoniot equation

[14] Reprinted from J.P. Barber and K.P. Bauer, "Contact Phenomena at Hypervelocities," Wear, Vol. 78, pp 163-169, Copyright 1982, with permission from Elsevier

of state (EOS) for the materials and the Rankine-Hugoniot jump conditions to determine the shock pressure that would be generated at impact. If the impact pressure exceeds the yield strength of both materials then gouging is assumed to occur.

The impact pressure generated under planar conditions is a function of the impact velocity, and the material properties. A model for the planar impact of two bodies is illustrated in Figure 2.2 as an X-T (position-time) diagram. Material "A" is moving towards material "B" and impacts it at time t=0. Prior to impact both materials are in a state of zero-stress. Once impact occurs, a compression wave is generated which propagates into both materials, and the interface between the materials moves with a new particle velocity u_I. The pressure behind the two shock waves is the same in both materials, but the wave velocities are different as determined by their material properties.

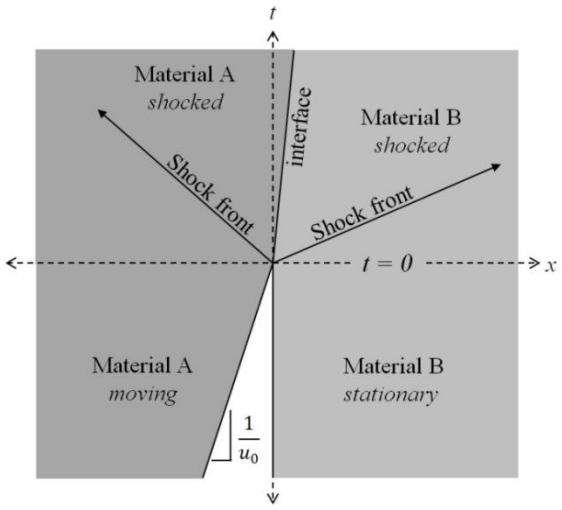

Figure 2.2. Position-time planar impact diagram

As discussed in the previous chapter, elastic materials can admit two forms of volumetric waves: dilatational (P-waves) and distortional (shear, or S-waves). Under planar normal impact conditions only P-waves are generated. The velocity for P-waves is given by Equation (1.4), which applies to materials under elastic loading. The typical elastic-plastic behavior of a shocked material is illustrated in Figure 2.3. The wave speed

in the elastic region is determined by the Lamé constants until the Hugoniot elastic limit (HEL) is reached. The HEL, given in Equation (2.1), represents the yield point of the material in planar shock propagation, where σ_Y is the uniaxial yield strength of the material.

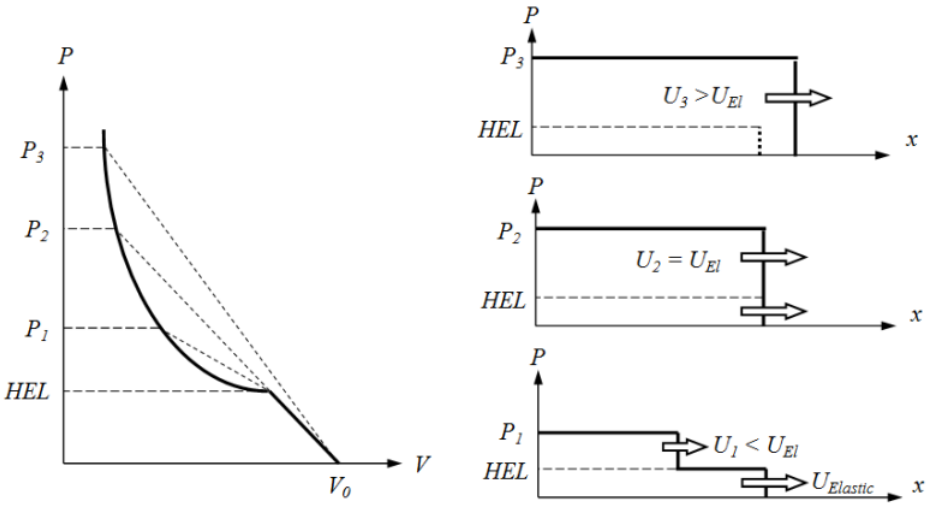

Figure 2.3. P-V curve showing HEL (left), and separation of elastic and plastic waves (right)

$$\sigma_{HEL} = \frac{1-\nu}{1-2\nu}\sigma_Y \tag{2.1}$$

For the plastic region a different approach must be used. In this case the plastic wave speed is given by slope of the *Rayleigh* line which connects the HEL of the material and the current stress/strain state. The slope of this line provides an effective modulus which is used in place of bulk modulus to determine the plastic wave speed, shown in Equation (2.2). An incident wave in this intermediate region will break into two fronts: an elastic wave, and a slower plastic wave. At a sufficiently high pressure, the sound speed in the compressed material exceeds that of the elastic sound speed and a single shock front is generated. A single shock front is an implicit assumption in the S-P model. In this and the following equations U_S is the shock velocity, u_p is the particle velocity, P is the pressure, V is volume, E is energy, σ is stress, and ε is strain.

$$U_{plastic} = \sqrt{\frac{\partial\sigma/\partial\varepsilon}{\rho}} \tag{2.2}$$

At high impact velocities the compression of a solid increases its density and hence its sound speed. An equation of state must be used that relates the pressure of the solid to its volume or density. A common equation of state used in impact mechanics for metals is the Mie-Grüneisen equation, given by Equation (2.3). Here, γ is the Grüneisen parameter, and the ratio γ/V is considered constant.

$$P - P_0 = \frac{\gamma}{V}(E - E_0) \tag{2.3}$$

The conservation of mass, momentum, and energy equations for the shock front are provided in (2.4)-(2.6). These are the Rankine-Hugoniot (R-H) jump conditions [67]. The subscripts 0 and 1 describe the material in front of (before) and behind (after) the shock front, respectively.

Conservation of mass: $\rho_0 U_S = \rho_1\left(U_S - u_p\right)$ (2.4)

Conservation of momentum: $P_0 + \rho_0 {U_S}^2 = P_1 + \rho_1\left(U_S - u_p\right)^2$ (2.5)

Conservation of energy: $E_1 - E_0 = \frac{1}{2}(P_1 + P_0)(V_0 - V_1)$ (2.6)

The three conservation equations are completed using a fourth equation that relates shock speed to particle speed. Most isomorphic materials follow a simple linear relationship given by (2.7), where c_0 and s are curve fitting parameters [111]. The combination of the EOS and the R-H conservation equations results in a P-V relation (2.8) which is used to describe the Hugoniot curve [112]. Examples of experimentally

determined Hugoniot curves are shown in Figure 2.4 [67]. The Hugoniot is a locus of end-states for a shocked material, and should not be confused with a particle path. Rather, a particle will follow a straight line from the initial P-V state to the end-state on the Hugoniot curve, assuming no phase changes occur.

$$U_S = c_0 + su_p \tag{2.7}$$

$$P - P_0 = \frac{c_0^2(V_0 - V_1)}{[V_0 - s(V_0 - V_1)]^2} \tag{2.8}$$

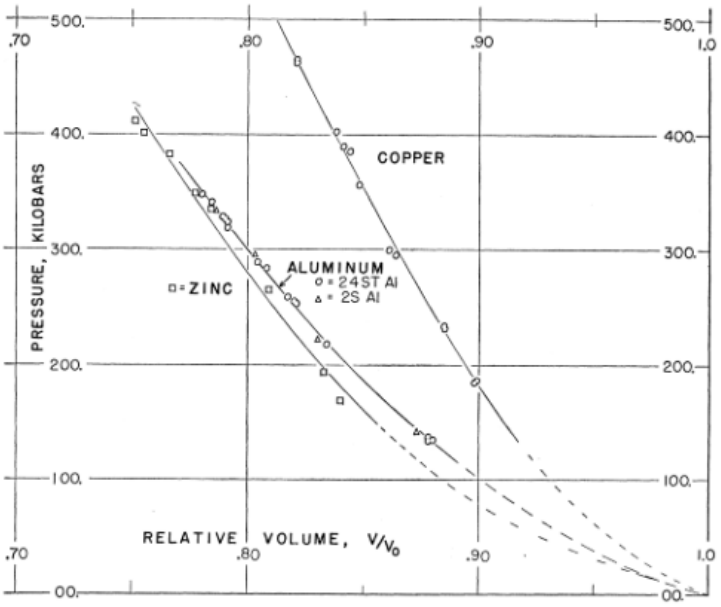

Figure 2.4. Hugoniot (P-V) curves for several isotropic materials [67]
© 1955, The American Physical Society

Referring back to Figure 2.2, the R-H jump conditions determine the pressures behind the shock fronts in materials A and B, given by Equations (2.9) and (2.10), respectively. However, since the impact interface is continuous, these two pressures must be identical. Setting $P_A = P_B$ one obtains a quadratic equation for the interface particle velocity u (2.11). Once u_p is determined, it can be plugged back in to either (2.9) or (2.10) to calculate the pressure (2.12).

$$P_A = \rho_A\left[c_A + s_A(u_0 - u_p)\right](u_0 - u_p) \tag{2.9}$$

$$P_B = \rho_B(c_B + s_B u_p)u_p \tag{2.10}$$

$$\begin{gathered}(\rho_B s_B - \rho_A s_A){u_p}^2 + (\rho_A c_A + \rho_B c_B + 2\rho_A s_A u_0)u_p \\ - \rho_A(c_A + s_A u_0)u_0 = 0\end{gathered} \tag{2.11}$$

$$u_p = \frac{-b \pm \sqrt{b^2 - 4ac}}{2a} \tag{2.12}$$

$$a = \rho_B s_B - \rho_A s_A \tag{2.12b}$$

$$b = \rho_A c_A + \rho_B c_B + 2\rho_A s_A u_0 \tag{2.12c}$$

$$c = -\rho_A(c_A + s_A u_0)u_0 \tag{2.12d}$$

Equations (2.9)-(2.12) can alternatively be used to determine a critical impact velocity as a function of a specified interface pressure, which results in (2.13). This form was previously given by Satapathy [30].

$$\mathrm{V}_{crit} = \frac{-C_s}{2s_s} + \frac{1}{2}\sqrt{\left(\frac{C_s}{s_s}\right)^2 + \frac{4P}{\rho_s s_s}} + \frac{-C_r}{2s_r} + \frac{1}{2}\sqrt{\left(\frac{C_r}{s_r}\right)^2 + \frac{4P}{\rho_r s_r}} \tag{2.13}$$

If the threshold condition of interest is the onset of yielding, it is tempting to use handbook values for yield strength or HEL for the pressure term in (2.13). Doing so results in the behavior shown in Figure 2.5. The approach using these assumptions does not result in a good correlation. What is lacking is the effect of strain and strain-rate hardening that will presumably occur in these loading conditions. Tabulated values for the material properties are provided in Table 2.1.

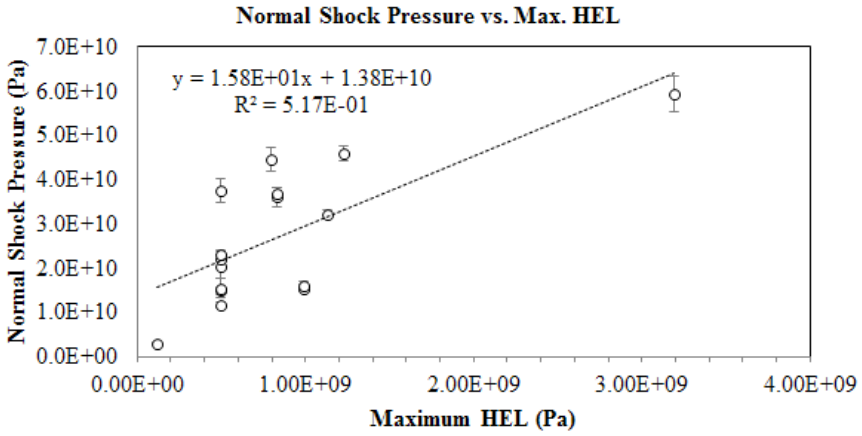

Figure 2.5. Normal shock pressures vs. Hugoniot Elastic Limit (HEL)

Table 2.1. Material properties used in shock pressure calculations

Material	**Hardness**	**Density**	**E**	**ν**	**λ**	**G**	**c_0**	**s**	**c_D**	**Z** x10^6
	HV	*kg/m^3*	*GPa*		*GPa*	*GPa*	*m/s*		*m/s*	*kg/m^2*s
Slider Materials										
AISI 304	129 ± 6	7,890	200	0.29	107	78	4,580	1.49	5,763	45.5
AISI 4340	228 ± 11	7,850	205	0.29	110	79	4,670	1.44	5,850	45.9
VascoMax 300	545 ± 27	7,970	190	0.28	97	74	3,940	1.60	5,541	44.2
Pb	10 ± 1	11,340	14	0.42	26	5	2,030	1.47	1,775	20.1
C11000-H02	109 ± 3	8,890	115	0.33	84	43	3,940	1.49	4,378	38.9
AA7075-T6	175 ± 9	2,810	72	0.33	52	27	3,940	1.49	6,149	17.3
C11000	88 ± 4	8,890	115	0.33	84	43	3,940	1.49	4,378	38.9
AA7075-T6	208 ± 17	2,810	72	0.33	52	27	5,200	1.36	6,149	17.3
Au80-Cu20	340 ± 13	17,767	83	0.41	128	29	3,203	1.55	3,245	57.6
AISI 1015 (A)	143 ± 8	7,870	200	0.29	107	78	4,670	1.44	5,771	45.4
Ag	75 ± 2	10,490	76	0.37	79	28	3,178	1.73	3,580	37.6
Mo	296 ± 17	10,210	275	0.31	171	105	5,080	1.29	6,110	62.4
Ni	207 ± 11	8,870	207	0.31	129	79	4,501	1.63	5,687	50.4
W	581 ± 47	19,200	400	0.28	199	156	4,040	1.23	5,161	99.1
Ti*	218 ± 17	4,500	116	0.34	92	43	4,842	1.14	6,299	28.3
AISI 4340	541 ± 27	7,850	205	0.29	110	79	4,670	1.44	5,850	45.9
Rail Materials										
AISI 1080	309 ± 15	7,850	205	0.27	95	81	4,670	1.44	5,712	44.8
Pb	10 ± 1	11,340	14	0.42	26	5	2,030	1.47	1,775	20.1
C11000-H00	50 ± 3	8,890	115	0.33	84	43	3,940	1.49	4,378	38.9
C11000-H02	88 ± 4	8,890	115	0.33	84	43	3,940	1.49	4,378	38.9

Strain hardening can be accounted for by using the measured micro-hardness of the materials, which was the approach used by Stefani and Parker. The hardness used in this method is the Vickers micro-hardness (HV, units in kg/mm^2) which is subsequently converted to Pa by multiplying by 9.81×10^6. This results in a better correlation between the normal shock pressure and the maximum hardness (correlation coefficient of 95% vs. 75%), as shown in Figure 2.6. The calculated values are also provided in Table 2.2

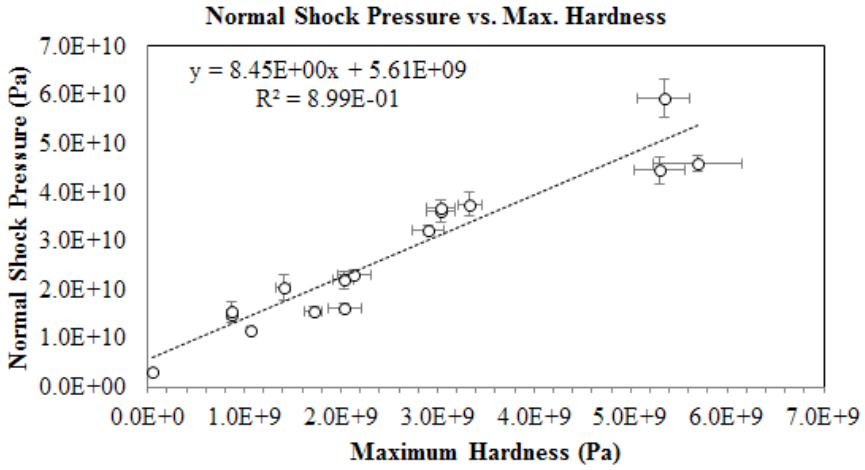

Figure 2.6. Normal shock pressure vs. maximum hardness

At low impact velocities the densities of the materials do not change appreciably and hence the "speed of sound" can be treated as a constant. In this case the curve fitting parameter *s* is set to zero and Equations (2.9)-(2.11) become Equations (2.14)-(2.16). Note that the dilatational sound speed given by Equation (1.4) should be used for c_A, as c_0 is from an experimental curve-fitting approach for high-pressure conditions.

$$P_A = \rho_A c_A (u_0 - u_p) \tag{2.14}$$

$$P_B = \rho_B c_B u_p \tag{2.15}$$

$$u_p = \frac{\rho_A c_A}{\rho_A c_A + \rho_B c_B} u_0 \tag{2.16}$$

Table 2.2. Shock pressure calculations

Slider	Rail	V_{gouge}	P_{shock}	P_{linear}
		m/s	*GPa*	*GPa*
AISI 304	AISI 1080	1,585 ± 79	36.1 ± 2.2	35.8 ± 1.8
AISI 4340	AISI 1080	1,610 ± 81	36.8 ± 1.5	36.5 ± 1.8
Vascomax 300	AISI 1080	2,438 ± 122	59.3 ± 3.9	54.2 ± 2.7
Pb	Pb	245 ± 12	3.1 ± 0.1	2.5 ± 0.1.0
C11000-H02	C11000	600 ± 30	11.7 ± 0.5	11.7 ± 0.6
AA7075-T6	C11000	1,400 ± 70	15.5 ± 1.0	16.8 ± 0.8
C11000	C11000	746 ± 50	14.9 ± 0.9	14.5 ± 1.0
AA7075-T6	C11000	1,300 ± 65	16.2 ± 1.0	15.6 ± 0.8
Au80-Cu20	C11000	1,346 ± 75	37.6 ± 2.6	31.3 ± 1.7
AISI 1015 (A)	C11000	977 ± 110	20.5 ± 2.7	20.5 ± 2.3
Ag	C11000	770 ± 90	15.5 ± 2.1	14.7 ± 1.7
Mo	C11000	1,268 ± 30	32.2 ± 0.9	30.4 ± 0.7
Ni	C11000	996 ± 70	22 ± 1.8	21.9 ± 1.5
W	C11000	1,474 ± 45	45.9 ± 1.7	41.2 ± 1.3
Ti*	C11000	1,420 ± 55	23 ± 1.0	23.3 ± 0.9
AISI 4340	C11000	1,878 ± 90	44.5 ± 2.7	39.6 ± 1.9

Combining (2.15) and (2.16) results in the interface pressure, given by (2.17). This method is also known as an acoustic impedance approach, since it can be written using characteristic impedances Z_i defined as $Z_i = \rho_i c_i$ [113], shown in (2.18). The shock method for determining impact pressure is not always practical if the Hugoniot constants c_0 and s are unknown, which is the case for many alloys of interest. The acoustic impedance approach does not suffer from this limitation, although it may not be as accurate for high-pressure impacts. To see how these two methods compare for gouging, the same procedure for correlating planar shock pressure to hardness is applied using the acoustic impedance method. The results are shown in Figure 2.7. The approach works about as well as the normal shock method (correlation of 94% vs. 95%).

$$P = \frac{\rho_A c_A \rho_B c_B}{\rho_A c_A + \rho_B c_B} u_0 \tag{2.17}$$

$$P = \frac{Z_A Z_B}{Z_A + Z_B} u_0 \tag{2.18}$$

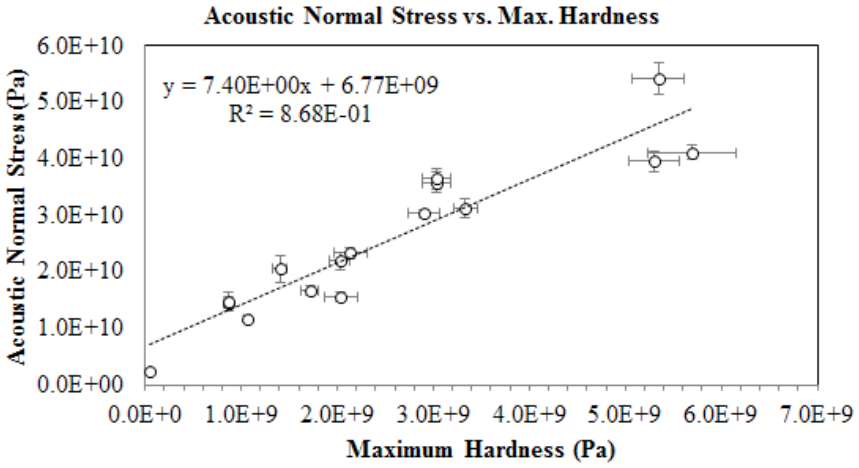

Figure 2.7. Acoustic normal stress vs. maximum hardness

An alternative to the normal acoustic impedance model is a shear impedance model. This approach has been used for solid/fluid interactions [114], as well as for the generalized slip waves discussed in the previous chapter [39]. The only difference between this and the normal impedance method is the impedance term $Z_i = \rho_i c_i$ is defined using the shear wave speed instead of the dilatational wave speed. The results of this method are shown below in Figure 2.8. The correlation is almost as good (91%). The resulting shear stresses in this approach are extremely high, roughly an order of magnitude higher than the fundamental crystallographic shear strength of metals. This is likely a by-product of the linear impedance approach over-estimating the actual shear stress.

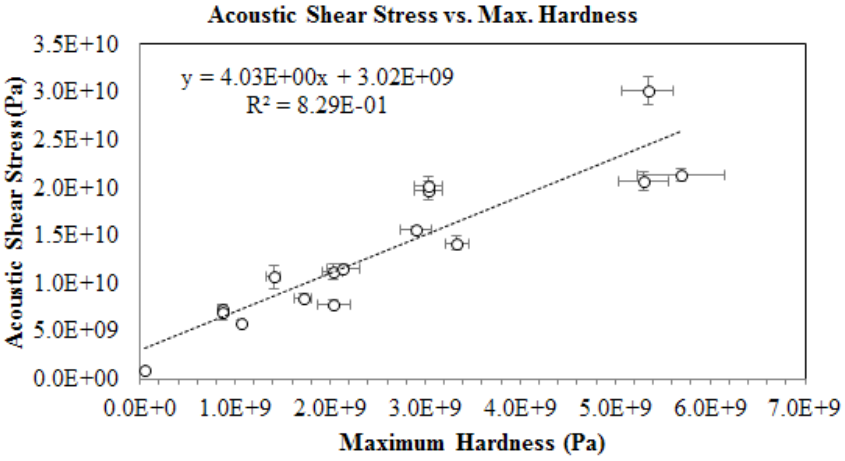

Figure 2.8. Acoustic shear stress vs. maximum hardness

2.2 Explosive Welding (Fluid Instability) Models

There is a remarkable degree of similarity between gouge craters and explosive welding waves. Both are dominated by the sliding velocity of the material pair, have similar damage morphologies, and have similar threshold velocities. The most successful approach to predicting the onset of welding waves is to use an effective Reynolds number *Re*, derived by Cowan [105] and given by Equation (2.19). Note that, unlike the approach used by Cowan, SI units for hardness (Pa) will be used here.

$$Re = \frac{(\rho_A + \rho_B)U^2}{2(H_A + H_B)} \tag{2.19}$$

To test the productiveness of this approach, the pressure term in (2.19) is plotted against the mean hardness for the gouging data, with the results shown in Figure 2.9. The slope of the linear regression line is the Reynolds number, which in this approach equals 4.7. The accuracy of this method is very good, with a correlation coefficient of 96%, better than the acoustic or normal shock methods employed earlier.

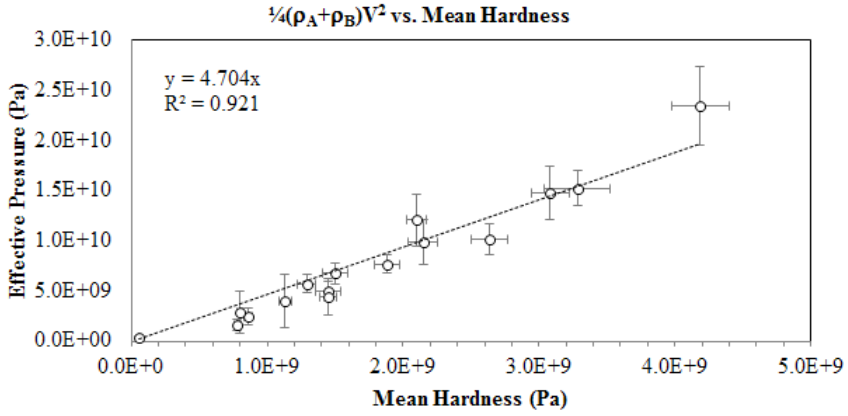

Figure 2.9. Effective Reynolds number vs. mean hardness

A problem with the Reynolds number approach is that it implicitly requires a characteristic length-scale – at least in the conventional formula for Reynolds number as given by (2.20). In this equation L is the *characteristic length*, and μ is the dynamic viscosity. As a general definition, the Reynolds number is the ratio of inertial forces to viscous forces. The Reynolds number equation in (2.20) is obtained by dividing the inertial fluid forces (ρV^2) by the Newtonian viscous stress ($\sim \mu V/L$). In Cowan's approximation, the viscous stress is replaced by the hardness of the materials so the characteristic length-scale is omitted.

$$Re = \frac{\rho U L}{\mu} \tag{2.20}$$

The critical effective Reynolds number from Equation (2.19) can be used to estimate the characteristic length-scale used in Equation (2.20). If the parameters for gouging on copper are used (V = 1,500, ρ = 8,940, Re = 5), the effective viscosity can be plotted as a function of length-scale. This is shown in Figure 2.10, over the range of 10^{-9} m to 1 m.

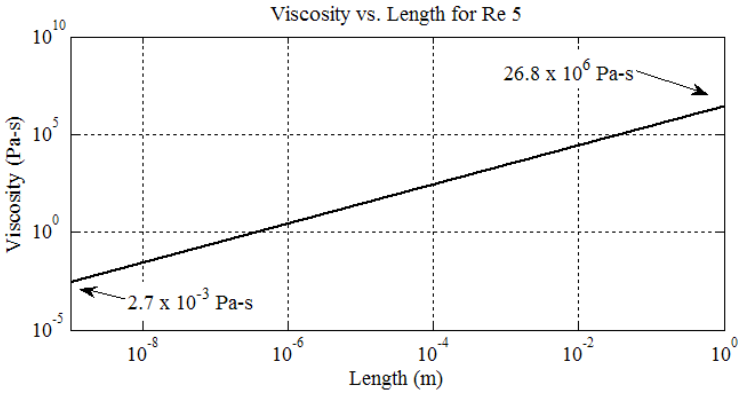

Figure 2.10. Viscosity as a function of characteristic length for Reynolds number = 5

It is prudent to search for another dimensionless parameter that is better suited to gouging (and explosive welding waves). In explosive welding, the waves have

historically been compared to Kelvin-Helmholtz (K-H) waves which occur in stratified fluids, shown in Figure 2.11 [115]. For K-H instability the threshold velocity can be derived using fluid mechanics and linear perturbation theory. It is usually assumed that the fluids are inviscid and that the only stabilizing forces are surface tension and gravity (assuming a denser fluid is on bottom). The dimensionless variable that relates to K-H instability is the Richardson number, given by (2.21). Here, g is gravitational acceleration, and h is flow height. This represents the ratio of potential to kinetic energy (the density terms in the numerator and denominator cancel out), but it still involves a characteristic length-scale.

Figure 2.11. Atmospheric Kelvin-Helmholtz waves [115]

$$Ri = \frac{gh}{U^2} \tag{2.21}$$

A third option is the Euler number, given in (2.22). This is also known as the cavitation number, and is the ratio of the pressure drop across an obstacle to the kinetic energy of the flow. This is a more appropriate parameter for gouging or explosive welding waves as it avoids a characteristic length-scale. The results obtained in Figure 2.9 can therefore be more thought of as determining the effective inverse Euler number for gouging.

$$Eu = \frac{\Delta p}{\rho U^2} \tag{2.22}$$

In Equation (2.22) the pressure term is applicable to a single fluid. Since multiple materials are involved in gouging it is appropriate to use the acoustic impedance method discussed earlier to determine the dynamic pressure. The outcome of this is shown in Figure 2.12 and Figure 2.13. The results using normal impact pressure provides a slightly better fit than the effective Reynolds approach. Both of these latter approaches are also better at capturing the middle region of the hardness curve, as the Reynolds number method tends to over-predict the pressure.

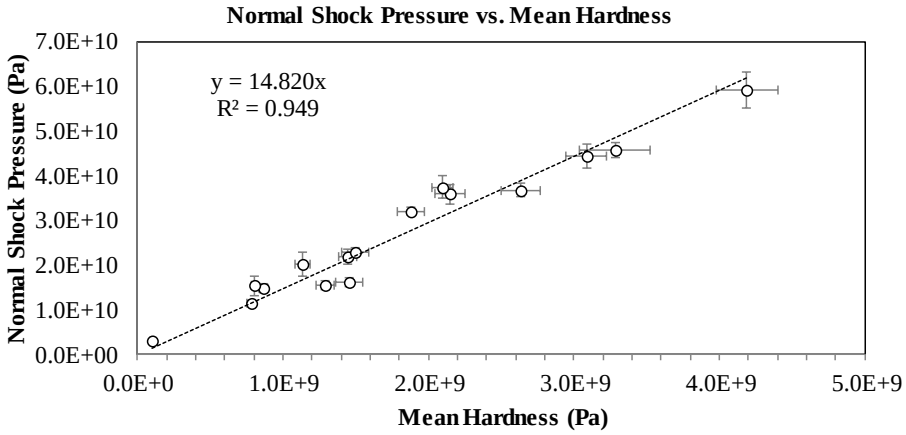

Figure 2.12. Normal shock pressure vs. mean hardness

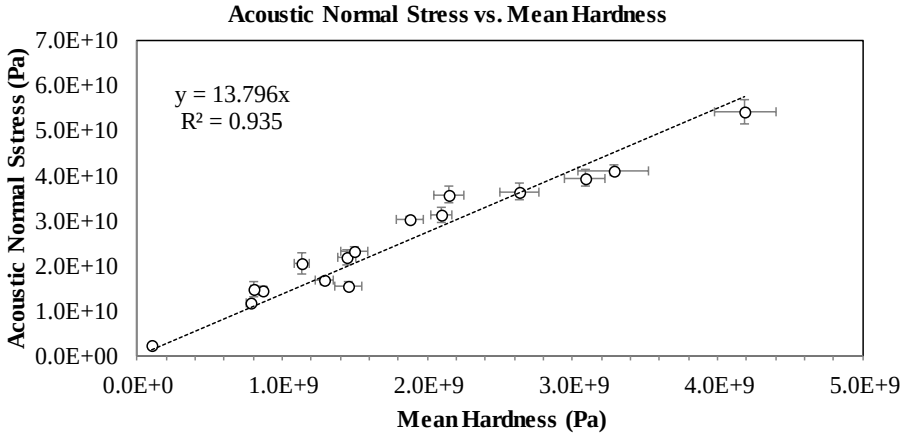

Figure 2.13. Acoustic normal stress vs. mean hardness

Results using the shear impedance method are shown in Figure 2.14. There is a better correlation with the average hardness value compared to the maximum hardness, as in the previous two comparisons. While the above approaches work well, the use of the mean hardness (as opposed to the maximum hardness) is questionable. In both gouging and explosive welding both materials are required to deform, so using the average hardness is counterintuitive. It is possible that this averaged-hardness approach is an example of a disconnect between correlation and causality.

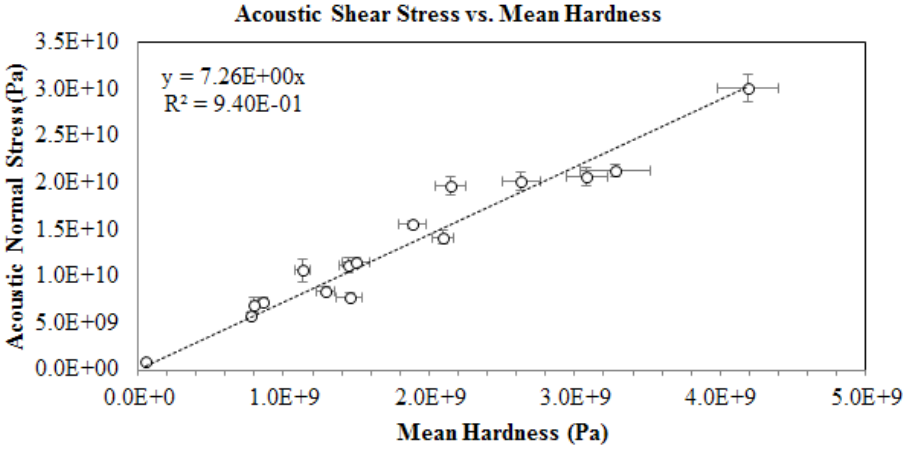

Figure 2.14. Shear impedance stress vs. mean hardness

2.3 Linear Stability Analysis

There is a strong conceptual correlation between gouging, explosive welding waves, and fluid instabilities. Using simple zeroth-order approaches, very good correlations can be made between the dynamic pressure and material strengths. However, to see if gouging can be treated as an instability, it is worthwhile to explore linear stability analysis.

A system is considered stable if random perturbations are damped out over time [116,117]. The general approach to instability analysis as discussed by Landau is to superimpose a non-steady perturbation onto a steady solution [118]. In the case of one fluid flowing over another or *stratified* flows, instability depends on several variables. If the densities are different, and the lighter fluid is on bottom then the system can experience so called "gravity waves" or the Rayleigh-Taylor (R-T) instability [119,120]. If one fluid is flowing relative to another, then the Kelvin-Helmholtz (K-H) instability can form.

In the instability approach discussed here, a spatial and temporal disturbance is superimposed on a steady flow, and solved to see if the perturbation grows over time. The analysis is limited to 2D disturbances. Squire's theorem states that any 3D velocity perturbation in a linear system can be reformulated as a 2D perturbation, with the 2D formulation being more unstable [121]. This also applies to pressure and temperature perturbations, which follow the same functional form as velocity [122]. Different perturbation types grow at different rates, have different characteristic wavelengths, and travel at different velocities. However, the velocities of perturbation waves in plane flow are expected to lie within the velocity range of the flow [123]. That is, disturbances cannot result in perturbation velocities that travel faster than the maximum flow velocity.

2.3.1 BACKGROUND

The analysis performed here is based on 2D planar stratified flow, as illustrated in Figure 2.15. In this scenario, both fluids have specified velocities at the outer boundaries. Planar incompressible Couette flow with a single fluid is considered stable at all Reynolds numbers [118]. However, as a property is allowed to vary throughout the fluid there is a chance of instability growth [124,125]. This is especially true for long wavelength disturbances [126]. Most of the published analysis on stratified flows has been for fluids of different viscosities, though density stratification has also been incorporated [127-129].

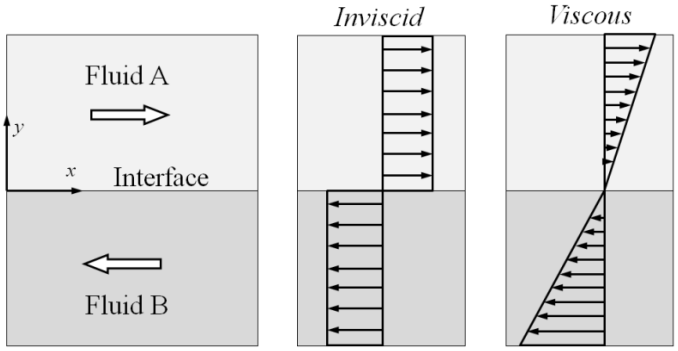

Figure 2.15. Illustration of stratified fluid flows.

For inviscid flows the fluids do not exert any shear stresses, so each region has a constant velocity profile and there is a discontinuity in velocity at the interface. For viscous flows the velocity varies linearly in each flow field, and is continuous across the interface (no-slip condition). In the general case of inviscid K-H instability where gravity, surface tension and viscosity are ignored, the fluid is unstable for all velocity perturbations [104].

The method of analysis in almost all published work on stratified flow instability takes the form of linear stability analysis. In this method, the governing equations are written for each flow field. Boundary conditions (BCs) are applied to the outside of each region, and jump conditions (JCs) specify the relationship between the two flows at the interface. These equations are then solved for the steady solution. Once the steady

solution is determined, a generic form for a perturbation is added to the governing equations. This results in a new set of equations for the two flow fields as well as the boundary and jump conditions. These perturbation equations are then solved to determine the perturbation coefficients. If the calculated perturbation coefficients result in an increase of perturbation size with time, the flow is unstable.

2.3.2 GOVERNING EQUATIONS

The governing equations for continuum mechanics employ conservation of mass, momentum, and energy. The Cartesian coordinate system is used, with the primary independent field variable for fluids being the velocity vector $\boldsymbol{u}$, given as $\boldsymbol{u} = u\hat{\imath} + v\hat{\jmath}$. The variables $\hat{\imath}$ and $\hat{\jmath}$ are the unit normal vectors in the *x* and *y* directions, respectively. The generalized equation for conservation of mass without chemical reactions is given by (2.23). Expanding the divergence operator and writing out all terms results in (2.24).

$$\frac{\partial \rho}{\partial t} + \nabla \cdot (\rho u) = 0 \tag{2.23}$$

$$\frac{\partial \rho}{\partial t} + \rho\left(\frac{\partial u}{\partial x} + \frac{\partial v}{\partial y}\right) + \frac{\partial \rho}{\partial x}u + \frac{\partial \rho}{\partial y}v = 0 \tag{2.24}$$

The conservation of momentum equation without body forces is given by Equation (2.25). Body forces would be included if gravity or electromagnetic forces were significant, but are ignored here. In fluid mechanics it is common to split the stress tensor **σ** into a deviatoric stress tensor **T** and a hydrostatic stress scalar *p*, since pressure is often a parameter of interest. The resulting equation is given by (2.26).

$$\frac{D(\rho u)}{Dt} = \nabla \cdot \sigma \tag{2.25}$$

$$\frac{D(\rho u)}{Dt} = \nabla \cdot \mathrm{T} - \nabla \mathrm{p} \tag{2.26}$$

For the case of linear isotropic properties, the full stress tensor can be written as (2.27), or as (2.28) using tensor notation. The variable $\dot{\varepsilon}$ is the strain-rate tensor for fluids (2.29). This is the constitutive equation for the material that relates stress to strain-rate. In fluid mechanics the fluid would be considered classical, as the "first viscosity" μ and "second viscosity" λ linearly relate stress to strain.

$$\sigma = \lambda \nabla \cdot u + \mu(\nabla \mathrm{u} + (\nabla \mathrm{u})^T) \tag{2.27}$$

$$\sigma_{ij} = \lambda \dot{\varepsilon}_{kk} \delta_{ij} + 2\mu \dot{\varepsilon}_{ij} \tag{2.28}$$

$$\dot{\varepsilon}_{ij} = \frac{1}{2}\left(\frac{\partial u_i}{\partial x_j} + \frac{\partial u_j}{\partial x_i}\right) \tag{2.29}$$

The pressure term called out in (2.26) is the negative average "normal" stress, given as (2.30). The deviatoric stress tensor is then calculated as shown in (2.31). In terms of the strain-rate tensor $\dot{\varepsilon}$, the deviatoric stress tensor is written as (2.32) or (2.33). In fluid mechanics it is common to assign the bulk viscosity *K* of the fluid a value of zero (Stokes' assumption). The bulk viscosity is related to the viscosities according to $K = \lambda + \frac{2}{3}\mu$, which results in the "second" viscosity becoming $\lambda = -\frac{2}{3}\mu$. Therefore, for *classical* fluid mechanics problems [136] the deviatoric stress tensor can be written as Equation (2.34). The equations for the deviatoric (2.34) and total stress (2.27) tensors are therefore identical on the surface. The only difference is in the value assigned to the second viscosity λ, which is a distinction often neglected in the literature.

$$\mathrm{p} = -\frac{1}{3}\sigma_{kk} = -\left(\lambda + \frac{2}{3}\mu\right)\dot{\varepsilon}_{kk} \tag{2.30}$$

$$\mathrm{T}_{ij} = \sigma_{ij} - \frac{1}{3}\sigma_{kk}\delta_{ij} = \sigma_{ij} + \mathrm{p}\delta_{ij} \tag{2.31}$$

$$\mathrm{T}_{ij} = 2\mu\dot{\varepsilon}_{ij} - \frac{2}{3}\mu\dot{\varepsilon}_{kk}\delta_{ij} \tag{2.32}$$

$$\mathrm{T} = \mu(\nabla \mathrm{u} + (\nabla \mathrm{u})^T) - \frac{2}{3}\mu(\nabla \cdot u) \tag{2.33}$$

$$\mathrm{T} = \mu(\nabla \mathrm{u} + (\nabla \mathrm{u})^T) + \lambda(\nabla \cdot u) \tag{2.34}$$

Applying the constitutive equation (2.27) to the conservation of momentum equation (2.26) results in Equation (2.35). This is more commonly known as the Navier-Stokes (N-S) equation, which applies to all classical fluids. The expanded form of this equation in the *x* and *y* directions are given in Equations (2.36) and (2.37).

$$\frac{\partial}{\partial t}(\rho u) + u \cdot \nabla(\rho u) = \mu\nabla^2 u + (\lambda + \mu)\nabla(\nabla \cdot u) - \nabla \mathrm{p} \tag{2.35}$$

$$\begin{aligned} \rho\frac{\partial u}{\partial t} + u\frac{\partial \rho}{\partial t} + \rho\left(u\frac{\partial u}{\partial x} + v\frac{\partial u}{\partial y}\right) + (u^2 + v^2)\frac{\partial \rho}{\partial x} \\ = \mu\left(\frac{\partial^2 u}{\partial x^2} + \frac{\partial^2 u}{\partial y^2}\right) + (\lambda + \mu)\frac{\partial}{\partial x}\left(\frac{\partial u}{\partial x} + \frac{\partial v}{\partial y}\right) - \frac{\partial p}{\partial x} \end{aligned} \tag{2.36}$$

$$\begin{aligned} \rho\frac{\partial v}{\partial t} + v\frac{\partial \rho}{\partial t} + \rho\left(u\frac{\partial v}{\partial x} + v\frac{\partial v}{\partial y}\right) + (u^2 + v^2)\frac{\partial \rho}{\partial y} \\ = \mu\left(\frac{\partial^2 v}{\partial x^2} + \frac{\partial^2 v}{\partial y^2}\right) + (\lambda + \mu)\frac{\partial}{\partial y}\left(\frac{\partial u}{\partial x} + \frac{\partial v}{\partial y}\right) - \frac{\partial p}{\partial y} \end{aligned} \tag{2.37}$$

The boundary conditions for planar flows are straightforward. An upper and lower velocity is specified, along with a pressure that is constant throughout (for Couette flow). For steady flow solutions the continuity equations are usually solved analytically. Typical jump conditions are continuity of vertical velocity, displacement, and shear stress [128,130]. For viscous fluids a no-slip condition is also employed, where the velocity must be continuous at the interface.

Once the continuity equations are solved for the steady solution, the perturbed flow can be analyzed. The first step is Reynolds decomposition, which writes the new flow parameter as a linear combination of its steady and perturbed counterparts [132]. This is shown in (2.38) for an arbitrary flow parameter *f*, where *F* is the steady solution and $\acute{f}$ is the perturbed component. The governing equations are then simplified by ignoring second-order perturbation terms (i.e. $\acute{f} \cdot \acute{f}$), with the final result being a new set of equations which are linear in the perturbation variables.

$$f = F + \acute{f} \tag{2.38}$$

Once the perturbations equations are derived, an assumed form for the perturbation is applied. This usually takes the form of (2.39), with the *y*-dependence being unknown [118,132]. In this equation, α is the wavenumber, *c* is the complex wave speed, and $\hat{f}(y)$ is an unknown function of *y*. If the imaginary component of the wave velocity *c* is greater than zero, the perturbation amplitude will grow in time and generates unstable flow [131]. A negative imaginary component reduces the perturbation amplitude with time and hence represents a "stable" solution. If the imaginary component of *c* is identically zero, then the condition is referred to as "neutral stability" where the perturbation propagates through time without increasing or decreasing in size.

$$\acute{f} = \hat{f}(y)e^{i\alpha(x-ct)} \tag{2.39}$$

2.3.3 INVISCID INCOMPRESSIBLE FLOW

For inviscid incompressible flow the governing equations are greatly simplified and exact solutions can be found for many stratified fluid flow problems. The classical Kelvin-Helmholtz stability problem is such a case, which involves two uniform inviscid fluids under a gravitational load with a horizontal discontinuity. The solution can be

obtained following Chandrasekhar [132], with the resulting condition for stability given in Equation (2.40). Here, T is surface tension, g is gravity, ρ is density, and U is velocity. Note that there is no characteristic length-scale associated with this equation [133]. It is simply a function of relative velocity and intensive fluid properties.

$$\frac{2(\rho_1+\rho_2)^2}{\rho_1\rho_2}\left\{Tg\frac{(\rho_1-\rho_2)}{(\rho_1+\rho_2)}\right\}^{\frac{1}{2}} > (U_1-U_2)^2 \tag{2.40}$$

There are three immediate conditions for which K-H instability occurs: no surface tension, no gravity, or no difference in density. The fact that the equation predicts unstable flow for all systems with identical upper and lower fluid densities presents a problem for our use here, as gouging and explosive welding have a distinct threshold for identical slider and rail materials.

2.3.4 VISCOUS INCOMPRESSIBLE FLOW

For incompressible flow the fluid density ρ is constant. The conservation of mass equation then reduces to (2.41). This specifies that the divergence of velocity ($\nabla \cdot \boldsymbol{u}$) is zero, which removes the conservation of momentum terms that involve the 2nd viscosity λ. The conservation of momentum equations then become (2.42)-(2.43).

$$\rho\left(\frac{\partial u}{\partial x}+\frac{\partial v}{\partial y}\right)=0 \tag{2.41}$$

$$\rho\frac{\partial u}{\partial t}+\rho\left(u\frac{\partial u}{\partial x}+v\frac{\partial u}{\partial y}\right)=\mu\left(\frac{\partial^2 u}{\partial x^2}+\frac{\partial^2 u}{\partial y^2}\right)-\frac{\partial p}{\partial x} \tag{2.42}$$

$$\rho\frac{\partial v}{\partial t}+\rho\left(u\frac{\partial v}{\partial x}+v\frac{\partial v}{\partial y}\right)=\mu\left(\frac{\partial^2 v}{\partial x^2}+\frac{\partial^2 v}{\partial y^2}\right)-\frac{\partial p}{\partial y} \tag{2.43}$$

The velocity perturbation analysis starts with Reynolds decomposition for the horizontal velocity, vertical velocity, and pressure, as shown in Equations (2.44)-(2.46). Substituting the velocity perturbations into Equations (2.42)-(2.43), and ignoring second-order perturbation terms results in the perturbation equations for conservation of momentum in the *x* and *y* directions (2.47)-(2.48). These two equations can be combined by taking the partial derivative of (2.47) with respect to *y*, the derivative of (2.48) with respect to *x*, and subtracting the second equation from the first [128]. This removes the pressure term, and results in a single partial differential Equation (2.49) that must be solved for the wave perturbation velocities $\acute{u}$ and $\acute{v}$.

$$u = U + \acute{u} \tag{2.44}$$

$$v = \acute{v} \tag{2.45}$$

$$p = P + \acute{p} \tag{2.46}$$

$$\frac{\partial \acute{u}}{\partial t} + U\frac{\partial \acute{u}}{\partial x} + \acute{v}\frac{\partial U}{\partial y} + \frac{1}{\rho}\frac{\partial p}{\partial x} - \frac{\mu}{\rho}\frac{\partial^2 U}{\partial y^2} = \frac{\mu}{\rho}\nabla^2\acute{u} \tag{2.47}$$

$$\frac{\partial \acute{v}}{\partial t} + U\frac{\partial \acute{v}}{\partial x} + \frac{1}{\rho}\frac{\partial p}{\partial y} = \frac{\mu}{\rho}\nabla^2\acute{v} \tag{2.48}$$

$$\begin{aligned}\frac{\partial}{\partial t}\left(\frac{\partial \acute{u}}{\partial y} - \frac{\partial \acute{v}}{\partial x}\right) + U\frac{\partial}{\partial x}\left(\frac{\partial \acute{u}}{\partial y} - \frac{\partial \acute{v}}{\partial x}\right) + \acute{v}\frac{\partial^2 U}{\partial y^2} \\ = \frac{\mu}{\rho}\left\{\frac{\partial}{\partial y}\left(\frac{\partial^2 \acute{u}}{\partial x^2} + \frac{\partial^2 \acute{u}}{\partial y^2}\right) - \frac{\partial}{\partial x}\left(\frac{\partial^2 \acute{v}}{\partial x^2} + \frac{\partial^2 \acute{v}}{\partial y^2}\right)\right\}\end{aligned} \tag{2.49}$$

For incompressible flow, the two perturbation velocities $\acute{u}$ and $\acute{v}$ can be written in terms of a stream function potential Ψ using Helmholtz decomposition, as shown in Equations (2.50)-(2.51). This converts (2.49) from a 3rd order PDE to a 4th order ODE. The last step is to assume a functional form for the perturbation, which is given by Equation (2.52). After some manipulation, the final result is Equation (2.53), which is the well-known Orr-Sommerfeld equation [134].

$$\acute{u} = \partial\Psi/\partial \mathrm{y} \tag{2.50}$$

$$\acute{v} = -\partial\Psi/\partial \mathrm{x} \tag{2.51}$$

$$\Psi(x, y, t) = \phi(y)e^{i\alpha(x-ct)} \tag{2.52}$$

$$(c - U)(\phi'' - \alpha^2\phi) + \phi U'' = \frac{i\mu}{\rho\alpha}\left(\phi^{(4)} - 2\alpha^2\phi'' + \alpha^4\phi\right) \tag{2.53}$$

For steady flow, all time dependencies ($\partial/\partial \mathrm{t}$) vanish, as well as any x-dependence of the flow velocities ($\partial\mathbf{u}/\partial \mathrm{x}$). Since we are also requiring that the flow be planar, there is no *y*-component of the steady flow velocity ($v = 0$). Applying these rules and replacing the flow parameters (u, p) with their steady counterparts (U, P) reduces the conservation of momentum equations to (2.54) and (2.55), respectively. If pressure is independent of x (Couette flow) then the steady velocity profile is linear (2.56).

$$0 = \mu\frac{\partial^2 U}{\partial y^2} - \frac{\partial P}{\partial x} \tag{2.54}$$

$$0 = \frac{\partial P}{\partial y} \tag{2.55}$$

$$U = c_b y + U_0 \tag{2.56}$$

To prevent numerical instabilities, the 4th order Orr-Sommerfeld ODE can be decomposed into two 2nd order ODEs by introducing a new variable ξ, shown in (2.57)-(2.58). The final set of equations is presented in matrix form in Equation (2.59), where I is the identity matrix. Since the derivatives of the potential function ϕ will be written as Chebyshev differentiation matrices (discussed below), the fourth-order derivatives translate into differentiation matrices being raised to the fourth power. Transforming the full Orr-Sommerfeld equation into two 2nd order equations reduces the potential round-off error, though at the expense of matrix size [136].

$$\xi = \phi'' - \alpha^2\phi \tag{2.57}$$

$$(c - U)\xi + \phi U'' = \frac{i\mu}{\rho\alpha}(\phi'' - \alpha^2\phi)\xi \tag{2.58}$$

$$\begin{bmatrix} (D^2 - \alpha^2 I) & -I \\ -U'' & \frac{i\mu}{\rho\alpha}(D^2 - \alpha^2 I) + U \end{bmatrix} \begin{bmatrix} u \\ \xi \end{bmatrix} = c \begin{bmatrix} 0 & 0 \\ 0 & I \end{bmatrix} \begin{bmatrix} u \\ \xi \end{bmatrix} \tag{2.59}$$

The perturbation potential function for the first fluid is ϕ, and for the second fluid is denoted χ. The jump conditions are continuity of vertical velocity, continuity of horizontal velocity (no-slip), continuity of shear stress, and continuity of normal stress. These conditions result in Equations (2.60)-(2.63), following the derivations of Yih [128,135]. The primes denote derivation with respect to *y*, subscript '0' refers to the value at the interface, while the subscripts '1' and '2' refer to the two fluids. The parameter m_μ is the ratio of fluid viscosities ($m_\mu = \mu_2/\mu_1$), and *Re* is the Reynolds number defined as $1/\mu_1$, with the flow equation normalized by setting $U_0/\rho_1 d_1 = 1$ [128].

$$\phi_0 - \chi_0 = 0 \tag{2.60}$$

$$\phi_0'' + \alpha^2\phi_0 - m_\mu\chi_0'' - m_\mu\alpha^2\chi_0 = 0 \tag{2.61}$$

$$(\phi_0''' - \alpha^2\phi_0') + 2\alpha^2\phi_0' + m_\mu(\chi_0''' - \alpha^2\chi_0') - 2m_\mu\alpha^2\chi_0' = 0 \tag{2.62}$$

$$-\left(U_{1,0}'\phi_0 - U_0\phi_0'\right) + \left(U_{2,0}'\chi_0 - U_0\chi_0'\right) = c(\phi_0' - \chi_0') \tag{2.63}$$

Once the velocity perturbation functions have been substituted into the continuity equations, the remaining step is to solve for the potential functions and the complex wave speed *c*. This is generally not possible using an analytic solution without significant assumptions about perturbation wavelengths, but there are several numerical approaches

which can be used without resorting to more computationally intensive approaches. The most common method used in fluid mechanics is the spectral collocation method.

In spectral collocation, a continuous domain is approximated with a series of *N* nodes, with the domain modeled using polynomials up to order *N*. Chebyshev polynomials, defined in Equation (2.64) and shown in Figure 2.16, are preferred because they exhibit exponential convergence rates, are suitable for variable coefficients, and are not as prone to producing spurious eigenvalues as the Tau and Galerkin numerical integration methods [136]. However, they are only applicable in the (-1,1) domain, so an appropriate change of coordinates is often required.

$$T_k(x) = \cos(k \cos^{-1} x), \qquad k = 0,1, \dots, N \tag{2.64}$$

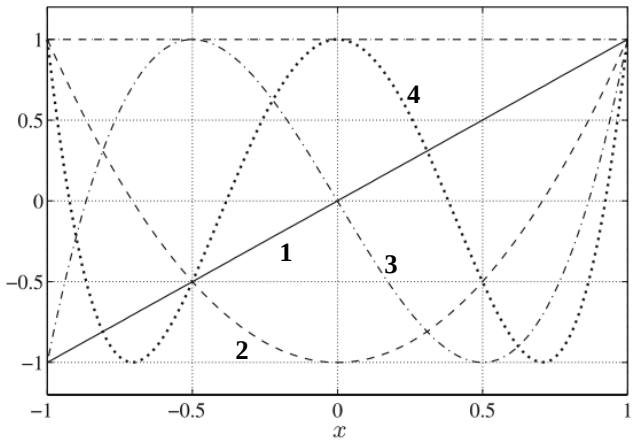

Figure 2.16. Chebyshev polynomials of degree 1 through 4 [136]

Chebyshev polynomials were first used by Orszag in 1971 to provide accurate solutions to viscous flow stability problems [137], and have since been used in many papers on 2D and 3D fluid instability as a result of their numerical efficiency compared to other approaches [138-140]. The collocation nodes x_k used in instability problems are typically taken at the *Chebyshev Gauss-Lobatto* points, defined in Equation (2.65). This provides for a high density of nodes near the boundaries of the domain, which reduces overshoot error (Runge's phenomenon) and improves overall accuracy.

$$x_k = cos\left(\frac{\pi k}{N}\right), \qquad k = 0,1,\dots,N \tag{2.65}$$

The perturbation equations obtained for the continuity equations and boundary conditions are re-written using Chebyshev polynomials T_k, in the form of Equation (2.66), or more concisely $p(x)=\boldsymbol{X}$ where $\boldsymbol{X}$ represents the *Chebyshev Gauss-Lobatto* points [141]. Following the work of Weideman and others, the governing differential equations are written using differentiation matrices [142], and solved using Matlab®. Using differentiation matrices allows the nth derivative of a polynomial to be written as Equation (2.67), where D is the differentiation matrix based on the properties of Chebyshev polynomials [142]. A convenient feature of Chebyshev polynomials is that their derivatives are recursive, that is, $D^{(n)}$ is equivalent to D^n, which is simply the matrix multiplication of D by itself n times.

$$p(x) = \sum_{k=1}^{N} T_k(x) X_k \tag{2.66}$$

$$p^{(n)}(x) = D^{(n)} X \tag{2.67}$$

The above procedure results in a generalized eigenvalue problem of $\mathbf{A}x=c\mathbf{B}x$, with c being the complex wave perturbation speed. The matrices **A** and **B** represent the linear system of perturbation coefficients, with derivatives replaced with differentiation matrices. The differentiation matrices are generated using Weidman's Matlab® script DMSUITE [142,143]. As the matrices generated for these instability problems are invariably singular, the eigenvalue problem is solved using the *eig* function in Matlab®, which is based on the QZ algorithm [144].

Once the eigenvalues are calculated, there are several options for determining if the system is considered stable or unstable. The usual approach is to only examine the most unstable (largest imaginary component) eigenvalues for an assumed wave number α

[145,146]. However, there are other methods worth considering, such as the rate of kinetic energy increase as studied by Boomkamp **[**147].

To satisfy the Chebyshev domain requirements, each flow field is mapped onto a (-1,1) domain. For two flow fields ($-d_1 < y_1 < 0$) and ($0 < y_2 < d_2$), the transformations into the domain ($-1 < z < 1$) are given by (2.68) and (2.69). This is done such that the interface ($y = 0$) lies at $z = -1$ for both flows, while the boundary conditions are at $z = 1$. The full derivation for this procedure is provided in Appendix A.

$$y_1 = \frac{-d_1}{2}(z+1) \tag{2.68}$$

$$y_2 = \frac{d_2}{2}(z+1) \tag{2.69}$$

Each flow field is subject to its own boundary conditions $\phi(-1) = \phi'(-1) = 0$, while the jump conditions span both flows. The full eigenvalue problem is shown in (2.70). The fourth variable ζ is the counterpart to ξ that splits the 2nd Orr-Sommerfeld equation for χ into two 2nd-order ODEs. The boundary and jump conditions are incorporated directly in to the matrix at rows 1 and N, respectively, for each variable. The original flow equations are limited to the internal nodes (2:N-1) of the matrix. In this formulation, N collocation nodes results in a $4N \times 4N$ matrix. The matrix coefficients are provided in Appendix B.

$$\begin{bmatrix} \begin{bmatrix} BC \\ A11 \\ JC \end{bmatrix} & \begin{bmatrix} BC \\ A12 \\ JC \end{bmatrix} & \begin{bmatrix} BC \\ A13 \\ JC \end{bmatrix} & \begin{bmatrix} BC \\ A14 \\ JC \end{bmatrix} \\ \begin{bmatrix} BC \\ A21 \\ JC \end{bmatrix} & \begin{bmatrix} BC \\ A22 \\ JC \end{bmatrix} & \begin{bmatrix} BC \\ A23 \\ JC \end{bmatrix} & \begin{bmatrix} BC \\ A24 \\ JC \end{bmatrix} \\ \begin{bmatrix} BC \\ A31 \\ JC \end{bmatrix} & \begin{bmatrix} BC \\ A32 \\ JC \end{bmatrix} & \begin{bmatrix} BC \\ A33 \\ JC \end{bmatrix} & \begin{bmatrix} BC \\ A34 \\ JC \end{bmatrix} \\ \begin{bmatrix} BC \\ A41 \\ JC \end{bmatrix} & \begin{bmatrix} BC \\ A42 \\ JC \end{bmatrix} & \begin{bmatrix} BC \\ A43 \\ JC \end{bmatrix} & \begin{bmatrix} BC \\ A44 \\ JC \end{bmatrix} \end{bmatrix} \begin{bmatrix} \begin{bmatrix} \phi_1(1) \\ \phi_1(2:N-1) \\ \phi_1(N) \end{bmatrix} \\ \begin{bmatrix} \xi_1(1) \\ \xi_1(2:N-1) \\ \xi_1(N) \end{bmatrix} \\ \begin{bmatrix} \chi_2(1) \\ \chi_2(2:N-1) \\ \chi_2(N) \end{bmatrix} \\ \begin{bmatrix} \zeta_2(1) \\ \zeta_2(2:N-1) \\ \zeta_2(N) \end{bmatrix} \end{bmatrix}$$

$$= c \begin{bmatrix} \begin{bmatrix} BC \\ B11 \\ JC \end{bmatrix} & \begin{bmatrix} BC \\ B12 \\ JC \end{bmatrix} & \begin{bmatrix} BC \\ B13 \\ JC \end{bmatrix} & \begin{bmatrix} BC \\ B14 \\ JC \end{bmatrix} \\ \begin{bmatrix} BC \\ B21 \\ JC \end{bmatrix} & \begin{bmatrix} BC \\ B22 \\ JC \end{bmatrix} & \begin{bmatrix} BC \\ B23 \\ JC \end{bmatrix} & \begin{bmatrix} BC \\ B24 \\ JC \end{bmatrix} \\ \begin{bmatrix} BC \\ B31 \\ JC \end{bmatrix} & \begin{bmatrix} BC \\ B32 \\ JC \end{bmatrix} & \begin{bmatrix} BC \\ B33 \\ JC \end{bmatrix} & \begin{bmatrix} BC \\ B34 \\ JC \end{bmatrix} \\ \begin{bmatrix} BC \\ B41 \\ JC \end{bmatrix} & \begin{bmatrix} BC \\ B42 \\ JC \end{bmatrix} & \begin{bmatrix} BC \\ B43 \\ JC \end{bmatrix} & \begin{bmatrix} BC \\ B44 \\ JC \end{bmatrix} \end{bmatrix} \begin{bmatrix} \begin{bmatrix} \phi_1(1) \\ \phi_1(2:N-1) \\ \phi_1(N) \end{bmatrix} \\ \begin{bmatrix} \xi_1(1) \\ \xi_1(2:N-1) \\ \xi_1(N) \end{bmatrix} \\ \begin{bmatrix} \chi_2(1) \\ \chi_2(2:N-1) \\ \chi_2(N) \end{bmatrix} \\ \begin{bmatrix} \zeta_2(1) \\ \zeta_2(2:N-1) \\ \zeta_2(N) \end{bmatrix} \end{bmatrix} \tag{2.70}$$

Dongarra *et al.* used the Chebyshev-Tau method to analyze the stability of stratified fluid flow [148]. Both Poiseuille flow (channel flow under a pressure gradient with fixed boundaries) and Couette flow (channel flow with no pressure gradient and moving boundaries) were analyzed to determine their stability spectra. The results were compared to prior work in the literature for different flow conditions, and therefore serve as the benchmark for testing the Matlab® code written for this research. The matrix problem shown in Equation (2.70) was solved using Weidman's DMSUITE for generating Chebyshev differentiation matrices. The flow parameters studied by Dongarra *et al.* were employed, with the eigenvalue calculations compared to Dongarra *et al.*'s in Figure 2.17, and in Appendix C. The results show that this approach works well.

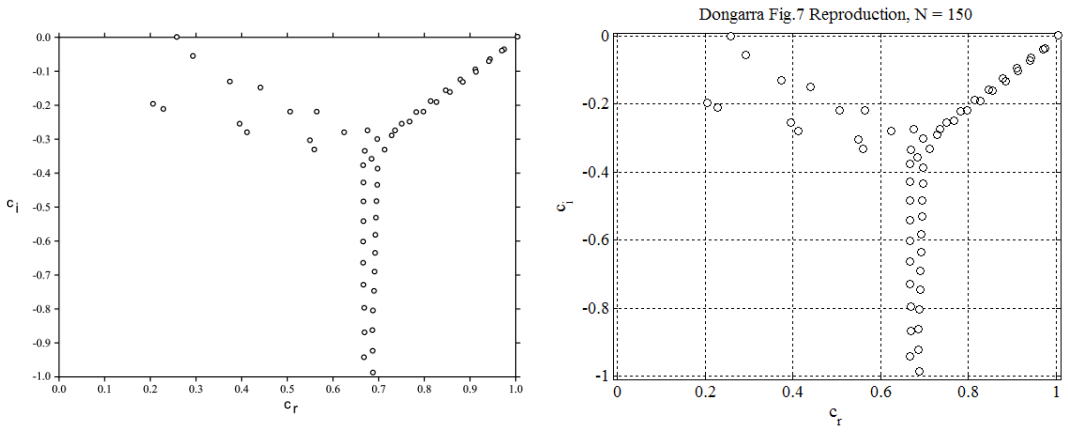

Figure 2.17. Dongarra *et al.* Fig. 7 eigenvalues (left)[15], and re-created using Matlab® script ($R = 10^4$, $\alpha = 1$, $m = 2$, $n = 1.2$, $V = 0$)

It is difficult to choose what effective viscosity to use for the materials. However, a reasonable lower bound is the viscosity of the metals in their molten state at the melting temperature. Viscosities for molten alloys are not always available, but the viscosities for pure molten metals, as well as certain compositions are available in the literature [149,150]. For the purposes of this investigation the viscosities reported by Battezzati *et al.* are used [149], and are provided in Table 2.3. Densities for the molten materials were taken from [151] and [152]. The implicit assumption here is that the two materials have melted at the interface prior to gouging. It is also possible to use an effective viscosity based on plastic deformation, which is addressed later. The aluminum/copper system is used as the benchmark for this analysis since it is a common railgun slider/rail material pair.

[15] Reprinted from J.J. Dongarra, B. Straughan, D.W. Walker, "Chebyshev tau – QZ Algorithm Methods for Calculating Spectra of Hydrodynamic Stability Problems," Applied Numerical Mathematics, Vol. 22, No. 4, pp. 399-434, Copyright 1996, with permission from Elsevier

Table 2.3. Properties of liquid metals at their melting temperature

Metal	T_m (K)	ρ (kg/m^3)	μ (mPa-s)
Titanium	1,958	4,110 [152]	2.20 [149]
Iron	1,809	6,999 [151]	5.50 [149]
Nickel	1,728	7,810 [152]	4.90 [149]
Copper	1,356	8,020 [152]	4.00 [149]
Aluminum	933	2,372 [151]	1.30 [149]
Lead	600	10,660 [152]	2.65 [149]

Figure 2.18 shows the eigenvalue spectra for Al/Cu with flow heights of 0.01 m and wavenumber α=0.1. As the number of nodes *N* decreases the lower regions of the spectra develop spurious eigenvalues. However, this research is primarily concerned with the eigenvalues possessing the largest imaginary components, and the accuracy of the lower "tail" region is not critical. This is important for later calculations since accurate tail spectra can be computationally expensive for certain flow properties.

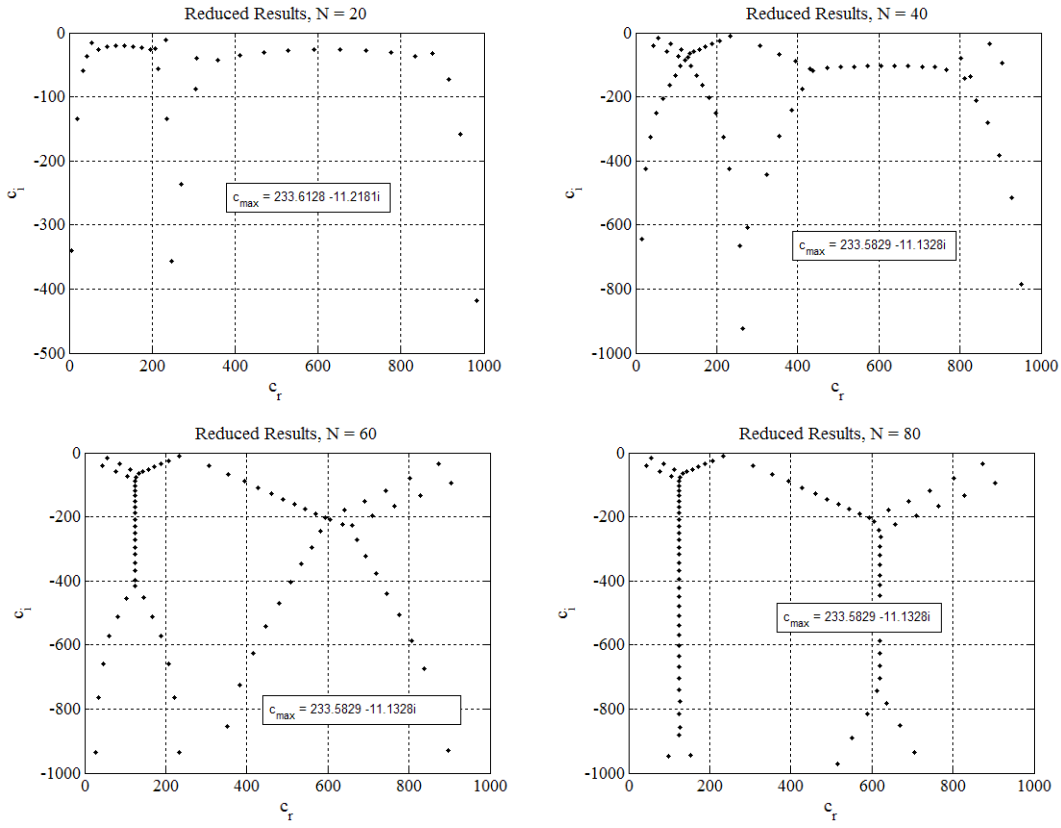

Figure 2.18. Eigenvalue spectra for Al/Cu (*α*=0.1, *V*=1000, *d*=0.01) with increasing nodes

The numerical accuracy of the eigenvalue calculations imposes certain limitations on the values for flow and material properties. Matlab® is incapable of resolving matrices using flow field heights *d* on the order of micrometers. As the flow field height is reduced, spurious eigenvalues are generated, as shown in Figure 2.19. For the Al/Cu system with a wavenumber of 0.1 the onset of spurious eigenvalues occurs at a flow height of 7 mm. Unlike the spurious eigenvalues shown in Figure 2.18, these are not eliminated by increasing the number of collocation nodes (Figure 2.19, bottom images).

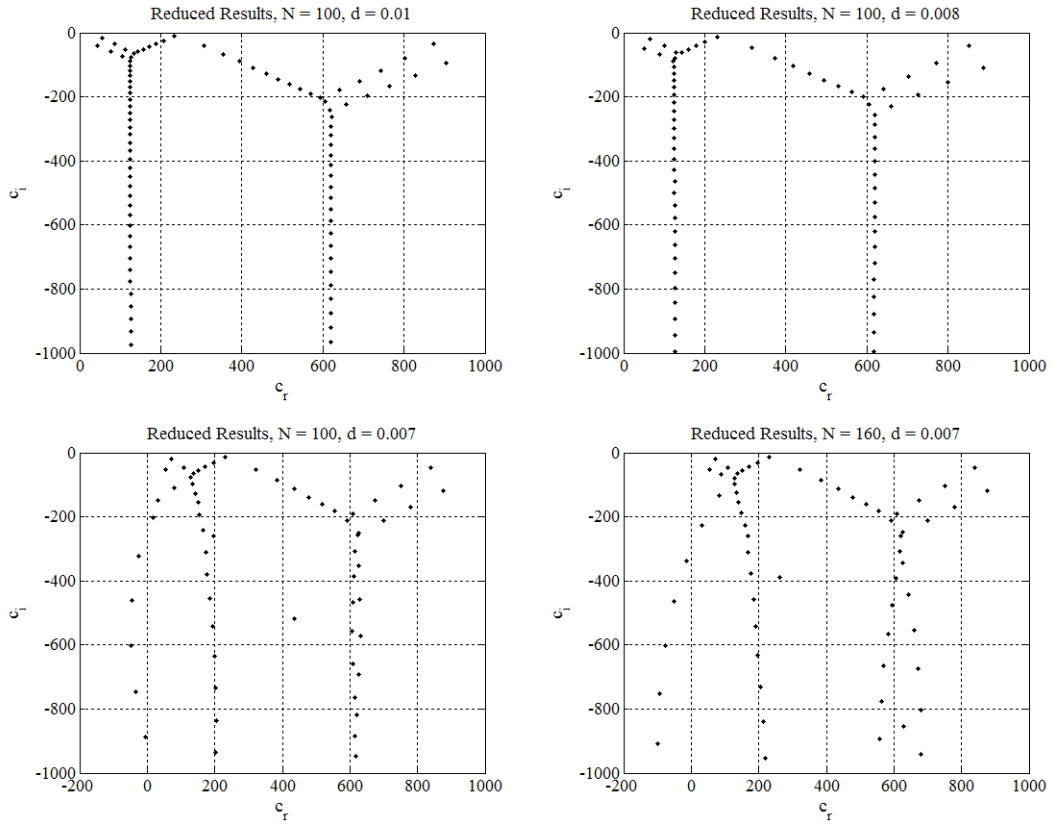

Figure 2.19. Eigenvalue spectra for Al/Cu system (α = 0.1, *V*=1000) with decreasing flow height *d*

One way to minimize spurious eigenvalues is to scale the equations. In this case we apply a scale factor *s* to all units of length. The results of this approach are shown in

Figure 2.20. This approach allows the length scale of the analyses to be extended down to 3 mm, but nowhere near the 10 μm needed to model a molten armature interface.

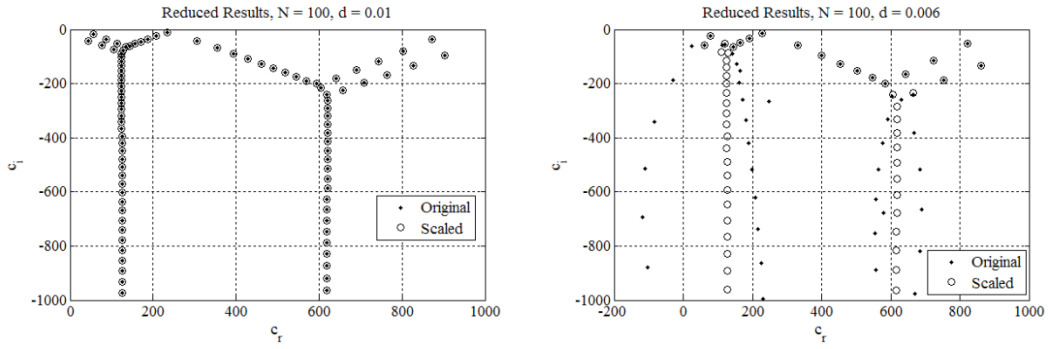

Figure 2.20. Eigenvalue spectra for scaled Al/Cu system (α = 0.1, *V*=1000, s = 10)

Using scale factors can prevent spurious eigenvalues from being generated, but only to a point. Increasing the scale factor itself can generate a loss of accuracy and introduce spurious eigenvalues, as shown in Figure 2.21. The remaining analysis must therefore be limited to flow heights around 1 cm.

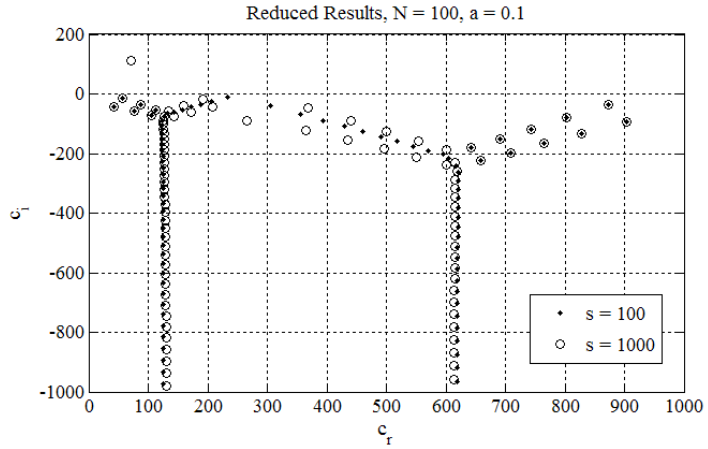

Figure 2.21. Eigenvalue spectra with scaling-generated spurious eigenvalues

It is useful to examine the physical meaning behind the eigenvalue spectra in the previous images. Examining the case of the Al/Cu system at 1 km/s, α = 0.1, and N=100 the flow fields for the 1st, 2nd and 5th eigenvalues (see Figure 2.22) were calculated at a

time of 1 μs. As shown in Figure 2.23 through Figure 2.25 these spectra represent flow perturbations focused at the interface, copper (lower) boundary, and aluminum (upper) boundary.

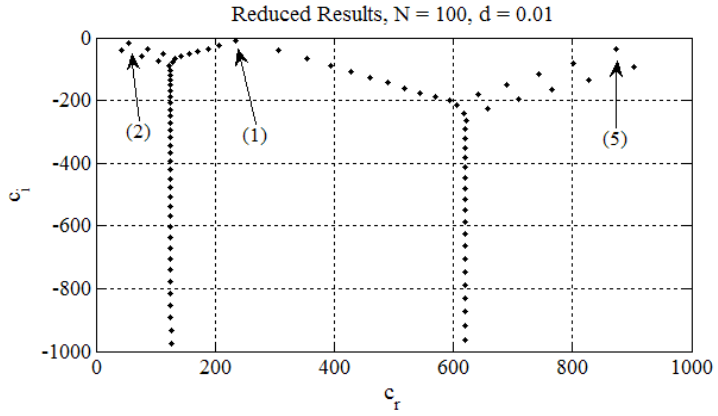

Figure 2.22. Eigenvalues spectra for Al/Cu system (α=0.1, V=1000)

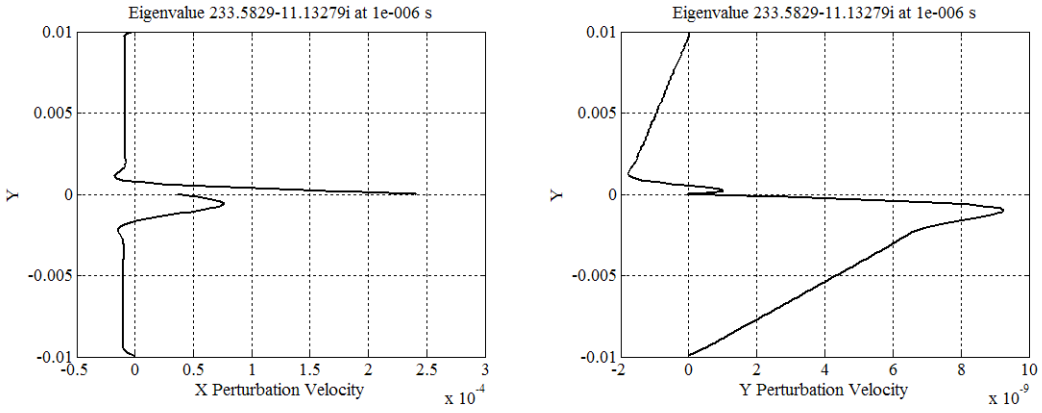

Figure 2.23. Flow perturbation velocities for 1st eigenvalue (t = 1 μs)

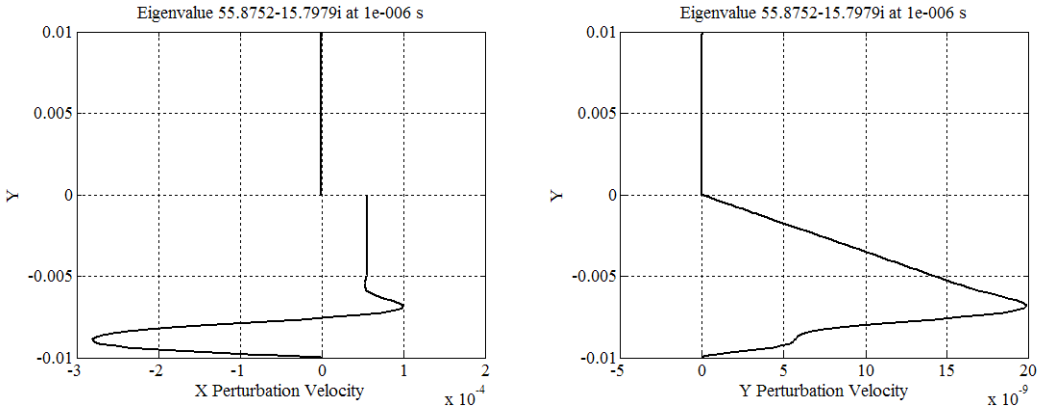

Figure 2.24. Flow perturbation velocities for 2nd eigenvalue (t = 1 µs)

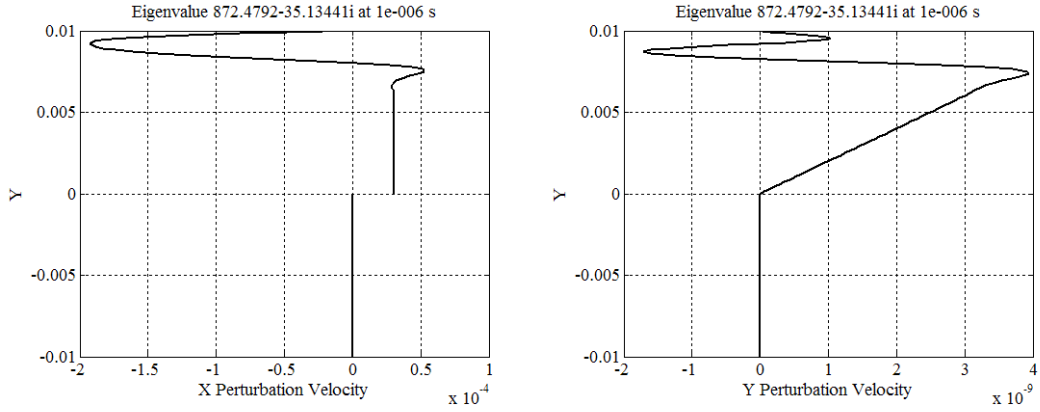

Figure 2.25. Flow perturbation velocities for 5th eigenvalue (t = 1 µs)

In literature on fluid instability, the eigenvalue spectra are often the only item of concern. However, it is prudent to examine behavior of the perturbations over time, which is not indicated by the eigenvalues. This is because the initial perturbation velocities can increase significantly with time, even for "stable" eigenvalues before they decay to zero. Thus, even a perturbation wave speed that is ultimately stable can produce significant pressures or kinetic energies prior to decay.

The evolution of the perturbation velocities shown in Figure 2.23 for the 1st eigenvalue were calculated at later times to illustrate the time-scales involved in perturbation growth and decay. The results are shown in Figure 2.26, which indicate the time for perturbation growth is on the order of 10^{-2} s.

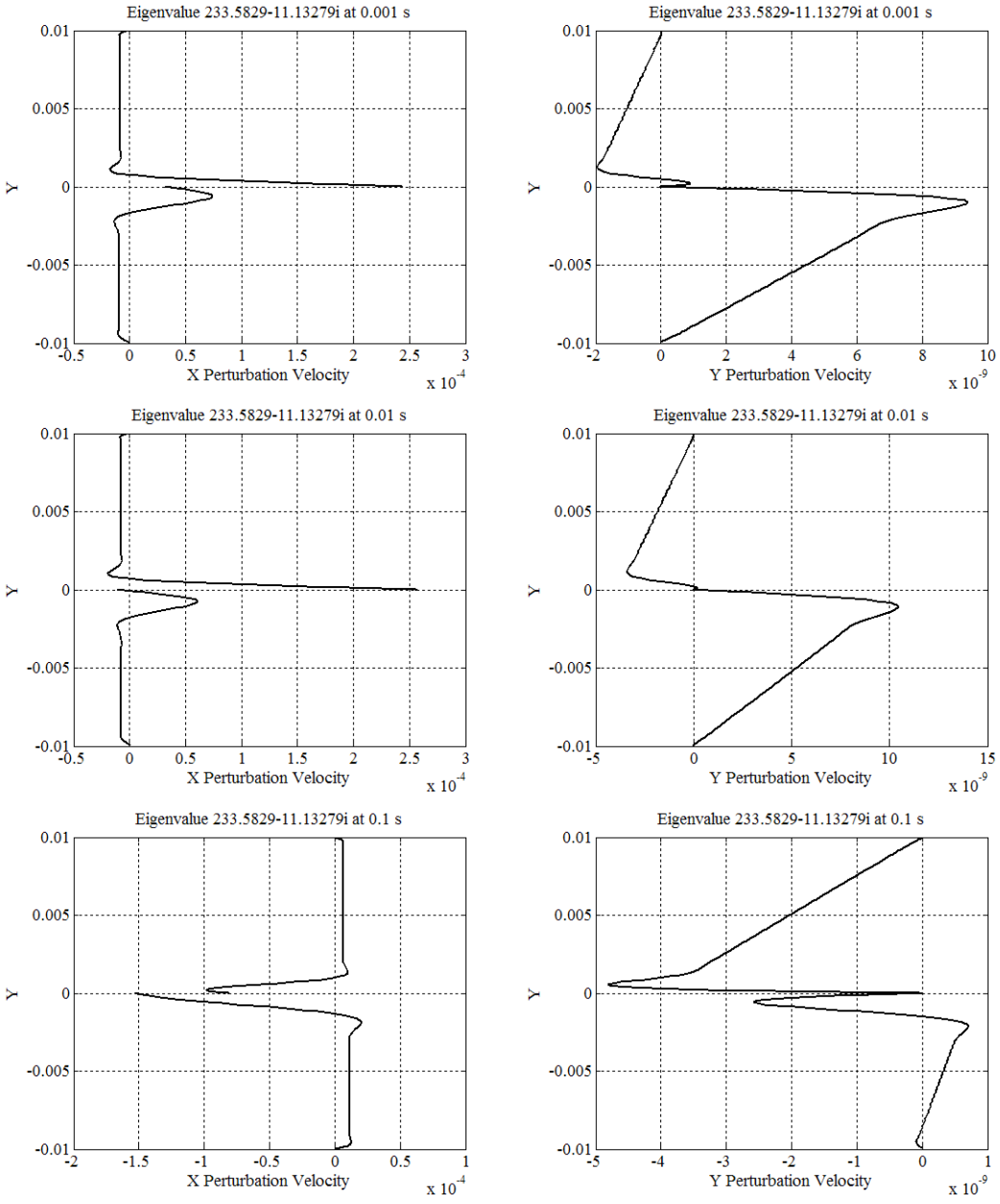

Figure 2.26. Flow perturbation velocities at increasing times (Al/Cu, α = 0.1, V=1000)

The time evolution of the flow perturbations is more succinctly shown by calculating the maximum perturbation kinetic energy in the flow field at a given time. This is done using Equation (2.71) at different times ranging from 10^{-6} to 10^{2} seconds. The perturbation flows for the first four eigenvalues were used in the calculations, and

the maximum kinetic energy across the entire flow field was determined. The results of these calculations are shown in Figure 2.27.

$$KE = \frac{1}{2}\rho(\acute{u}^2 + \acute{v}^2) \tag{2.71}$$

There are several important observations to be made from this: First, the most unstable eigenvalue is not necessarily the most energetic. Second, even stable eigenvalues can increase significantly before decaying. Lastly, the timescale required for perturbation growth is on the order of hundreds of milliseconds. This is much longer than the time required to initiate gouging (which is on the order of microseconds).

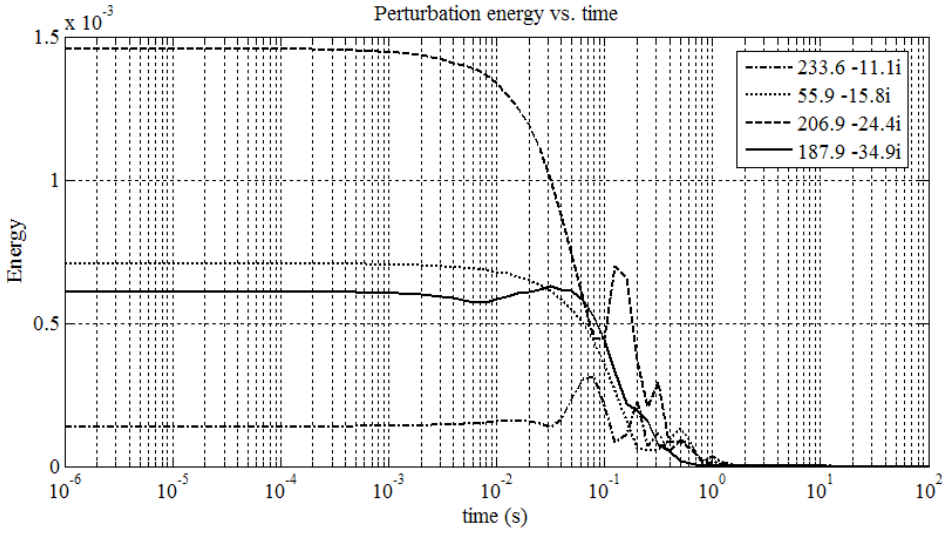

Figure 2.27. Maximum perturbation kinetic energy vs. time for 1st four eigenvalues (Al/Cu, α=0.1, V=1000, d=0.01)

Figure 2.28 illustrates the relative peak kinetic energy associated with each eigenvalue. Each circle is a relative measure of the maximum energy obtained by that eigenvalue's perturbation. The most energetic eigenvalue is the 3rd most unstable.

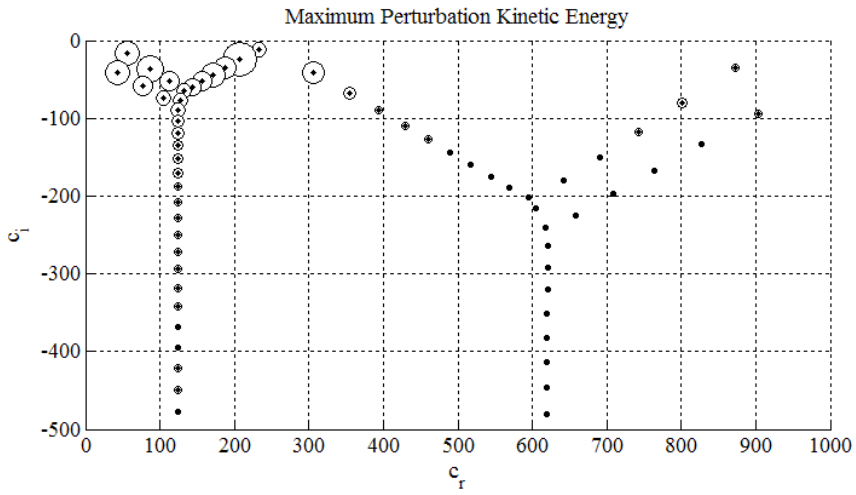

Figure 2.28. Relative kinetic energy spectrum for different Al/Cu eigenvalues (α=0.1, V=1000)

To see if unstable eigenvalues could be produced, the velocity was set at 2,000 m/s for the Al/Cu material pair, well above the observed gouging velocity of 1,300 m/s. Table 2.4 shows the largest eigenvalues calculated for this system with increasing velocity. An opposite trend with velocity is observed, with the imaginary component of the wave speed decreasing with increasing velocity. This is true for both the most unstable (interface) mode, as well as the most energetic (3rd most unstable) mode. A similar trend is observed with perturbation kinetic energy.

Table 2.4. Eigenvalue calculations for different velocities (Al/Cu, α=1, V=2000)

V (*m/s*)	C_i (*m/s*)	C_{max} (*m/s*)	KE_{max} (J/m^3)	Time to peak (*s*)
1,000	239.852 -5.17i	227.47 -11.32i	3.6448e-004	0.0079
1,200	288.207 -5.84i	274.22 -12.79i	2.7555e-004	0.0063
1,400	336.600 -6.47i	321.10 -14.17i	2.6697e-004	0.0050
1,600	385.024 -7.07i	368.08 -15.49i	2.8864e-004	0.0025
1,800	433.473 -7.65i	415.15 -16.76i	2.9202e-004	6.3096e-004
2,000	481.945 -8.20i	462.29 -17.97i	2.0701e-004	0.0032

Table 2.5 shows the effects of increasing the wavenumber from 0.01 to 10. Increasing the wavenumber corresponds to decreasing the perturbation wavelength. As the wavelength decreases the 1st eigenvalue becomes more unstable, the maximum kinetic energy decreases, and the time required to obtain the maximum energy decreases.

The results for the 1st eigenvalue are shown graphically in Figure 2.29. If the relationship between wavelength and time-to-peak continues, then a wavenumber of 1000 (wavelength of 1 mm) should produce a time-to-peak of 2 μs which is on the timescale of gouging. This estimate was verified using 400 collocation nodes, with the results shown in Figure 2.30.

Table 2.5. Eigenvalue calculations for different wavenumbers (Al/Cu, *V*=2000)

α (m^{-1})	**C_i** (m/s)	**KE_{max}** (J/m^3)	**Time to peak** (s)
0.01	450.55 -38.07i	0.0011571	0.3981
0.1	471.99 -17.67i	0.0002229	0.03981
1	481.95 -8.203i	9.2436e-005	0.001585
10	486.56 -3.807i	1.4195e-005	0.0001995

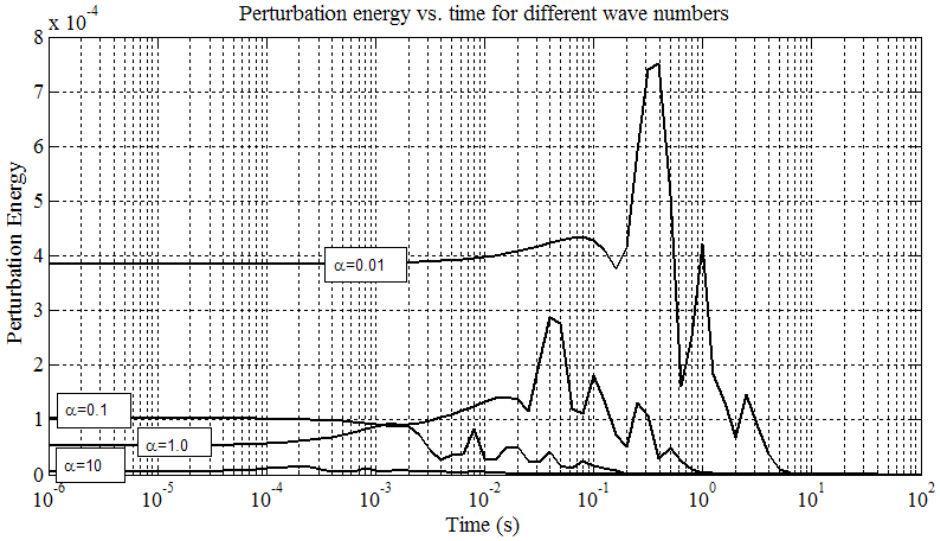

Figure 2.29. Perturbation kinetic energy vs. time and wavenumber (*V*=2000)

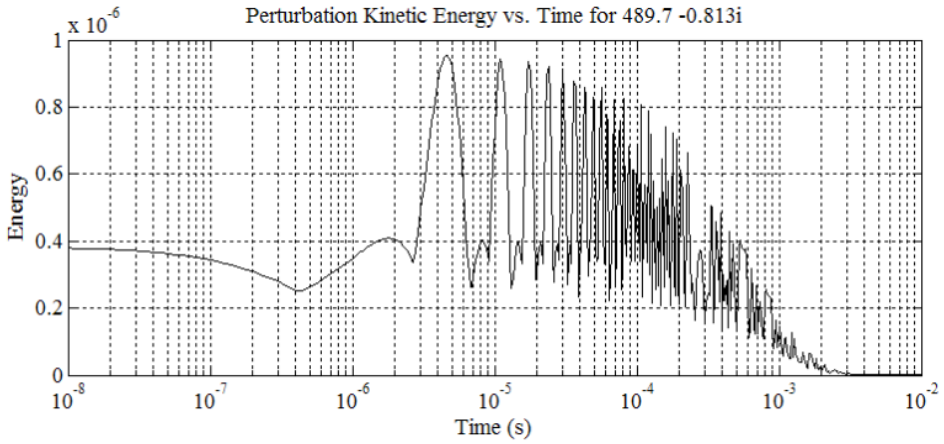

Figure 2.30. Perturbation kinetic energy vs. time (*α*=1000, *V*= 2000)

Another flow parameter that may change considerably is the viscosity. The actual viscosity of the fluids can be significantly greater than the macroscopic melting temperature values, owing to incomplete melting and entrained particles [153,154]. At the extreme end of the spectra is the effective structural viscosity of metals as they are dynamically deforming. Savenkov suggested the dynamic viscosity depends strongly on the scale of the phenomenon under consideration [155]. At the microscopic level (10^{-7}-10^{-6} m) the viscosity is low (30-50 Pa-s) and is governed by point defects and dislocation-dislocation interactions. "Low" in this context is still four orders of magnitude higher than liquid viscosities. High viscosities (10^{5}-10^{6} Pa-s) are associated with processes in the 10^{-5}-10^{-3} m range, involving the collective motion of strain carriers in the solid. While employing such high viscosities is impractical given the resulting numerical instabilities, the effect of viscosity can still be examined. A ten-fold increase in the viscosity of both fluids reduces the imaginary wave speeds of the eigenvalues, but increases their kinetic energies (shown in Figure 2.31).

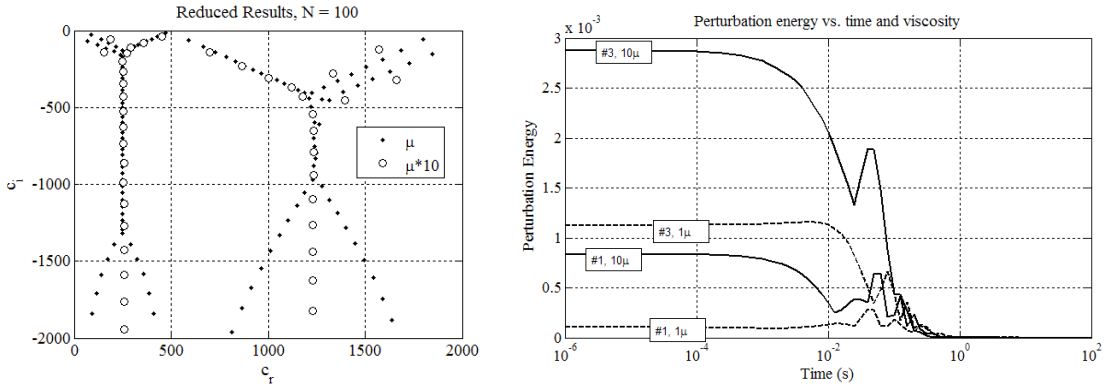

Figure 2.31. Effect of viscosity increase on eigenvalue spectra at 2 km/s (most unstable wave speed changes from 472.0 - 17.67i to 450.6 - 38.07i)

The last flow parameter that can be adjusted is the relative flow heights. If the flow height of the aluminum is doubled, the resulting eigenvalues are shown in Figure 2.32. While the wave speed's imaginary component is increased from -17 to -12 (slower rate of decay), the perturbation energy behavior is largely unchanged. An unintended consequence of this adjustment is the region of spurious eigenvalues created in the aluminum flow. This "triangle of instability," as referred to by Dongarra, can be alleviated by employing higher precision arithmetic. However, it does not affect the most unstable eigenvalues.

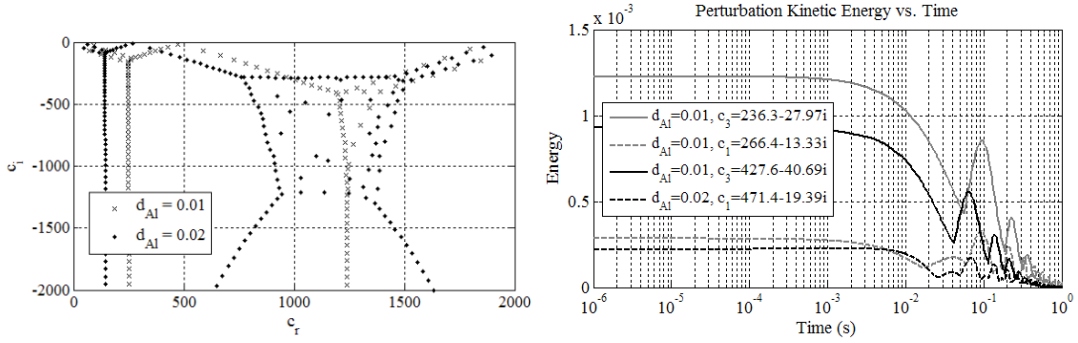

Figure 2.32. Effect of upper (Al) flow height increase on Al/Cu eigenvalue spectra *α*=1, *V*=2000, N=200

The eigenvalue spectra were calculated for seven slider/rail material combinations that have generated gouges, with the results shown in Table 2.6. There is no positive

correlation between either the perturbation wave-speeds or perturbation energies with the observed gouging behavior for the corresponding material pairs. Another unforeseen complication is a numerical instability if identical material properties are used (e.g. Cu/Cu). This can be alleviated by applying a small (0.01%) modification to the viscosity or density values (see Figure 2.33). In the case of similar materials, the most unstable perturbations lie at the outer boundaries. Dissimilar materials have the most unstable perturbations near the interface.

Table 2.6. Eigenvalue calculations for different materials (α = 1, *V*=2000, d=0.01)

Material Pair	**μ_1 / μ_2**	**C_1** *(m/s)*	**KE_1** *(kJ/m^3)*	**C_3** *(m/s)*	**KE_3** *(kJ/m^3)*
Al / Cu	1.3 / 4.0	239.69 -5.668i	102.89	226.88 -11.897i	317.88
Cu / Cu	4.0 / 4.0	955.98 -11.73i	124.74	931.62 -27.279i	129.28
Ti / Cu	2.2 / 4.0	348.11 -9.021i	191.66	946.54 -14.210i	45.421
Fe / Cu	5.5 / 4.0	954.42 -12.24i	127.24	571.22 -15.181i	267.31
Ni / Cu	4.9 / 4.0	955.79 -11.83i	133.53	544.04 -18.956i	240.07
Fe / Fe	5.5 / 5.5	51.128 -13.70i	104.28	79.421 -31.799i	142.87
Pb / Pb	2.65 / 2.65	34.966 -9.247i	60.925	54.295 -21.565i	68.242

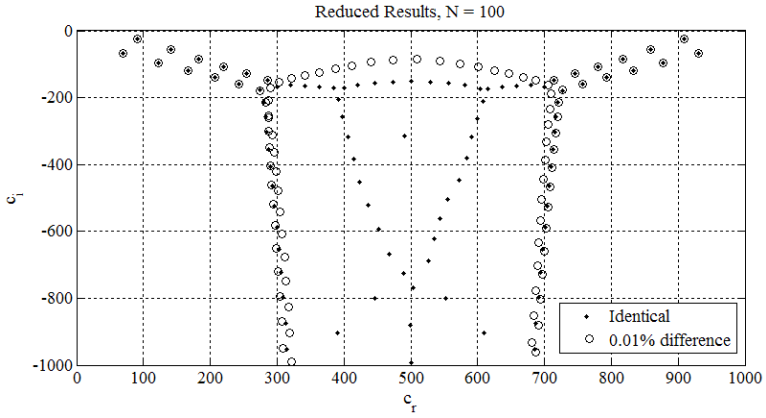

Figure 2.33. Effect of identical upper and lower fluid properties (Cu/Cu, α=0.1, *V*=1000, d=0.01)

While the governing equations for flow behavior are generally agreed upon, the jump conditions between fluids are not. Yih assumed that the shear stress could be evaluated at the original interface location [123]. Boomkamp modified this by taking the

continuity at the perturbed location [139], which changes the related jump condition from Equation (2.72) to Equation (2.73).

$$c_{y1}^2 D^2\phi_0 + \alpha^2\phi_0 - m_\mu c_{y2}^2 D^2\chi_0 - m_\mu\alpha^2\chi_0 = 0 \tag{2.72}$$

$$2\alpha^2 U_0\phi_0 + U_0\xi_0 + 2m_\mu\,\alpha^2 U_0\chi_0 + m_\mu\, U_0\zeta_0 = c\{-2\alpha^2\phi_0 - \xi_0 + 2m_\mu\alpha^2\chi_0 + m_\mu\,\zeta_0\} \tag{2.73}$$

The results of Boomkamp's JC are shown in Figure 2.34. The modified JC creates an unstable eigenvalue at velocities as low as 10 m/s and wave numbers as small as 0.001. The corresponding energy plot is shown in Figure 2.35.

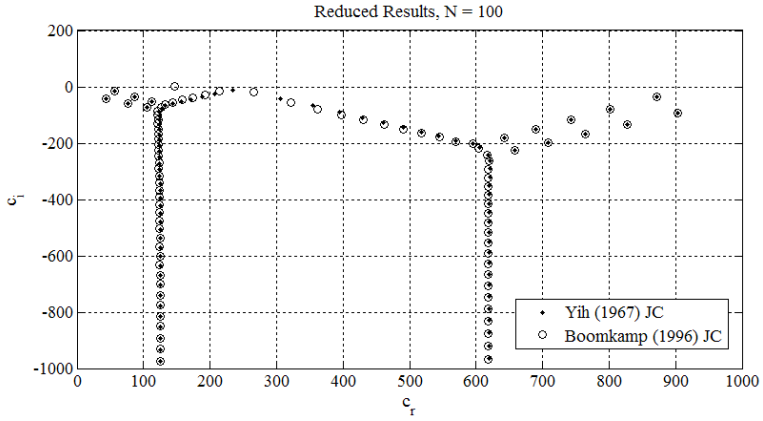

Figure 2.34. Effect of shear stress jump condition on eigenvalue spectra (*α*=1, *V*=1000)

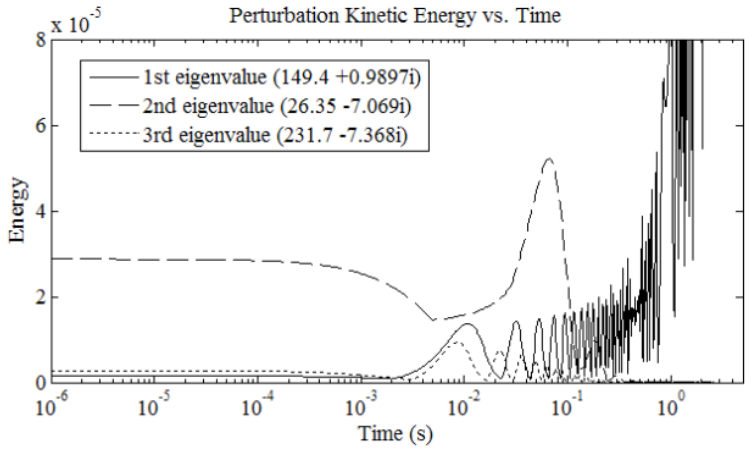

Figure 2.35. Perturbation kinetic energy vs. time for Boomkamp JC (*α*=1, *V*=1000)

As before, the viscosities and flow field heights were reduced to see if the incubation time for perturbation growth was reduced. The results are provided in Table 2.7, and show similar behavior to Yih's JC. The wavenumber was also varied, with the results shown in Table 2.8. The unstable growth rates for the modified JC are about three orders of magnitude longer than for the original (stable) eigenvalues to peak prior to decaying.

Table 2.7. Eigenvalue calculations for different depths and viscosities (Al/Cu, Boomkamp JC, α = 1, *V*=1000)

μ / μ_0	d *(m)*	C_i *(m/s)*	Time to peak *(s)*
1	0.1	150.315 +0.105i	12.59
1	0.05	150.209 +0.209i	7.943
1	0.01	149.367 +0.990i	1.259
2	0.01	148.937 +1.364i	0.3
10	0.01	147.180 +2.771i	0.2
100	0.01	140.405 +6.512i	0.1

Table 2.8. Eigenvalue calculations for different wavenumbers (Al/Cu, Boomkamp JC, *V*=1000)

α (m^{-1})	C_i *(m/s)*	Time to peak *(s)*
0.01	287.23 +10.538i	12.59
0.1	296.20 +4.1137i	2.512
1	299.35 +1.4264i	0.7943
10	300.37 +0.4666i	0.3981

The corresponding perturbation velocity profiles for the unstable eigenvalue are shown in Figure 2.36. Unlike the previous calculations, the perturbation growth occurs primarily at the lower boundary, near the "wall". This is counterintuitive, and raises doubt about the validity of this equation. The energy vs. time curve for the most unstable eigenvalue was calculated for wavenumber α=1,000 using 400 nodes, with the results shown as a log-log plot in Figure 2.37. Increasing the wavenumber from 10 to 1,000 only decreased the instability time from 0.40 to 0.03 seconds.

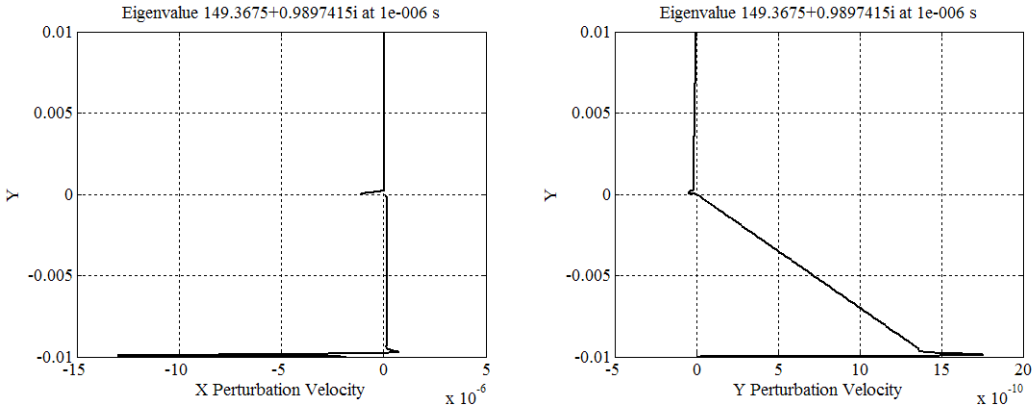

Figure 2.36. Perturbation velocities for Boomkamp JC (α=1, *V*=1000, d=0.01, N=200)

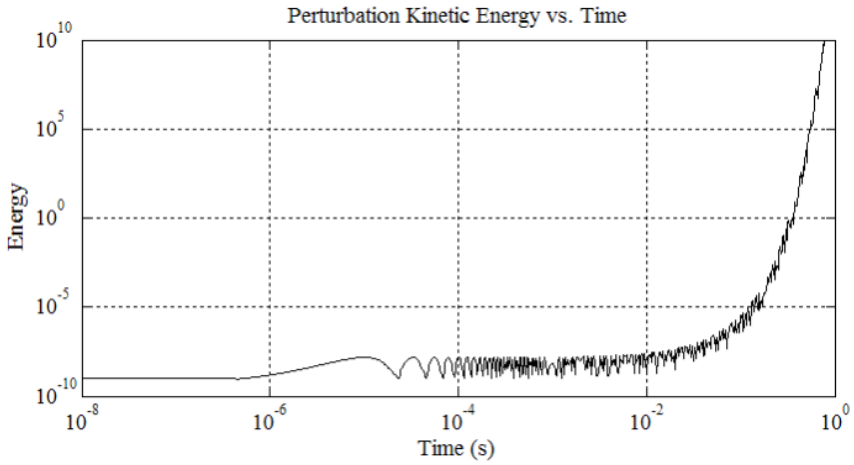

Figure 2.37. Energy vs. time for Boomkamp JC unstable eigenvalue (α=1000, *V*=1000, N=400)

2.3.5 COMPRESSIBLE FLOW

The majority of published work on compressible flow stability deals with inviscid fluids. Blumen used a Runge-Kutta technique to examine arbitrary perturbation velocities in parallel shear flow of a compressible ideal gas up to Mach 1, finding that compressibility was largely a stabilizing feature since work must go into elastic energy before it can go into destabilizing the flow [156]. Blumen *et al.* later showed that instabilities could exist in a compressible fluid up to Mach $\sqrt{2}$ [157], in contrast to previous assumptions that instabilities should not exist above a critical Mach number (usually Mach 1) [104]. Drazin *et al.* calculated that a compressible shear layer is unstable to 2D perturbations regardless of Mach number [158].

For stratified compressible fluids both inviscid and viscous flows have been analyzed. As in inviscid flows, the real component of the perturbation wave speed has to lie within the velocity of the baseline flow, even if supersonic [159]. The general condition for stability in inviscid flow is that the Richardson number be greater than 1.0 [160]. For viscous flows, the dispersive properties of the fluids result in a tangential discontinuity being unstable at all Mach numbers according to Sibgatullin [161]. However, this is dependent on the constitutive laws for the fluids, with the bulk of analyses dealing with supersonic flow of gases and not liquids [162].

There is a dearth of literature dealing with the stability of supersonic liquids, whose viscosities have a fundamentally different dependence on temperature than gases. Based on the above results, the severe approximations that must be made for liquid equations of state and constitutive models, and the general tendency of compressible flow to stabilize perturbations, the effects of compressibility were not examined.

2.4 Dynamic Material Behavior

One of the implicit assumptions in most of the previous models is constant material properties. In reality, the strength of materials changes significantly with strain, strain-rate, and temperature. Such effects are inherently nonlinear, and are usually reserved for more complicated finite element codes. However, they can be investigated to see what role they *should* have on the predictive models.

The strength of a solid is determined by the resistance of crystallographic defects (dislocations) to motion under an applied stress. This can be broken down into competing processes of strain hardening (dislocation multiplication and interactions), strain-rate hardening (dislocation and phonon drag), and thermal softening (thermally activated dislocation climb) [36,163].

An example of steady state vs. rapid heating is shown in Figure 2.38, which shows the yield strength of aluminum under steady state (equilibrium) and rapid heating conditions [164]. The effect of time at temperature is significant, with the rapidly-heated aluminum having several times the yield strength of its equilibrium counterpart at high temperatures. A more common example of the time at temperature effect is the formation of Martensite in medium- or high-carbon steels, whose microstructural and mechanical properties can vary significantly with cooling rate.

At moderate strain rates the flow stress is dominated by thermal effects, especially for FCC crystals [165]. At high strain rates, effects like twinning (especially in BCC and HCP crystals) and martensitic transformation can become important [36]. Because dislocations move via lattice vibrations, they can only propagate as fast as the speed of those vibrations. This results in relativistic effects near the shear and dilatational sound speeds [166], and is known as *phonon drag*. Electron drag is also possible, though is usually only important at very low temperatures [166].

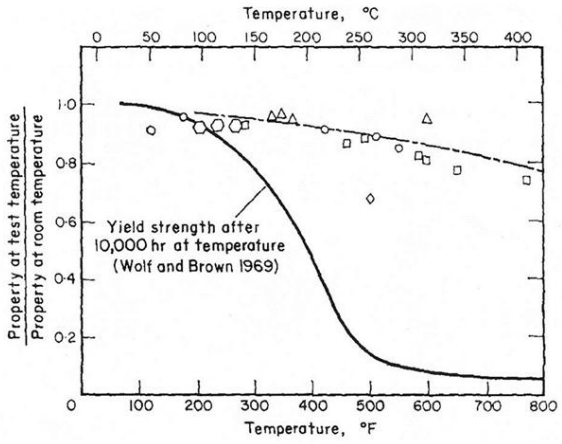

Figure 2.38. Steady state and "adiabatic" material strength[16]

The most widely used models that approximate these collective effects are the Johnson-Cook (J-C) and Zerilli-Armstrong (Z-A) models [36]. These are typically employed in hydrocodes such as EPIC and CTH to model material failure [167]. The J-C constitutive model for flow strength is shown in Equation (2.74), with the Z-A model shown in Equation (2.75). Both models are based on dislocation mechanics, but each requires 5+ constants that must be determined experimentally though split-Hopkinson bar, expanding ring, Taylor impact, or isentropic compression experiments depending on the strain rate of interest [59,168,169]. The J-C model works well for iron-based alloys and some Al alloys, but is not as accurate for modeling copper compared to the Z-A model [170,171].

$$\sigma = (A + B\varepsilon^{n})(1 + Cln\dot{\varepsilon}^{*})(1 - T^{*m}) \tag{2.74}$$

The Z-A model is based on calculating the "activation area" swept by a dislocation as it overcomes an obstacle, and the available thermal activation energy [167]. For FCC (face-centered cubic) crystals the activation area is largely determined by

[16] Reprinted with permission from J.C. Swearengen, J. Lipkin, C.M. Percival, "Influence of microstructure on the dynamic high-temperature elastic moduli of aluminum," Journal of Applied Physics, Vol. 44, No. 12, pp. 5209-5212, 1973. Copyright 1973, American Institute of Physics.

dislocation "forests." For BCC (body-centered cubic) crystals the activation area is dominated by the Peirls-Nebarro barrier stress. The Z-A model also incorporates temperature rise from heat generated by dispersive dislocation motion, which can be significant at high strain rates. The Z-A models for FCC, BCC and HCP crystals were originally written as separate equations, but can be written as a single equation [21] as shown in (2.75). In this formulation the constant c_1 is set to zero for FCC materials, while c_2 is set to zero for BCC materials. The first term A incorporates the dislocation density and grain-size or "Hall-Petch" stresses, ε is strain, $\dot{\varepsilon}$ is strain rate, and T is temperature. The constants $c_1 \ldots c_5$, A, n are all determined experimentally.

$$\sigma = A + \left(c_1 + c_2\sqrt{\varepsilon}\right)e^{(c_4 ln\dot{\varepsilon} - c_3)T} + c_5\varepsilon^n \tag{2.75}$$

Many improvements have been made to the Z-A model in recent years [172,173]. One of the early improvements of the model was adding the effect of twinning, which occurs for iron (BCC) around 600 MPa, while copper (FCC) requires a stress of 1.6-2.8 GPa [64,174,175]. Twinning is incorporated in the Z-A model by changing the grain size used in the Hall-Petch term to accommodate the existing over-stress [176]. Adiabatic heating (shear banding) has also been incorporated, which is particularly important for titanium alloys [177,178]. More recent isentropic compression experiments (ICE) have extended the Z-A model to strain rates approaching 10^7 s^{-1} [179]. At these high strain rates the flow stress for FCC materials is governed by dislocation generation, while BCC flow stress is governed by twinning formation [180]. A plot of flow stress vs. strain rate for copper up to 10^7 s^{-1} is provided in Figure 2.39. The relativistic effect of phonon drag begins to dominate around 10^4 s^{-1}.

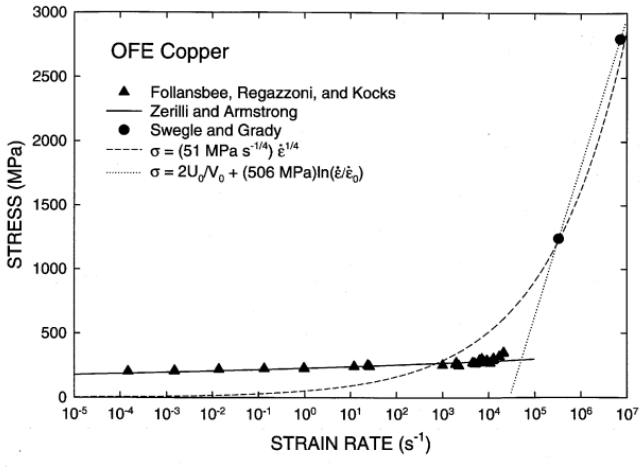

Figure 2.39. Yield strength as a function of strain rate for copper[17]

It is difficult to determine the relevant strain, strain-rate, and temperature of slider and rail materials from first principles. One possibility is to employ the semi-empirical models and determine the conditions required for the materials to match the overall curve-fit. For this analysis the acoustic shear impedance approach was used as it is readily employable and about as accurate as the shock pressure method.

The data was plotted vs. the maximum hardness of the material pair. While previous curve-fits using the mean hardness resulted in a better correlation, we are resuming the assumption that both materials are required to fail and thus the maximum hardness is the parameter of interest. The Y-intercept for this exercise will also be set to zero, as the original curve fit would result in unrealistic behavior for the lead/lead material pair. The resulting curve fit is shown in Figure 2.40.

By using the shear impedance calculation to determine the maximum hardness, the deviation from the measured hardness values can be determined. The results of this calculation are shown in Table 2.9. Reductions in hardness imply thermal softening, while increases in hardness imply strain or strain-rate hardening. It is presumed here that

[17] Reprinted with permission from R.W. Armstrong, W. Arnold, F.J. Zerilli, "Dislocation Mechanics Under Extreme Pressures," Shock Compression of Condensed Matter, Vol. 955, pp. 623-626, 2007. Copyright 2007, American Institute of Physics.

the hardness values with less deviation from their prediction are responsible for the governing behavior.

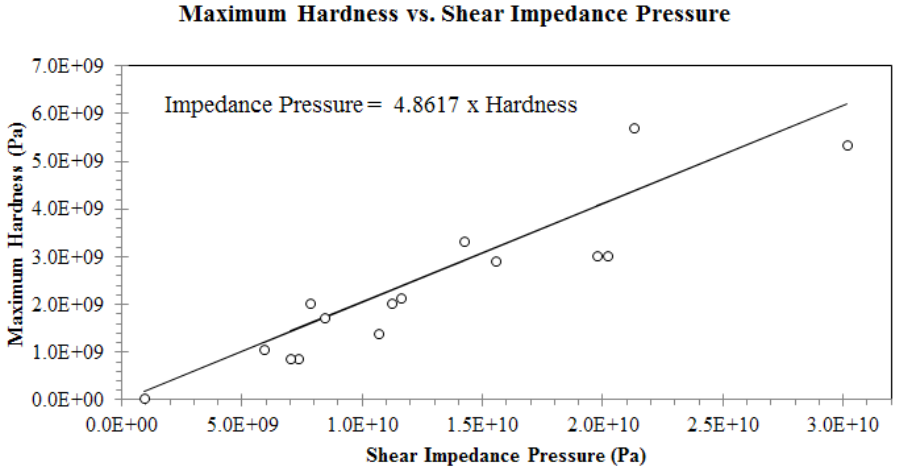

Figure 2.40. Maximum hardness vs. shear impedance stress with zero Y-intercept

Table 2.9. Hardness variations based on shear impedance method

Slider	**Hardness**	**Rail**	**Hardness**	**Est. Max. Hardness**	**Hardness Increase**	
	GPa		*GPa*	*GPa*	Slider	Rail
AISI 304	1.265	**AISI 1080**	3.030	4.067	221%	**34%**
AISI 4340	2.236	AISI 1080	3.030	4.151	86%	37%
Vascomax 300	5.345	AISI 1080	3.030	6.199	16%	105%
Lead	0.054	Lead	0.054	0.188	247%	247%
C11000	1.069	C11000	0.490	1.210	13%	147%
AA7075-T6	1.716	C11000	0.863	1.736	1%	101%
C11000	0.863	C11000	0.863	1.504	74%	74%
AA7075-T6	2.040	C11000	0.863	1.612	-21%	87%
Au80-Cu20	3.334	C11000	0.863	2.923	-12%	239%
AISI 1015 (A)	1.402	C11000	0.863	2.196	57%	155%
Silver	0.735	C11000	0.863	1.445	96%	67%
Molybdenum	2.903	C11000	0.863	3.198	10%	271%
Nickel	2.030	C11000	0.863	2.307	**14%**	167%
Tungsten	5.698	C11000	0.863	4.377	-23%	407%
Titanium	2.138	C11000	0.863	2.381	11%	176%
AISI 4340	5.305	C11000	0.863	4.243	-20%	392%

Two materials from Table 2.9 were examined as an exercise. AISI 1080 steel and Nickel 200 both show an increase in hardness relative to their baseline values, while their

counterparts have a much greater deviation from the model. To obtain an estimate of the conditions possible for this behavior the Johnson-Cook model was employed, with the values provided in Table 2.10.

Table 2.10. Johnson-Cook Material Constants for AISI 1080 and Nickel

	A *(MPa)*	**B** *(MPa)*	**C**	**m**	**n**
AISI 1080 [169]	792	510	0.014	1.03	0.26
Nickel 200 [170]	163	648	0.006	1.44	0.33

The original J-C model can be rewritten in terms of temperature as shown in (2.76). The stress term in the numerator was set equal to the room temperature value, and increased by the deviation value listed in Table 2.9. A Matlab® script was then run using this equation for strains from 10^{-2} to 10^{2}, and strain rates from 10^{-2} to 10^{6} s^{-1}. At each condition the temperature that would result in the observed yield strength deviation was calculated. The results for AISI 1080 and Nickel are shown in Figure 2.41 and Figure 2.42, respectively.

$$T^{*m} = 1 - \frac{\sigma}{(A + B\varepsilon^{n})(1 + Cln\dot{\varepsilon}^{*})} \tag{2.76}$$

Other models can also be investigated, such as simple power-law hardening, to get an estimate of critical strain or strain-rate required for gouging. In this case the more complex J-C model was employed due to its proven accuracy for steel in CTH models, though the Z-A model would be preferred for modeling copper. However, it is difficult to proceed further without making significant assumptions about sources of heat at the slider/rail interface. As a benchmark, Cinnamon asserts that gouges in 1080 steel rails result in the material reaching the melt temperature of 1,753 K, though this corresponds to after the gouge has started [16].

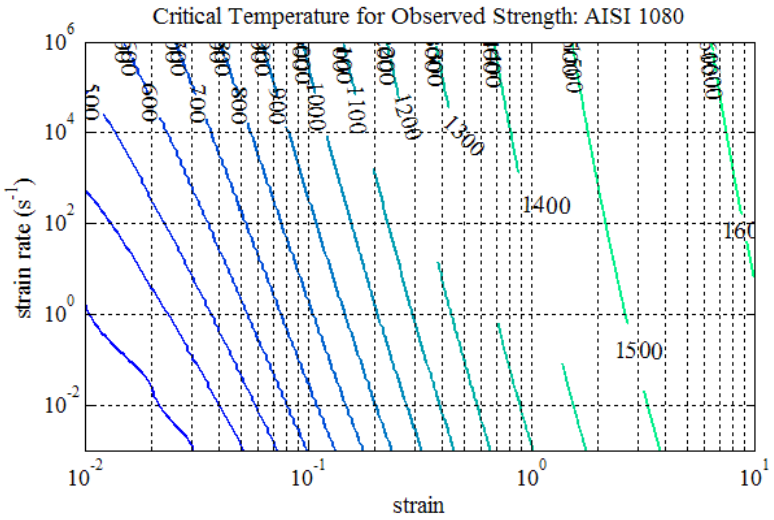

Figure 2.41. Strain/strain-rate/temperature map for AISI 1080 hardness estimate (34% strength increase compared to baseline)

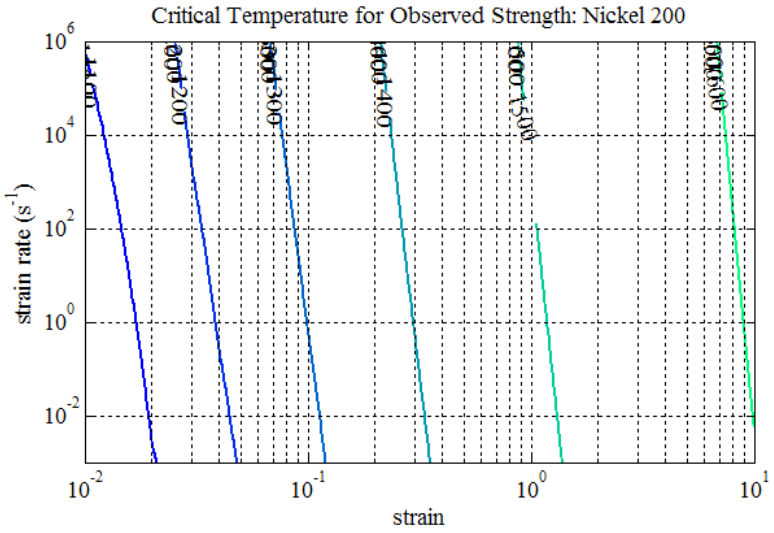

Figure 2.42. Strain/strain-rate/temperature map for nickel hardness estimate (14% strength increase compared to baseline)

2.5 Summary of Modeling Results

The semi-empirical models developed for gouging do a remarkably good job of predicting the observed threshold behavior. The Stefani-Parker normal impact model requires Hugoniot data which may not be available for the materials of interest. However, the calculations are relatively straightforward, and a threshold velocity can readily be determined using Equations (2.77)-(2.78). This method is accurate over a wide range of velocities, with a correlation of 96%.

$$\mathrm{V}_{Shock} = \frac{-C_A}{2s_A} + \frac{1}{2}\sqrt{\left(\frac{C_A}{s_A}\right)^2 + \frac{4P}{\rho_A s_A}} + \frac{-C_B}{2s_B} + \frac{1}{2}\sqrt{\left(\frac{C_B}{s_B}\right)^2 + \frac{4P}{\rho_B s_B}} \tag{2.77}$$

$$P = 8.45(H_{max}) + 5.61 \times 10^9 \tag{2.78}$$

A simplified version of the S-P model avoids the use of Hugoniot data and relies instead on the acoustic impedances of the materials. This is the normal acoustic impedance approach, shown in Equations (2.79)-(2.80). The results are about as accurate as the normal shock method, with a correlation of 93%. The predictive outputs of both models are shown in Figure 2.43.

$$\mathrm{V}_{Normal} = \frac{(Z_A + Z_B)}{Z_A Z_B} P \tag{2.79}$$

$$P = 7.40(H_{max}) + 6.77 \times 10^9 \tag{2.80}$$

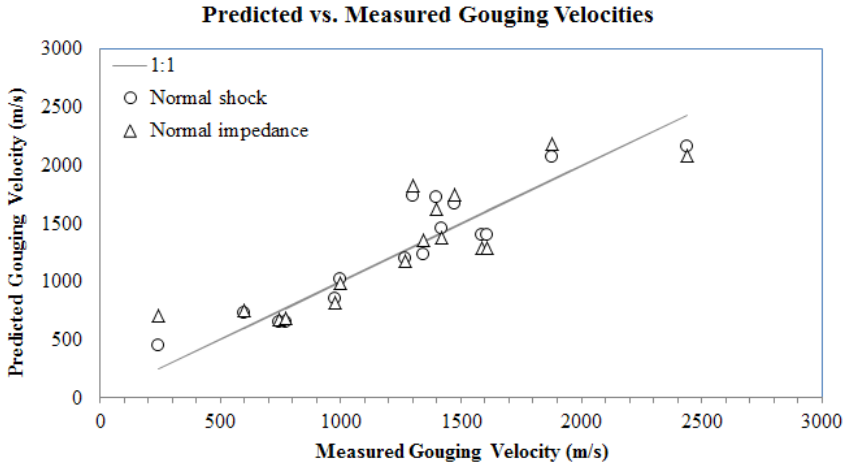

Figure 2.43. Predicted gouging velocities for normal shock and normal acoustic impedance methods

Based on research in the field of explosive welding, the effective Reynolds number approach was applied to gouging. Cowan's effective Reynolds number, reformulated in Equation (2.81), is based on the ratio of dynamic pressure (hardness) and pressure (ρv^2). However, it does an extremely good job of predicting the gouging velocities, with an overall correlation of 98.4%. The Reynolds number for gouging is about half of the Reynolds number for explosive welding.

$$V_{Reynolds} = \sqrt{\frac{2(H_A + H_B)}{(\rho_A + \rho_B)} Re}, \qquad Re = 4.7 \tag{2.81}$$

The last model developed was the shear impedance model. This has the same functional form as the normal acoustic approach, but is based on the transmission of shear waves instead of dilatational waves. This method is given in Equations (2.82)-(2.83), and provides an overall correlation of 97.7%. In this method the mean hardness is used, as in the Reynolds number approach. The maximum hardness can be used if desired, though the correlation is reduced by a few percent. This is a conceptual compromise, since using the maximum hardness is more appropriate for a process that

requires simultaneous slider/rail material failure. It is likely that using the mean hardness has the effect of mimicking the results that would be obtained if the dynamic properties of the materials were known. Both the Reynolds number and shear impedance approaches are shown in Figure 2.44. The tabulated predictions using all the models are listed in Table 2.11.

$$V_{Shear} = \frac{(Z_A + Z_B)}{Z_A Z_B} P \tag{2.82}$$

$$P = k_S H_{avg}, \qquad k_S = 7.26 \tag{2.83}$$

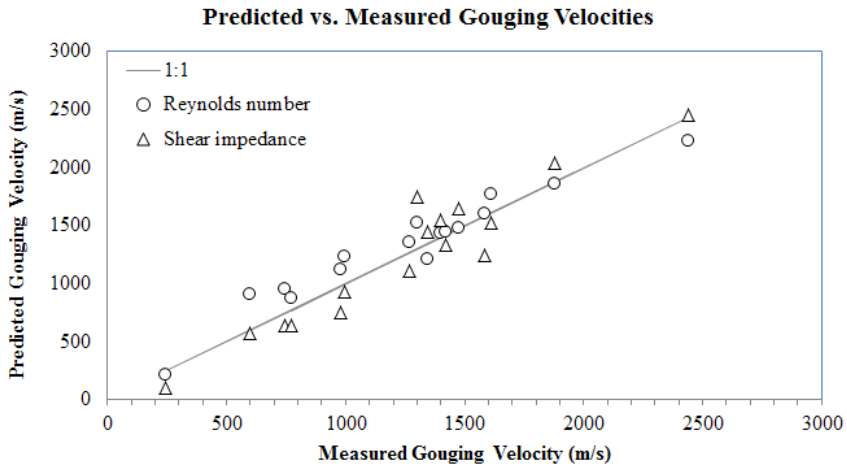

Figure 2.44. Predicted gouging velocities for Reynolds number and shear impedance methods

Table 2.11. Gouge velocities and model estimates

Slider	Rail	V_{gouge}	V_{Shock}	V_{Normal}	$V_{Revnolds}$	V_{Shear}	Source
		m/s	*m/s*	*m/s*	*m/s*	*m/s*	
AISI 304	AISI 1080	1,585 ± 79	1,404	1,293	1,602	1,250	Tarcza [28]
AISI 4340	AISI 1080	1,610 ± 81	1,401	1,286	1,776	1,525	"
Vascomax 300	AISI 1080	2,438 ± 122	2,161	2,081	2,231	2,460	"
Pb	Pb	245 ± 12	453	713	212	106	"
C11000-H02	C11000	600 ± 30	734	754	908	578	Stefani [25]
AA7075-T6	C11000	1,400 ± 70	1,723	1,627	1,439	1,554	"
C11000	C11000	746 ± 50	656	676	955	639	“
AA7075-T6	C11000	1,300 ± 65	1,734	1,827	1,527	1,749	"
Au80-Cu20	C11000	1,346 ± 75	1,233	1,353	1,217	1,444	"
AISI 1015	C11000	977 ± 110	850	818	1,127	753	"
Ag	C11000	770 ± 90	656	688	881	636	"
Mo	C11000	1,268 ± 30	1,198	1,178	1,361	1,115	"
Ni	C11000	996 ± 70	1,025	992	1,237	933	"
W	C11000	1,474 ± 45	1,676	1,751	1,482	1,650	"
Ti	C11000	1,420 ± 55	1,456	1,377	1,451	1,336	"
AISI 4340	C11000	1,878 ± 90	2,077	2,184	1,861	2,039	"

CHAPTER 3. EXPERIMENTAL METHODS

Railgun experiments were conducted at the Institute for Advanced Technology's Electromagnetic Launch Facility (ELF, illustrated in Figure 3.1). The ELF consists of 18 1-MJ capacitor banks powered by a 24 Amp, 22 kV power supply. Two MCM 350 coaxial cables connect each capacitor bank to one of three electromagnetic launchers through a distribution table. The capacitor banks are triggered independently via fiber optic signals so that pulse shaping can be performed to yield a variety of current wave shapes to the launchers. Capacitor bank and launcher diagnostics are connected to the control room via coaxial cables in grounded cable trays. These signals are recorded with a digital data acquisition (DAQ) system at a normal sampling rate of 1 MS/s (mega-sample per second).

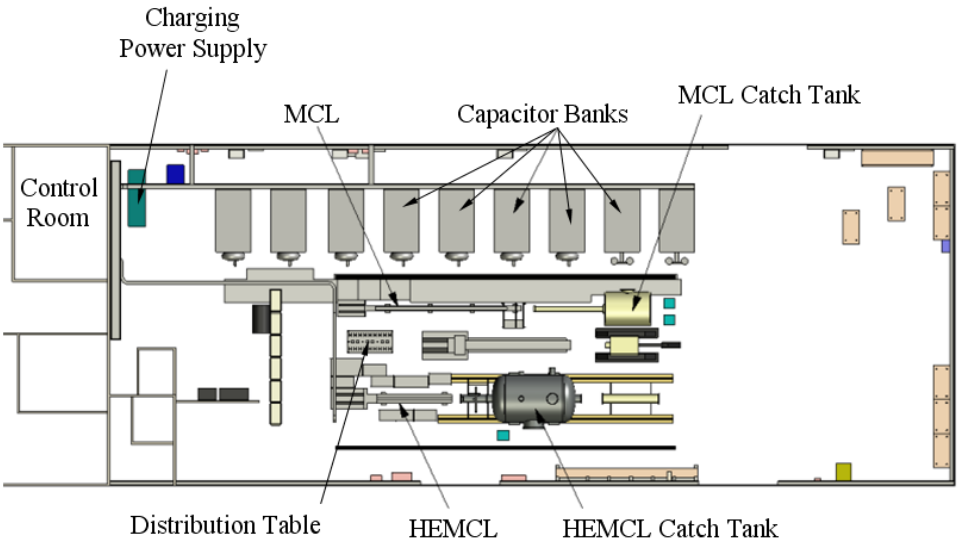

Figure 3.1. The IAT Electric Launch Facility (ELF)

A total of four test series were performed (see Table 3.1). The first series used copper armatures on copper rails to examine the evolution of galling and gouging damage

at relatively low velocities (~1 km/s). The second series used aluminum armatures with modified payloads to hold isolated material samples in contact with the copper rails. These tests were designed to examine different gouging materials that would be difficult to use as armature materials such as high-strength steels and ceramics. The third series used aluminum-electroplated copper rails to test the effect of thin coatings on the onset of gouging. The fourth series used aluminum armatures on copper rails with indented contact surfaces. These experiments were designed to assess the role of macroscopic surface indentations on gouging threshold velocity as well as crater morphology.

Table 3.1. Experimental overview

Series	Description	Funding	Launcher	# Tests	Slider	Exit Velocity
1	Basic Armatures	ONR[18]	MCL	3	AA7075, Cu	1.2 km/s
2	Sample Sliders	ONR[18]	MCL	10	4xxx Steels, Al, Ta, Zr, MACOR®	2.2 km/s
3	Coated Rails	ARL[19]	MCL	7	AA7075	3.5 km/s
4	Rail Indentations	ARL[19]	HEMCL	2	AA7075	2.1 km/s

The next section covers the test and analysis equipment used for the experiments. The remaining sections will describe the experimental procedures used in each of the four test series described above. Results from the experiments are discussed in Chapter Four.

3.1 Test and Analysis Procedure

3.1.1 Electromagnetic Launchers

Two launchers were used in the course of the experiments: IAT's Medium Caliber Launcher (MCL) and High-Energy Medium Caliber Launcher (HEMCL) [181]. Both of these launchers use a laminated steel clam-shell containment structure illustrated in Figure 3.2: The conductors are surrounded by G10/FR4 fiberglass-epoxy insulators that

[18] Office of Naval Research MURI Contract No. N00014-04-1-0599
[19] U.S. Army Research Laboratory Contract No. W911QX-07-D-0002

set the rail-to-rail and rail-to-containment spacing, and insulate the rails from each other and the metal containment. The rails and insulators constitute the “core” of the railgun. The clam-shell laminated containments are held together by external C-clamps. The clamps are tightened by set screws that push on wedges to compress the laminated containments. This clamping establishes the insulator-to-insulator pre-compression. The rail-to-rail compression is determined primarily by the interference fit between the rails, insulators, and containments. This interference is controlled by adjusting the thickness of Mylar® sheets inserted between the insulators and containment.

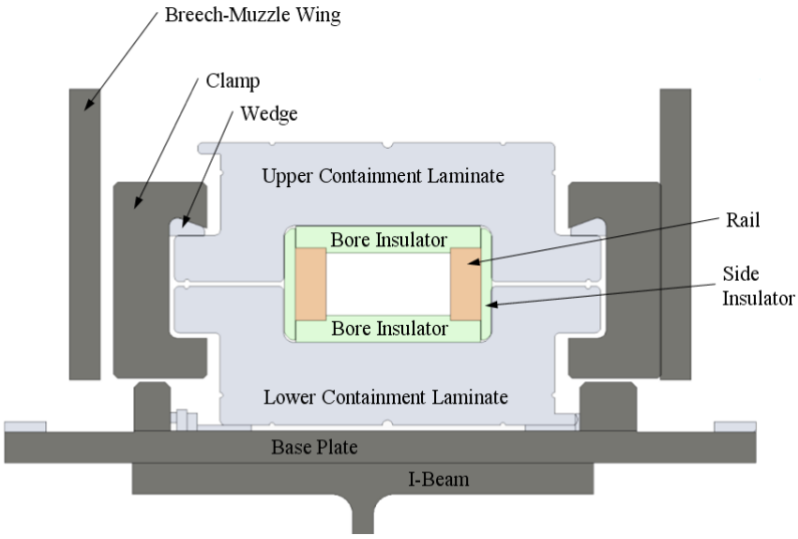

Figure 3.2. Laboratory railgun barrel components

The top containments are pressed down onto the core either by using large dead-blow hammers or a hydraulic compression assembly, depending on the preload required. Once all the containments are installed, the side “wings” are first bolted to the breech and then tightened down onto the muzzle plate or “shroud”. The tightening of the wings provides an axial pre-compression and also transfers axial loads imparted to the core back through the wings into the breech frame. Without this mechanism the core could be gradually pulled downstream by the electromagnetic and friction loads imparted during the launch cycle. An isometric rendering of the HEMCL highlighting these components

is provided in Figure 3.3. Both the MCL and HEMCL are “hard mounted” to the concrete laboratory floor through a large steel breech stand and numerous concrete anchors.

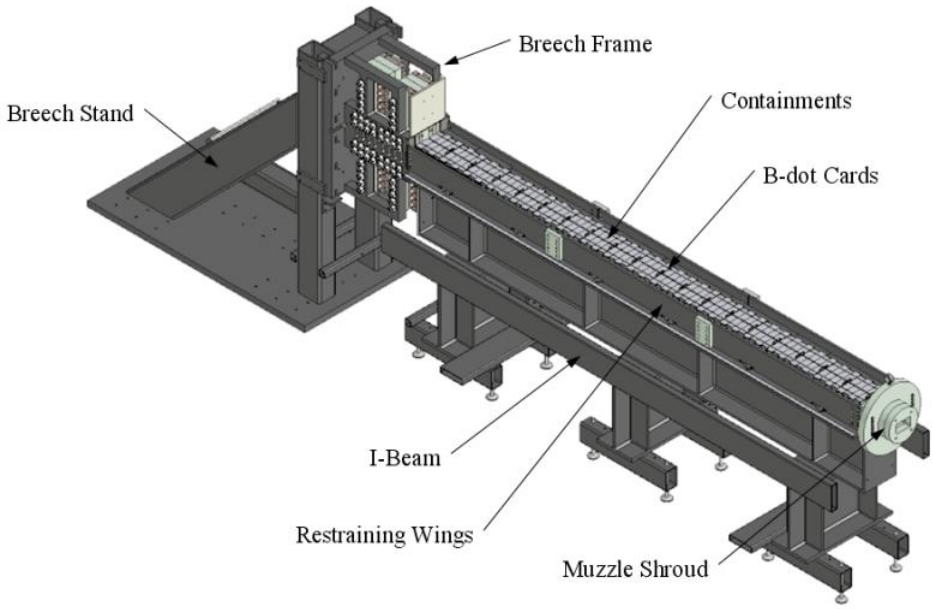

Figure 3.3. Laboratory railgun (HEMCL)

Figure 3.4 shows photographs of the laminated steel containments used in the HEMCL. The containments are built this way to prevent large eddy current loops from being induced in the containment structure. Since the electromagnetic launchers are long (up to 7 m), using a solid metal containment structure would trap the magnetic field and result in large image currents induced in both the top and bottom containment halves that would divert much of the magnetic energy otherwise available to accelerate the armature. This is illustrated below in Figure 3.5, which shows the magnetic flux lines for a solid containment (left) and laminated containment (right).

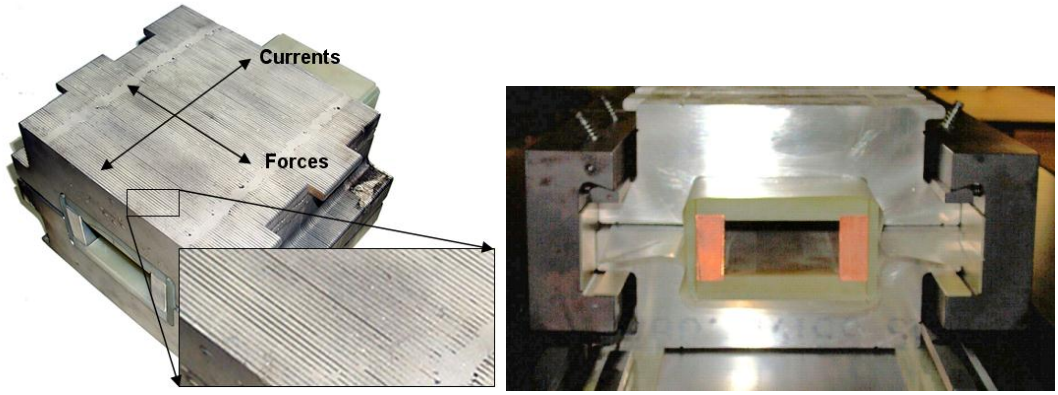

Figure 3.4. Laminated steel containment used in HEMCL

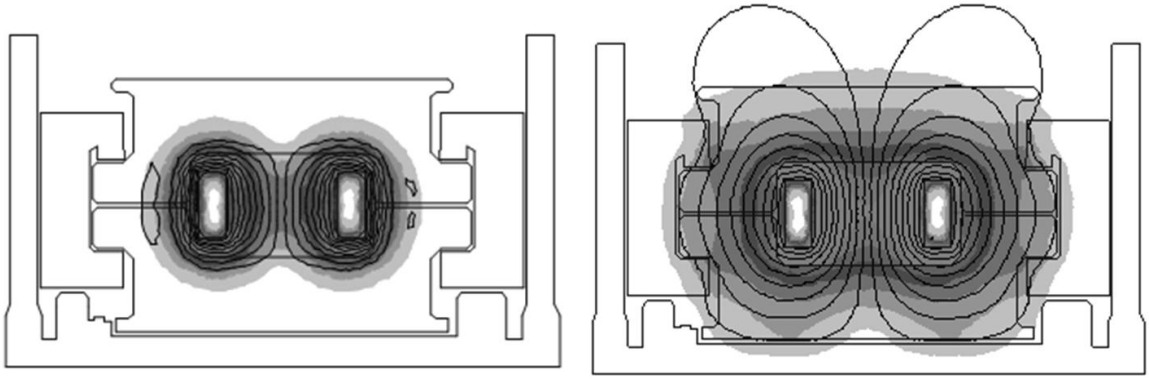

Figure 3.5. Effect of laminated steel containment on magnetic field
Solid containment (left: 0.31 μH/m), laminated containment (right 0.59 μH/m)

The performance of the various configurations is a function of the core geometry, projectile design, and applied current waveform. A summary of the salient information for the two launchers is provided in Table 3.2. The bore size is the "height" and "width" measurement between the bore insulators and rail contact surfaces, respectively. L' is the propulsive inductance gradient, which is a measure of propulsive efficiency for a railgun. The electromagnetic force F acting on a railgun projectile is given by Equation (3.1), where I_A is the current passing through the armature. Information on each of these configurations is provided in the immediately following sections.

$$F = \frac{1}{2} L' {I_A}^2 \tag{3.1}$$

Table 3.2. Launcher configurations

Launcher	Bore	L'	Peak Current
MCL	40 × 40 mm	0.38 μH/m	1,200 kA
HEMCL	38 × 76 mm	0.54 μH/m	1,460 kA

3.1.2 MEDIUM CALIBER LAUNCHER (MCL)

The Medium Caliber Launcher (MCL) was designed and fabricated by IAP Research (Dayton, OH) and installed in 1995 at IAT's laboratory facilities in Leander, TX. The MCL's laminated steel containment structure is capable of supporting peak currents up to 1,200 kA. The MCL is nominally a 1 MJ class launcher, meaning that it can accelerate projectiles to muzzle kinetic energies ($\frac{1}{2}mv^2$) up to 1 MJ. The majority of research performed on this launcher involves accelerating a 200-g projectile to around 2.5 km/s, or 0.63 MJ. The standard core for MCL is a 40 x 40 mm square-bore using rails with a cross-section of 0.75" x 1.75", up to a total launch length of 7 m. An illustration of the cross-section used in the experiments reported here is shown in Figure 3.6.

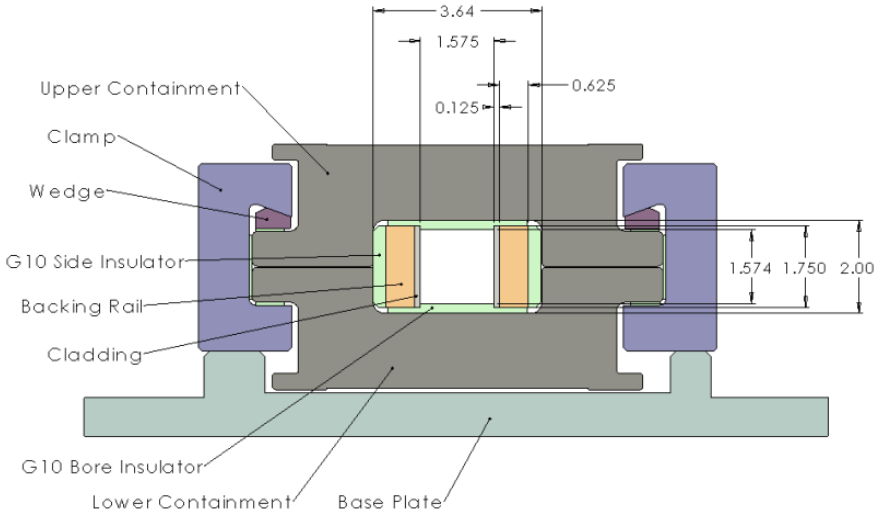

Figure 3.6. MCL railgun barrel cross-section (dimensions in inches)

The peak current is limited by the $J \times B$ forces that act to push the rails apart and result in high stresses in the containments and assembly clamps. Exceeding the peak current limit can result in damage to the containment and clamping hardware. Another operational limit is the exit or muzzle current, which is set by the muzzle arc formed when the armature leaves the gun. The muzzle arc creates a significant amount of light, heat and pressure from the rapid ablation of rail and insulator components. Larger muzzle arcs result in gas and shock pressures which can result in damage to the nearby surroundings. For the MCL the operational limit on exit current is about 200 kA, based largely on practical laboratory experience. The projectiles that leave the MCL travel through a magnetic muzzle sensor coil and open air space with orthogonal flash X-rays. The sensor coil is used to trigger the X-rays, and is one of the first components to be damaged by excessive muzzle arcs. An overview of the MCL gun line is shown in Figure 3.7, with photographs provided in Figure 3.8.

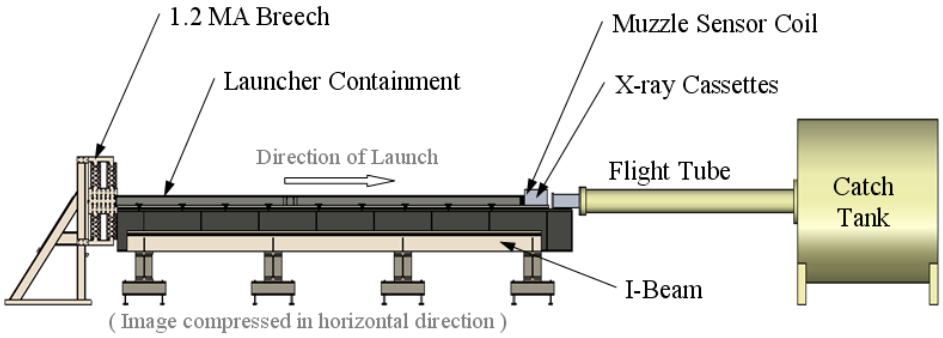

Figure 3.7. MCL test range

Figure 3.8. MCL with X-ray hardware (left) and catch-tank (right)

In test series 1-3 the MCL was configured to have a 40 x 40 mm square-bore that was 7 m long, with 0.75" x 1.75" (19 x 44.5 mm) rails separated by G10 insulators. The test series used composite rails composed of Aluminum 6061-T651 backing conductors and either C11000 or C15725 rail claddings (see Figure 3.6). This configuration allows the claddings to be removed after testing while the backing conductors can be re-used to reduce costs and re-build time.

3.1.3 HIGH-ENERGY MEDIUM CALIBER LAUNCHER (HEMCL)

The High Energy Medium Caliber Launcher (HEMCL) was installed at IAT in 2002 in support of an Army-funded effort to launch medium-caliber projectiles to muzzle kinetic energies of 2 MJ. The overall design of the HEMCL is essentially the same as the MCL with larger containment, clamps, and breech hardware. The larger containment and clamps allow the HEMCL to operate at peak currents up to around 1,750 kA using a bore cross-section of 38 mm x 76 mm. The same 0.75" x 1.75" rails as the MCL are used in the HEMCL (Figure 3.9, Figure 3.10), but are spaced farther apart which results in a higher L'. The HEMCL is also shorter than the MCL, with a total launch length of 4 m.

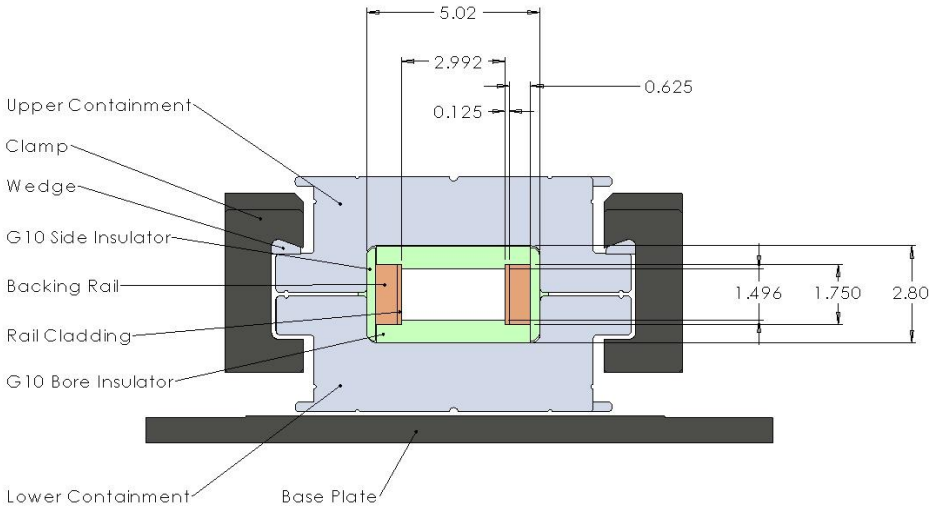

Figure 3.9. HEMCL cross-section view (dimensions in inches)

Figure 3.10. HEMCL photograph

Unlike the MCL, the HEMCL flight-line does not incorporate an open-air section for X-ray viewing. Instead, the launcher is moved up against a flight tube attached to a catch tank which is evacuated below 40 Torr (5.3 kPa) prior to the shot. The front of the flight tube is sealed by a Mylar® diaphragm which the projectile punctures as it exits the launcher. The system is illustrated in Figure 3.11 through Figure 3.13. As the armature leaves the bore and the muzzle arc forms, the catch tank acts as a low-pressure reservoir which draws in the resulting muzzle arc products. This configuration allows the HEMCL

to operate at much higher exit currents. While the MCL is limited to around 200 kA at exit, the HEMCL can safely operate at exit currents up to 800 kA.

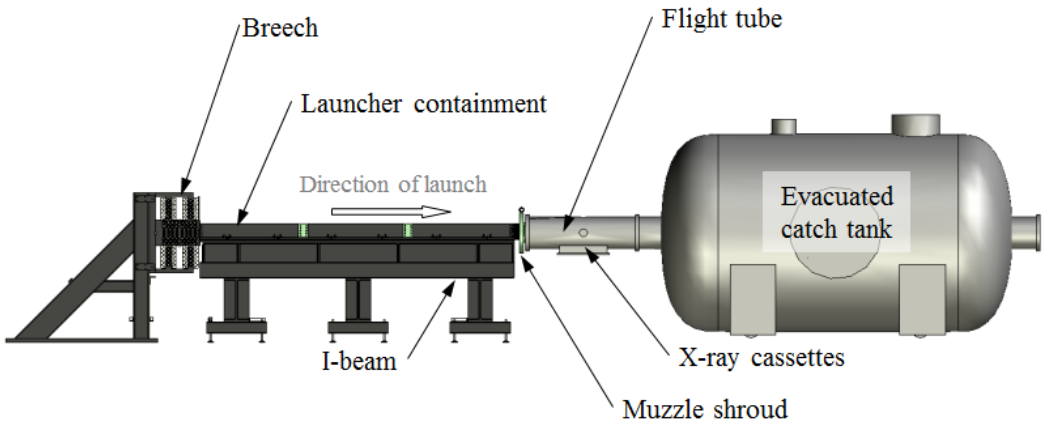

Figure 3.11. HEMCL test range

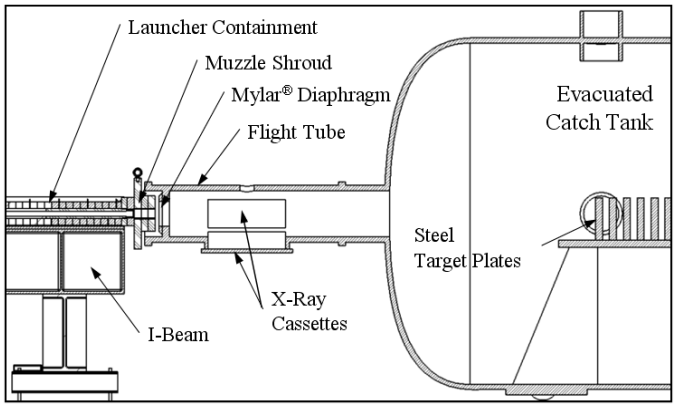

Figure 3.12. HEMCL flight tube and catch tank illustration

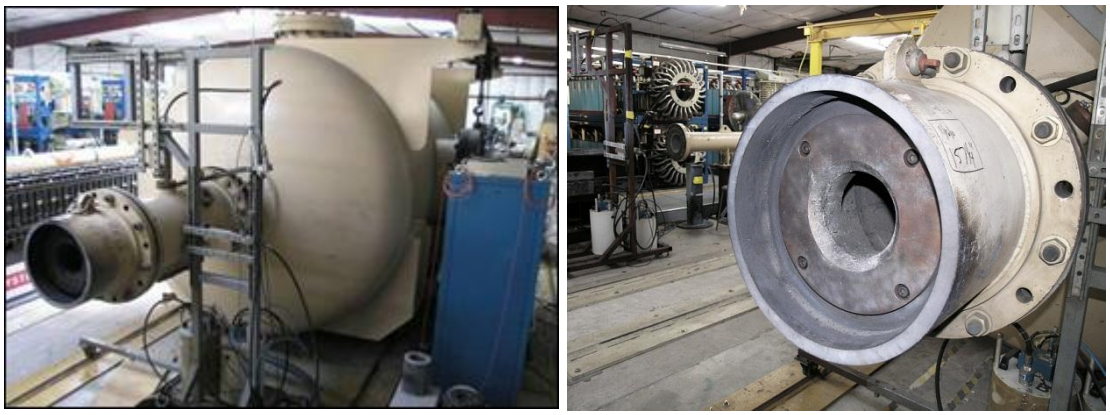

Figure 3.13. HEMCL catch-tank (left) and flight tube opening (right)

3.1.4 PULSED POWER SUPPLY (PPS)

The power supply used to charge the capacitor banks is connected to the local utility grid via a dedicated 1 kV 3-phase transformer rated at 500 kVA (Figure 3.14). The power supply can output up to 22 kV at up to 24 Amps. This permits the capacitor banks to be charged to 10-16 kV in 30-60 seconds. Once the banks have reached the desired voltage, they are disconnected from the power supply using fiber-optically controlled Ross relays.

Figure 3.14. 22 kV charging power supply

When the ELF was originally commissioned, 13 capacitor banks were installed to power the MCL. Each bank used 22 electrolytic capacitors rated at 0.2 mF with a maximum voltage of 22 kV. Each bank used a 22 μH toroid inductor on the output bus to slow the output current pulse and help match the impedance of the power supply to the launcher. The banks used ignitrons as both closing switches for the capacitors, and crowbar diode switches to prevent the capacitors from developing a reverse voltage during the launch cycle. A schematic of the capacitor bank arrangement is shown in Figure 3.15. A rendering and photograph of assembled banks are shown in Figure 3.16.

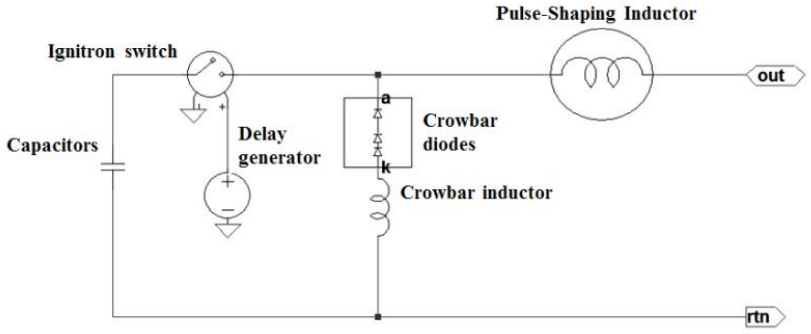

Figure 3.15. Capacitor bank circuit schematic

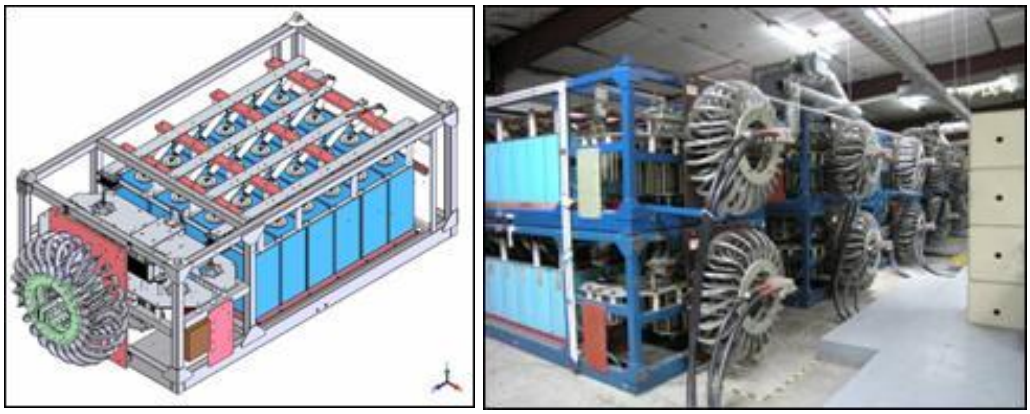

Figure 3.16. Capacitor bank with toroid inductors

Several upgrades occurred since the original installation of the MCL and the 13 capacitor banks. In 2002 the 13 banks were upgraded with solid state crowbar diode switches and new MCM 350 flexible coaxial cables. A two-way distribution table was

also installed at the time so that the power supply could be switched between the two launchers. In 2005 and 2006 the banks were upgraded from 22 capacitors per banks to 24, and five new banks were added to the system for a total of 18 capacitor banks. These coincided with the addition of a third launcher and a new three-way distribution table. The five new capacitor banks were essentially the same as the previous design, except that they used a new solenoid design for the pulse-shaping inductors in an attempt to reduce cost. A rendering and photograph of the new banks are shown in Figure 3.17. Figure 3.18 shows the distribution table used to switch between the three launchers.

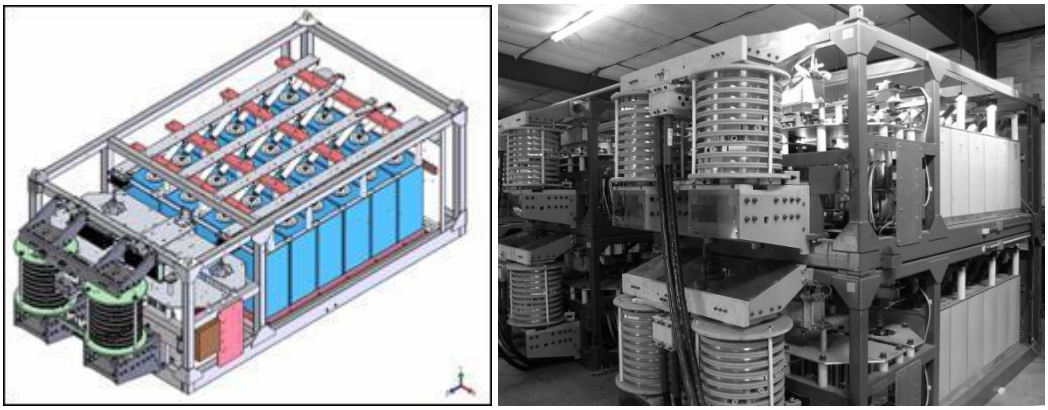

Figure 3.17. Capacitor bank with solenoid inductors

Figure 3.18. Three-way coaxial cable distribution table

The full array of capacitor banks is shown in Figure 3.19. By performing a rigorous set of calibrations, measurements, and individual banks testing, a reasonably

accurate circuit model has been developed which is capable of predicting the output pulse of the banks to within 1% of measurement. Using these parameters, appropriate modeling techniques, and experimentally-verified launcher parameters, the capacitor banks can be charged and fired in such a way as to render a well-controlled, repeatable current profile to the breech of the launcher (Figure 3.20).

Figure 3.19. Capacitor-based pulse-forming network (PFN)

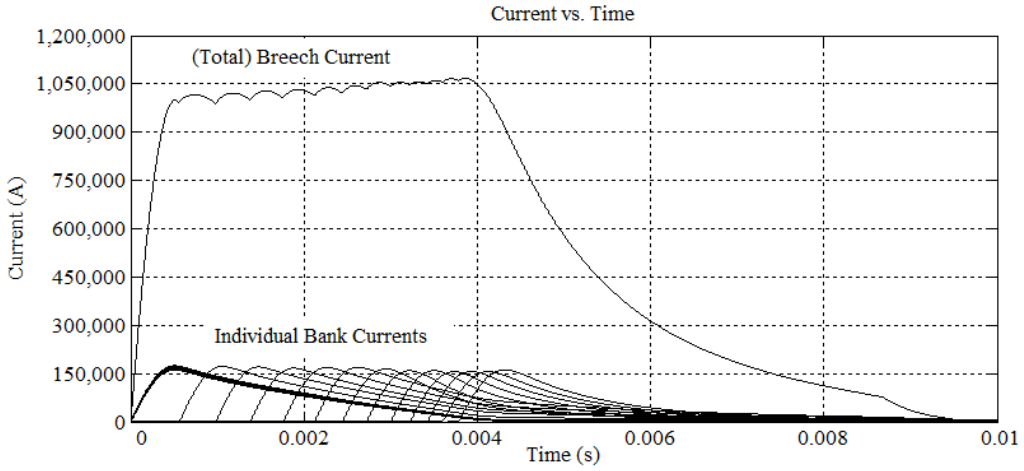

Figure 3.20. Current pulse shape obtained using staged capacitor bank timings

3.1.5 RAILGUN DIAGNOSTICS

The current flowing through the armature is a critical parameter for determining many variables of interest such as Lorentz force and electrical action. In the ELF, current measurements are made by means of dI/dt (I-dot) measurements on each capacitor bank with a Rogowski coil. The dI/dt signals are recorded and then numerically integrated to get the total output current of each bank, then summed together to calculate the total current flowing into the breech and through the armature. A Rogowski coil is essentially a wire wound in the shape of a toroid that is looped around the conductor to be measured (see Figure 3.21) [182]. When current flows in the central conductor, it induces eddy currents in the loop which create a voltage in the wire that is linearly proportional to dI/dt. The Rogowski coil acts as a current transformer, where no electrical connection is made between the conductor and the probe.

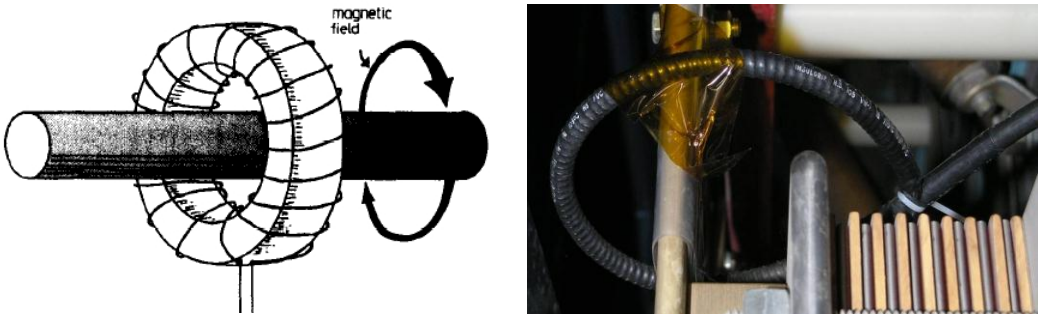

Figure 3.21. Illustration of Rogowski coil (left, © 1993 IEEE) [182], and Rogowski coil on capacitor bank output bus (right)

The Rogowski coils mounted on the capacitor bank output buses were designed, fabricated, and calibrated in-house in 1995 during commissioning of the pulsed power supply. The signal output is sent back to the control room's data acquisition (DAQ) system via coaxial cables in a grounded cable tray. The front of the capacitor bank with the output bus work and connected coaxial cables are shown in Figure 3.22 (left), with a close-up of the installed Rogowski coil shown in Figure 3.22 (right).

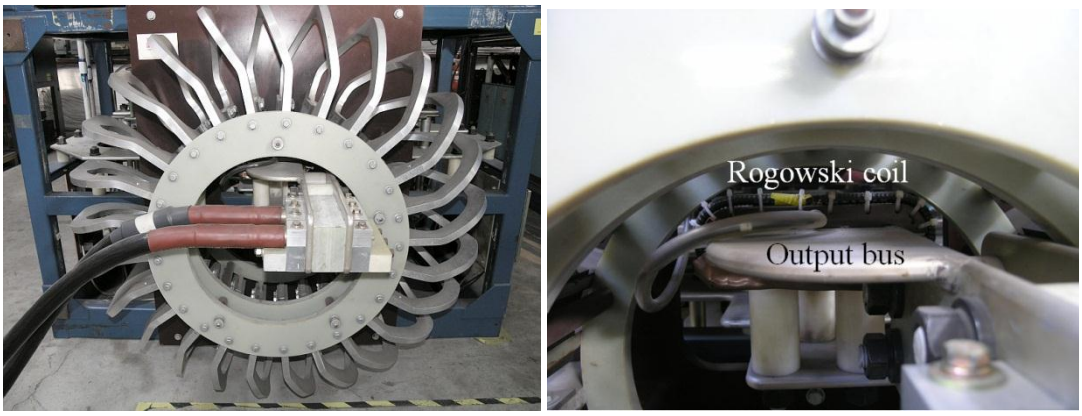

Figure 3.22. Photograph of capacitor bank output bus (left) and the attached Rogowski coil (right)

One of the issues experienced with Rogowski coils, and diagnostics in general, is measurement drift. To account for this, all signals are recorded for approximately 500 samples prior to the first capacitor banks being triggered. These data points serve as a baseline which is subtracted from the rest of the signal to correct for bias error (see Figure 3.23).

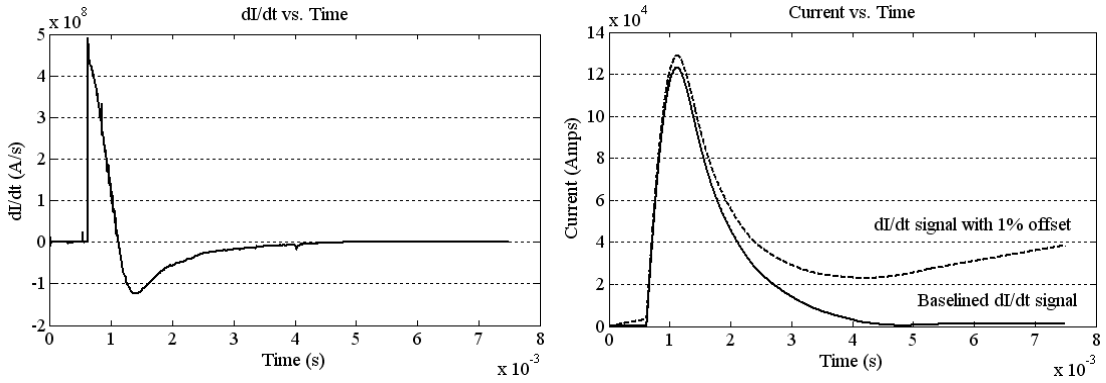

Figure 3.23. Effect of bias error on integration of raw I-dot signal to produce current

While current measurements are normally done in an isolated manner, voltage measurements are often not. To ensure that all diagnostics were floating with respect to the launcher, the voltage measurements in these experiments were taken using a current-viewing resistor wound around a current transformer. The current transformers used in these tests were Pearson™ current monitors (models 110 and 110A). The output of the

current transformer is linearly proportional to the muzzle voltage, and is routed back to the DAQ system using coaxial cables.

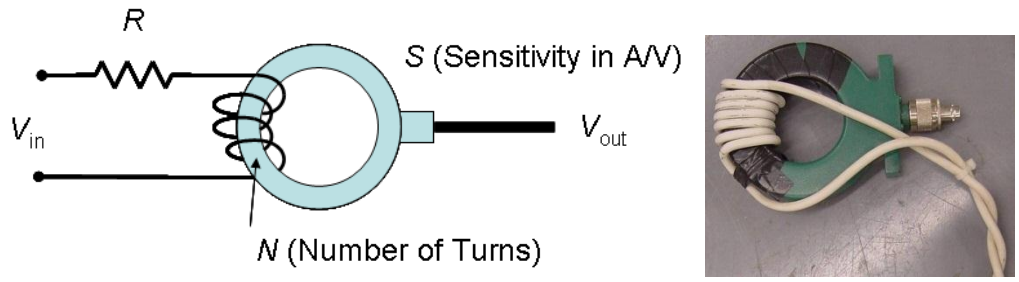

Figure 3.24. Pearson™ coil used for measuring voltage: schematic (left) and photograph (right)

The third real-time diagnostic used in the experiments are B-dot cards. B-dot measurements use essentially the same mechanism as the Rogowski coil and other current transformers used to monitor the local magnetic field. A B-dot is a thin loop of wire placed in the bore of the railgun near the armature as it passes by. The ends of the loop are carried out of the bore in a twisted-pair configuration and then connected to a coaxial cable which goes back to the DAQ system. As the armature passes by the B-dot, the rapidly changing magnetic field induces a voltage in the B-dot loop. The amplitude of the signal is a function of the current in the armature and its velocity. Depending on the orientation of the loop, different output waveforms are produced. The loops used in these experiments are so-called “rail B-dots” as they measure the B-field in the direction orthogonal to armature motion, and hence measure current flowing in the direction of launch. The B-dot signal experiences a peak which corresponds roughly to the location of the armature (Figure 3.25).

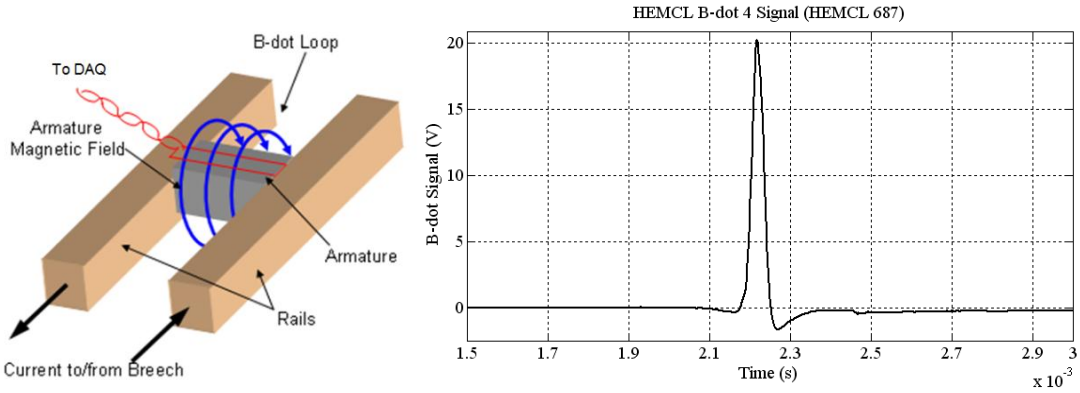

Figure 3.25. B-dot signal used to detect armature position

The B-dot cards used in the experiments were manufactured on circuit cards, and placed between containment sections down the length of the launcher. Fourteen cards were used in the MCL tests (Figure 3.26), while 18 cards were used in the HEMCL tests. Once all the B-dot signals are recorded, they can be used to provide a position vs. time curve for the armature (Figure 3.27), which can be used to estimate velocity and acceleration.

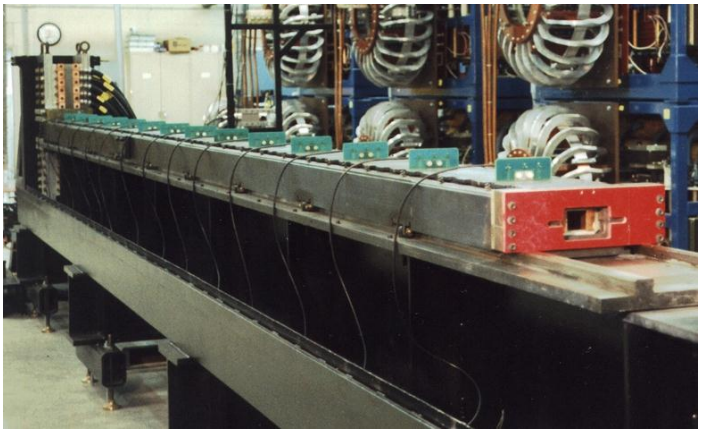

Figure 3.26. B-dot card array on MCL

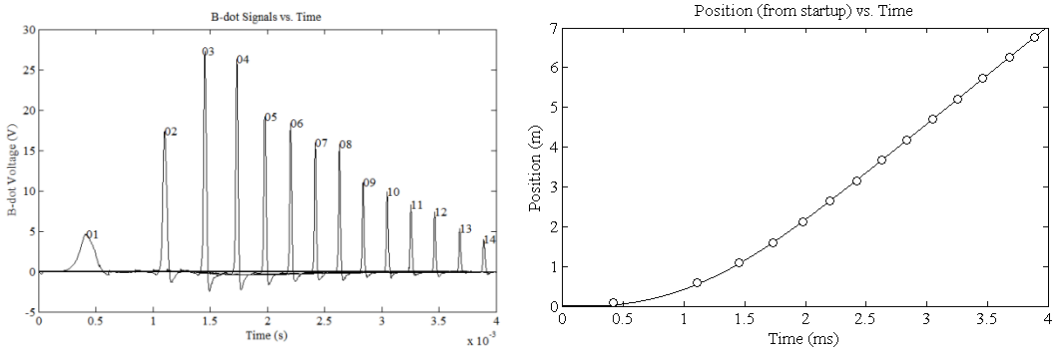

Figure 3.27. B-dot card array signals (left), and resulting position vs. time points (right)

The last diagnostics were orthogonal flash X-rays located downstream of the muzzle. In the MCL the X-rays were placed in an open-air region between the muzzle of the MCL and the beginning of the flight tube. In the HEMCL the X-rays were mounted to the evacuated flight tube (Figure 3.28). The X-ray system for both launchers used Scandiflash XT 150 X-ray heads, with the MCL X-ray heads powered by Scandiflash TA 400s and the HEMCL powered by TA 500s. The X-ray pulse was 30 ns long, which results in an image blur of 75 μm at 2.5 km/s. The X-rays were triggered for the MCL using a muzzle sensor, while the HEMCL X-rays were triggered using two of the B-dot signals and an up/down counter.

The MCL muzzle sensor works by energizing the sensor and waiting for a change in inductance which corresponds to a metallic object passing through it. This change in inductance shows up as a voltage spike which is then used to trigger the X-rays. The up-down counter for the HEMCL works by splicing the signals from B-dot 16 and 18 and using the times when both signals exceed a specified voltage threshold (usually ~1 V). The times between these two events, combined with the measured distance between B-dot cards, and measured distance between the last B-dot card and the X-ray cassettes, determines the time when the X-rays are triggered.

Figure 3.28. 150 keV flash X-ray systems on HEMCL

3.1.6 CONTROL AND DATA ACQUISITION (DAQ) SYSTEM

The control of the charging power supply and triggering system is done using a custom programmed MODSOFT touch panel control system, and Calev 113CR trigger delay generators. The patch panel, voltage monitors, and trigger generators are shown in Figure 3.29. The output of each trigger generator is sent via a fiber-optic cable to a trigger module attached to each capacitor bank. This trigger module is energized prior to charging the capacitor banks. When triggered, the module sends a pulse which activates the ignitron switches that close the circuit between the capacitors and output bus.

Figure 3.29. Control system used to charge and trigger banks and DAQ system

The DAQ system was installed alongside the MCL in 1994, and consists of CAMAC crates with 64 channels of 12-bit LeCroy digitizers capable of running up to 5 MS/s with a total record length of 8000 samples per channel. Usually the system is run at a sample rate of 1 MS/s since this is long enough to capture a typical railgun launch of 4-5 ms. A typical MCL experiment requires approximately 36 channels of data to be recorded (18 bank Rogowski coils + 14 B-dots + 2 voltages + 2 X-ray trigger signals). Most of the experiments reported on here used this DAQ system, shown in Figure 3.30.

The last set of experiments in Series 2 used a new DAQ system acquired in 2010, which was purchased under AFOSR MURI Contract DOA-8910 to support plasma railgun experiments. The new system, purchased from National Instruments, consists of 166 channels recording at a resolution of 14-bits at 2.5 MS/s. Other channels are capable of recording up to 100 MS/s at 14-bit, but were not used in the experiments. Both DAQ systems were used in parallel during this series.

Figure 3.30. IAT ELF control and data acquisition system

3.1.7 POST-SHOT ANALYSIS

Once an experiment is completed, the rails are removed from the launcher for inspection. The projectile's velocity profile is calculated by numerically integrating the acceleration vs. time curve. The acceleration of the projectile is determined using Equation (3.2), where *m* is the projectile mass, ρ_{air} is the density of air, and *A* is the bore cross-sectional area [183]. This is integrated to obtain the velocity and position vs. time curves, which are compared to the recorded B-dot traces as shown in Figure 3.27. A least-squares fit is then performed to obtain the best L' that matches the B-dot measured position vs. time to the current-calculated position vs. time. An example of the measured current, calculated velocity, and B-dot velocity is shown in Figure 3.31

$$a = \frac{1}{m}\left(\frac{1}{2}L'{I_A}^2 - 1.2\rho_{air}Av^2\right) \tag{3.2}$$

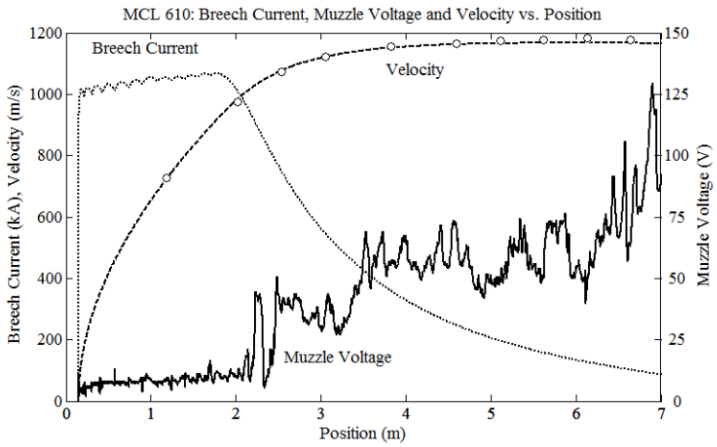

Figure 3.31. Breech current, velocity and muzzle voltage vs. position

Images of the post-shot rails were taken with an Olympus digital camera using external lighting to highlight the topography of the gouge craters. Some of the rail surfaces were subsequently etched to remove the aluminum armature deposits. This was done using either diluted NaOH or Drano®, followed by rinsing with distilled water. This procedure allowed small gouges and other features to be seen that would otherwise be obscured by the armature deposits.

Selected rail samples were sectioned for microstructural analysis. The samples were mounted in Bakelite and ground with a Handimet® II Roll Wet Grinder (Buehler) using 240-, 320-, 400- and 600-grit papers. After grinding, the samples were polished using a MasterSystem 800 Rotary Grinder/Polisher (SBT) with ultrasonic cleaning between steps. Samples were polished using 800-grit silicon carbide (SiC), 6 μm diamond paste, and 1-μm alumina slurry. The samples were then etched using a solution of 14% hydrogen peroxide, 43% distilled water, and 43% dilute ammonia hydroxide for 5-10 minutes to reveal the grain structure.

Samples were examined with a Nikon Optiphot-100 optical polarizing microscope capable of up to 1500x magnification, and a JEOL 5610 scanning electron microscope (SEM) equipped with a back-scattered electron detector and X-ray energy dispersive spectroscopy (EDS).

3.2 Series 1, Basic Armature Experiments

The first test series used a basic armature/rail configuration to serve as a baseline for future experiments as well as a benchmark against previously reported experimental results. Three experiments were performed. The first two tests used copper armatures on copper rails. The third test used aluminum armatures on brass rails.

The first two tests were designed to address the evolution of sliding damage with the copper/copper material pair. At low velocities (<100 m/s) this material pair is known to result in severe adhesive and abrasive wear and galling damage [3]. Around 600-800 m/s gouging is expected to occur [25]. The way in which one wear mechanism transitions into the other is not well understood.

The tests used the composite rail configuration shown previously in Figure 3.6 with AA6061-T6 backing rails and copper rail claddings (see Figure 3.32). The first two tests used half-hard copper (C11000-H02). The second test also used Glidcop® C15725 claddings as a startup material to prevent severe startup damage seen on the soft copper during the first test. Based on circuit simulations, the armatures were expected to reach exit speeds of about 1100 km/s, with an anticipated gouging speed of 800 m/s. A brief summary of the experiments is provided in Table 3.3.

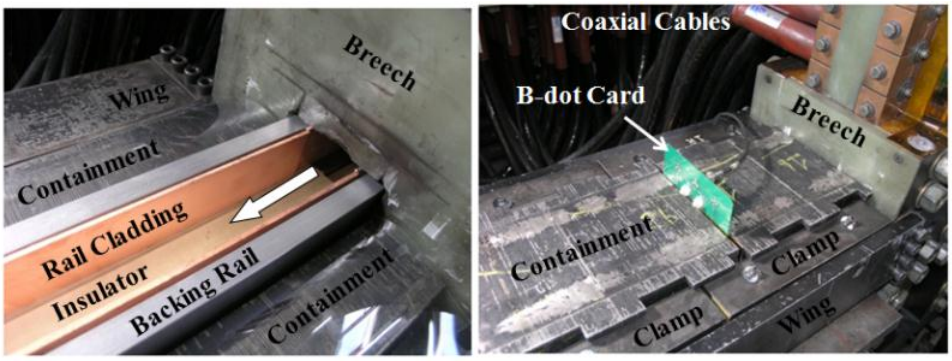

Figure 3.32. MCL build photographs: Core with aluminum backing rails and copper claddings (left), and as-built with laminated steel containment and B-dot card (right)

The third test used an aluminum alloy armature (AA7075-T651) on brass rails (C26000-H02). Brass was chosen because shock Hugoniot data was available for it, and its hardness can be significantly varied using appropriate cold working and heat treating. The estimated gouging velocity for this material pair was 1.55 km/s, based on the Stefani-Parker impact theory. Since brass rails were only (readily) available in 72" lengths, the armature was started on C15725 rail claddings as in the previous Cu/Cu experiment. This allowed a velocity range of 1-2 km/s to be obtained on the test cladding. AA6061-T6 backing rails were again used in this experiment.

Table 3.3. Series 1 experimental overview

MCL #	Armature (Slider)	Rail	I_{pk} *kA*	V_{exit} *km/s*	V_{range} *km/s*	Notes
609	C11000-H04	C11000-H00	1,100	1.2	0.0-1.0	
610	C11000-H04	C11000-H04	1,100	1.2	0.0-1.0	C15725 for 1st meter
687	AA7075-T651	C26000-H02	1,200	2.1	1.0-2.0	C15725 for 1st meter

3.2.1 MATERIAL PROPERTIES AND PROJECTILE DESIGN

The relevant material properties for the armatures and rails for all three experiments are show below in Table 3.4. The hardness was measured by cutting off several pieces of the rail stock and testing with a Buehler Micromet® 2004 Vickers micro-hardness tester, and a Service Diamond 8B Rockwell hardness tester. Electrical conductivity was measured with a Verimet® M 4900C eddy current surface conductivity probe. Composition was measured via Energy Dispersive Spectroscopy (EDS), or was taken from handbook values.

Table 3.4. Series 1 material properties

Material	Hardness	Conductivity	Composition (at. %)	Notes
AA7075-T651	HV 176 ± 2	33% IACS	93.9 Al, 3.2 Mg, 2.5 Zn, 0.4 Cu[1]	Armature material
C11000-H00	HV 82 ± 1	99.9% IACS	99.9 Cu[2]	Soft Rail
C11000-H02	HV 88 ± 1	99.9% IACS	99.9 Cu[2]	Hard Rail
C11000-H04	HV 139 ± 4	99.9% IACS	99.9 Cu[2]	Armature material
C15725	HV 169 ± 5	86% IACS	0.26 Al, 99.56 Cu[3]	Rail material
C26000-H02	HV 137 ± 5	27% IACS	70.2 Cu, 29.8 Zn[1]	Rail material

[1] Measured with EDS
[2] Handbook value (ASM International)
[3] Provided by supplier (J.L. Anthony Specification Sheet)

The experiments used existing C11000-H04 and AA7075-T651 "C-type" armatures from previous fabrication runs (denoted KJ7700). In both instances, armatures were cut from a 2" thick rolled plate with a wire electric-discharge machine (WEDM) and final machined on a CNC vertical mill. The polycarbonate bore rider was milled from a 2" thick plate of Lexan®. Assembly bolts were ½-13 grade-8 steel hex head cap screws. The C11000 armature mass was approximately 690 g, with a total projectile mass of 782 g for both experiments. The AA7075-T651 armature mass was 223 g, with a total projectile mass of 315 g. Dimensions of the armatures are provided in Figure 3.33.

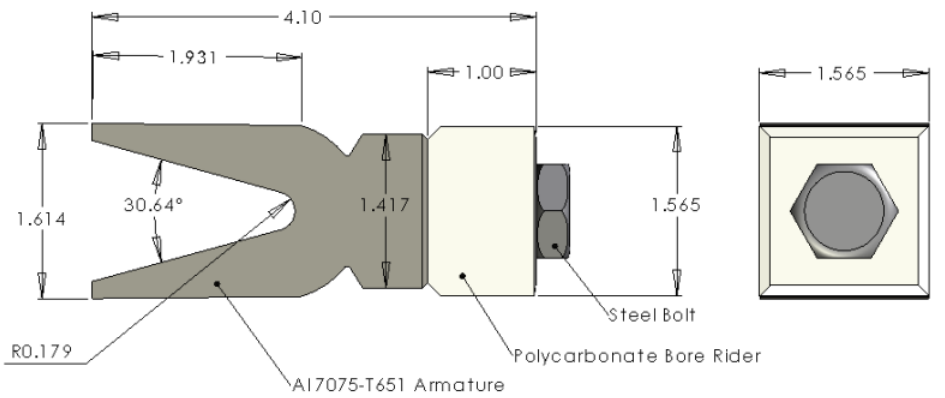

Figure 3.33. KJ7700 projectile dimensions (dimensions in inches)

3.2.2 SOFT-CATCH SYSTEM

The expected exit velocity of the Cu/Cu tests was around 1 km/s. It was hoped that the armatures could be recovered to see what gouging damage on the armature contact surface looks like. This was to be accomplished by stuffing the flight tube with cotton rags, an approach that has been successful at velocities up to 700 m/s [184,185]. A photograph of the rag-filled flight tube extending back to the catch tank is shown in Figure 3.34, with a schematic shown in Figure 3.35. Armatures have not previously been successfully recovered after a railgun gouging event.

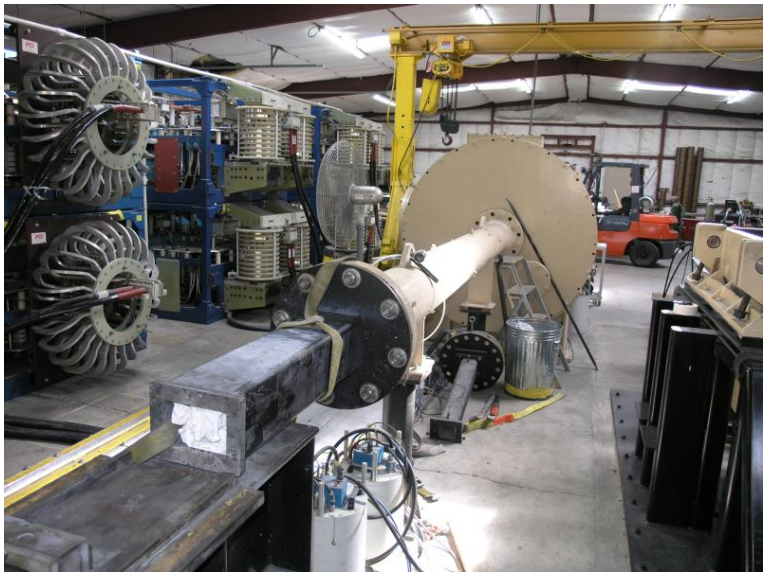

Figure 3.34. Catch tank with rag-filled flight tube to soft-catch projectiles

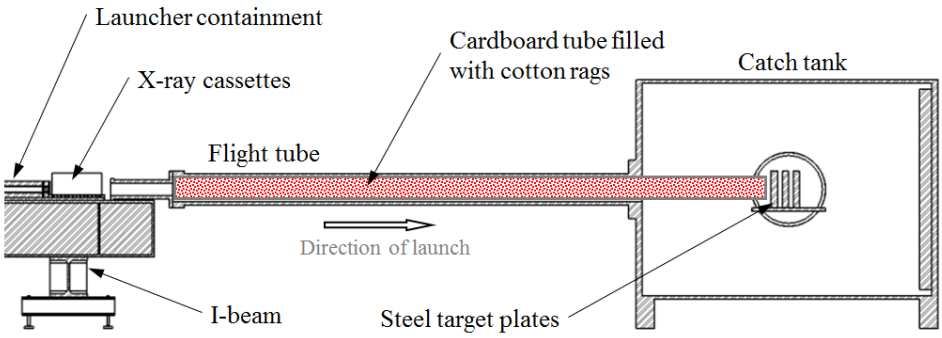

Figure 3.35. Soft-catch system schematic

3.2.3 CIRCUIT SIMULATIONS

Before each experiment a circuit simulation was performed. This was done partly to verify the desired current and velocity vs. position curve, and to ensure that the operational limits of the launcher and power supply were not exceeded. The circuit for the power supply and railgun was modeled in LTspice IV (Linear Technology Corporation), using power supply and launcher parameters obtained from previous measurements. Each capacitor bank module is modeled using the circuit shown previously in Figure 3.15. The 18 modules are connected to the breech of the launcher via coaxial cable models. The voltage at the breech of the launcher is approximated by Equation (3.3), where R' is the resistance gradient (Ohm/m), x is the armature position relative to the breech wall, and V_{arm} is the armature voltage drop [186].

$$V_{breech} = I_A R' x + L' x \frac{dI_A}{dt} + I_A L' v + V_{arm} \tag{3.3}$$

Because the launch timescales are on the order of milliseconds, the effect of magnetic diffusion must be considered. This is accounted for by using an inductive/resistive ladder network for the larger conductors [187]. The pulse-shaping inductors for each capacitor bank, coaxial cables, and the railgun rails each have a ladder network used to define their respective inductive/resistive voltage drop. Equation (3.3) therefore becomes Equation (3.4).

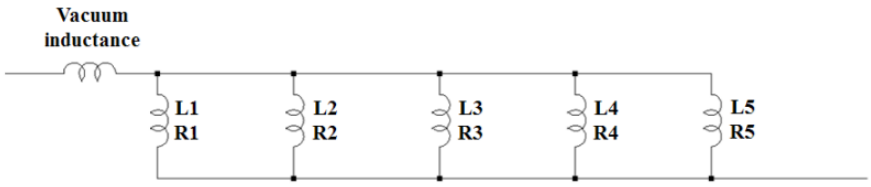

Figure 3.36. Inductive-resistive ladder network schematic

$$V_{breech} = [\text{Ladder network voltage drop}] + I_A L' v + V_{arm} \tag{3.4}$$

Each capacitor bank is charged from a single power supply to the same voltage, but is individually triggered, as illustrated in Figure 3.20. The bank timings used for the basic armature experiments are provided in Table 3.5. Circuit simulation waveforms for the Cu/Cu and Al/brass tests are shown in Figure 3.37 and Figure 3.38, respectively. The practical goal of the experiments was to have the armature exceed the gouging velocity on the rail sample before it transitioned to arcing contact. Transition is undesirable because it replaces the armature/rail metallic contact with a plasma interface that not only prevents solid contact (and hence gouging) but also causes significant ablative damage to the bore components.

Table 3.5. Power supply parameters for basic armature experiments

MCL 609-610 Charge Voltage 14.0 kV				**MCL 678** Charge Voltage 12.6 kV			
Bank #	**Time (µs)**	**Bank #**	**Time (µs)**	**Bank #**	**Time (µs)**	**Bank #**	**Time (µs)**
0	1,000	9	2,760	0	500	9	1,510
1	1,000	10	1,000	1	500	10	500
2	1,000	11	3,440	2	500	11	1,720
3	3,120	12	3,720	3	500	12	1,900
4	1,000	13	4,000	4	500	13	2,080
5	1,000	14	4,220	5	500	14	2,220
6	1,560	15	4,420	6	500	15	2,340
7	1,980	16	4,600	7	1,040	16	2,460
8	2,380	17	4,780	8	(error)	17	2,580

To ensure the armature does not transition on the sample, the armature must leave the sample before the current decays past ~85% of the peak current value. This is based on previous experiments where armatures often undergo transition to arcing contact via down-slope transition [188]. In this mechanism, the in-bore magnetic field decreases faster than it can diffuse out of the armature, which results in a local magnetic force that pulls the armature contact away from the rail. For the Cu/Cu tests, 85% of the current down-slope corresponds to a velocity of 1.01 km/s, well above the expected gouging velocity of ~800 m/s. For the Al/brass tests the related velocity is 1.92 km/s; again well above the expected value.

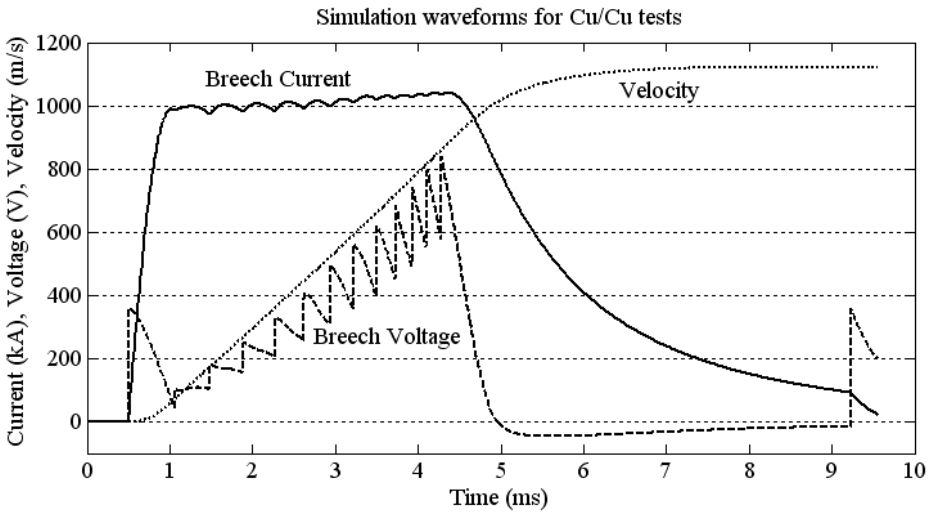

Figure 3.37. Simulation of breech current, breech voltage and velocity for Cu/Cu tests

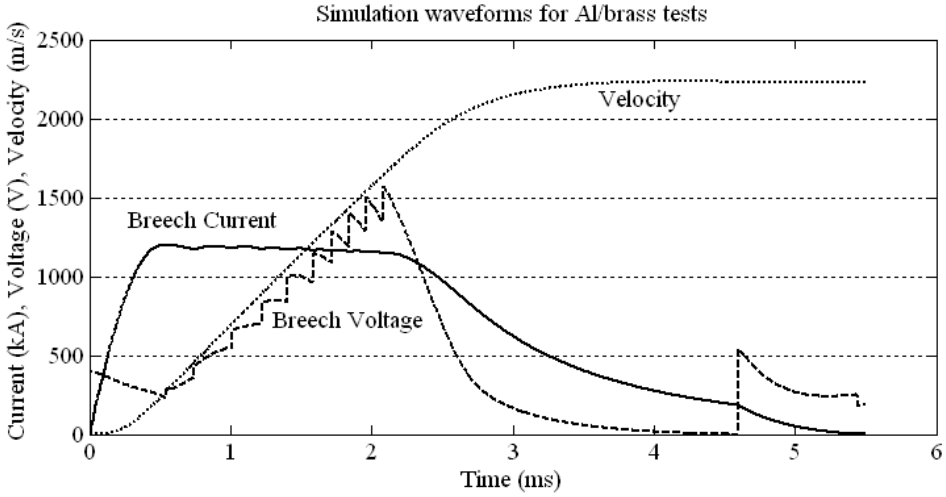

Figure 3.38. Simulation of breech current, breech voltage and velocity for Al/brass tests

3.3 Series 2, Sample Slider Experiments

The second test series focused on exploring previously untested materials, including those not suitable for use as an armature contact material. All experiments in series 2 used C11000-H02 copper rail claddings with AA6061-T6 backing rails, as in the previous test series. The experiments used a new launch package with electrically isolated gouge samples mounted on inertially-loaded wedges, illustrated in Figure 3.39. This design permits different size geometries (flat or round) as well as different masses.

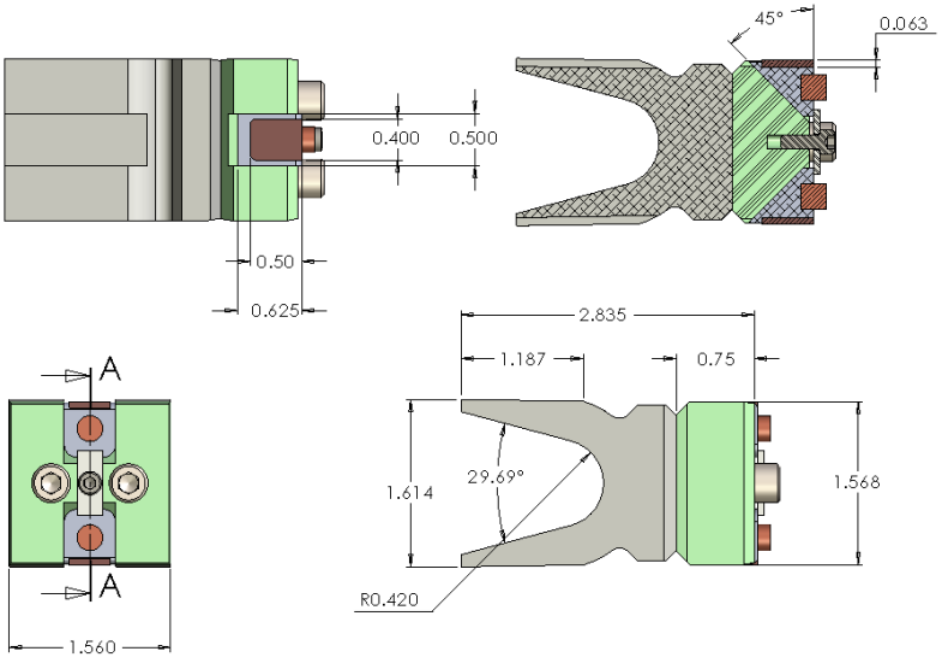

Figure 3.39. MTP projectile (dimensions in inches)

Armatures and wedges were made from AA7075-T651, while the wedge holder was made from G10/FR4 composite. To prevent the armature from running over any gouge craters created by the sample, a channel was milled into the contact surface 0.1" (2.54 mm) wider than the slider sample. Assuming an armature wear rate of

approximately 1 mm/m [189] and a 2 mm channel depth, it was expected that the armature channel base should not make contact with the rail surface until after approximately 2 m of travel. The expected launch acceleration for this projectile with a 1 MA driving current was approximately 9.8×10^5 m/s^2 or 100 kGee. Over a distance of 1 meter this corresponds to a velocity increment of 1.4 km/s, enough to capture the onset of gouging if the initial estimate is at least within around 500 m/s.

3.3.1 PROJECTILE FINITE ELEMENT ANALYSIS

Unlike the other experiments reported on herein, this series used a new projectile design which warranted structural analysis prior to testing. Several design iterations were undertaken with the final design being shown in the previous images. The projectile model was developed in SolidWorks® 2009, with the structural analysis performed using the SolidWorks® Simulation static structural solver. A rendering of the CAD model used in the analysis is shown in Figure 3.40. The geometry of the problem allowed the model to be analyzed in quarter-symmetry. The symmetry boundary conditions are also shown in Figure 3.40.

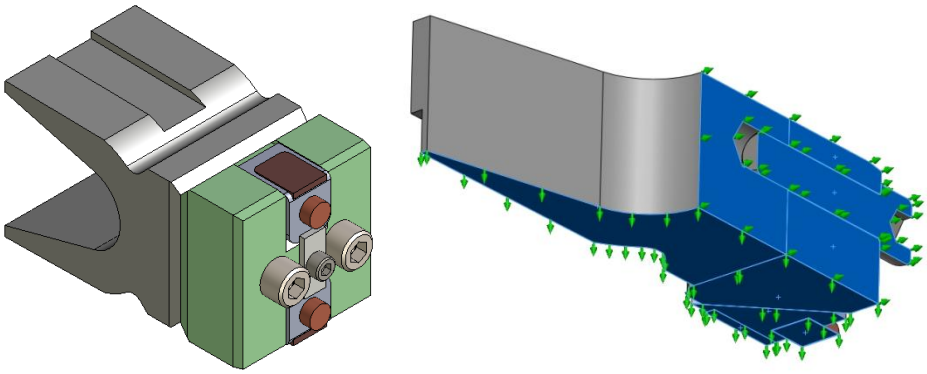

Figure 3.40. CAD model of MTP: full model (left), and quarter-symmetry model with BCs (right)

The material properties used for the components are provided in Table 3.6. Isotropic linear elastic properties were used for all components. As indicated previously,

the model was analyzed using quarter symmetry reduction. The remaining boundary conditions are shown in Figure 3.41. Symmetry boundary conditions (BCs) were applied to the sectioned faces of the assembly lying on the two orthogonal symmetry planes that intersect on the axis of the bore (shown in Figure 3.40). Since the magnetic forces are not being modeled in this analysis, a no-translation boundary condition was applied to the back faces of the armature trailing arms (Figure 3.41, left). This prevents the armature from moving backwards, which should result in the appropriate stresses inside the payload assembly. This BC does allow motion in the two orthogonal directions, and rotation in all three directions. This choice of boundary condition will therefore result in non-physical stresses in back of the armature, so only the payload components are scrutinized. The last boundary conditions applied were no-displacement in the rail-to-rail direction, applied to the armature contact face and sample slider contact face. This fully defines the problem.

Table 3.6. Material properties used in structural analysis

	Material	**Young's Modulus**	**Poisson's Ratio**	**Mass Density**
		GPa		*kg/m^3*
Armature / Wedge	AA7075-T6	71.98	0.33	2,800
Fore Body	G10/FR4	18.62	0.24	1,800
Bolts	Alloy Steel	206.8	0.28	7,801
Slider Sample	C11000	110.3	0.37	8,977

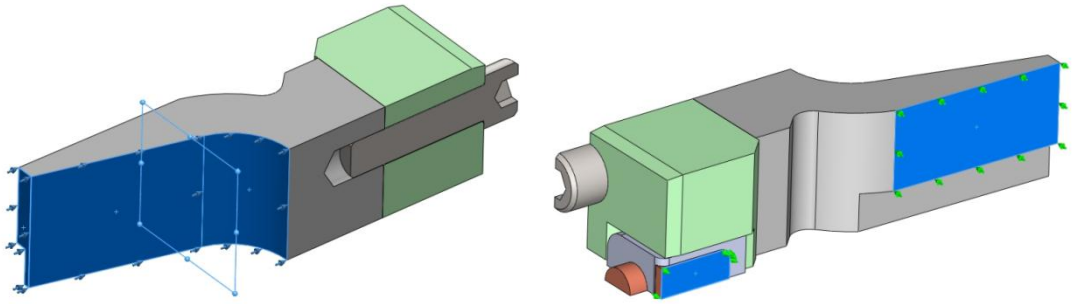

Figure 3.41. FEA boundary conditions: Left = no axial displacement, right = no lateral displacement.

Accurate armature stresses are only possible using a coupled EM/structural analysis with temperature-dependent elastic-plastic material properties. That level of analysis is beyond the scope of this effort. Numerous papers deal with this level of armature analysis if the reader is interested [190-194].

Sliding interfaces were applied to all touching component faces using the "surface to surface" option which allows lateral motion, separation, but no penetration. Frictionless interfaces were assumed. The model was meshed using simple tetrahedral elements. Mesh controls were applied to improve accuracy in the regions of interest, with the final mesh shown in Figure 3.42. The final mesh consisted of 14,568 nodes and 66,935 elements.

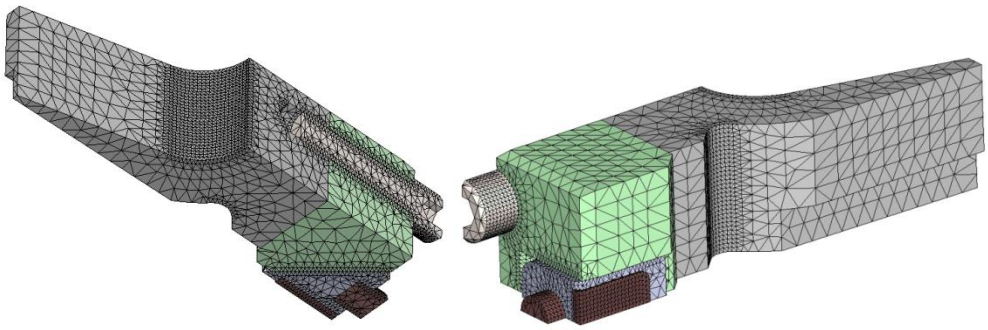

Figure 3.42. FEA tetrahedral mesh

An acceleration of 147 kGee (1.44×10^6 m/s^2) was applied to the assembly. This corresponds to a launch current of 1.2 MA, which is equivalent to 274 kN using the Lorentz force equation and a propulsive inductance gradient of 0.38 μH/m. This propulsive inductance gradient is based on experimental results with similar projectiles. The expected launch mass was 190 g, which results in the specified acceleration. Analysis was performed on a desktop PC using the Direct Sparse solver, with results typically obtained in a few minutes. The analysis results are shown in Figure 3.43.

The critical components in this analysis are the aluminum wedge and G10 body. The peak von Mises stress in the wedge is approximately 300 MPa, well below the yield strength of ~500 MPa. The peak von Mises stress in the G10 is around 80 MPa, also well

below its anticipated minimum yield strength of 200 MPa. Since the actual launch conditions would use a peak current closer to 1.0 MA instead of 1.2 MA, the acceleration loads should be reduced and the components would therefore not be expected to fail under normal operating conditions.

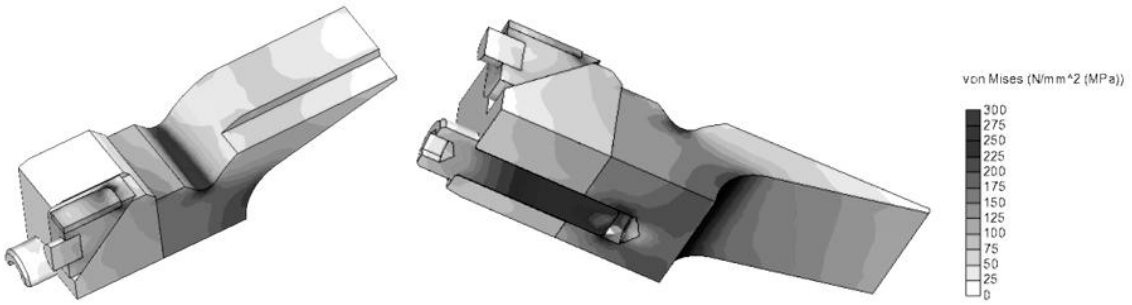

Figure 3.43. von Mises stress results of acceleration calculation

3.3.2 RAIL AND SLIDER MATERIALS

All the experiments used the same overall configuration, with slider plate specimens mounted on the projectile, and 72"-long C11000-H02 rail samples. The armatures began on C15725 for the initial portion of the launch, and then traveled onto the C11000 rails. This was done to prevent gouging of the armature since AA7075-T651 gouges C15725 at around 1.9 km/s [195]. A summary of the 10 experiments is provided in Table 3.7. I_{pk} is the peak current, V_{exit} is the exit (muzzle) velocity, V_{est} is the estimated gouging velocity, and V_{range} is the velocity range on the test cladding.

The location of the cladding was varied to coincide with the expected gouging range. The estimated gouging velocity was determined using the Stefani-Parker impact model, as well as the Reynolds number approach discussed in Chapter Two. The results of the two models determined the range shown in Table 3.7.

Table 3.7. Series 2 experimental overview (see text for description of variables)

MCL #	Slider	Rail	I_{pk} *kA*	V_{exit} *km/s*	V_{est} *km/s*	V_{range} *km/s*
-	AA7075-T6	C11000-H02	-	-	1.3	-
623	4140 plate	C11000-H02	1,000	2.6	1.3-1.4	0.0-2.2
677	Tantalum	C11000-H02 striped	1,200	2.4	0.6-0.8	0.5-1.5
678	AA1100	C11000-H02 striped	"	"	0.9-1.2	0.5-1.5
679	Zirconium	C11000-H02 striped	"	"	1.1	0.5-1.5
680	MACOR®	C11000-H02 striped	"	"	1.3	1.1-1.8
681	4340 HRC35	C11000-H02 striped	"	"	1.3-1.4	1.1-1.8
682	4340 HRC27	C11000-H02 striped	"	"	1.1-1.3	1.1-1.8
684	4340 HRC41	C11000-H02 striped	"	"	1.6-1.7	1.1-1.8
685	4340 HRC51	C11000-H02 striped	"	"	1.7-2.1	1.4-2.0
686	4340 HRC59	C11000-H02 striped	"	"	2.0-2.7	1.4-2.0

While using a separate slider material has numerous benefits as already mentioned, the principle drawback is that armature/rail gouging can occur during or prior to sample/rail gouging. This is undesirable since armature/rail gouging generates large stresses in the armature which could influence the sliding behavior of the sample. In an attempt to prevent armature/rail gouging, every test after the 1st was performed using partially electroplated rails. These "stripe" electroplated rails are shown in Figure 3.44.

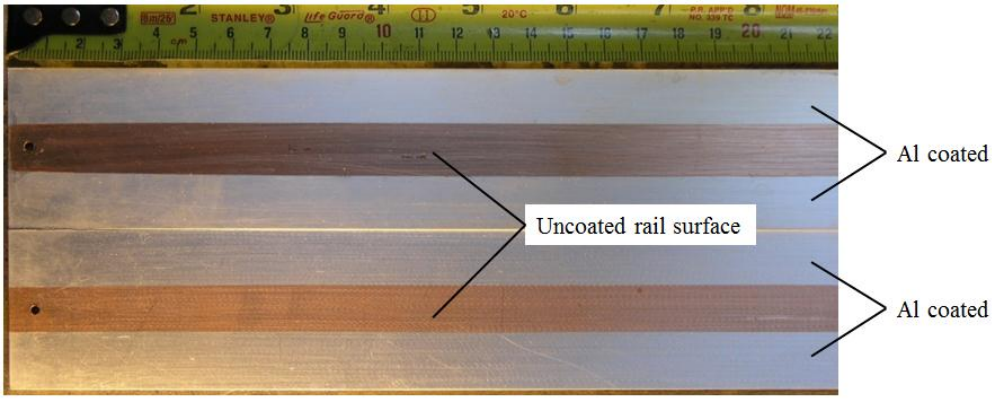

Figure 3.44. Photograph of "stripe" Al-plated C11000 rails

The center region of the rails was masked so only the armature-contacting portion of the rail had aluminum deposited onto it. Previous tests with electroplated rails have

resulted in the elimination of gouging [195], so it was hoped that this would prevent the armature from gouging the rails while at the same time permitting the sliders to gouge the uncoated surface. A photograph of the front of the assembled projectile on the stripe-electroplated rails is shown in Figure 3.45.

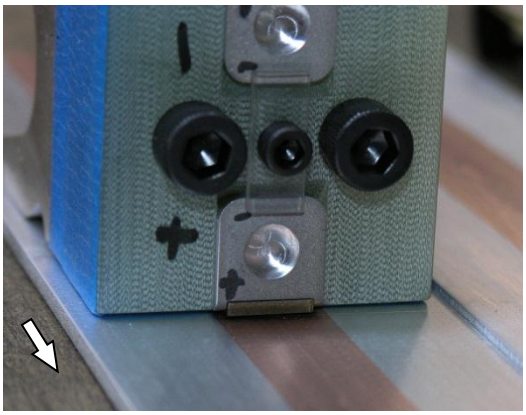

Figure 3.45. Sliding sample on stripe-electroplated rails

Material properties for the rail and slider materials are provided in Table 3.8. Tantalum, zirconium and AA1100 were chosen largely as additional data points to compare with the existing database of gouge velocities. The annealed tantalum had the additional benefit of being a relatively soft and dense material, which would hopefully provide a data point below the cluster of known gouge velocities. MACOR®, a machinable ceramic, was also used as a test sample. To the author's knowledge there has been no reported data for gouging with ceramic materials. The five 4340 steel alloys from HRC 27 to 59 were chosen to provide an independent assessment of gouging behavior as a function of slider hardness.

Table 3.8. Series 2 material properties

Material	Hardness *HV*	Conductivity	Composition (at. %)	Notes
4140 HRC 35	318 ± 6	7.7% IACS	0.38-0.43 C, 0.75-1.0 Mn, 0.15-0.30 Si, 0.80-1.10 Cr, 0.15-0.25 Mo[1]	Slider
4340 HRC 27	276 ± 9		0.38-0.43 C, 0.60-0.80 Mn, 0.20-0.35 Si, 1.62-2.0 Ni, 0.7-0.9 Cr, 0.2-0.3 Mo[1]	Slider
4340 HRC 35	348 ± 16			Slider
4340 HRC 41	420 ± 18			Slider
4340 HRC 51	597 ± 16			Slider
4340 HRC 59	724 ± 28			Slider
AA1100 H14	42 ± 2	55.4% IACS	99.9 Al[2]	Slider
AA7075-T651	176 ± 2	33% IACS	93.9 Al, 3.2 Mg, 2.5 Zn, 0.4 Cu[2]	Armature material
C11000-H02	83 ± 4	100% IACS	99.9 Cu[2]	Rail material (stripe-EP)
C11000-H02/Al	86 ± 5	100% IACS	99.9 Al[2]	Coated portion of rail
MACOR®	80 ± 20	N/A	47.5 O, 9.6 Mg, 8.8 Al, 24.3 Si, 7.9 K + 2 Pd/Au[2,3]	Slider
Tantalum	129 ± 6	12.7% IACS	99.9 Ta[2]	Slider
Zirconium	210 ± 12		73.5 Zr, 26.5 O[2]	Slider

[1] Composition information taken from ASM Alloy Digest
[2] Composition measured with EDS
[3] Composition of MACOR® contains trace Au and Pd from sputter-coating prior to EDS

The armature contacts were modified since the as-received aluminum electroplating was not within specification, as shown in Figure 3.46. In most of the received rail specimens, the electroplating did not extend far enough into the rail to prevent contact with the armature and rail substrate. This would likely result in gouging of the armature/rail interface. The inside contact edges of the armatures were therefore chamfered with a rotary tool to prevent armature/uncoated-rail contact in this region of the rail.

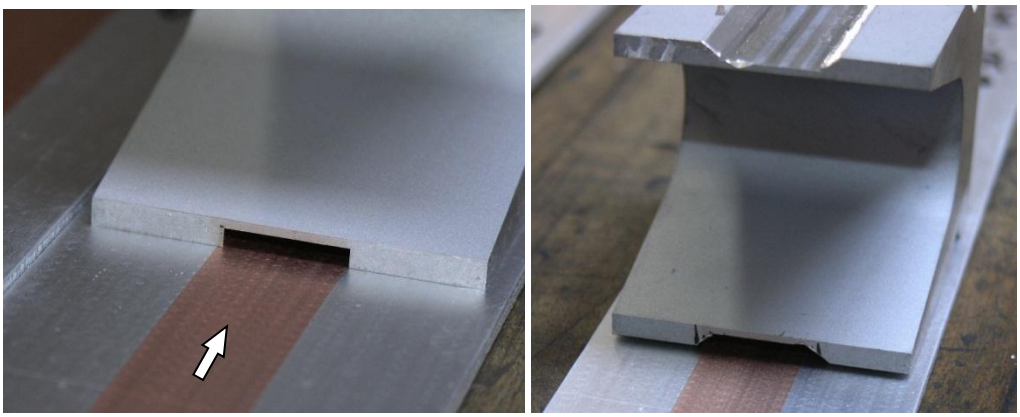

Figure 3.46. Photographs of stripe-electroplated rails with armature before (left) and after (right) modification. The internal edge chamfer was done to prevent contact between the armature and uncoated rail surface.

3.3.3 CIRCUIT SIMULATIONS

The same circuit simulation program used in series 1 was used for the slider experiments. The parameters for the tests are provided in Table 3.9. The parameters were changed after MCL 677 so a higher current could be used with more banks. Increasing the number of banks reduces the required charge voltage, which reduces strain on the capacitors.

Table 3.9. Power supply parameters for basic armature experiments

MCL 623 Charge Voltage 14.0 kV				**MCL677-686** Charge Voltage 11.2 kV			
Bank #	**Time (µs)**	**Bank #**	**Time (µs)**	**Bank #**	**Time (µs)**	**Bank #**	**Time (µs)**
0	~	9	1,060	0	~	9	500
1	~	10	500	1	~	10	500
2	~	11	1,410	2	~	11	500
3	~	12	1,710	3	500	12	1,030
4	500	13	1,960	4	500	13	1,120
5	500	14	2,160	5	500	14	1,340
6	500	15	2,330	6	500	15	1,500
7	500	16	2,480	7	500	16	1,620
8	500	17	2,610	8	500	17	1,740

Circuit simulation waveforms are shown in Figure 3.47. The simulation predicted a peak current of 1.0 MA and an exit current of ~200kA. Transition to arcing contact was expected at around 2 km/s, which should be acceptable for all materials except the hardest steels (see Table 3.7), assuming that transition adversely influences the slider/rail interaction. The current pulse was unchanged across all the experiments. However, the starting location of the test cladding was varied depending on the anticipated gouging velocity range. The details of this are discussed in Chapter Four.

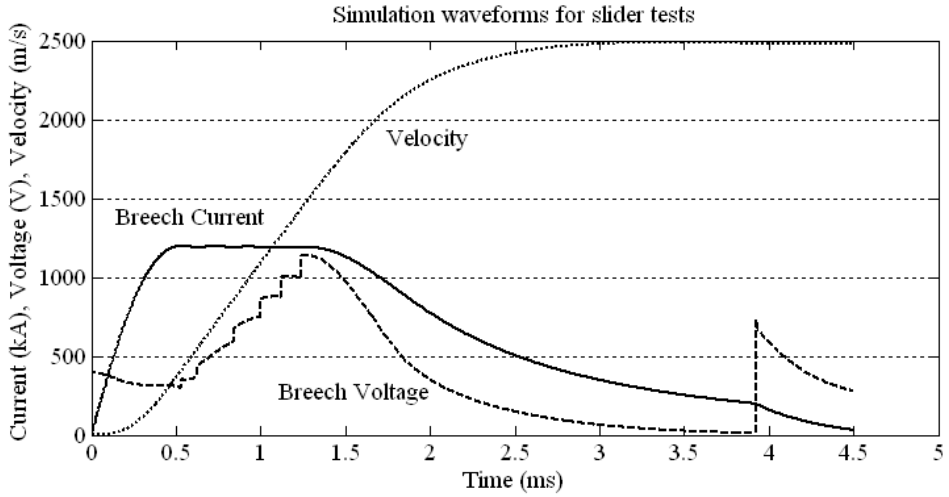

Figure 3.47. Circuit simulation results for slider experiment

3.4 Series 3, Coated Rail Experiments

One approach to delay or prevent gouging is the use of rail coatings. In this case, a thin layer of material is applied to the rail which prevents interactions between the slider and the rail. The only prescribed requirement is that gouging should not occur on the coating itself to prevent the interaction from propagating through to the substrate. This can be accomplished by using either a very hard or low density coating. The principal benefit to this approach is that the system requirements of the substrate material are isolated from the requirements of the running surface. Rocket sled experiments have seen success using both epoxy (low density) and iron oxide (hard) coatings on the rail surface to prevent gouging [26]. Epoxy coatings in this case were applied to AISI 1080 steel rail surfaces in thicknesses of at least 150 micrometers.

In railguns, gouging has been delayed by "pre-coating" the rails. This is accomplished by launching several armatures at velocities below the gouging threshold speed of the armature/rail pair. The high speed wear of the armatures lays down a thick layer (tens of micrometers) of deposits on the rail surface [33,34]. The deposits are irregular, porous, and consist of aluminum, aluminum oxides, and Al-Cu inter-metallic compounds [35]. An example is shown below in Figure 3.48.

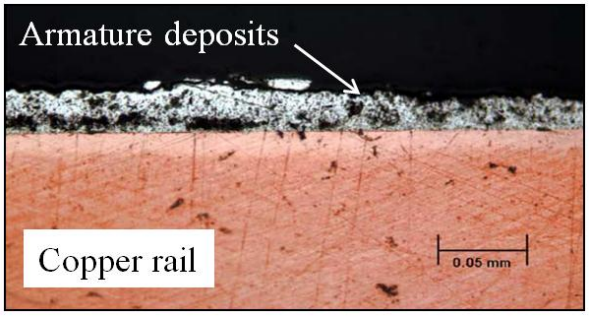

Figure 3.48. Microscope image of copper rail with aluminum armature deposits (© 2011 IEEE) [195]

In the case of armature deposits, it is unclear whether gouging is prevented because the coating has a low acoustic impedance or because it contains hard inter-metallic and oxide phases. Reduced acoustic impedance would lessen the impact pressure generated during armature/rail asperity impact events. The oxides and hard particles in the coating could increase the effective strength of the coating. Both of the effects could delay the onset of gouging in the coating, and hence the substrate. The goal of this series was to determine if the acoustic properties of the coating were the dominant factor for delaying gouging by plating copper rails with pure aluminum and testing in a railgun.

By testing various coating thicknesses, it was hoped that insight can be gained into how gouges initiate, and how robust the use of thin coatings is in preventing them. Two categories of coating thickness were chosen for the experiments: Thicker coatings (25 and 50 micrometers) which are on the order of the armature deposits that would be seen in a railgun, and thin coatings (2 and 5 micrometers) which are an order of magnitude thinner than regular armature deposits. The rail material chosen for the tests was UNS C15725 Glidcop® Al-25, an aluminum oxide (0.25 wt. %) dispersion-hardened copper alloy. It should be noted that the average surface roughness of the rails (~0.2 μm) was well below the coating thicknesses tested.

To ensure a uniform coating, pure aluminum (99.9% Al) was electroplated onto the rails using an electrolytic cell process [196]. A cross-section of an electroplated rail surface is shown in Figure 3.49. The electroplated coating contains some porosity, albeit less than the armature deposits seen in Figure 3.48. It is also well bonded to the C15725 substrate, unlike the armature deposits. It should be noted that the coating thickness was not found to be uniform across the rails surface. For the “50 micrometer” sample (Figure 3.49), the coating thickness varied from around 60 micrometers at the edges to around 40 micrometers in the center of the rail. This was measured by sectioning part of a coated rail and examining it under an optical light microscope (see Figure 3.50). This trend was consistent across all the examined coatings.

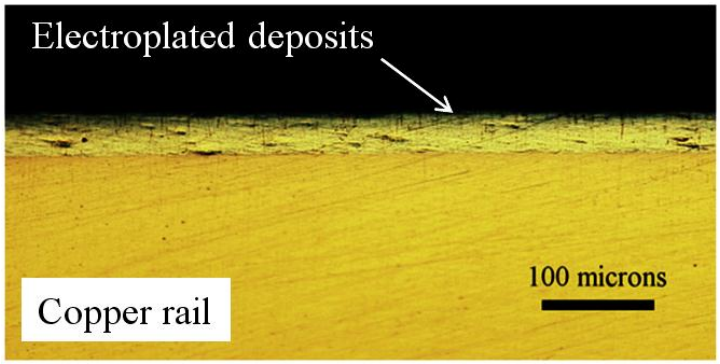

Figure 3.49. Electroplated C15725 rail

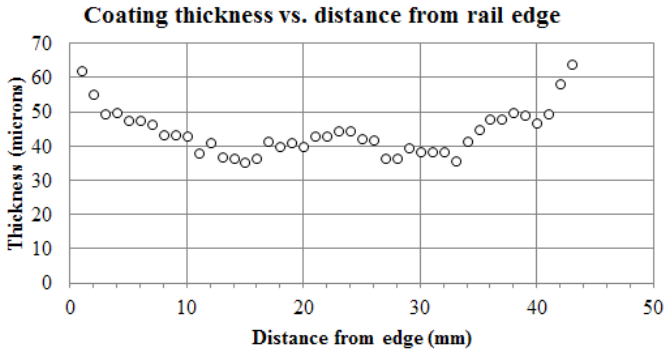

Figure 3.50. Coating thickness measurements for "50 µm" coating

An overview of the experimental parameters used in the tests is provided in Table 3.10. Material properties are provided in Table 3.11. It should be noted that conductivities were measured using an eddy current device, with a typical penetration depth of 100 micrometers. Therefore, the measured conductivity of the coating also contains the properties of the C15725 substrate.

A total of seven experiments were performed with various coating thicknesses. One shot on the 2 µm, 25 µm and 50 µm coatings were performed. A benchmark shot was also performed on uncoated (bare) rails. Three shots were performed on 5 µm coating samples for repeatability purposes and to benchmark two batches of electroplated materials. In all cases the 72" samples were located such that the armature would be at velocities from 1.8 to 2.5 km/s, based on circuit simulations. The theorized gouging velocity of AA7075-T651 on pure aluminum is around 2.4 km/s, so it was hoped that

gouging could be seen at the higher speeds through gouge initiation in the coating material.

Table 3.10. Series 3 experimental overview

MCL #	Slider	Rail	I_{pk} *kA*	V_{exit} *km/s*	V_{range} *km/s*
628	AA7075-T651	C15725 + 25 μm Al	1,200	3.4	1.8-2.5
629	AA7075-T651	C15725 + 50 μm Al	"	"	"
630	AA7075-T651	C15725 + 5 μm Al	"	"	"
650	AA7075-T651	Bare C15725	"	"	"
651	AA7075-T651	C15725 + 5 μm Al	"	"	"
652	AA7075-T651	C15725 + 5 μm Al	"	"	"
653	AA7075-T651	C15725 + 2 μm Al	"	"	"

Table 3.11. Series 3 material properties

Material	Hardness	Conductivity	Composition (at. %)	Notes
AA7075-T651	HV 176 ± 2	33.2% IACS	93.9 Al, 3.2 Mg, 2.5 Zn, 0.4 Cu[1]	Armature material
Al Coating	HV 47 ± 2	85.0% IACS	100 Al[1]	"50 μm" coating, HV/50
C15725	HV 169 ± 5	85.8% IACS	100 Cu[1]	Base rail material

[1] Compositions measured with EDS

The launch package used in the experiments was a ~140 g lightweight projectile, illustrated in Figure 3.51. This launch package is composed of an AA7075-T6 armature and a polycarbonate payload, and has been used for numerous high-speed experiments at IAT. Due to its light weight, it is capable of extremely high accelerations, on the order of 200 kGee (~2×10^6 m/s^2) with a 1.2 MA driving current.

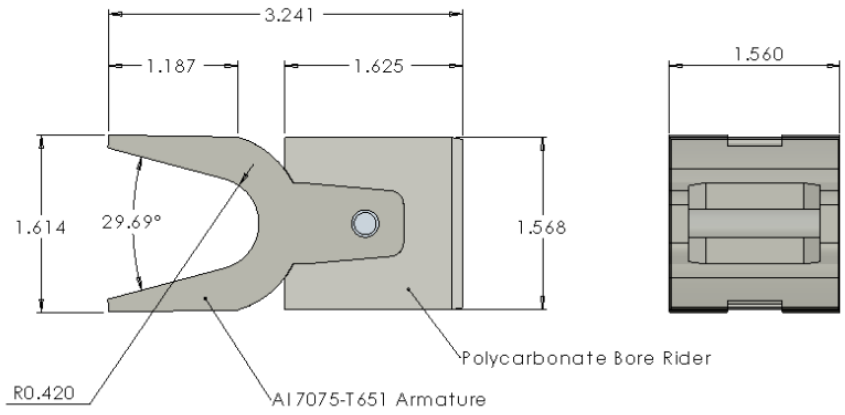

Figure 3.51. KJ-200 projectile dimensions (dimensions in inches)

The power supply parameters used in the electroplated rail experiments are provided in Table 3.12. Circuit simulation waveforms for the experiments are shown in Figure 3.52. A driving current of 1.2 MA is applied to the armature, resulting in a predicted exit velocity of around 3.4 km/s at 300 kA. However, since transition is not modeled in the circuit code, the exit current was expected to decay to at least 250 kA by exit, based on previous experiments. The anticipated transition velocity is around 2.45 km/s, with a velocity range on the test cladding of 1.8-2.5 km/s.

Table 3.12. Power supply parameters for coated rail experiments

MCL # V_{charge}	**628-630, 650-653** 11.3 kV		
Bank #	**Time (μs)**	**Bank #**	**Time (μs)**
0	500	9	1,080
1	500	10	500
2	500	11	1,290
3	500	12	1,430
4	500	13	1,540
5	500	14	1,630
6	500	15	1,720
7	500	16	1,810
8	1,030	17	1,880

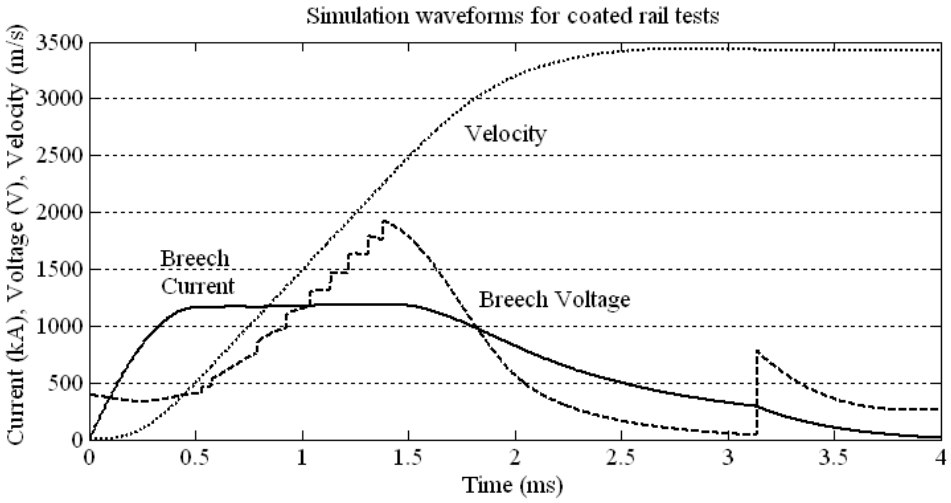

Figure 3.52. Circuit simulation for electroplated rail experiments

3.5 Series 4, Surface Indentation Experiments

The last test series focused on the initiation of gouges in the presence of macroscopic rail surface defects. The majority of observed gouges are generally tear-drop shaped, starting at a very small initiation site and fanning out until (presumably) a free surface of the slider or rail is reached. However, in some cases a slider will encounter a sufficiently large surface discontinuity, and the gouge will then initiate at this defect. Often, a large gouge can initiate across some macroscopic width and then propagate "normally" until a free surface is reached. This is a common occurrence in cases where the slider runs over a joint between rail surfaces, as shown in Figure 3.53.

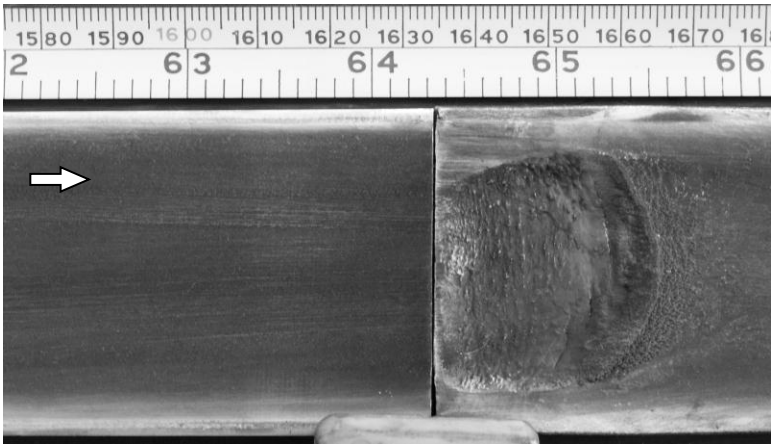

Figure 3.53. Gouge initiation at a rail joint. Direction of armature motion is left to right.

If the onset of gouging can be considered a linear instability problem, then according to Squire's theorem [121] the shape of the perturbation which triggers the instability should not matter. That is, a 2D instability and 3D instability should both result in gouging. This argument is based on linear instability theory discussed in Chapter Two. In nonlinear instability theory as discussed by Landau [118], the size of the perturbation can be important if the slider is in the *metastable* velocity range for instability. In that

case, unstable flow will only result from a sufficiently large perturbation. If gouging can be characterized as an instability process, then it may be subject to metastable wave formation [197].

To address the role of macroscopic surface indentations on the onset of gouging, AA7075-T651 armatures were launched against C11000 rails with large 2D indentations. If the large indentations result in gouging at a lower velocity than "smooth" rails, then gouging may be better characterized as a nonlinear instability process. If gouging occurs at the same velocity as smooth rails then linear instability should be a more accurate description. This was addressed in two experiments: one experiment with large surface indentations on the rails, and one without. At the time these tests were planned the MCL was being used for other experiments, so the HEMCL was used for the indentation tests. An overview of the two experiments is provided in Table 3.13, with the relevant material properties given in Table 3.14.

Table 3.13. Series 4 experimental overview

HEMCL #	Slider	Rail	I_{pk} *kA*	V_{exit} *km/s*	V_{range} *km/s*
1341	AA7075-T651	C11000 dented	1,500	2.05	0-1.48
1342	AA7075-T651	C11000	"	"	0-1.74

Table 3.14. Series 4 material properties

Material	Hardness	Conductivity	Composition (at. %)	Notes
AA7075-T651	HV 176 ± 2	33% IACS	93.9 Al, 3.2 Mg, 2.5 Zn, 0.4 Cu[1]	Armature material
C11000-H02	HV 89 ± 2	100% IACS	100 Cu[1]	Rail material

[1] Compositions measured with EDS

The projectile used in the experiments was a "monolithic" armature design shown in Figure 3.54. The design uses a standard C-shaped armature made from AA7075-T651 as in the MCL experiments. The trailing arm profile for this armature is actually scaled-up version of the KJ200 armature used in the coated rail experiments. The monolithic

design is used in this case since the high acceleration loads preclude the use of long polycarbonate bore riders.

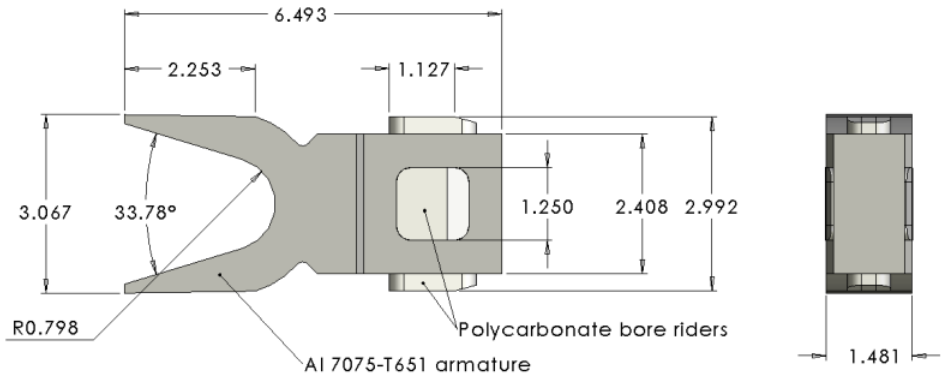

Figure 3.54. HEMCL projectile dimensions (dimensions in inches)

To place the indentations onto the rail surface, a 2D triangular indenter was fabricated. The indenter hardware is illustrated in Figure 3.55, and consists of a tungsten-carbide lathe tool mounted to a steel base such that the indenter edge creates a 45° angle with the rail surface. Tungsten carbide (WC) was chosen as an indenter because of its high hardness (HV ~2000) and availability. The steel base bolts onto a piece that mounts to a hydraulic ram assembly capable of 20 tons. The rail was placed on a load cell, while the hydraulic ram was controlled manually through a lever arm attached to a piston. The fixture is shown below in Figure 3.56.

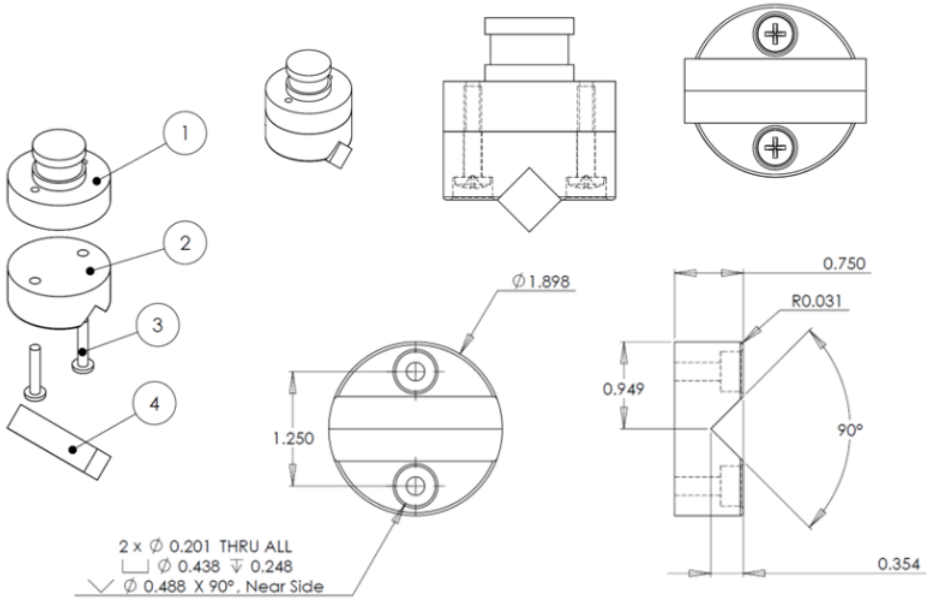

Figure 3.55. Indenter hardware (dimensions in inches):
1 = hydraulic ram attachment, 2 = indenter base, 3 = assembly bolts, 4 = WC indenter

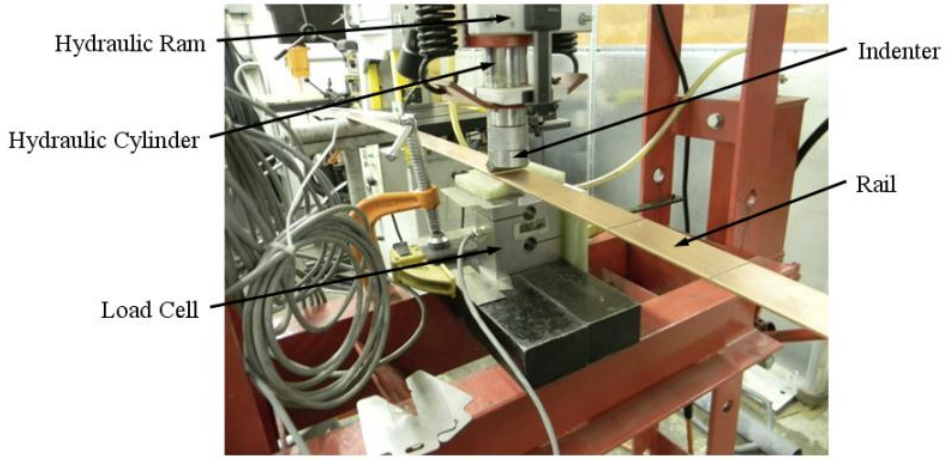

Figure 3.56. Hydraulic press assembly photograph

A series of tests were performed with both C11000 and C15725 rail stock. Indentations were done using loads from 1,000 lb. to 10,000 lb. in 1,000 lb. increments. Photographs of the indented C11000 rails after sectioning and coarse polishing are shown in Figure 3.57 for the 5,000 lb. and 10,000 lb. cases. Figure 3.58 provides measurements

of the width and depth of the indentations for the load cases tested. Measurements were made using the microscope photographs and scale reticules.

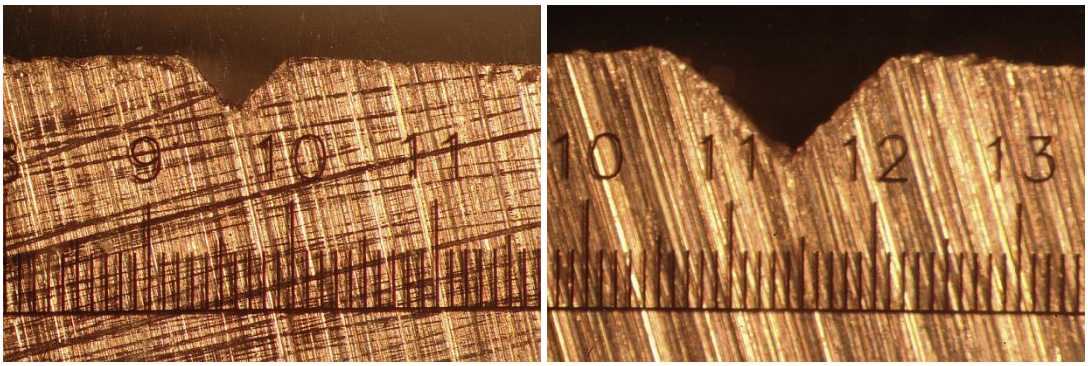

Figure 3.57. Microscope photographs of C11000 indentations at 5,000 lb. (left), and 10,000 lb. (right) Scale markers are in mm

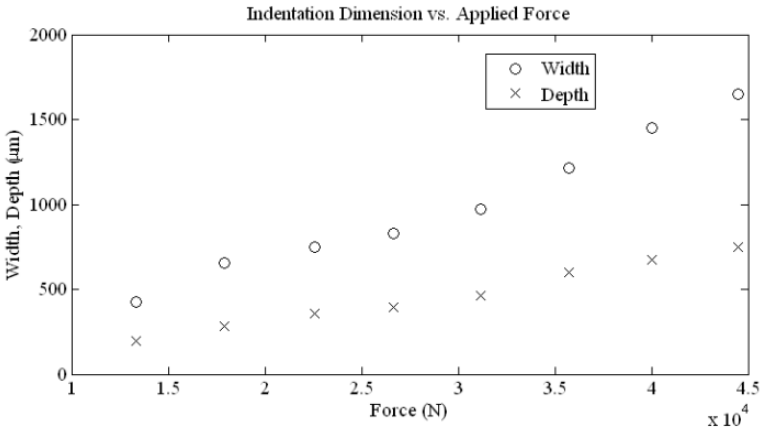

Figure 3.58. Plot of indentation depth and width vs. applied force on C11000

A 5,000 lb. load was used to apply the indentations to use in the railgun tests. This would result in an indent depth and width of approximately 350 μm and 750 μm, respectively. The indentations were applied to two 72" C11000-H02 rail claddings, and placed 10 cm apart down the length of the claddings, about twice the contact length of the armature.

The power supply parameters used in the circuit simulation are provided in Table 3.15, with the resulting waveforms shown in Figure 3.59. The flat-top current pulse was

designed to be as long as possible to yield the greatest velocity range on the 72" test cladding. The simulation estimated a velocity of 180 m/s at the beginning of the flat-top at 1.0 ms (0.2 m), and a velocity of 1,580 m/s at the end of the flat-top at 2.98 ms (1.92 m). The estimated gouging velocity based on previous MCL results for AA7075 on C11000 is 1,300 m/s [25], so gouging was expected to occur.

Table 3.15. Power supply parameters for indented rail experiments

HMCL # V_{charge}	**1341-1342** 15.7 kV		
Bank #	**Time (μs)**	**Bank #**	**Time (μs)**
0	500	9	~
1	500	10	500
2	500	11	1,670
3	500	12	1,950
4	500	13	2,180
5	500	14	2,380
6	900	15	2,520
7	1,300	16	2,660
8	~	17	2,800

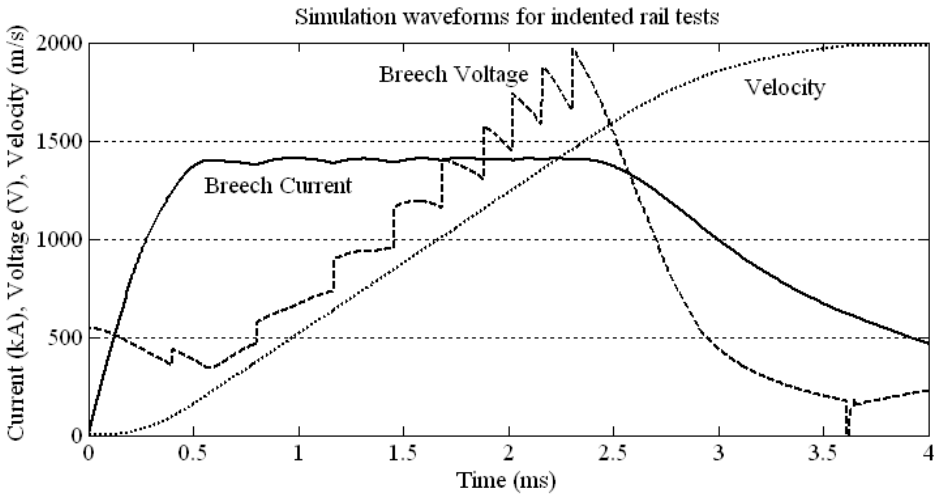

Figure 3.59. Circuit simulation results for indented rail tests

CHAPTER 4. EXPERIMENTAL RESULTS

This chapter presents the results from the railgun gouging experiments. Each series is presented separately, and will include test summaries, experimental waveforms, and rail photographs. Additional results are presented using optical and electron microscopy where appropriate. Supplemental information from the experiments (B-dot traces, etc.) can be found in Appendix E. A summary of the gouging measurements is provided in Table 4.1. Greyed out velocities coincide with the leading edge of rail inserts and do not represent a "normal" damage mode.

Table 4.1. Experimental Results Overview

Test #	Slider	Rail	Slider *HV*	Rail *HV*	V_{gall} *m/s*	V_{gouge} *m/s*
Baseline Experiments						
MCL 609	C11000-H04	C11000-H02	139 ± 4	83 ± 1	683 ± 16	820 ± 12
MCL 610	C11000-H04	C11000-H02	139 ± 4	88 ± 4	731 ± 4	820 ± 3
MCL 687	AA7075-T6	C26000	176 ± 2	137 ± 5	~	1,731 ± 26
Slider Experiments						
MCL 623	4140 HRC 35	C11000	318 ± 6	83 ± 4	997 ± 11	1,285 ± 11
MCL 677	Tantalum	"	129 ± 6	"	756 ± 44	1,495 ± 63
MCL 678	AA1100 H14	"	42 ± 2	"	~	1,341 ± 23
MCL 679	Zirconium	"	210 ± 12	"	770 ± 161	1,495 ± 49
MCL 680	MACOR®	"	80 ± 20	"	~	1,267 ± 23
MCL 682	4340 HRC 27	"	276 ± 9	"	1,130 ± 37	1,447 ± 46
MCL 681	4340 HRC 35	"	348 ± 16	"	1,073 ± 95	1,743 ± 65
MCL 684	4340 HRC 41	"	420 ± 18	"	1,478 ± 10	~
MCL 685	4340 HRC 51	"	597 ± 16	"	1,440 ± 19	1,879 ± 68
MCL 686	4340 HRC 59	"	724 ± 28	"	1,435 ± 26	~
Coated Rail Experiments (C15725 rail)						
MCL 628	AA7075-T6	25 μm Al	176 ± 2	169 ± 5	~	~
MCL 629	"	50 μm Al	"	"	~	~
MCL 630	"	5 μm Al	"	"	~	~
MCL 650	"	Bare C15725	"	"	~	1,960 ± 100
MCL 651	"	5 μm Al	"	"	~	~
MCL 652	"	5 μm Al	"	"	~	~
MCL 653	"	2 μm Al	"	"	~	~
Indented Rail Experiments						
HEMCL 1341	AA7075-T6	C11000 dented	176 ± 2	89 ± 2	688 ± 17	1,109 ± 14
HEMCL 1342	"	C11000 flat	"	"	719 ± 20	1,138 ± 17

4.1 Series 1, Baseline Experiments

4.1.1 Series 1 Experimental Overview and Waveforms

The goal of Series 1 was to perform tests with "baseline" launch packages. "Baseline" in this context means that the launch package is composed of a metallic armature (copper or aluminum) and a plastic fore-body, with the armature running on a "smooth" bare rail surface. Gouging is expected to be a result of the armature interacting with the rail. Three configurations were tested: Two C11000 armatures on C11000, and one AA7075-T651 armature on brass (C26000) rails. The copper/copper material pair in railguns has been reported on previously [1,25], but with little discussion of the damage mechanisms preceding gouging. The aluminum/brass combination is untested in railguns. Photographs of the launch packages used in the experiments are shown in Figure 4.1.

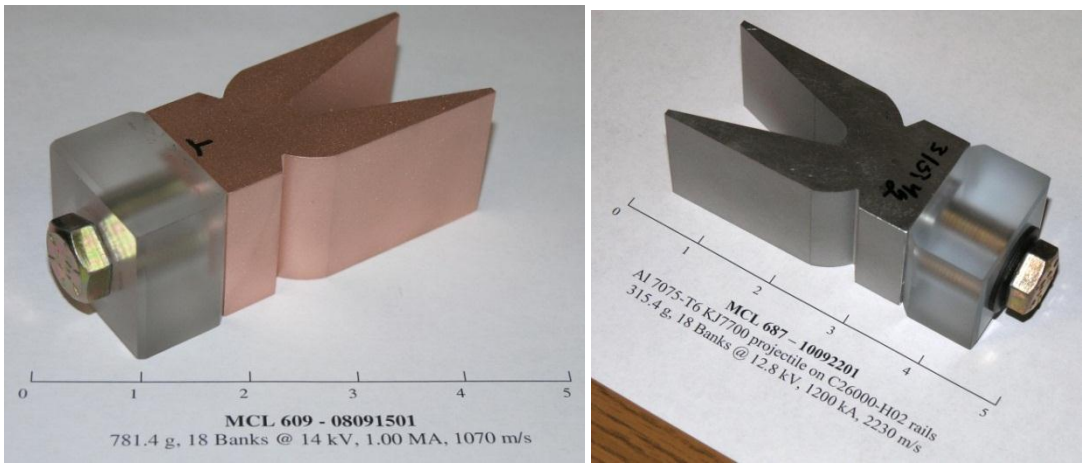

Figure 4.1. C11000-H04 armature (left), and AA7075-T651 armature (right)

Table 4.2 provides a summary of the test conditions for the three experiments. I_{pk} is the peak current during launch, I_{exit} is the current at armature exit, V_{exit} is the velocity at armature exit, X_{trans} is the transition position measured from the breech, and V_{trans} is the transition velocity. For the copper/copper experiments the launch packages were launched with a peak current of ~1,100 kA, resulting in an exit velocity of ~1,100 m/s.

The aluminum/brass experiment had a peak current of ~1,200 kA with an exit velocity of 2,100 m/s. The different velocities were due largely to the difference in launch package masses, which were 781 g for MCL 609-610 (copper armature) and 315 g for MCL 687 (aluminum armature).

Table 4.2. Series 1 (baseline) experimental results

MCL #	Slider (Armature)	Rail	I_{pk} *kA*	I_{exit} *kA*	V_{exit} *m/s*	X_{trans} *m*	V_{trans} *m/s*
609	C11000-H04	C11000-H02	1,105	107	1,126	-	-
610	C11000-H04	C11000-H02	1,068	86	1,166	5.98	1,167
687	AA7075-T651	C26000-H02	1,192	139	2,115	2.42	1,880

Gouging results are summarized in Table 4.3, along with measured hardness values of the slider and rail materials. The galling and gouging velocities were determined by measuring the related feature from the breech of the launcher. The velocity vs. position curve was then used to determine the corresponding velocity. Since the continuous velocity is based on a kinematic equation described in Chapter Three, it is compared to the measured B-dot velocities to get an error estimate. At each B-dot velocity, an error is calculated based on the difference between the measured B-dot velocity and the continuous velocity. This establishes a velocity-error vs. position function. A specified velocity for galling or gouging is then used to interpolate a corresponding error estimate. If the velocity is between two B-dot velocities then linear interpolation is used. If the velocity is outside the bounds of the B-dot velocities then the error of the nearest B-dot velocity is used.

Table 4.3. Series 1 gouging results

MCL #	Slider	Rail	Slider *HV*	Rail *HV*	V_{gall} *m/s*	V_{gouge} *m/s*
609	C11000-H04	C11000-H02	139 ± 4	82 ± 2	683 ± 16	820 ± 12
610	C11000-H04	C11000-H02	139 ± 4	88 ± 4	731 ± 4	820 ± 3
687	AA7075-T651	C26000-H02	176 ± 2	137 ± 5	None	1,731 ± 26

The first test (MCL 609) used a C11000 armature and C11000 claddings for the entire length of the launcher. The first test experienced several instrumentation issues: the

Pearson coil at the muzzle did not provide a muzzle voltage signal, and one of the bank current digitizers produced an erroneous signal resulting in an artificially high peak current. The remaining tests experienced no instrumentation issues. The breech current, muzzle voltage and velocity traces for MCL 609 are shown in Figure 4.2.

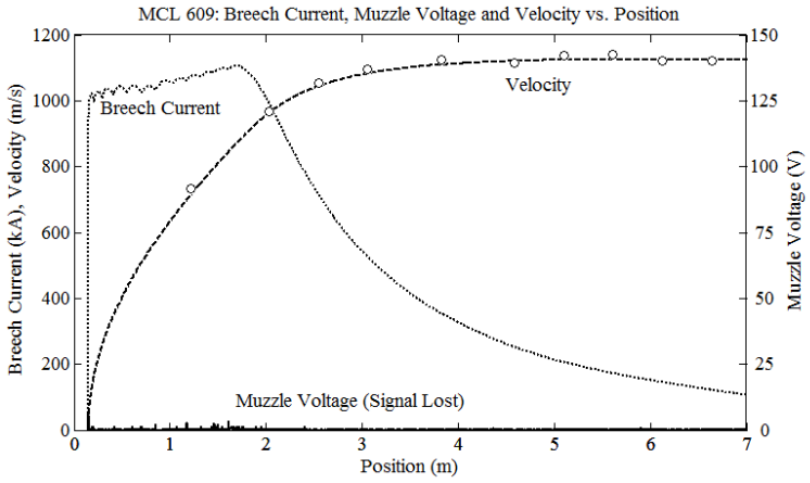

Figure 4.2. MCL 609 (Cu/Cu) breech current, muzzle voltage (signal lost), and velocity

Figure 4.3 shows the B-dot signal traces for MCL 609. For most solid armature experiments the B-dots provide little useful information besides the position vs. time information. The B-dot waveforms for all subsequent tests are provided in Appendix E.

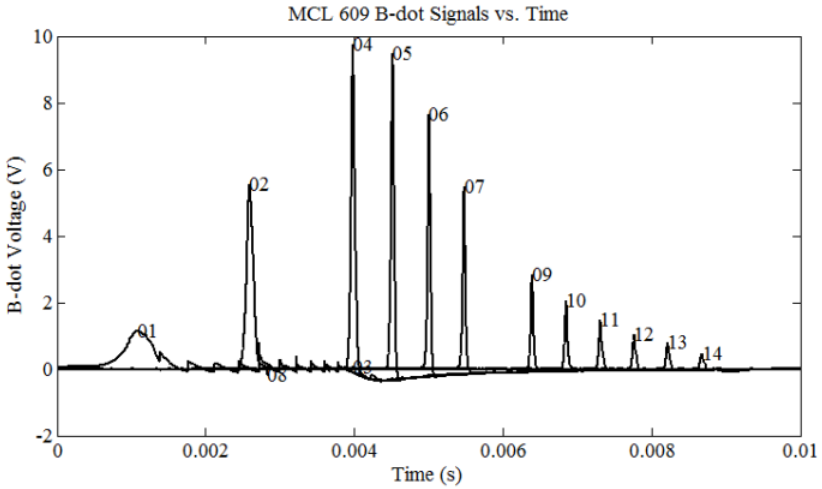

Figure 4.3. MCL 609 (Cu/Cu) B-dot signals

The second test (MCL 610) also used a C11000 armature, but used Glidcop® Al-25 (UNS C15725) dispersion-strengthened copper claddings for the first meter, and C11000 for the remainder of launch. This was done to reduce galling damage in the startup region observed after MCL 609. Experimental waveforms are shown in Figure 4.4. At 2 m there is a sudden muzzle voltage spike lasting approximately 0.2 m. Since arcing contact begins around 2 m, any conclusions regarding gouging after this location are suspect.

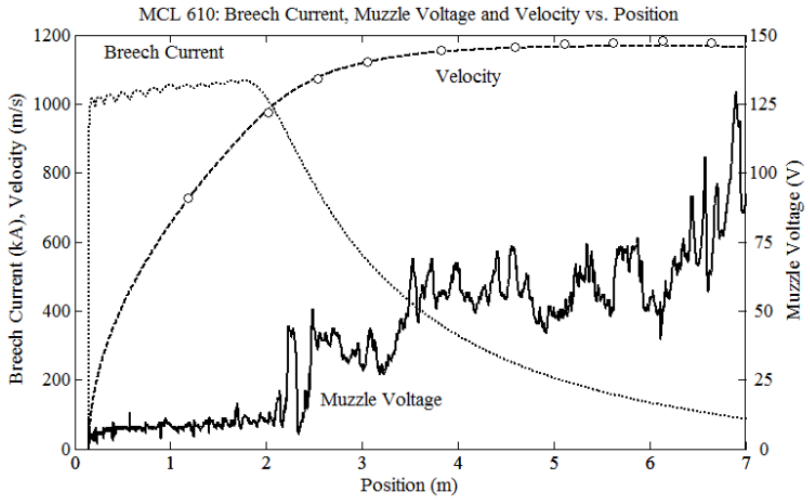

Figure 4.4. MCL 610 (Cu/Cu) breech current, muzzle voltage and velocity

These two tests (MCL 609-610) were performed with the soft-catch mechanism discussed in the previous chapter. However, due to the high momentum of the launch package, the soft-catch system was unsuccessful at recovering the armatures intact. Instead, the heavy copper armatures penetrated the cotton rags and impacted the steel target plates in the catch tank. The resulting damage to the armatures was severe enough that no meaningful information was gleaned from their analysis.

Figure 4.5 shows the experimental waveforms for the third experiment (AA7075 armatures on C26000 rail claddings). The behavior of the muzzle voltage for this experiment was very similar to the previous two tests, despite the higher velocity and different materials.

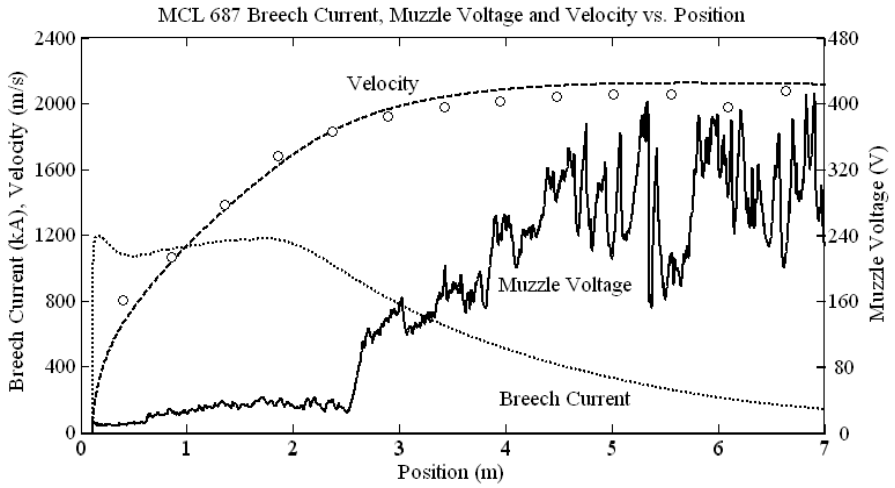

Figure 4.5. MCL 687 (AA7075/C26000) breech current, muzzle voltage and velocity

X-rays of the MCL 687 launch package after leaving the muzzle of the launcher are shown in Figure 4.6. Ideally, the presence of gouge craters could be discerned given enough fidelity in the X-rays. However, transition to arcing contact (which began at 2.5 m) eroded a significant portion of the armature contact face. Therefore, no obvious gouging damage is apparent in the X-ray.

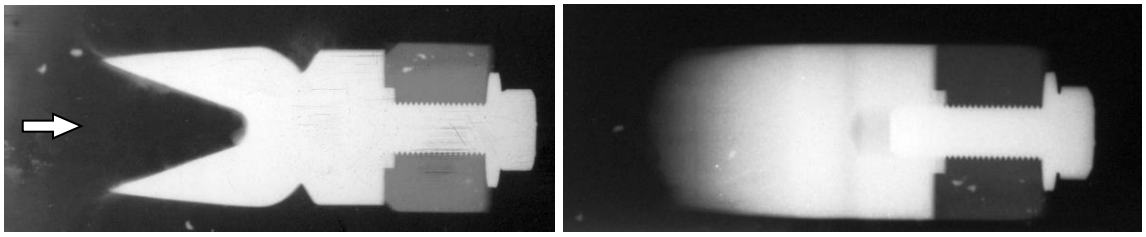

Figure 4.6. MCL 687 muzzle X-rays (left = top view, right = side view)

4.1.2 SERIES 1 RAIL PHOTOGRAPHS AND GOUGE LOCATIONS

Photographs of the as-shot rail surfaces for MCL 609 are provided in Figure 4.7 and Figure 4.8. In all the rail photographs the direction of armature motion is left to right, unless otherwise indicated. While there was no muzzle voltage signal recorded for this

experiment, transition is apparent at 1.98 m (78") on the positive (top) rail. The terms *positive* (+) and *negative* (-) refer to the electrical polarities of the rails, and are a function of how the coaxial cables are attached to the breech of the launcher.

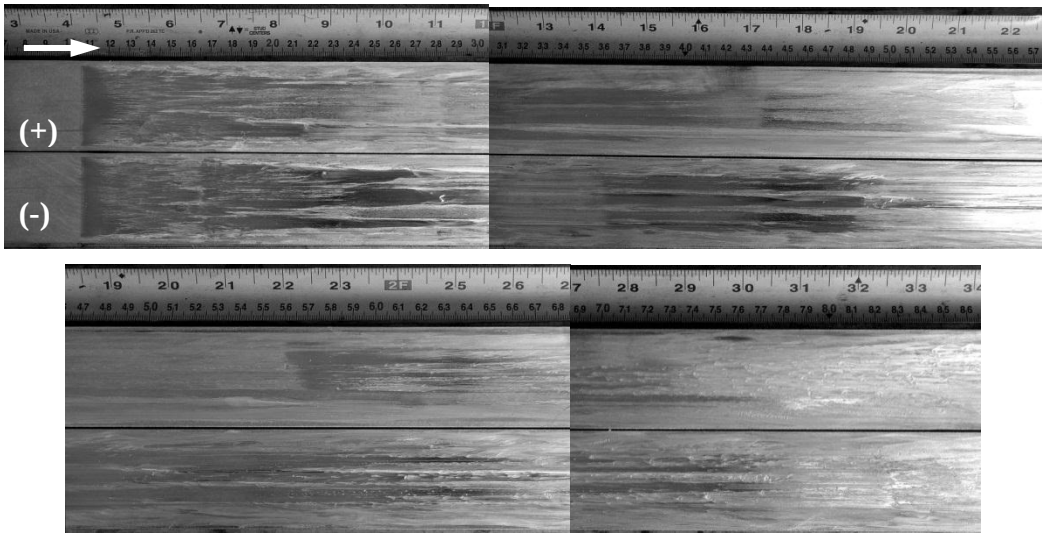

Figure 4.7. MCL 609 (Cu/Cu) rail photographs (0-0.86 m, 33.9")

The onset of gouging is difficult to determine for this experiment because of the excessive galling damage. Significant galling damage is first observed on the (+) rail at 1.13 m (44.5", 683 m/s). The “best guess” for the first teardrop-shaped gouge crater is 1.53 m (60.2", 820 m/s).

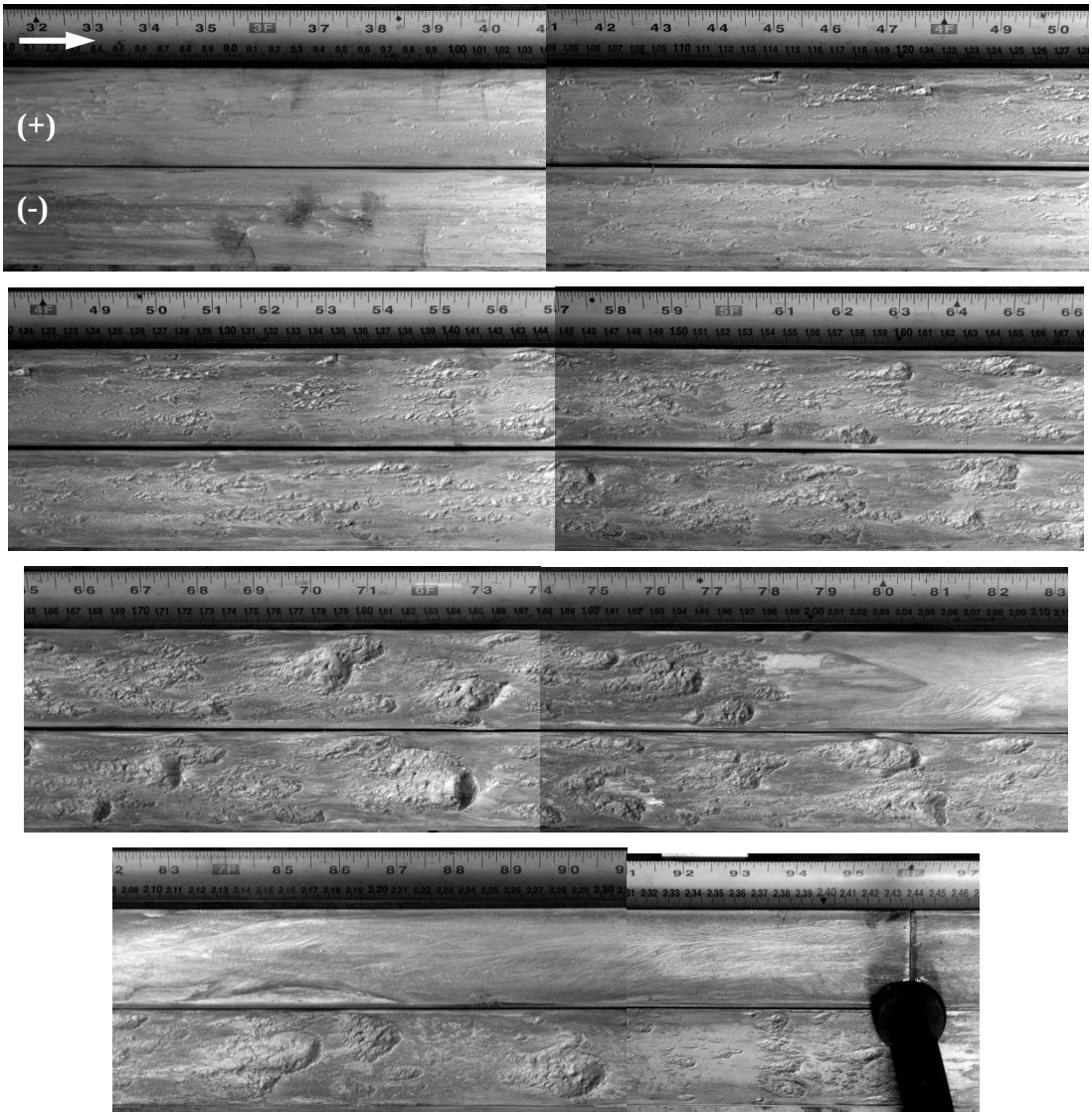

Figure 4.8. MCL 609 (Cu/Cu) rail photographs (0.80-2.46 m, 31.5-96.9")

The evolution of damage for MCL 609 is shown in Figure 4.9 at increasing velocities. Sliding damage initially takes the form of burnishing (Figure 4.9a). Around 500 m/s small pits are seen across the contact surface (Figure 4.9b). These pits get larger with increasing velocity (Figure 4.9c) until they are gradually replaced by galling tracks (Figure 4.9d). The galling damage exhibits more gouge-like behavior (Figure 4.9e) until large gouge craters are observed on the rail surface (Figure 4.9f). Once the armature reaches ~900 m/s there are no more galling tracks, and all damage takes the form of gouge craters. However, there is a wide variety of crater size at any given location (Figure 4.10).

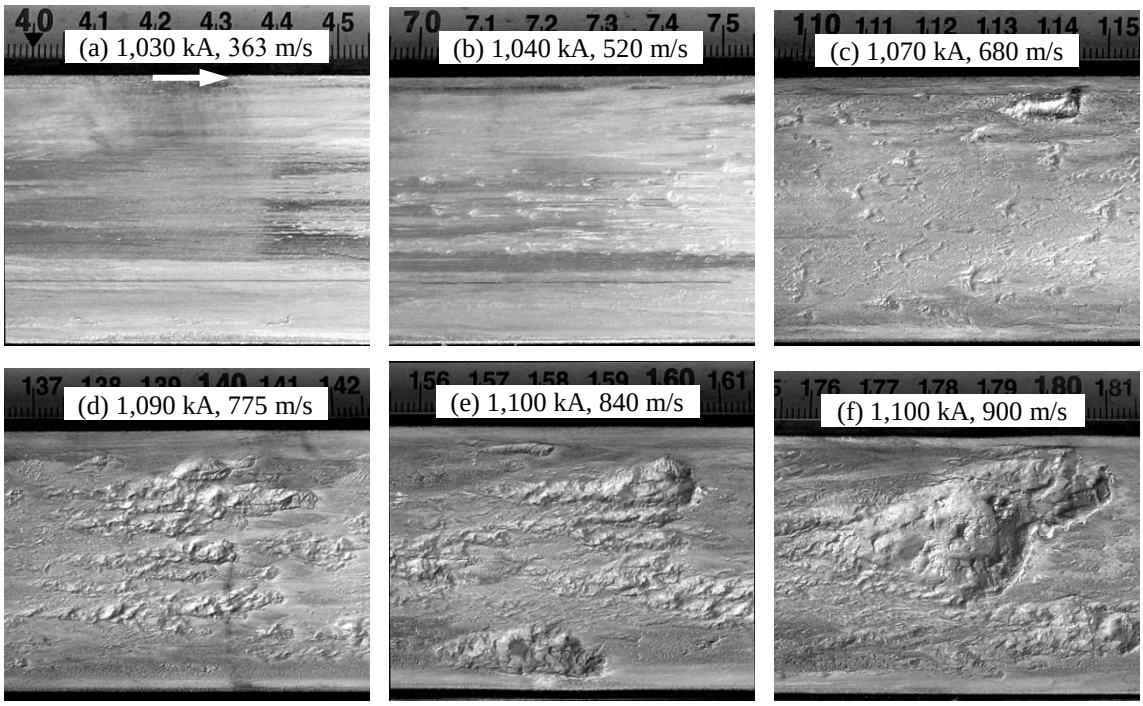

Figure 4.9. Cu/Cu rail damage at increasing velocities, (+) rail, MCL 609

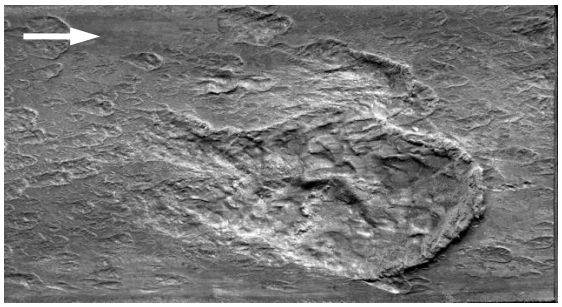

Figure 4.10. Cu/Cu gouging at 1,000 m/s, MCL 609, (-) rail, 2.25 m (88.6")

Photographs of the as-shot rail surface for MCL 610 are provided in Figure 4.11 and Figure 4.12. The primary difference between this and the previous experiment are that this test used C15725 startup claddings and slightly harder (HV 88 vs. 82) C11000 rail claddings. Galling "pits" begin immediately on the C11000 claddings, while only burnishing damage is seen on the C15725 claddings. The first large galling damage occurs on the (+) rail at 1.2 m (47.2", 731 m/s). The first teardrop shaped gouge crater is seen at 1.46 m (57.5", 820 m/s).

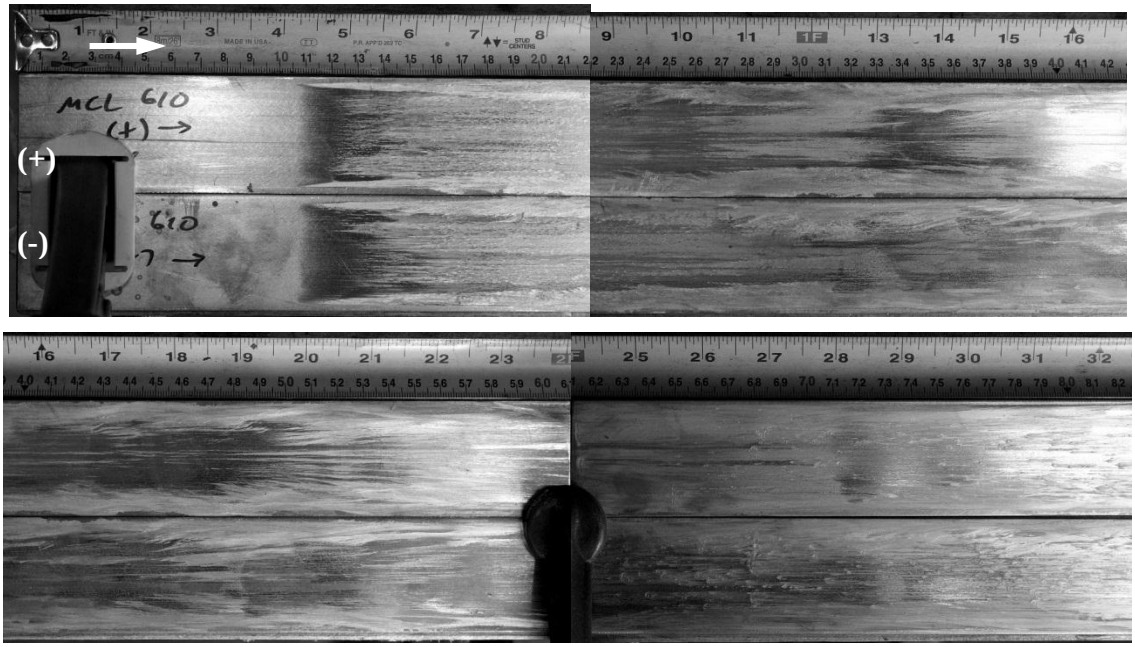

Figure 4.11. MCL 610 (Cu/Cu) rail photographs (0-0.82 m, 0-32.3")

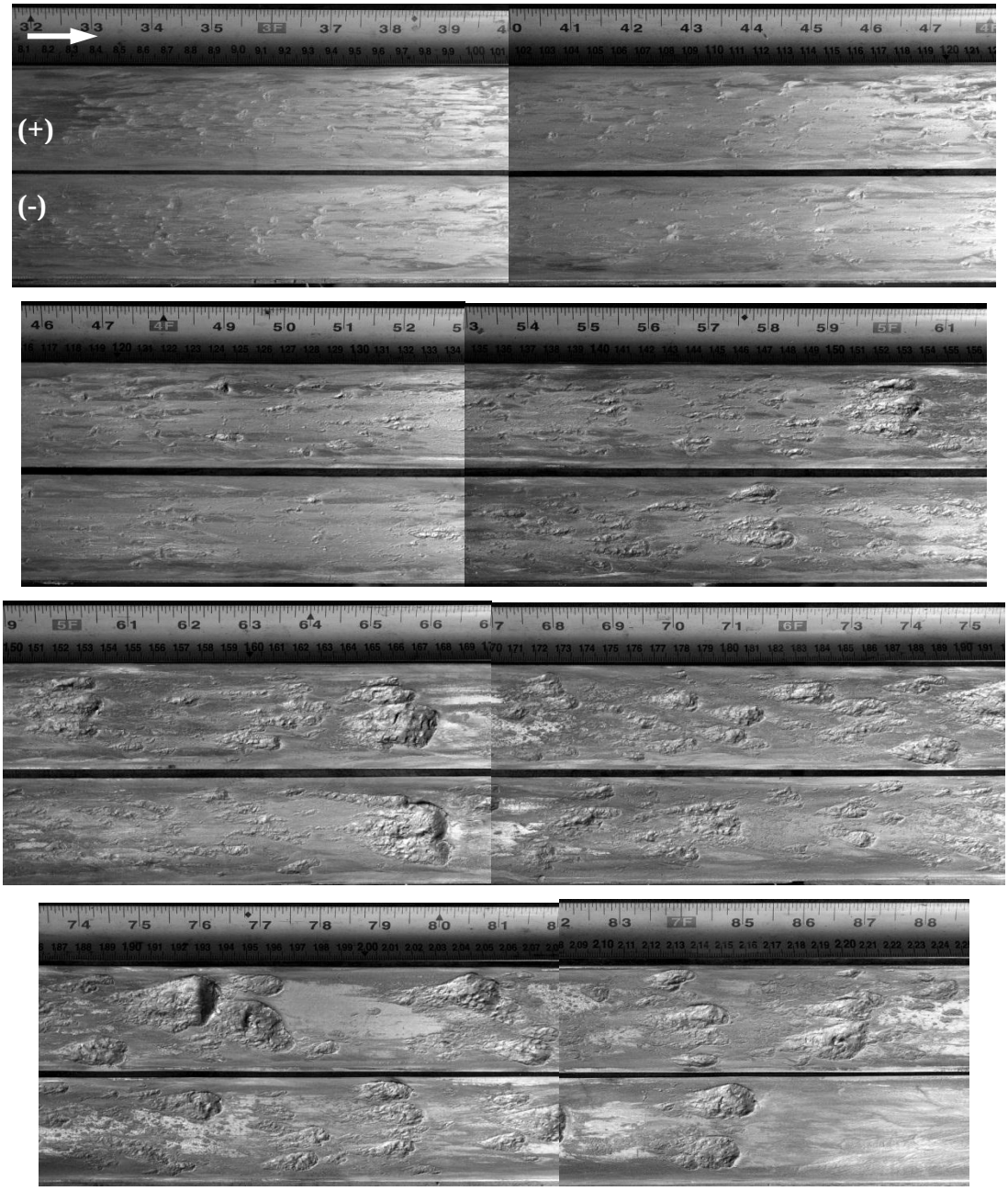

Figure 4.12. MCL 610 (Cu/Cu) rail photographs (0.81-2.42 m, 31.9-95.3")

Figure 4.13 shows the startup region for the C11000 (MCL 609) and C15725 (MCL 610) rail claddings. In this location the current is at its maximum but the armature is only traveling about 400 m/s. The test on C11000 resulted in significant plastic

deformation in the rails, followed by galling damage. Damage to the C15725 primarily consists of burnishing near the armature/rail contact edges. Damage to the two C11000 surfaces at increasing velocities are shown in Figure 4.14 through Figure 4.16. At approximately 580 m/s (Figure 4.14) the damage takes the form of small pits. Qualitatively, there is little difference in the damage between the two coppers.

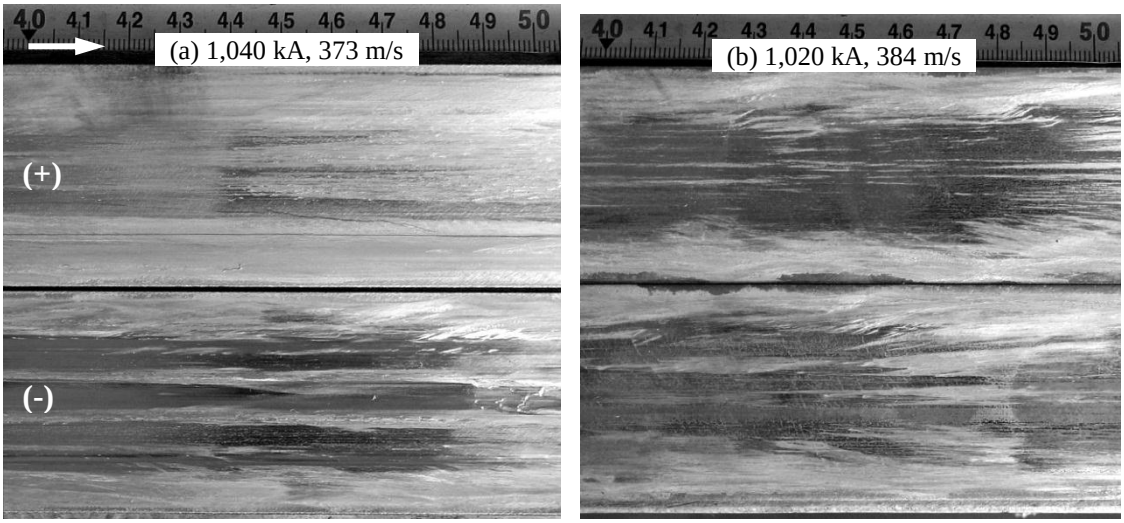

Figure 4.13. Damage on (a) C11000 and (b) C15725 at ~380 m/s

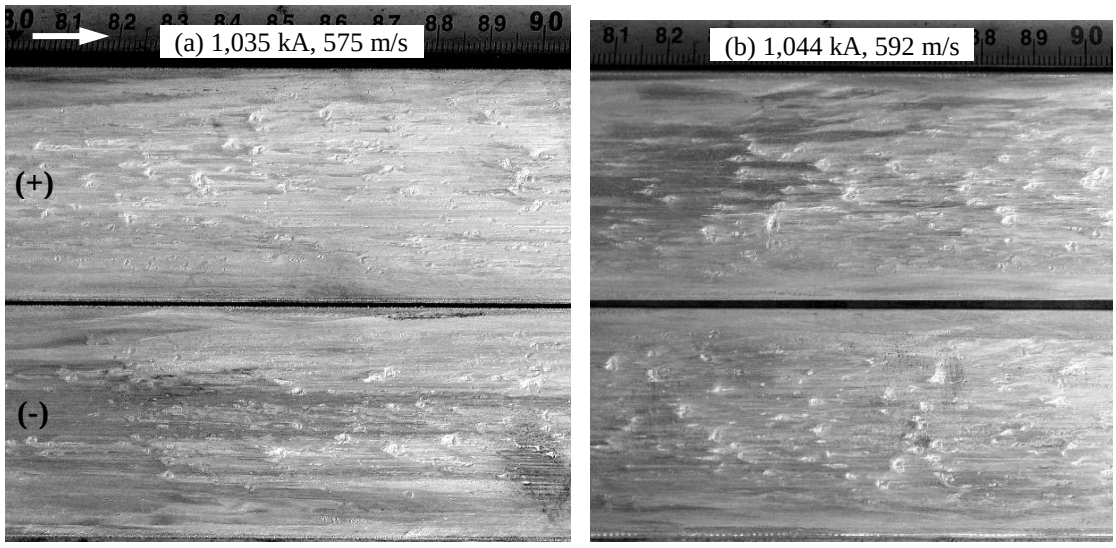

Figure 4.14. Damage on (a) C11000-HV82 and (b) C11000-HV88 at ~580 m/s

Figure 4.15 shows damage downstream at approximately 830 m/s where galling appears to be the dominant damage mechanism. Once the armature velocity approaches 900 m/s the damage is predominantly gouging (Figure 4.16). The gouging craters appear to be slightly larger (on average) for the C11000-HV82 rails compared to the C11000-HV88 rails.

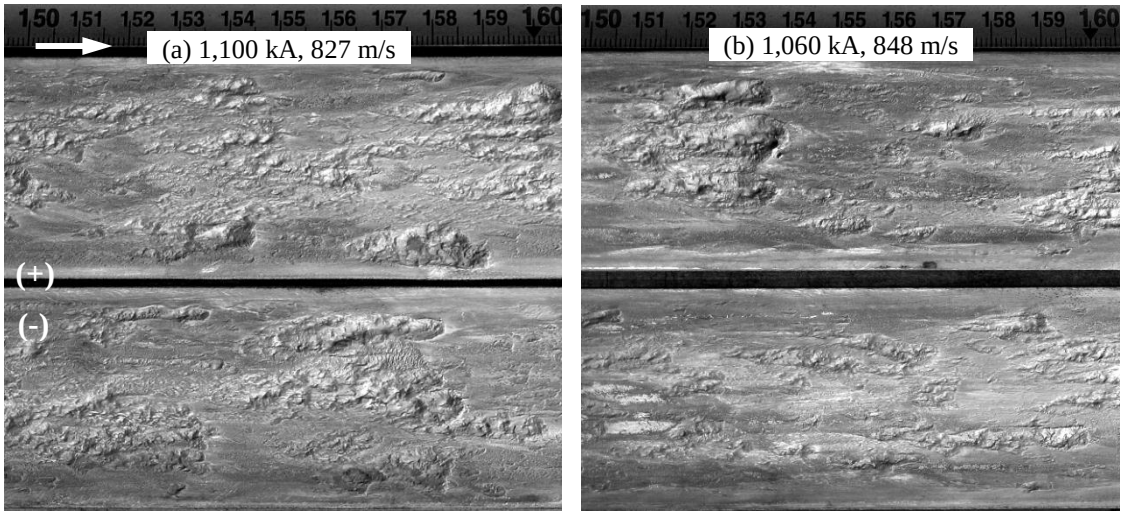

Figure 4.15. Damage on (a) C11000-HV82 and (b) C11000-HV88 at ~830 m/s

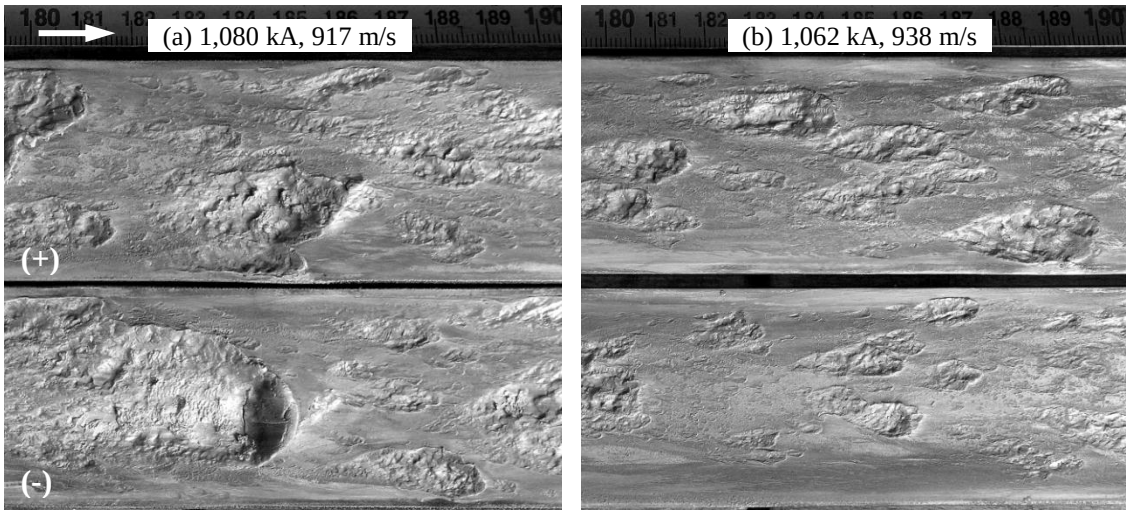

Figure 4.16. Damage on (a) C11000-HV82 and (b) C11000-HV88 at ~930 m/s

Photographs of the as-shot rail surfaces for MCL 687 are provided in Figure 4.17 and Figure 4.18. Unlike the previous two experiments there is no apparent galling damage prior to gouging, which is first seen at 1.4 m (55.1", 1,730 m/s). This behavior is more consistent with “classical” gouging, where damage to the rails is minimal up to the gouging threshold velocity.

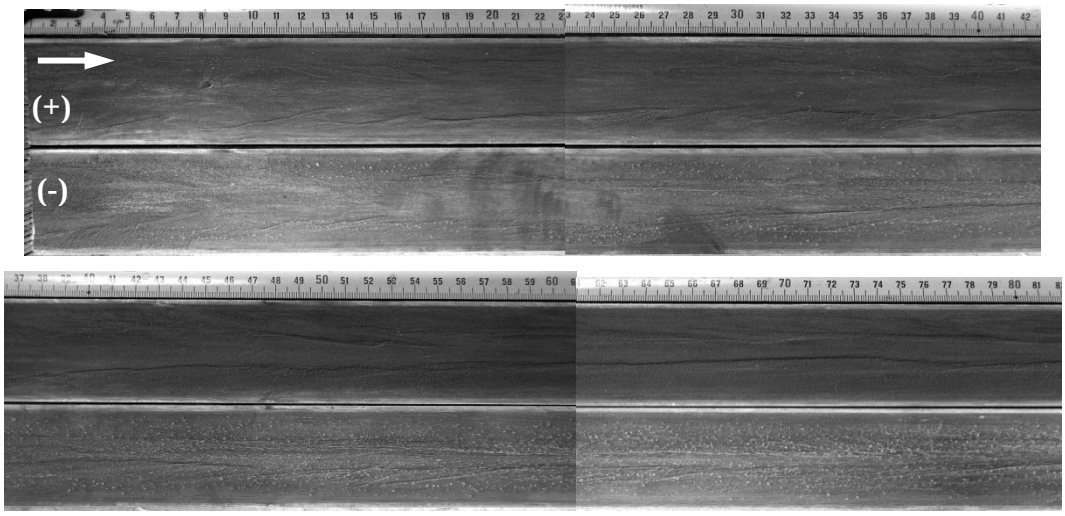

Figure 4.17. MCL 687 (AA7075/C26000) rail photographs (0-0.82 m, 0-32.3"), 0.65 m cladding offset

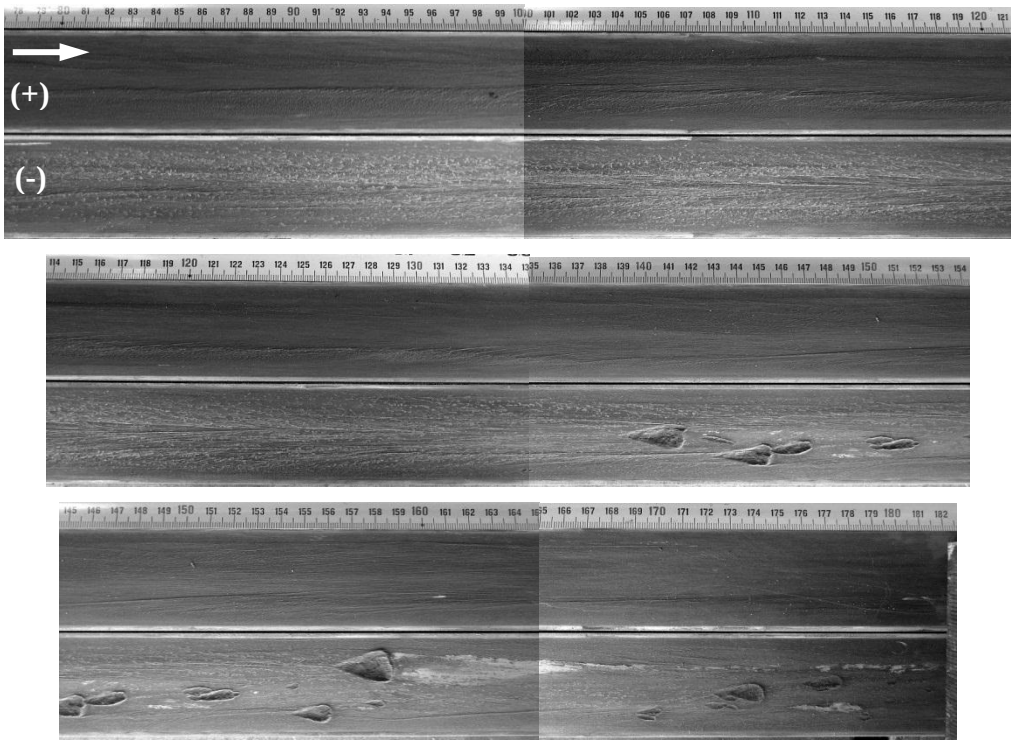

Figure 4.18. MCL 687 (AA7075/C26000) rail photographs (0.78-1.82 m, 30.7-71.7"), 0.65 m (25.6") cladding offset

4.1.3 SERIES 1 MICROSCOPY

The sliding damage for the Cu/Cu material pair in MCL 609 at 510 m/s (Figure 4.14) is further examined in Figure 4.19. Analysis was performed with a JEOL 5610 scanning electron microscope (SEM). The numbers in the SEM image indicate (from left to right) beam voltage, magnification, and scale marker size. SEM examination of the "pits" discussed earlier reveals shallow trenches in the rail that produce parabolic craters. The trenches start at existing defects (machining/polishing marks) and contain bands of sheared material, with the bands angled at about 45 degrees with respect to the rail surface. Figure 4.20 shows several SEM images of a shallow gouge created at 900 m/s. Prior to the crater, there is a region of surface damage which is similar to the bands shown in Figure 4.19. However, the bands are 100-300 nm wide, about two orders of

magnitude smaller than those at lower speeds. Within 20-50 μm, the bands are replaced by re-solidified material, though there is still evidence of a band-like structure.

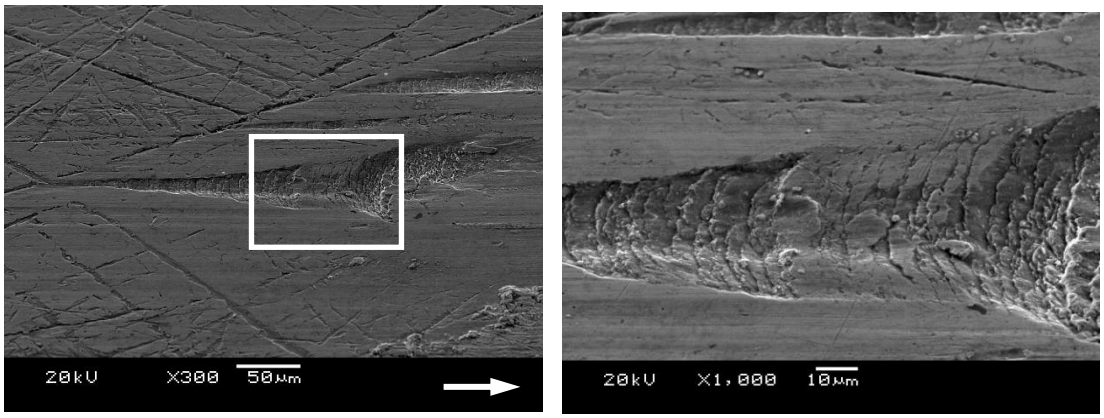

Figure 4.19. SEM image for Cu/Cu galling damage at 510 m/s (MCL 609)
Image taken at an elevation angle of 45 degrees

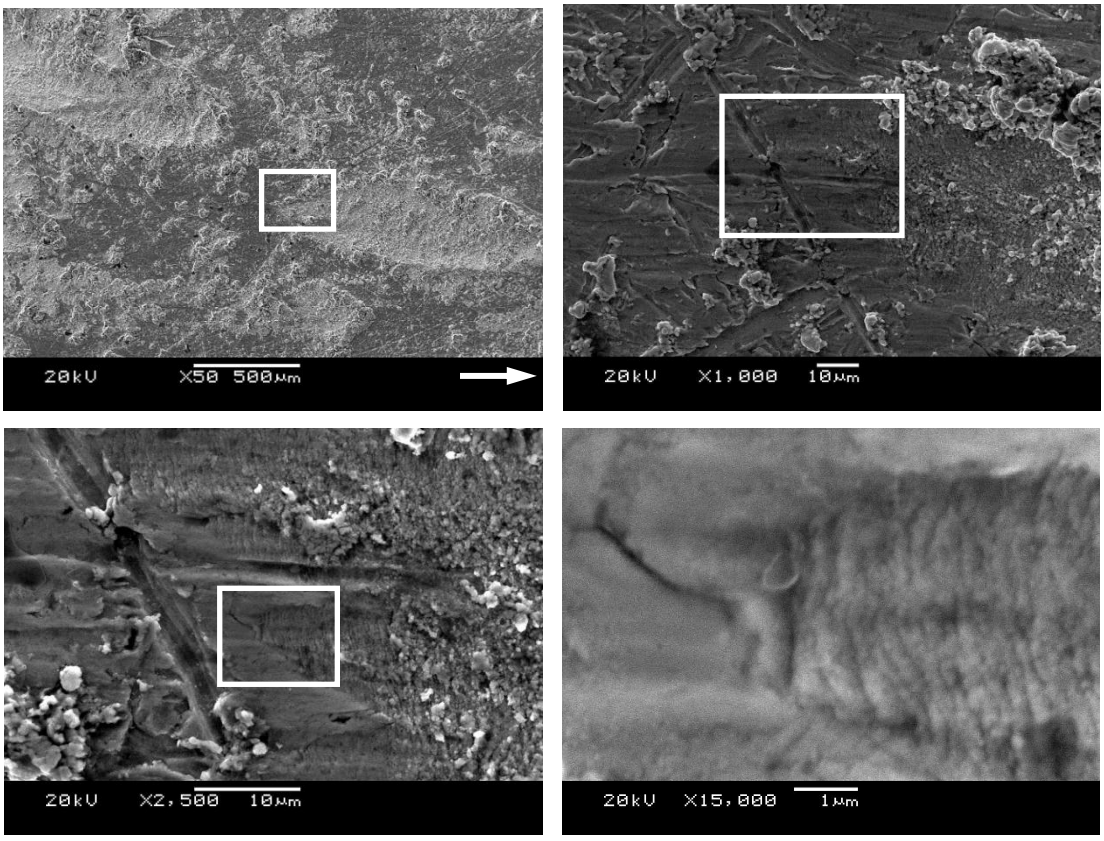

Figure 4.20. SEM image of Cu/Cu gouge initiation at 960 m/s (MCL 609)
Boxes indicate the region shown in the next higher magnification

SEM images of the rail surface from MCL 610 are shown in Figure 4.21 through Figure 4.23. These images were taken around 0.22 m (8.7") from the beginning of the C11000 rail (~580 m/s). A low magnification image of a pit is shown in Figure 4.21.

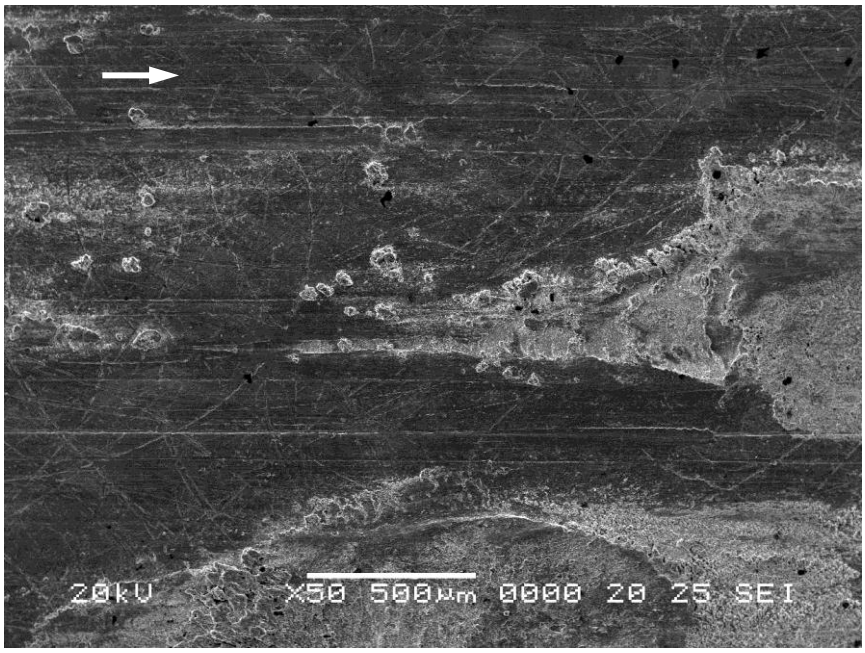

Figure 4.21. SEM image of Cu/Cu damage at 580 m/s (MCL 610), 0.83 m (32.7")

Figure 4.22 shows the beginning of the pit, which takes the form of a long trench in the rail surface. Early on, the trench contains similar bands to those seen in Figure 4.19, though the wavelength is somewhat less. About 400 μm after the trench starts, the bands become narrower and appear to have undergone melting or softening. As the trench continues it widens to form a shallow crater (Figure 4.23), though the bands remain unchanged.

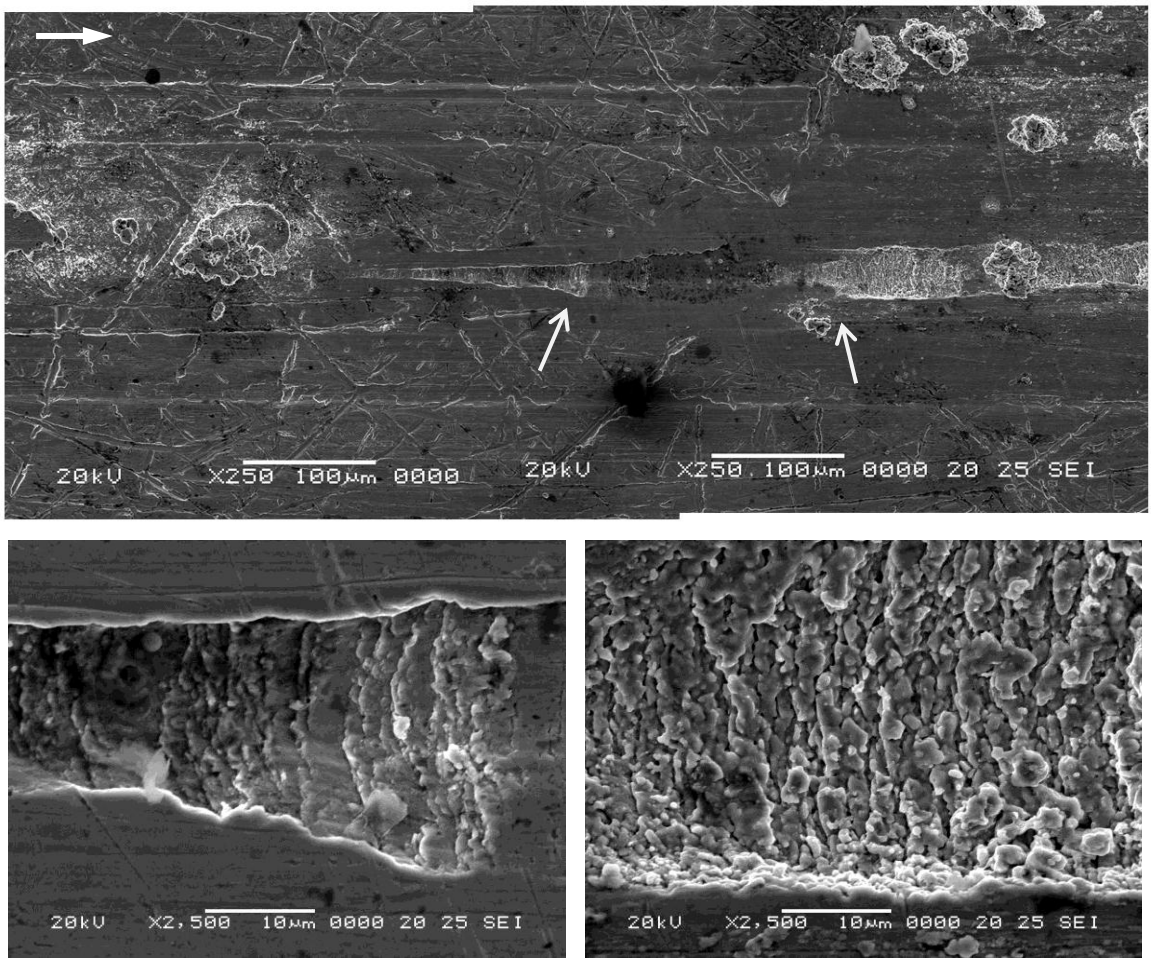

Figure 4.22. SEM image of Cu/Cu damage at 580 m/s (MCL 610), 0.83 m (32.7")
Arrows in the upper image indicate the locations of the lower, higher-magnification images

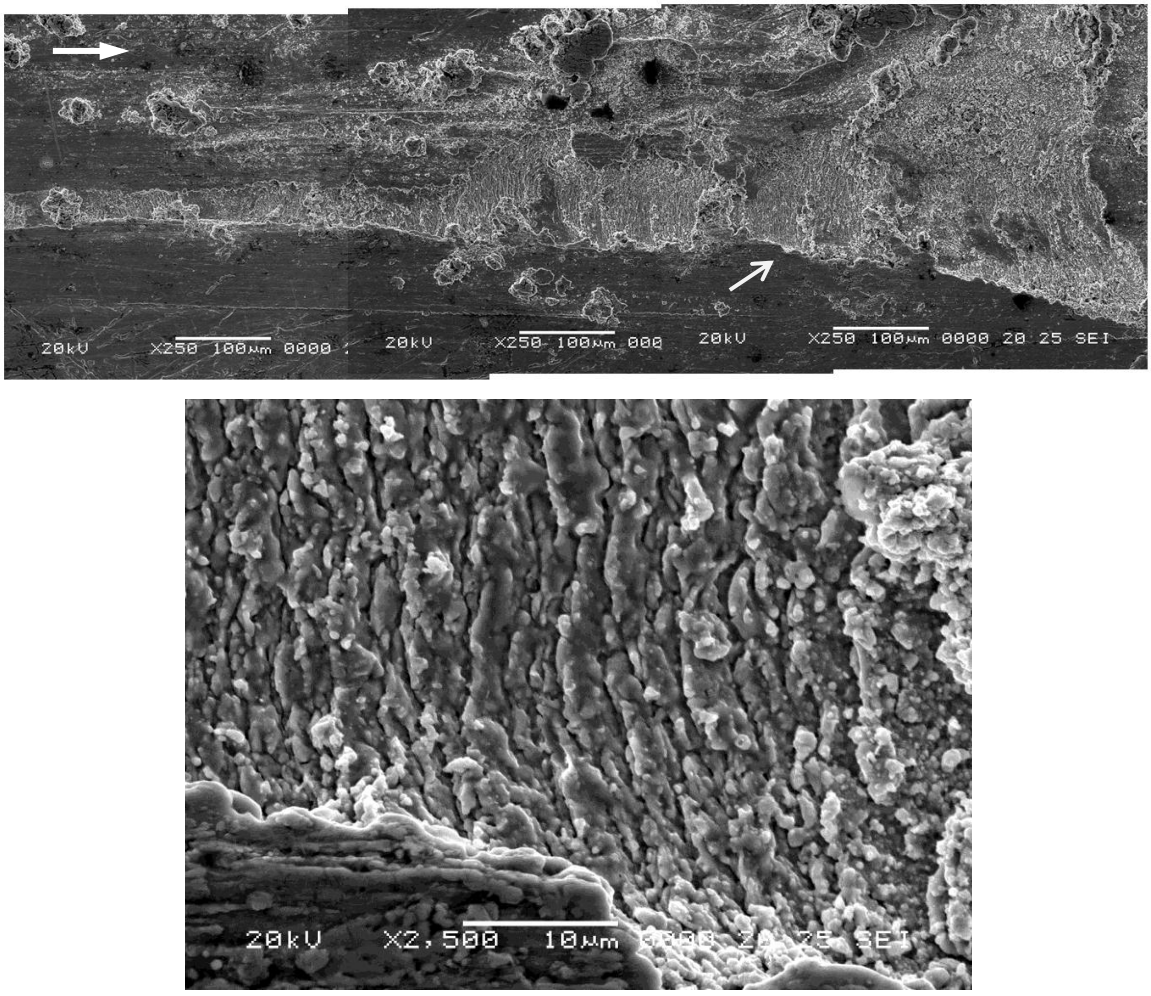

Figure 4.23. SEM image of Cu/Cu damage at 580 m/s (MCL 610), 0.83 m (32.7")

4.2 Series 2, Sample Slider Experiments

4.2.1 Series 2 Experimental Overview and Waveforms

In Series 2, the launch package incorporated a flat plate positioned ahead of the armature (see Figure 4.24). This was done so that different materials could be tested against copper rails that would otherwise be infeasible for use as an armature material. A summary of the ten experiments is provided in Table 4.4. The test conditions were approximately the same for all cases, with a peak current of 1.1-1.2 MA and exit velocity of ~2,500 m/s.

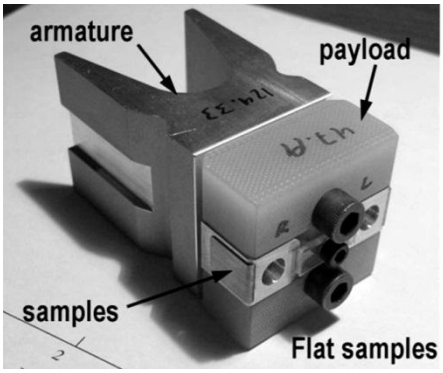

Figure 4.24. Gouging sample slider launch package

Table 4.4. Series 2 (sample slider) experimental results

MCL #	Slider	Rail	I_{pk} *kA*	I_{exit} *kA*	V_{exit} *m/s*	X_{trans} *m*	V_{trans} *m/s*
623	4140 HRC 35	C11000-H02	1,044	223	2,700	2.31	2,200
677	Tantalum	C11000-H02 EP	1,198	145	2,440	1.70	2,040
678	AA1100-H14	"	1,195	135	2,430	1.78	2,070
679	Zirconium	"	1,201	126	2,430	1.68	2,030
680	MACOR®	"	1,184	120	2,400	1.68	2,020
682	4340 HRC 27	"	1,194	129	2,440	2.17	2,220
681	4340 HRC 35	"	1,180	117	2,380	1.79	2,050
684	4340 HRC 41	"	1,187	133	2,440	1.77	2,080
685	4340 HRC 51	"	1,190	131	2,480	1.93	2,180
686	4340 HRC 59	"	1,185	136	2,460	2.00	2,180

The first test was performed on bare C11000 rails. The remaining tests were performed on partially Al-electroplated rails as described in the previous chapter. These tests also used "startup" claddings made of C15725, and AA7075-T6 claddings after the test samples. Since there were different anticipated gouging velocities for the different material combinations, the sample claddings were moved by changing the length of the startup C15725 cladding. The anticipated gouging velocities were calculated by using the Stefani-Parker gouging relationship, as well as the effective Reynolds number approach taken from explosive welding wave research discussed in Chapter Two.

Table 4.5 shows the experimental results, including the velocities at which gouging begins. Grayed out velocities are for damage mechanisms that coincide with the leading edge of a rail sample. They therefore serve as an upper bound for the velocity that would be measured under normal contact conditions.

Table 4.5. Series 2 gouging results: sliders (C11000-H02 rails)

MCL #	Slider	Slider *HV*	Rail *HV*	V_{gall} *m/s*	V_{gouge} *m/s*
623	4140 HRC 35	318 ± 6	83 ± 4	997 ± 11	1,285 ± 11
677	Tantalum	129 ± 6	"	756 ± 44	1,495 ± 63
678	AA1100 H14	42 ± 2	"	N/A	1,341 ± 23
679	Zirconium	210 ± 12	"	770 ± 161	1,495 ± 49
680	MACOR®	80 ± 20	"	N/A	1,267 ± 23
682	4340 HRC 27	276 ± 9	"	1,130 ± 37	1,447 ± 46
681	4340 HRC 35	348 ± 16	"	1,073 ± 95	1,743 ± 65
684	4340 HRC 41	420 ± 18	"	1,478 ± 10	~
685	4340 HRC 51	597 ± 16	"	1,440 ± 19	1,879 ± 68
686	4340 HRC 59	724 ± 28	"	1,435 ± 26	~

Table 4.6 shows the gouging results for the armature/rail contact. For un-coated rails there should be little variation in this threshold velocity, and therefore whatever variation is observed is presumably caused by the thin aluminum layer. It is not clear why there are such large variations in galling and gouging velocities on coated rails, though it could be due to variations in coating thickness between samples.

Table 4.6. Series 2 gouging results: armatures (AA7075-T6 on C11000-H02)

MCL #	Slider *HV*	Rail Base *HV*	Rail Surf *HV/25*	V_{gall} *m/s*	V_{gouge} *m/s*
623	176 ± 2	83 ± 4	~	975 ± 11	1,285 ± 11
677	"	"	41 ± 1	899 ± 37	1,312 ± 32
678	"	"	"	975 ± 18	1,370 ± 23
679	"	"	"	894 ± 161	1,347 ± 11
680	"	"	"	1,095 ± 84	1,543 ± 54
681	"	"	"	1,289 ± 20	1,392 ± 15
682	"	"	"	~	1,574 ± 55
684	"	"	"	1,440 ± 10	1,807 ± 57
685	"	"	"	~	1,500 ± 9
686	"	"	"	~	1,544 ± 9

MCL 623: The experimental waveforms for the first test with AISI 4140 sliders on plain C11000-H02 rails are shown in Figure 4.25. The armature transitioned at around 2.4 m (94.5"), or 2,200 m/s. This corresponds to the location of a rail cladding joint.

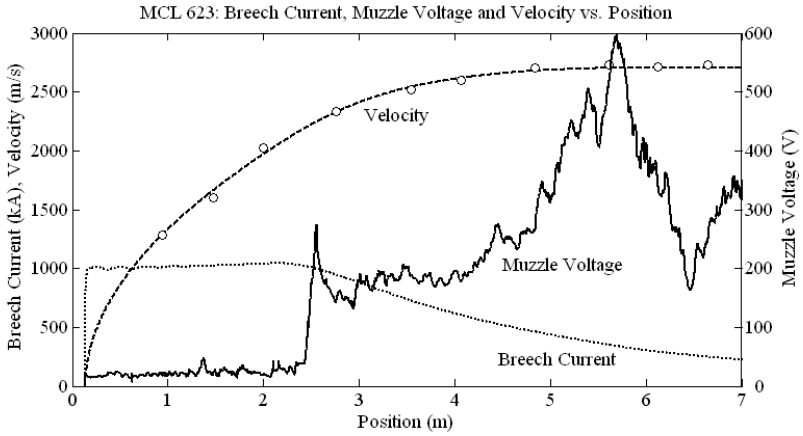

Figure 4.25. MCL 623 (4140 HRC 35 slider) breech current, muzzle voltage and velocity

MCL 677: The results for the tantalum slider are shown in Figure 4.26. This was the first experiment to use the partially Al-electroplated rails. The gouging estimate for Ta on C11000-H02 was between 600 and 800 m/s. The cladding was therefore started 0.25 m (9.8") from breech, which resulted in an estimated velocity range of 550-1,500 m/s on the test cladding. The rise in muzzle voltage at 1 m (39") corresponds to the armature moving from the C11000-H02 cladding to the more resistive AA7075-T6

cladding. Transition to arcing contact occurred at 1.7 m (66.9") and 2,040 m/s at 83% of the peak current.

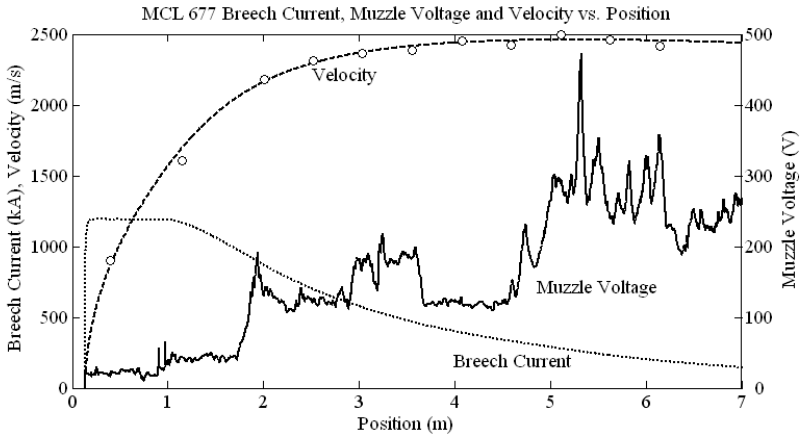

Figure 4.26. MCL 677 (Tantalum slider) breech current, muzzle voltage and velocity Startup material: 0.25 m (9.8") C15725

MCL 678: Figure 4.27 shows the waveforms for the AA1100-H14 slider test. The gouging estimate for AA1100-H14 was between 900 and 1,200 m/s, so the cladding was left in the same location as the previous test. Similar transition performance to the last shot was observed, with transition occurring at 1.78 m (70.1") and 2,070 m/s at 80% of peak current.

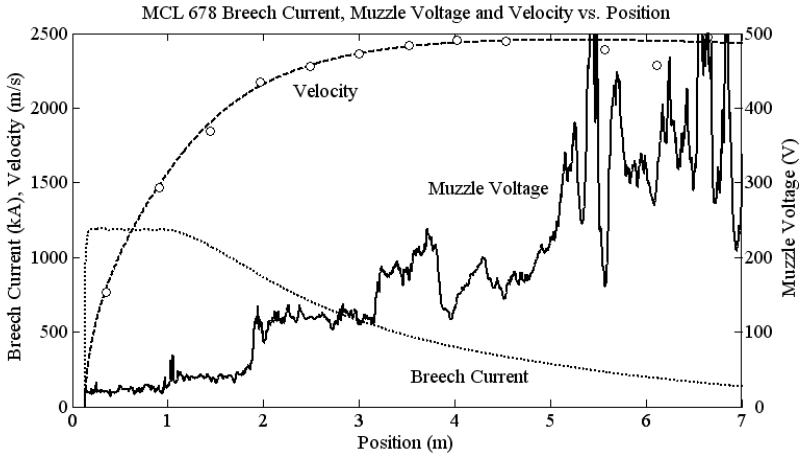

Figure 4.27. MCL 678 (AA1100 slider) breech current, muzzle voltage and velocity Startup material: 0.25 m (9.8") C15725

MCL 679: Figure 4.28 shows the results from the Zirconium sliders. Since the gouging estimate for Zirconium on C11000-H02 was 1,100 m/s, the test cladding was put in the same location as before. Muzzle voltage performance is again similar to the previous test, with transition occurring at 1.68 m (66.1") and 2,030 m/s at 83% of peak current.

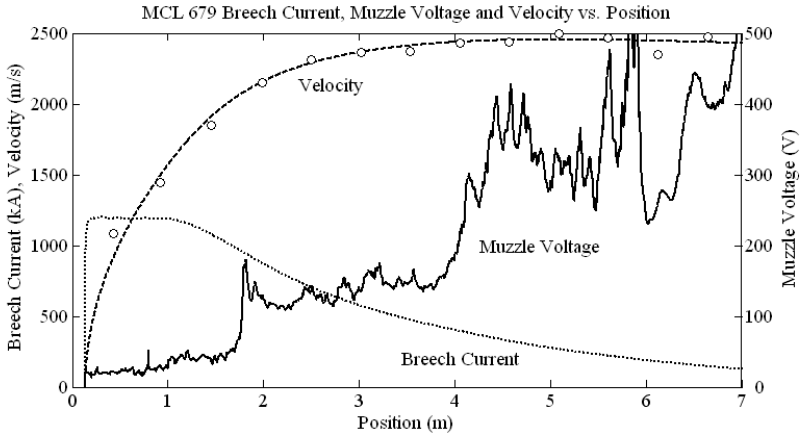

Figure 4.28. MCL 679 (Zirconium slider) breech current, muzzle voltage and velocity Startup material: 0.25 m (9.8") C15725

MCL 680: The gouging estimate for MACOR® ceramic was estimated to be around 1,300 m/s. Because the velocity at the end of the test cladding in the previous tests was around 1,500 m/s the cladding in this test was started at 0.55 m (21.7") instead of 0.25 m. This provided a velocity range on the cladding of 1,100-1,800 m/s. Figure 4.29 shows the waveforms from the experiment, with transition occurring at 1.68 m (66.1") and 2,020 m/s at 83% of peak current.

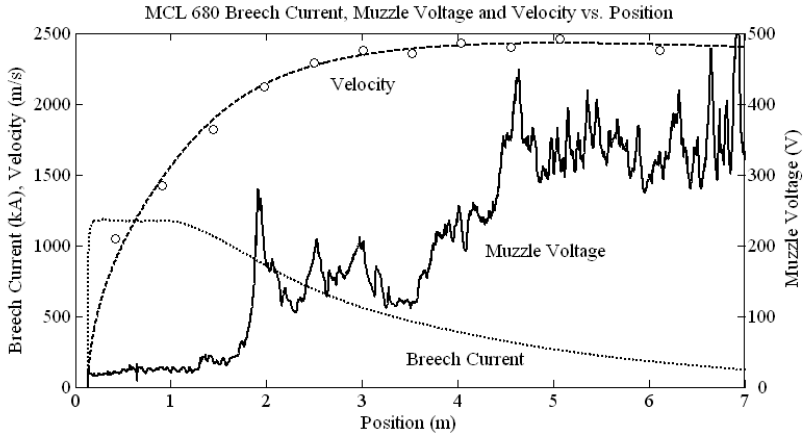

Figure 4.29. MCL 680 (MACOR® slider) breech current, muzzle voltage and velocity Startup material: 0.55 m (21.7") C15725

MCL 682, 681, 684: The waveforms for the AISI 4340 steel sliders with hardness values HRC 27, 35, and 41 (HV 276, 343, 420, respectively) are shown in Figure 4.30 through Figure 4.32. The corresponding gouging estimates for the sliders were 1,150-1,290 m/s, 1,330-1,400 m/s, and 1,560-1,690 m/s. The same cladding specimen offset was used in these three experiments as the MACOR® test, with transition occurring around 2.0 m (78.7") and 2,100 m/s at 72% of peak current.

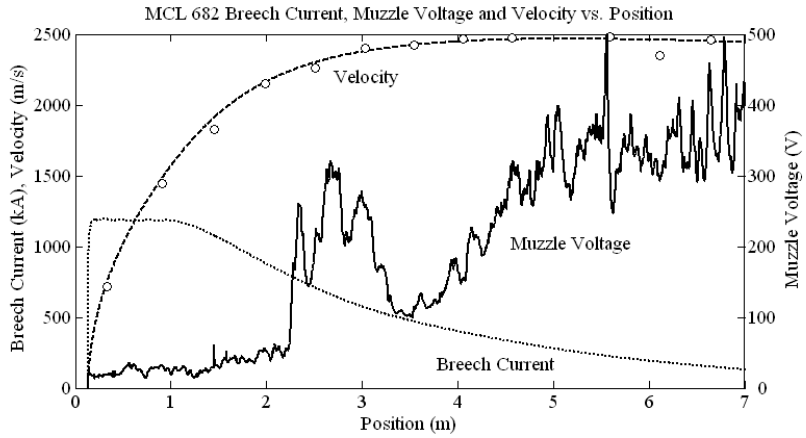

Figure 4.30. MCL 682 (AISI 4340 HRC 27 slider) breech current, muzzle voltage and velocity Startup material: 0.55 m (21.7") C15725

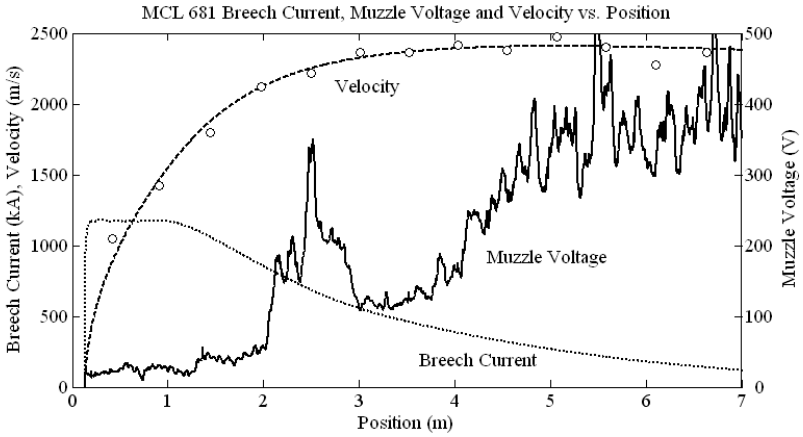

Figure 4.31. MCL 681 (AISI 4340 HRC 35 slider) breech current, muzzle voltage and velocity Startup material: 0.55 m (21.7") C15725

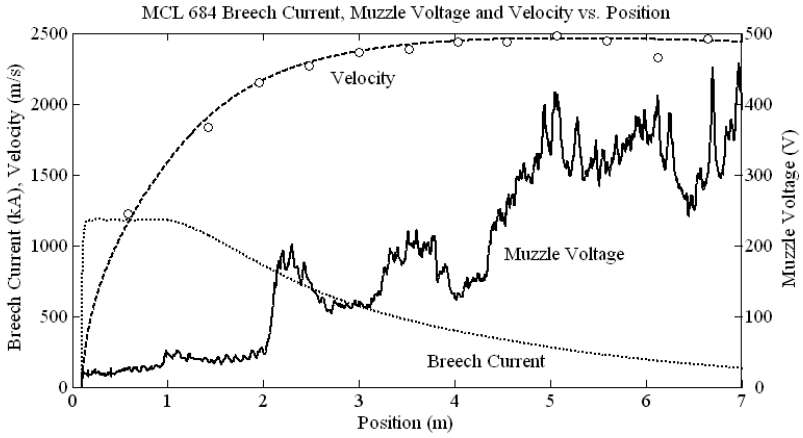

Figure 4.32. MCL 684 (AISI 4340 HRC 41 slider) breech current, muzzle voltage and velocity Startup material: 0.55 m (21.7") C15725

MCL 685-686: The last two slider experiments are shown in Figure 4.33 (AISI 4340 HRC 51) and Figure 4.34 (AISI 4340 HRC 59). The gouging estimates for these two steels were 1,760-2,100 m/s and 2,000-2,700 m/s, respectively. For these tests the specimen cladding was moved farther downstream to start at 0.80 m (31.5"), which would give an estimated velocity range of 1,400-1,970 m/s.

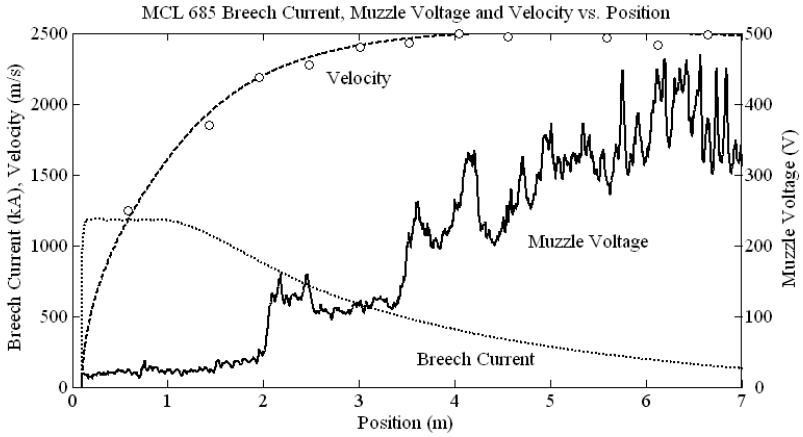

Figure 4.33. MCL 685 (AISI 4340 HRC 51 slider) breech current, muzzle voltage and velocity Startup material: 0.80 m (31.5") C15725

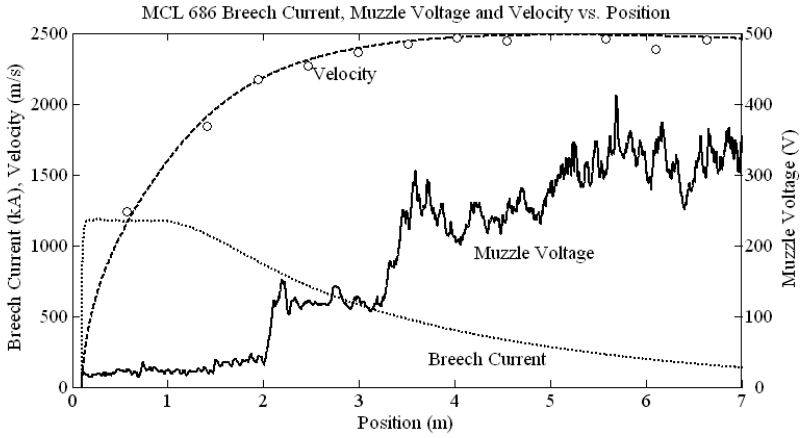

Figure 4.34. MCL 686 (AISI 4340 HRC 59 slider) breech current, muzzle voltage and velocity Startup material: 0.80 m (31.5") C15725

X-ray Analysis: Figure 4.35 through Figure 4.38 show muzzle X-rays from four of the steel slider experiments where X-rays were successfully obtained. These images show slider material that appears to be in good condition, which suggests that "classical" gouging (simultaneous anti-symmetric rail/slider failure) did not take place in the experiments. This is because of the significant amount of rail damage, which is discussed next.

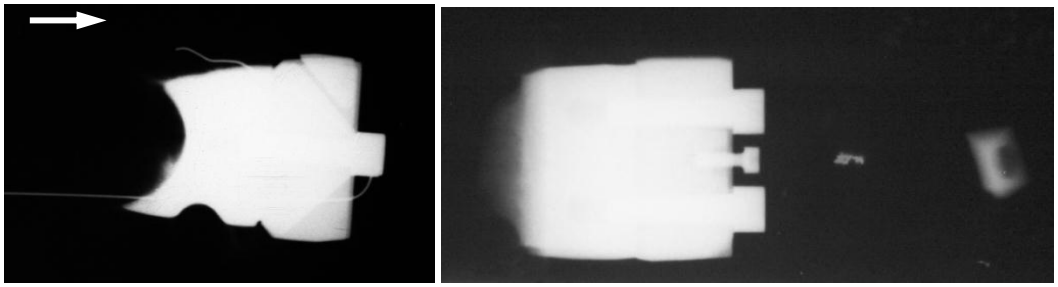

Figure 4.35. Muzzle X-rays for MCL 623 (AISI 4140 HRC 35 slider)

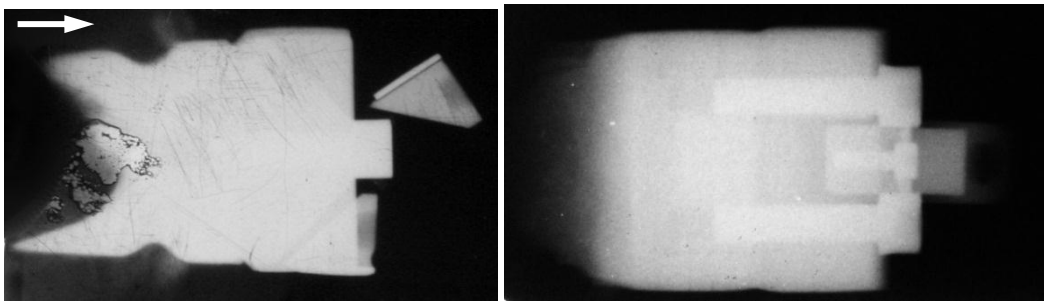

Figure 4.36. Muzzle X-rays for MCL 684 (AISI 4340 HRC 41 slider)

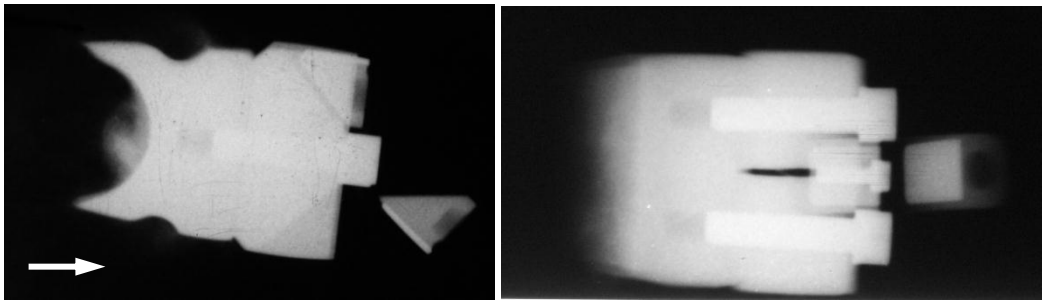

Figure 4.37. Muzzle X-rays for MCL 685 (AISI 4340 HRC 51 slider)

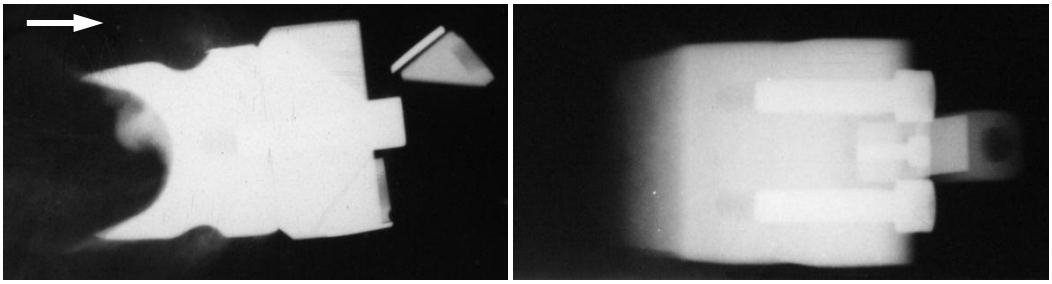

Figure 4.38. Muzzle X-rays for MCL 686 (AISI 4340 HRC 59 slider)

4.2.2 SERIES 2 RAIL PHOTOGRAPHS AND GOUGE LOCATIONS

Photographs of the rail surfaces are shown below. The tape measure in the figures starts at the beginning of the test cladding. Since the test claddings were placed at different locations in the launcher, the measured position must be added to the cladding offset to match the waveforms presented in the previous section. This offset is provided in the individual figure captions. It should also be noted that the armature contact length was 1.2" (30.5 mm), while the slider contact length was 0.4" (10.2 mm). The leading edge of the armature contact was approximately 1.2" (30.5 mm) behind the slider.

Post-shot rails for the AISI 4140 slider (MCL 623) are shown in Figure 4.39. Damage to the rails is first observed around 0.6 m (23.6", 975 m/s) in the form of long galling marks in the armature contact region. At 0.62 m (24.4", 997 m/s), small pits up to 0.5 mm wide are seen in the slider portion of the rail. Damage is not observed on the (-) rail until 0.94 m (37.0", 1,285 m/s) when a long gouge-shaped crater is seen on the (-) rail. However, this crater is approximately 45 mm long, compared to the slider length of 10 mm, and has a relatively constant depth. Gouge craters are usually limited to the approximate length of the longest contacting surface.

The first teardrop shaped gouge crater is seen in the armature contact region on the (+) rail at 0.94 m (37.0", 1,285 m/s). As distance (and velocity) increases the gouges become larger until they span the width of the original armature contact. In some cases, gouges propagate into the slider region. The first teardrop shaped gouge in the slider region, about 4 mm long, is observed around 1.60 m (63.0", 1,745 m/s), followed by a dense cluster of gouges starting at 1.94 m (76.4", 1,937 m/s). As in the case of Cu/Cu gouging, the concurrent galling and gouging damage makes establishing a threshold velocity difficult.

Because of the armature gouges observed in MCL 623, the rest of the slider experiments were performed on partially-electroplated rails, as discussed in the previous chapter. Photographs of the “stripe-electroplated” rails for MCL 681 are shown in Figure 4.40.

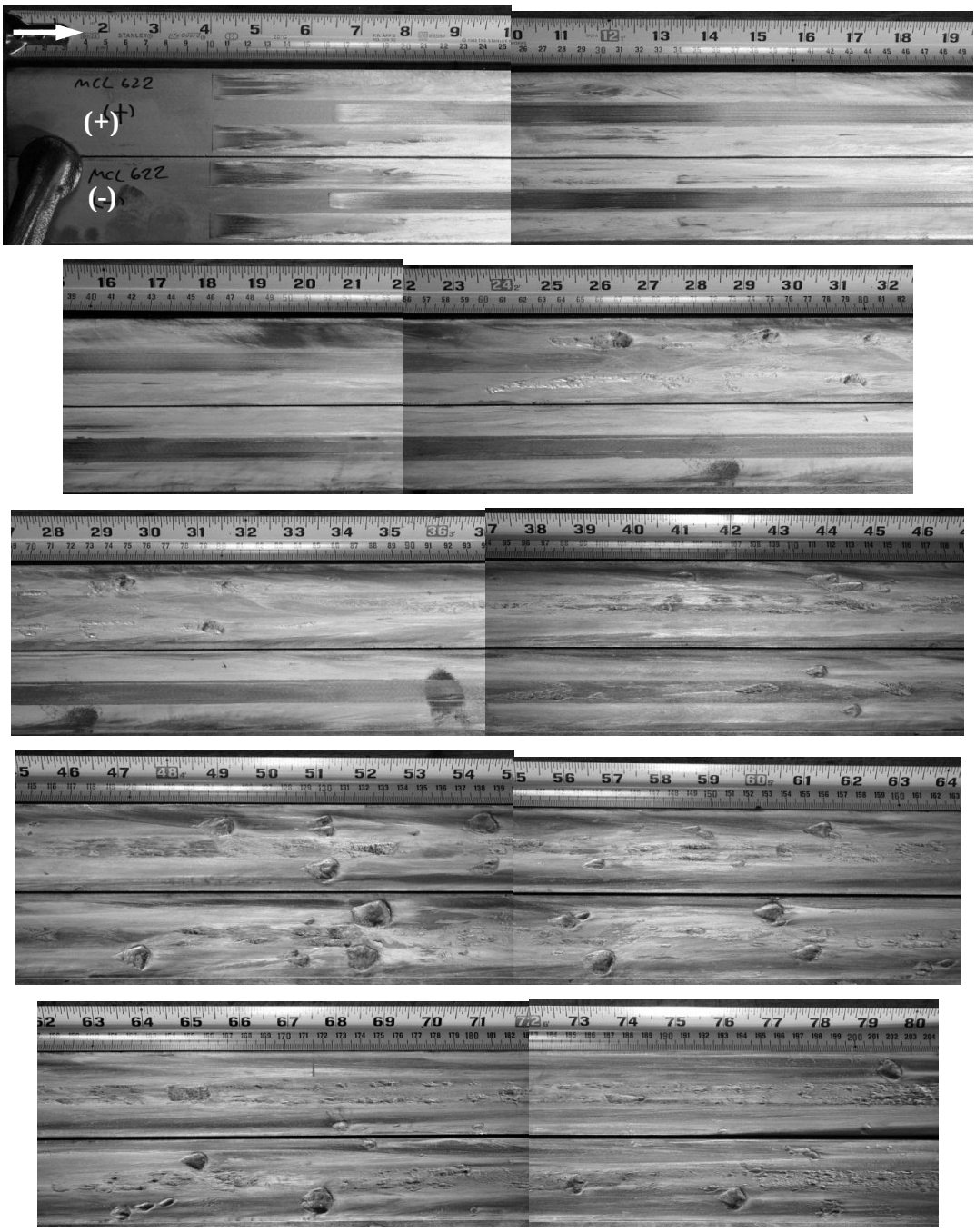

Figure 4.39. MCL 623 rail photographs (AISI 4140 HRC 35 slider, no cladding offset)

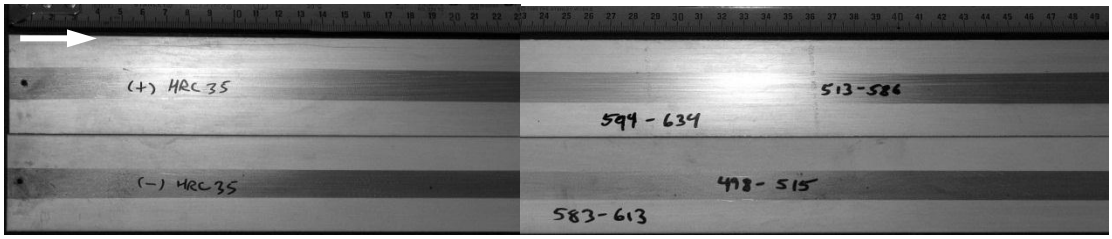

Figure 4.40. Pre-shot stripe-electroplated rails (MCL 681)

The rails from the tantalum slider experiment are shown in Figure 4.41. In the Ta/Cu interface, shallow galling is first observed on the (-) rail at 0.338 m (756 m/s). This is followed by galling in the Al/Cu interface at 0.420 m (899 m/s). Large galling damage is then observed in the Ta/Cu interface starting at 0.510 m 1,033 m/s) which persists for the rest of the cladding. Teardrop shaped slider/rail gouging is seen at 0.900 m (1,476 m/s), though the transition between galling and gouging is difficult to determine. The first teardrop gouge in the Al/Cu interface is at 0.738 m (1,312 m/s). The coating in this experiment was unsuccessful in preventing armature/rail gouging.

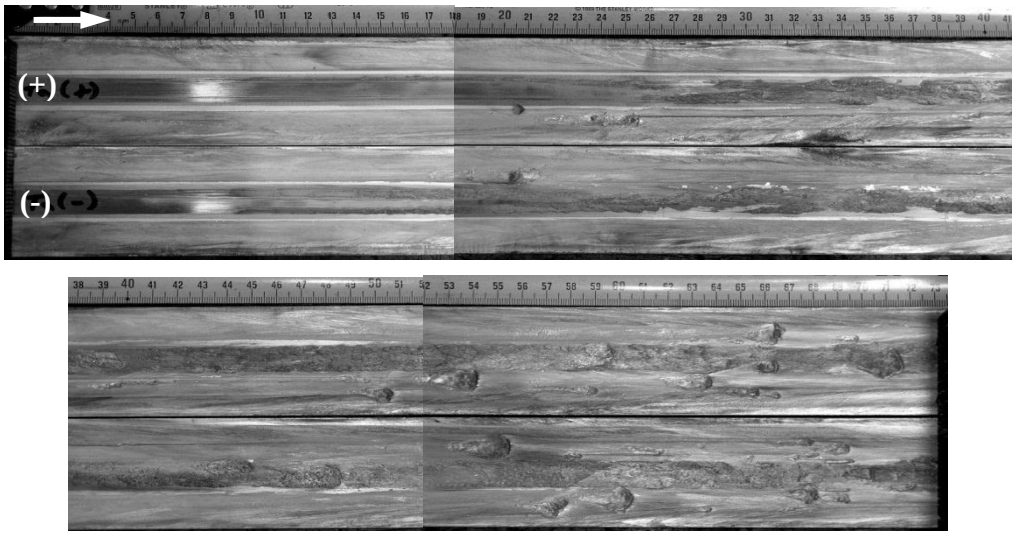

Figure 4.41. MCL 677 rail photographs (Tantalum slider, 0.25 m cladding offset)

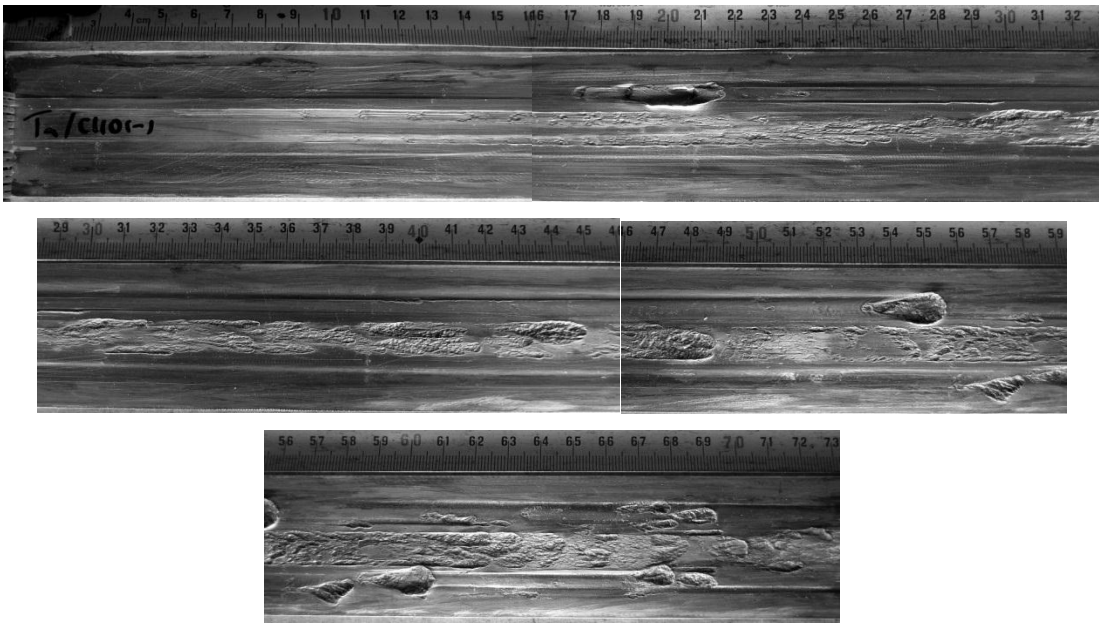

Figure 4.42. MCL 677 etched rail photographs (Tantalum slider, 0.25 m cladding offset)

The rails for the AA1100 sliders are shown in Figure 4.43. The first slider/rail gouge is seen at 0.765 m (1,341 m/s). This is slightly above the predicted gouging range of 900-1,200 m/s. There are no obvious galling marks prior to the first gouge. The first damage to the armature/rail interface is seen at 0.467 m (975 m/s), and consists of a deep galling crater. The first teardrop shaped armature/rail gouge is seen at 0.792 m (1,370 m/s). In both galling and gouging of the armature/rail interface, the damage is restricted to the interior contact edges of the armature.

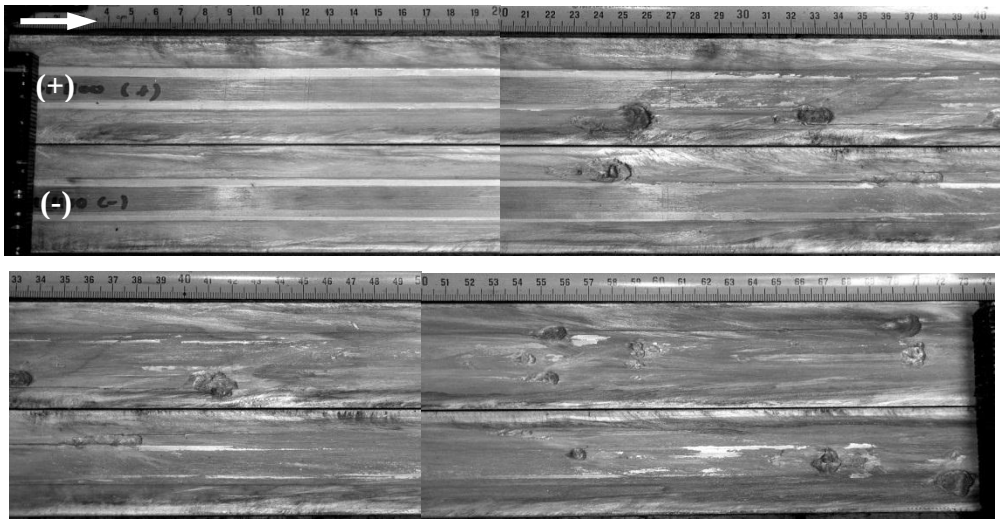

Figure 4.43. MCL 678 rail photographs (AA1100 H14 slider, 0.25 m cladding offset)

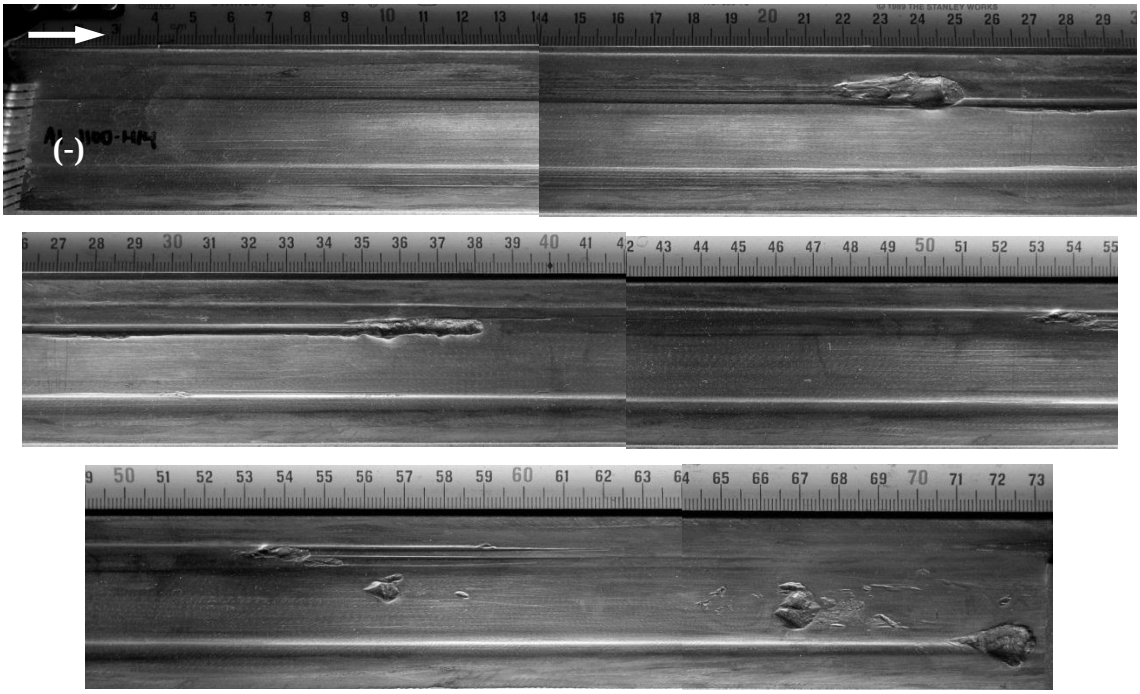

Figure 4.44. MCL 678 etched rail photographs (AA1100 H14 slider, 0.25 m cladding offset)

Photographs of the zirconium slider results (MCL 679) are shown in Figure 4.45. For the Zr/Cu (slider/rail) interface small galling trenches are seen on the (-) rail at 0.35 m (770 m/s). Longer galling marks are then observed on both rails starting around 0.43 m (907 m/s). The first large crater is observed on the (+) rail at 0.59 m (1,133 m/s),

with the first tear-drop gouging crater observed at 0.92 m (1,495 m/s). The predicted gouging velocity of 1,100 m/s best corresponds to the larger galling craters, as opposed to the gouging craters. Galling in the Al/Cu interface is first observed on the (-) rail at 0.42 m (894 m/s), and then on the (+) rail at 0.49 m (1,001 m/s). The first teardrop-shaped gouge crater in the Al/Cu contact is seen on the (-) rail at 0.77 m (1,347 m/s).

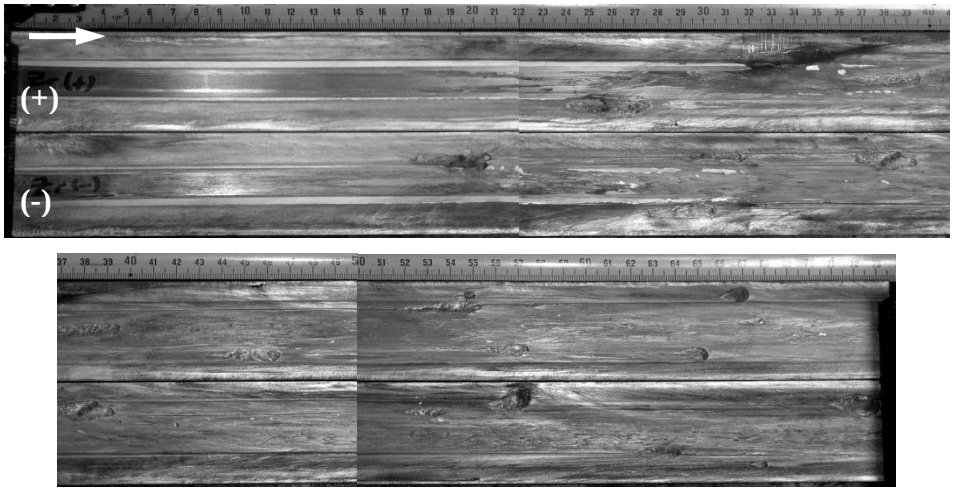

Figure 4.45. MCL 679 rail photographs (Zirconium slider, 0.25 m cladding offset)

The (-) rail from MCL 679 was etched with a solution of sodium hydroxide (described in the previous chapter), with the results shown in Figure 4.46. The plastic deformation suffered by the rail is obvious, with the deformed contact edges coinciding with the initiation of several armature/rail gouges. During the first three experiments on stripe-electroplated rails, gouges were observed in the coated region of the rail. This was not anticipated since prior experiments with coatings were consistent in prevent gouge formation [195]. Since the modified armature contacts discussed in Chapter Three were unable to eliminate armature gouging, the remaining experiments were done without any armature contact modifications to the armatures.

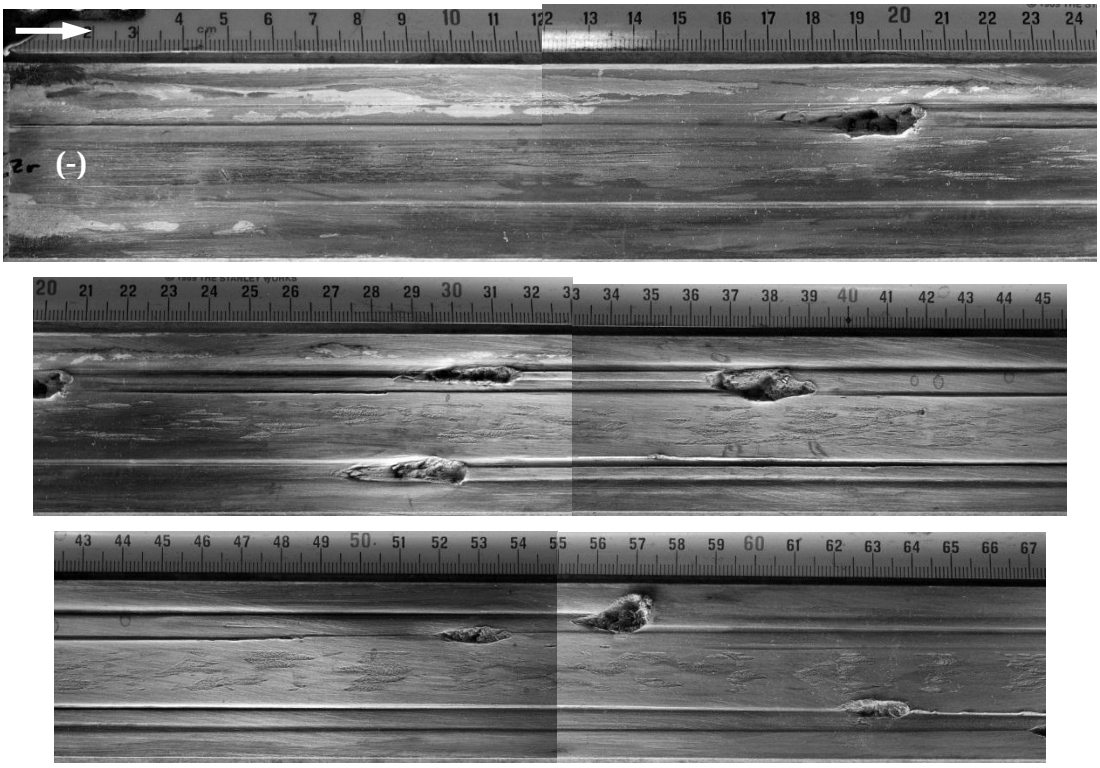

Figure 4.46. MCL 679 etched (-) rail photographs (Zirconium slider, 0.25 m cladding offset)

Figure 4.47 shows photographs from the MACOR® slider experiment (MCL 680). Armature/rail galling is observed just after the start of the cladding at 0.56 m (1,095 m/s), while armature/rail gouging first occurs on the (+) rail at 0.98 m (1,543 m/s). There is no observable galling in the slider/rail interface. Small 1.5 mm-long gouges are first observed on the (+) rail at 0.70 m (1,267 m/s), with medium-sized (5-mm long) gouges starting at 0.75 m (1,316 m/s). A large gouge is later observed at 1.21 m (1,735 m/s). There are no observed slider/rail gouges on the (-) rail. The predicted gouging velocity of 1,300 m/s corresponds well with the observed (+) gouge craters.

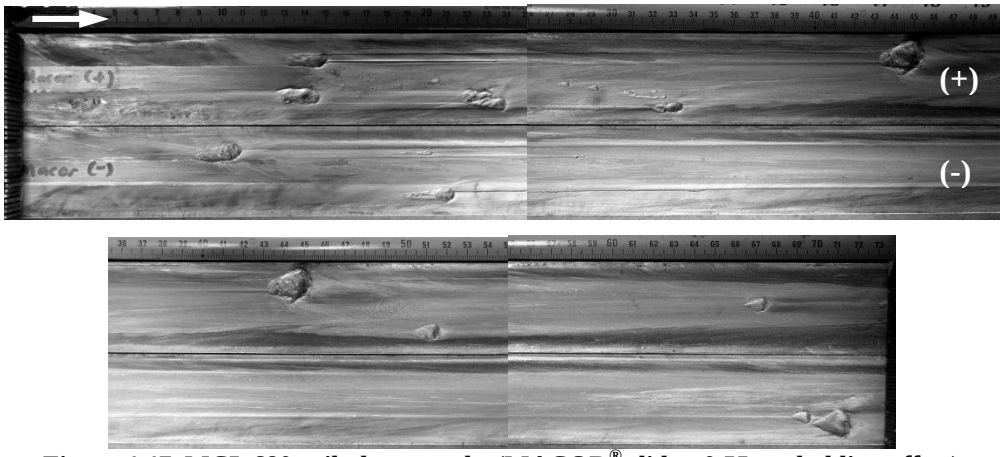

Figure 4.47. MCL 680 rail photographs (MACOR® slider, 0.55 m cladding offset)

Photographs of the etched (-) rail from MCL 680 are shown in Figure 4.48. A distinguishing feature of the galling and gouge craters in the armature/rail contact is that they are often followed by long narrow trenches. This could be the result of heavily strain-hardened rail particles that get embedded into the armature during galling and then act to plastically deform the incoming rail material.

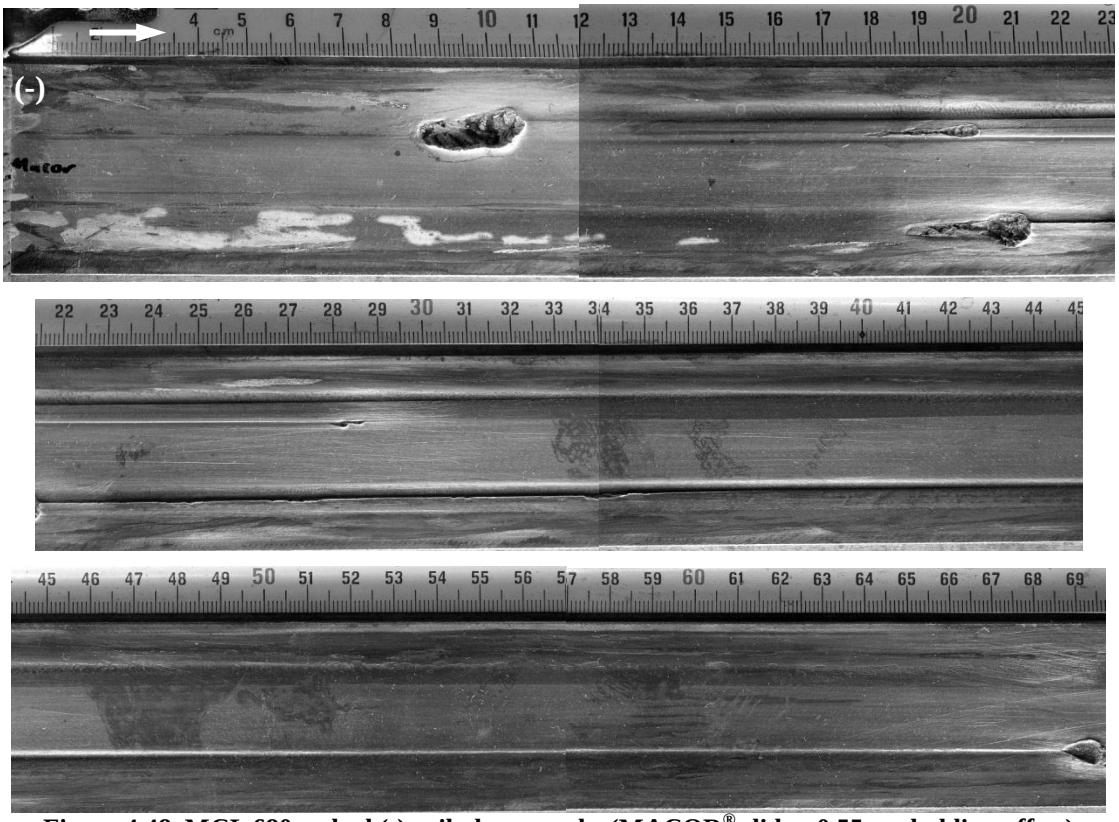

Figure 4.48. MCL 680 etched (-) rail photographs (MACOR® slider, 0.55 m cladding offset)

The as-shot rails for MCL 682 (AISI 4340 HRC 27) are shown in Figure 4.49. The armature/rail interface does not experience any noticeable galling damage. Gouging for the armature/rail interface is observed on the (+) rail at 1.00 m (1,574 m/s). Galling damage for the slider/rail begins at 0.58 m (1,130 m/s) on the (-) rail and 0.65 m (1,213 m/s) on the (+) rail. The first teardrop gouge crater is observed on the (+) rail at 1.13 m (1,684 m/s), though gouge-like craters as discussed previously are seen on the (-) rail at 0.94 m (1,517 m/s). The predicted gouging velocity range of 1,150-1,290 m/s corresponds closely with the onset of galling damage.

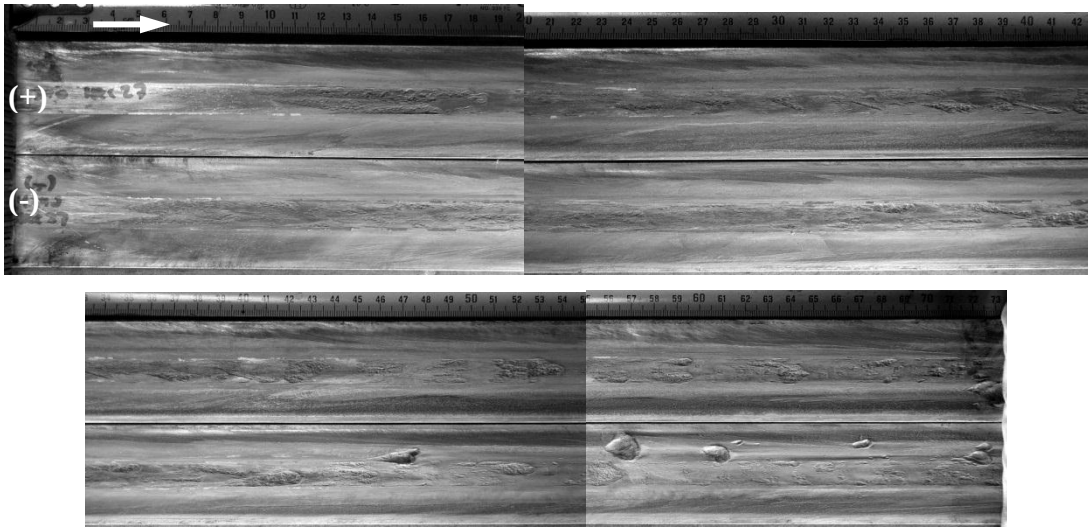

Figure 4.49. MCL 682 rail photographs (AISI 4340 HRC 27 slider, 0.55 m cladding offset)

Figure 4.50 shows the etched (-) rail, which reveals a moderate (~9 mm long) gouge crater in the slider/rail interface at 0.87 m (1,447 m/s). This is then surrounded by long galling/gouging craters than extend for several centimeters.

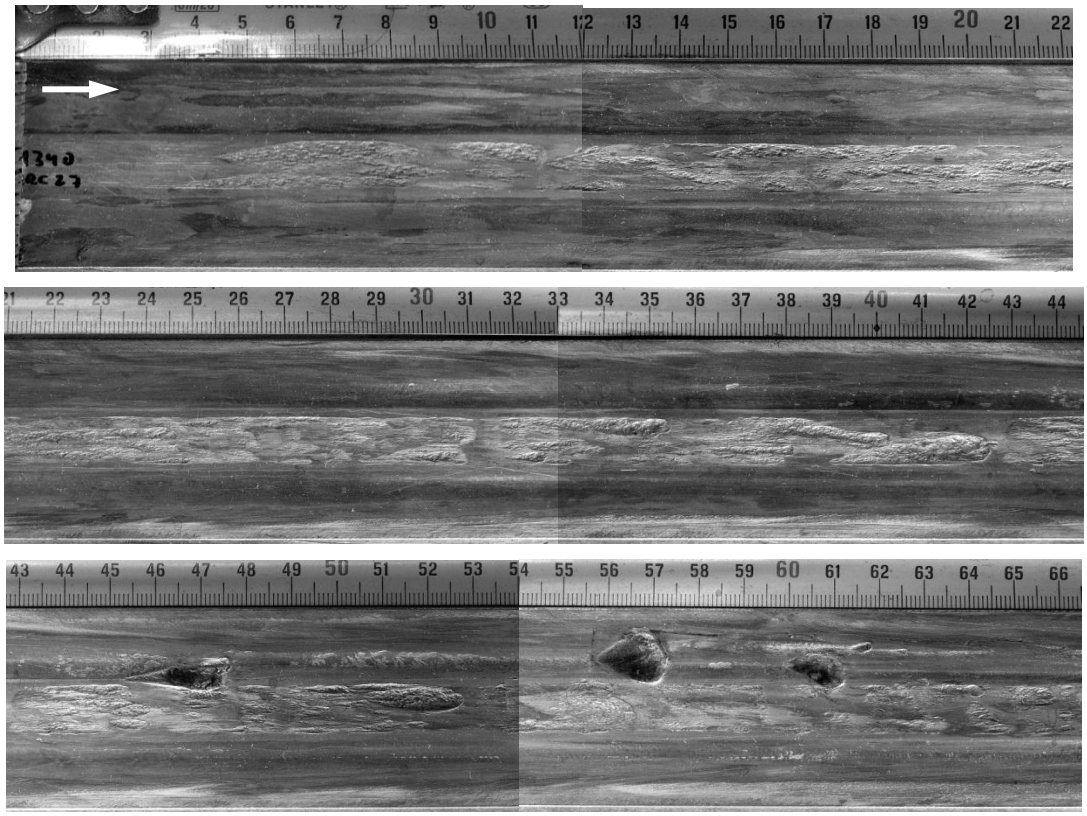

Figure 4.50. MCL 682 etched (-) rail photographs (AISI 4340 HRC 27 slider, 0.55 m cladding offset)

The rails for MCL 681 (AISI 4340 HRC 35 sliders) are shown in Figure 4.51. In this test armature/rail galling is first observed at 0.734 m (1,289 m/s), with gouging becoming apparent at 0.83 m (1,392 m/s). The slider/rail interface shows galling damage starting at the beginning of the rail (0.550 m, 1073 m/s). The slider/rail galling becomes more severe with increasing velocity, though gouging is only observed near the end of the rail at 1.24 m (1,743 m/s). The predicted gouging velocity of 1,330-1,400 m/s lies between distinct galling and gouging behavior.

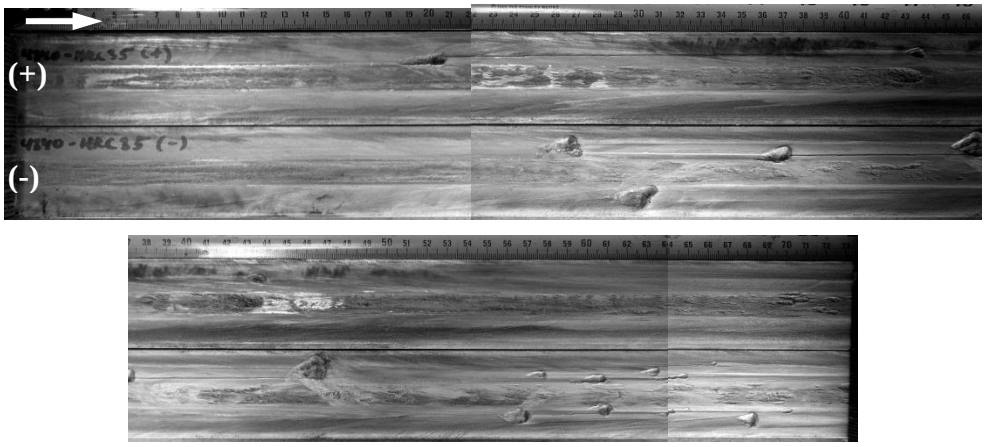

Figure 4.51. MCL 681 rail photographs (AISI 4340 HRC 35 slider, 0.55 m cladding offset)

The etched (-) rail photographs for MCL 681 are shown in Figure 4.52. Once the armature deposits are removed, there appear to be numerous galling craters that exhibit more gouge-like behavior than observed prior to etching. An example of this is shown in Figure 4.53. The first cluster of these appears at 0.83 m (1,391 m/s), and correspond rather well with the predicted gouging velocity of 1,330-1,400 m/s. What distinguishes these from previous galling tracks is that they grow in both width and depth as the armature moves downstream. However, they are not typical gouge craters in that they do not possess the characteristic teardrop shape, and are longer than the slider contact length.

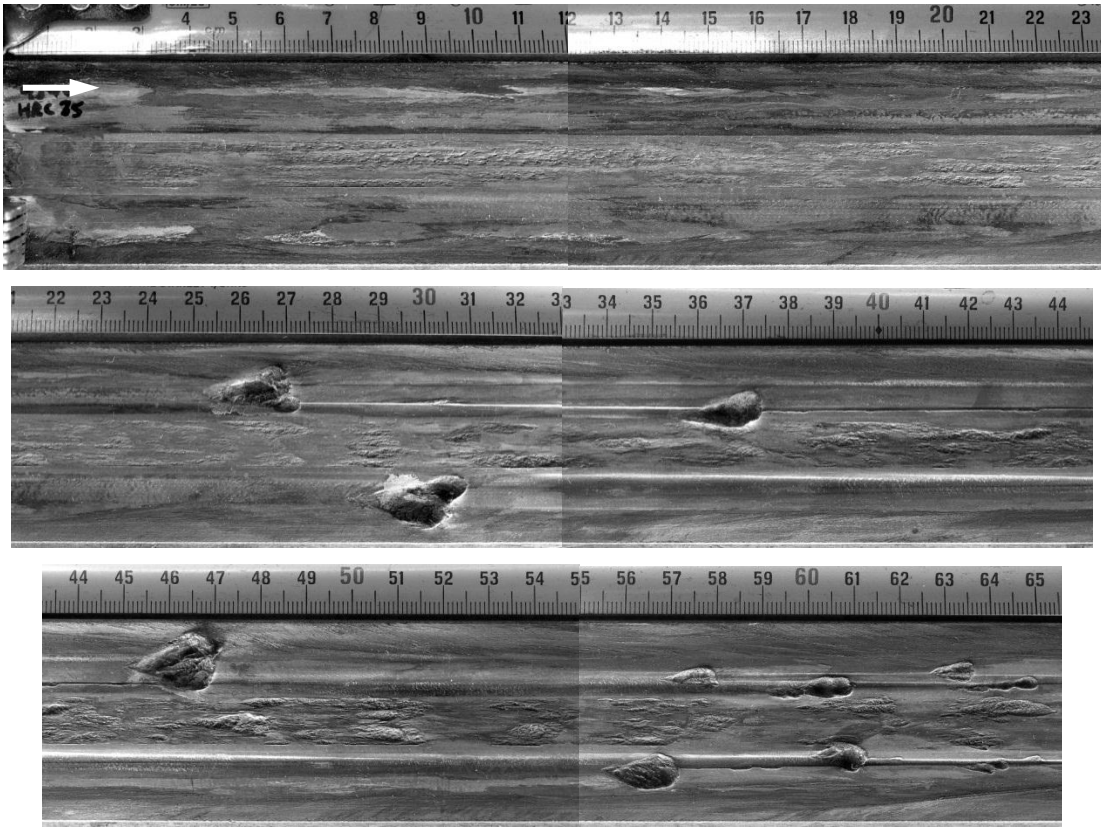

Figure 4.52. MCL 681 etched (-) rail photographs (AISI 4340 HRC 35 slider, 0.55 m cladding offset)

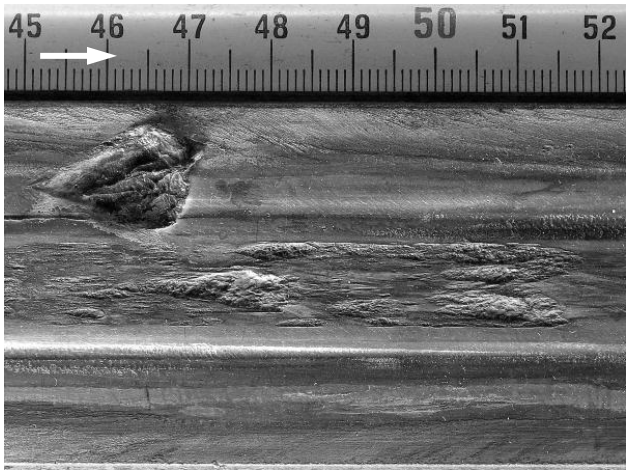

Figure 4.53. Close-up of damage on etched rail from MCL 681 (AISI 4340 HRC 35 slider)

The rails for MCL 684 (AISI 4340 HRC 41) are shown in Figure 4.54. Galling in the armature/rail interface begins on the (-) rail at 0.84 m (1,440 m/s), and on the (+) rail at 0.90 m (1,501 m/s). A traditional gouge crater is only seen in the armature/rail interface towards the end of the cladding at 1.27 m (1,807 m/s). For the slider/rail interface thin galling tracks are seen on the (-) and (+) rails starting around 0.88 m (1,478 m/s).

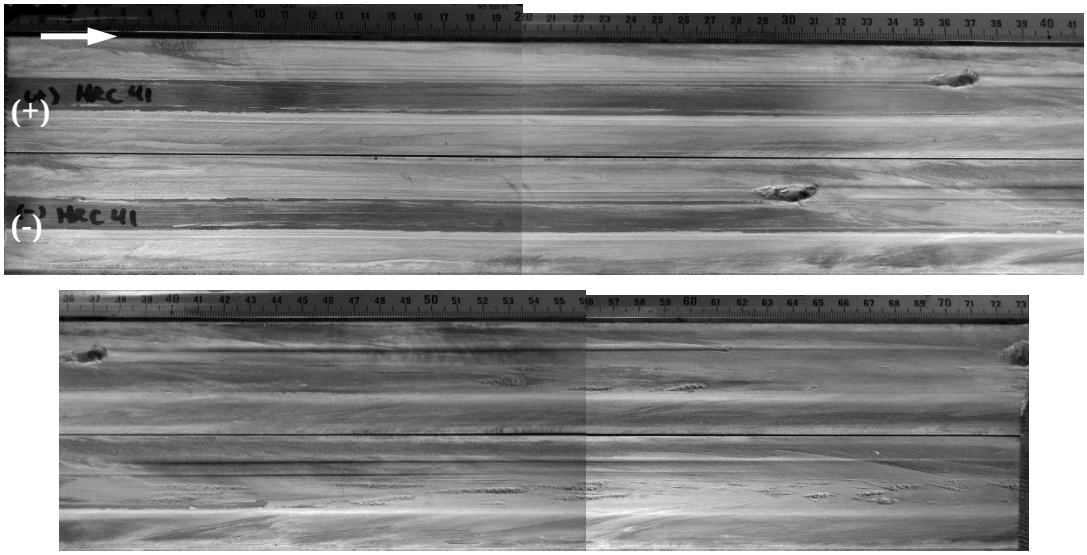

Figure 4.54. MCL 684 rail photographs (AISI 4340 HRC 41 slider, 0.55 m cladding offset)

Etched photographs of the (-) rail are shown in Figure 4.55. No classical gouge craters are observed on either rail in the slider/rail interface. The predicted gouging velocity of 1,560-1,690 m/s again corresponds well with the onset of galling damage.

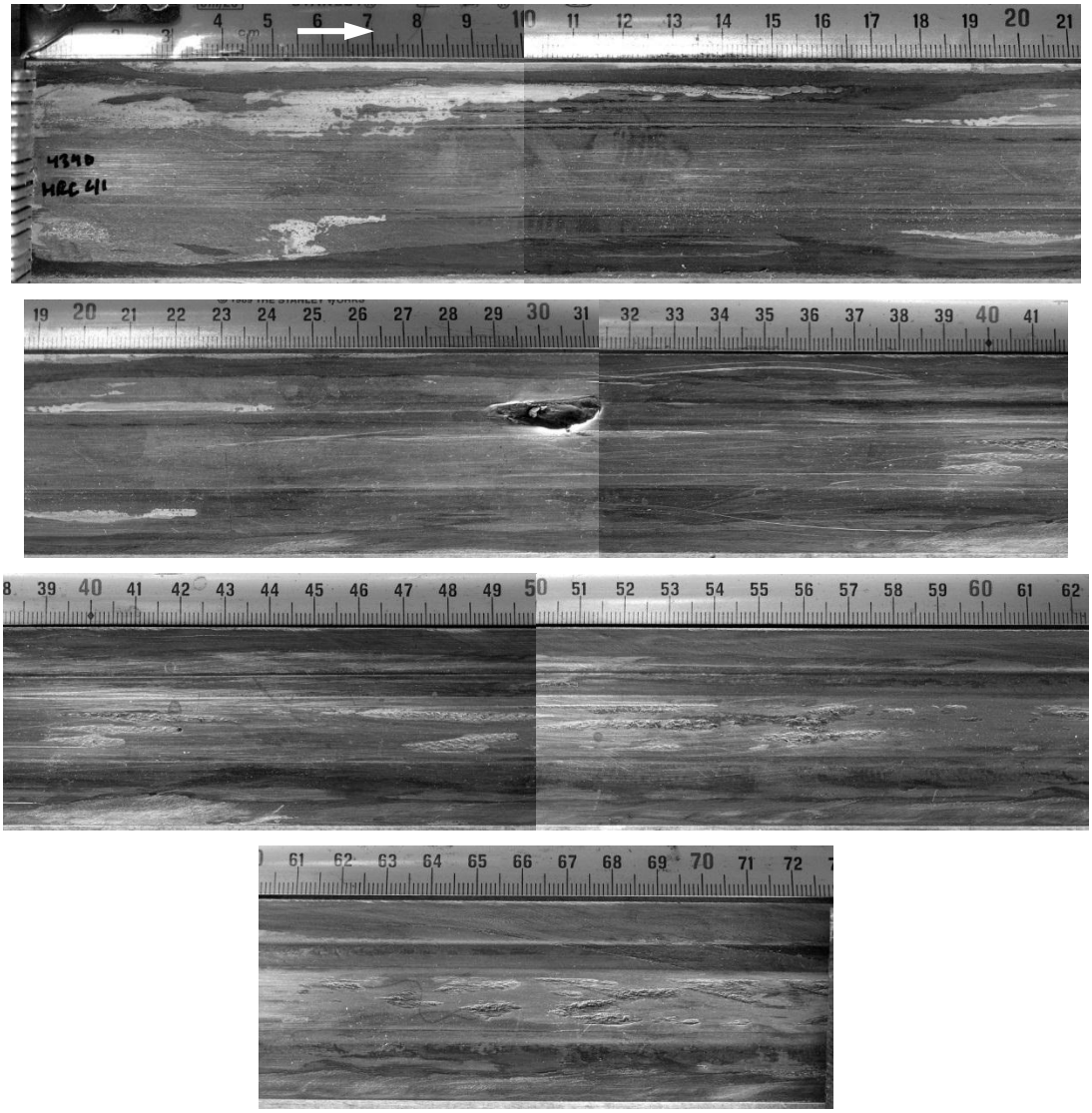

Figure 4.55. MCL 684 etched (-) rail photographs (AISI 4340 HRC 41 slider, 0.55 m cladding offset)

The rails for MCL 685 (AISI 4340 HRC 51 slider) are shown in Figure 4.56. These claddings were moved downstream to start at 0.80 m (1,423 m/s). Gouging at the leading edge of the cladding is observed for all four armature contact interfaces. The first flat-surface gouge is seen on the (+) rail at 0.88 m (1,500 m/s), and on the (-) rail at 0.96 m (1,576 m/s). There are gouges at the edge of the slider/rail interface on the (-) rail at 0.84 m (1,467 m/s) and on the (+) rail at 1.00 m (1,609 m/s). However, it is not clear if

they are a result of Al/Cu or Fe/Cu gouging. Slider/rail galling is observed on the (+) rail at 0.96 m (1,582 m/s). Farther downstream on the (-) a galling track ends in the formation of a classical gouge crater which starts at 1.11 m (1,704 m/s). This latter damage is close to the predicted gouging velocity range of 1,760-2,100 m/s.

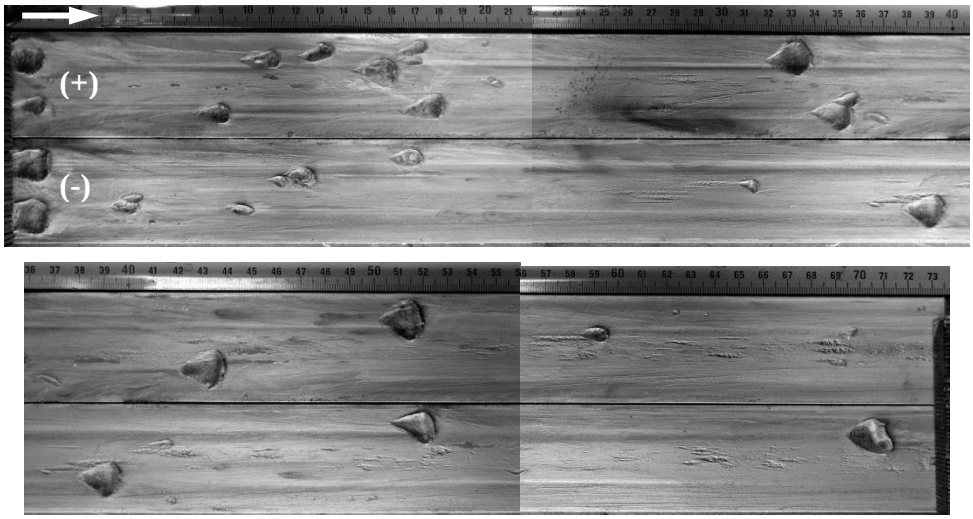

Figure 4.56. MCL 685 rail photographs (AISI 4340 HRC 51 slider, 0.80 m cladding offset)

Etched rail photographs for the (+) rail are shown in Figure 4.57. Shallow galling tracks are seen shortly after the start of the cladding at 0.82 m (1,440 m/s). The first teardrop-shaped crater that does not appear to be armature-generated is seen at 1.34 m (1,879 m/s), which lies in the predicted gouging velocity range of 1,760-2,100 m/s. A cluster of narrow gouge craters are then observed at 1.48 m (1,965 m/s) shortly before the end of the cladding.

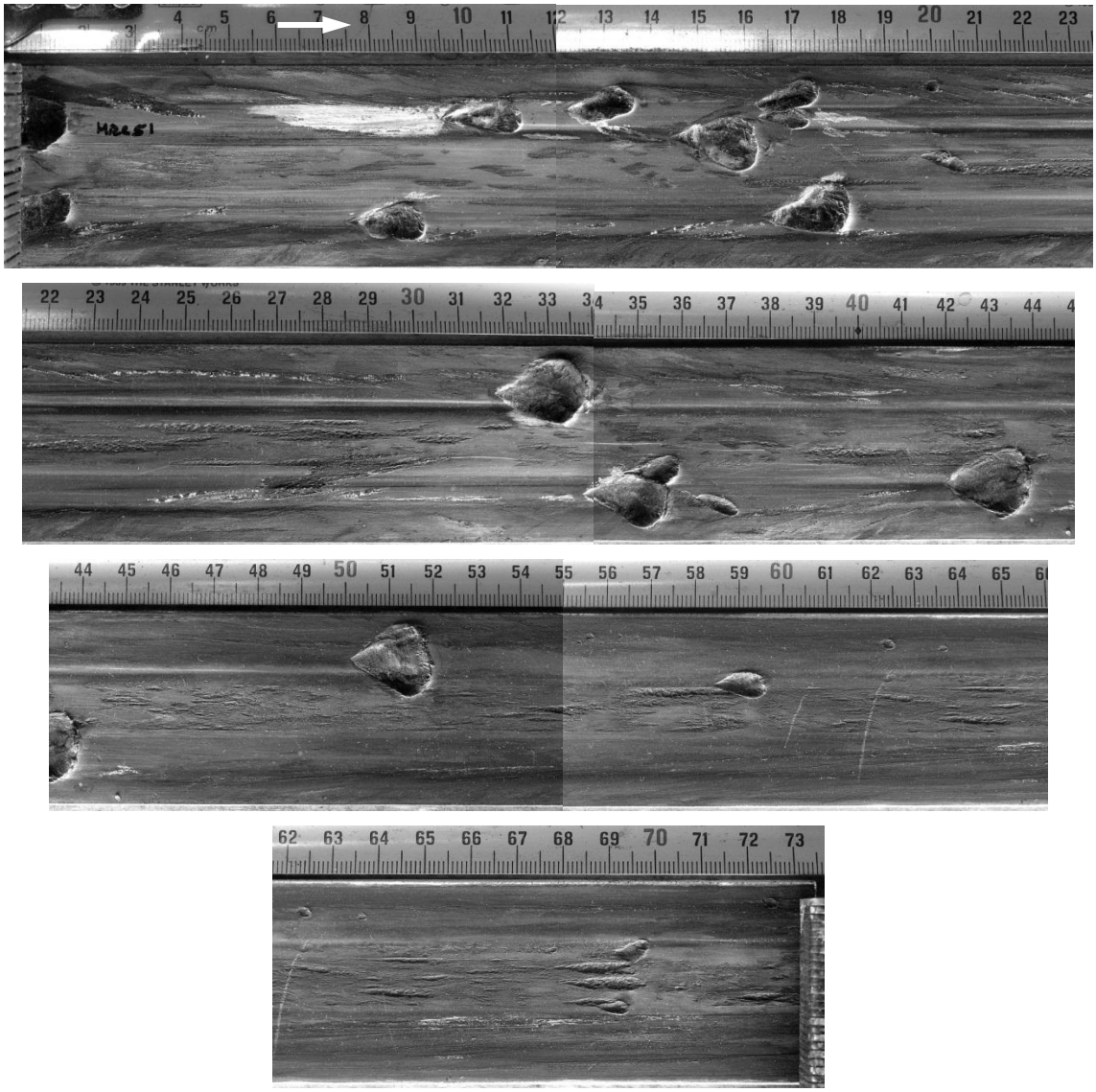

Figure 4.57. MCL 685 etched (-) rail photographs (AISI 4340 HRC 51 slider, 0.80 m cladding offset)

The photographs for the last rails (AISI 4340 HRC 59 sliders) are shown in Figure 4.58. As in the previous test, gouges are triggered on the leading edge of the claddings at 0.80 m (1,413 m/s). The first flat-surface gouges occur on the (+) rail at 0.94 m (1,544 m/s), which fan out into the slider contact region. Slider/rail galling is observed shortly after the cladding at 0.82 m (1,435 m/s). Small gouges are seen in the slider

contact region starting at 1.16 m (1,730 m/s), but again it is not clear if these are caused by the slider or armature. Etched photographs of the (-) rail are shown in Figure 4.59.

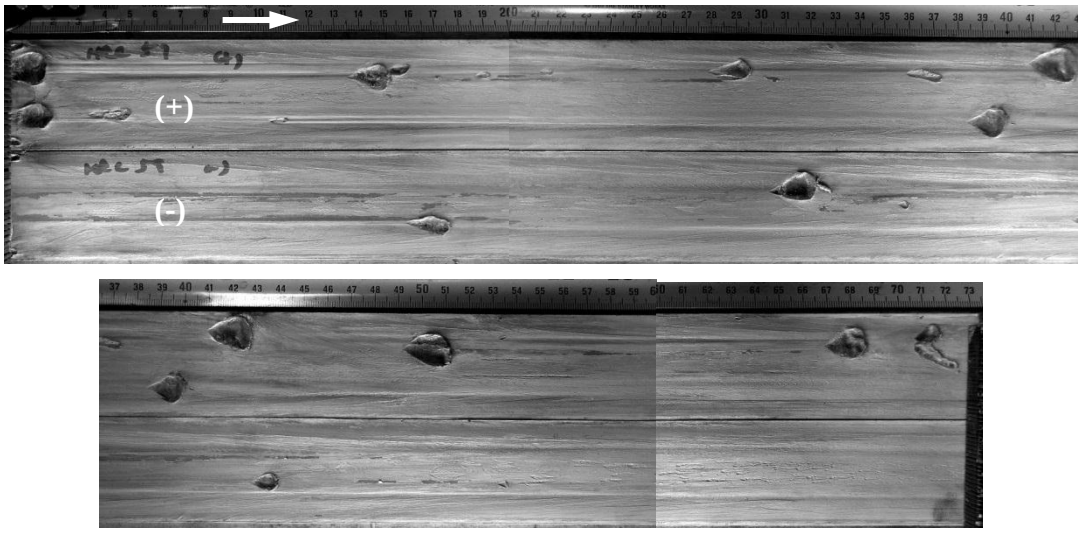

Figure 4.58. MCL 686 rail photographs (AISI 4340 HRC 59 slider, 0.80 m cladding offset)

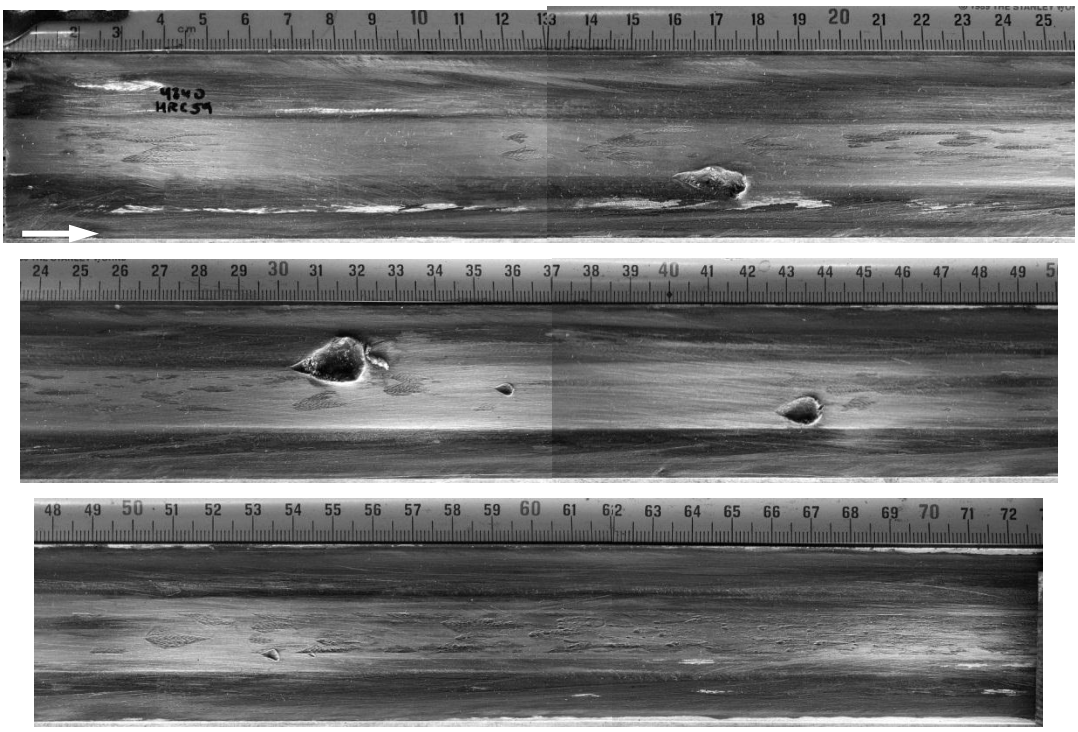

Figure 4.59. MCL 686 etched (-) rail photographs (AISI 4340 HRC 59 slider, 0.80 m cladding offset)

A comparison of the five different AISI 4340 steel sliders is shown in Figure 4.60 (~1,400 m/s) and Figure 4.61 (~1,700 m/s). As slider hardness increases the galling craters become shallow and less frequent. As slider velocity increases the craters become deeper and more frequent.

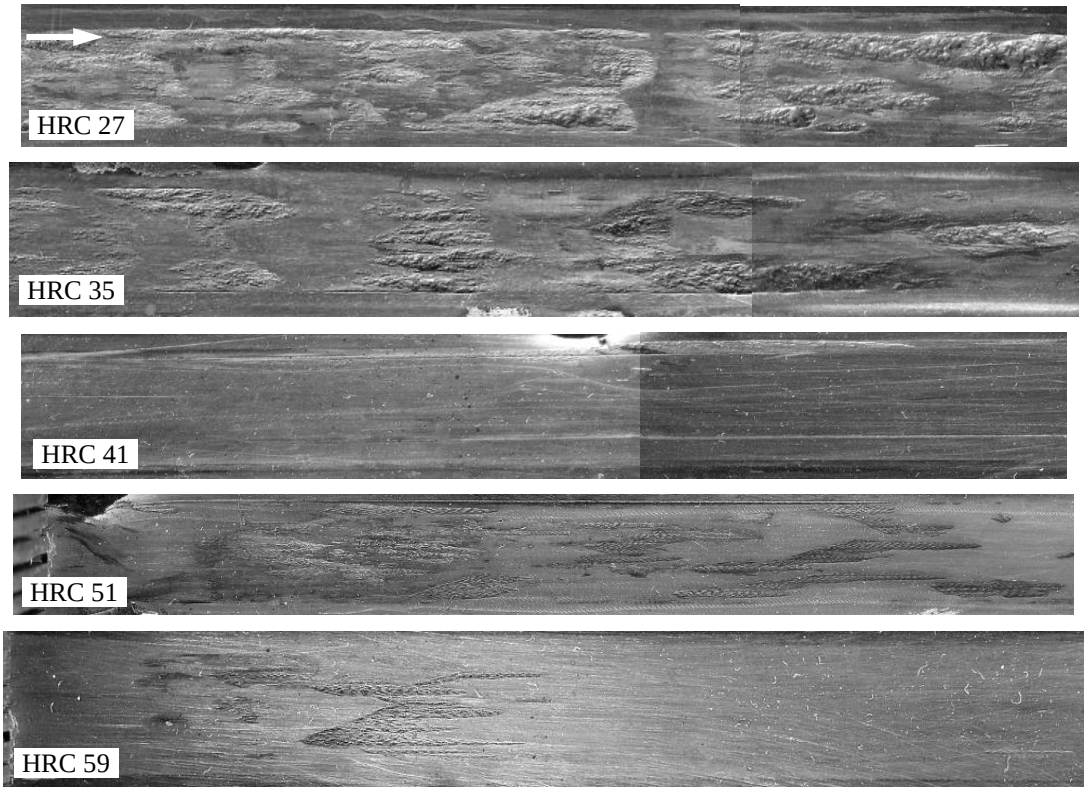

Figure 4.60. Rail damage for different steel slider hardness values 0.8-0.9 m (1,410-1,510 m/s)

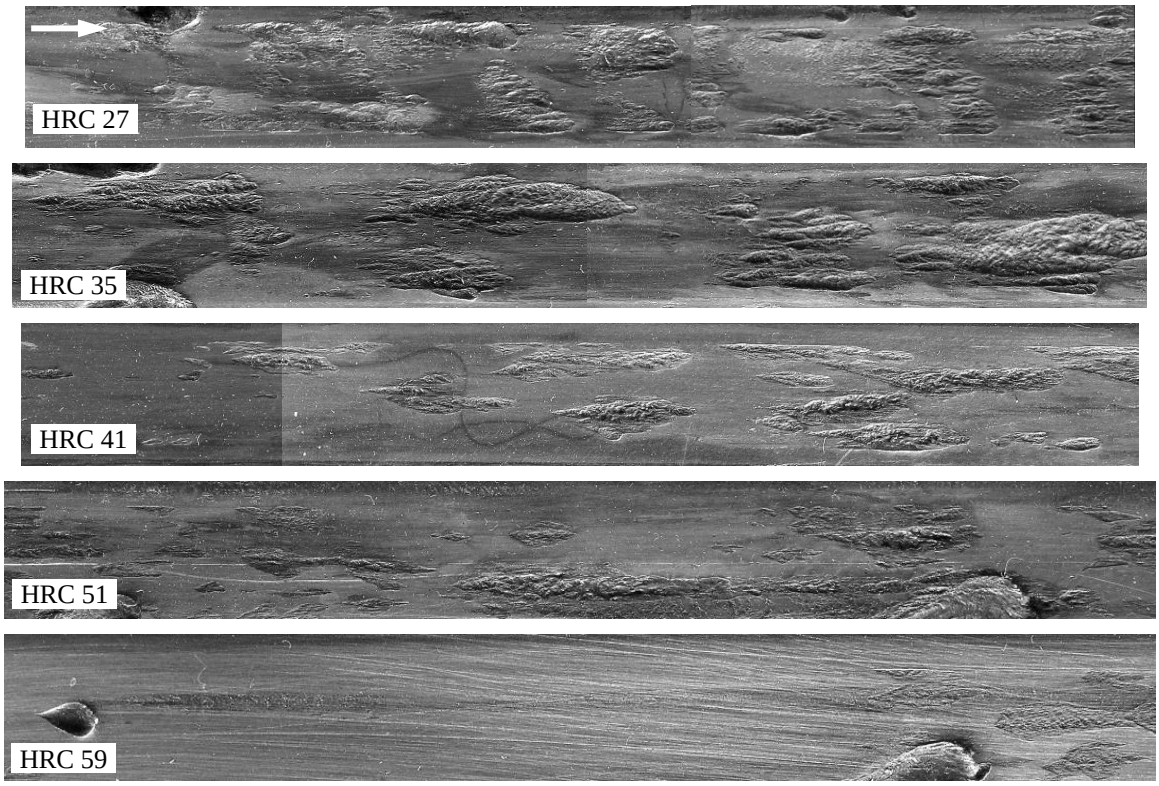

Figure 4.61. Rail damage for different steel slider hardness values 1.15-1.25 m (1,700-1,780 m/s)

Figure 4.62 shows the rail surface from an experiment with the steel slider samples (MCL 623). Laser profilometry was used to map the indicated Al/Cu gouge crater, with the results shown in Figure 4.62 (bottom). This contour is a good example of a typical gouge, with a teardrop shaped crater and raised lip at the downstream end. There is small-scale wave-like character observed throughout the gouge crater, especially near the deepest part of the gouge. From this it is apparent that the initiation site of the gouge takes place on a length-scale of less than half a millimeter. The armature deposits prevent a clearer view of the gouge initiation region.

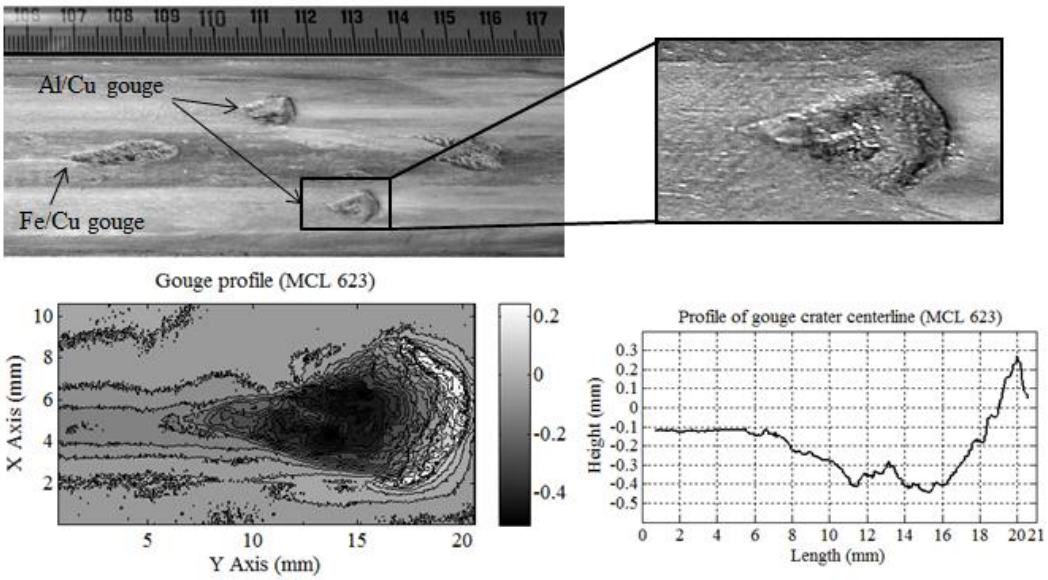

Figure 4.62. Top: photograph of AA7075-T6/C11000 and AISI 4140/C11000 gouges (1,400 m/s sliding velocity). Bottom: laser profilometry contour and centerline profile

4.2.3 SERIES 2 MICROSCOPY

An SEM image of the Al/Cu gouge (shown in Figure 4.62) is shown in Figure 4.63. There is a layer of resolidified aluminum that coats the rail and obscures gouge onset. However, an interesting feature is observed in the region where the gouge is believed to start (gouge crater progression indicated by long arrows): The aluminum layer contains numerous pores (indicated by small arrows) suggesting a much hotter interface compared to the surroundings. It is speculated that the copper surface underneath this region has melted, and that immediately prior to this region there is a small patch of rail surface that is banded as is shown in Figure 4.20.

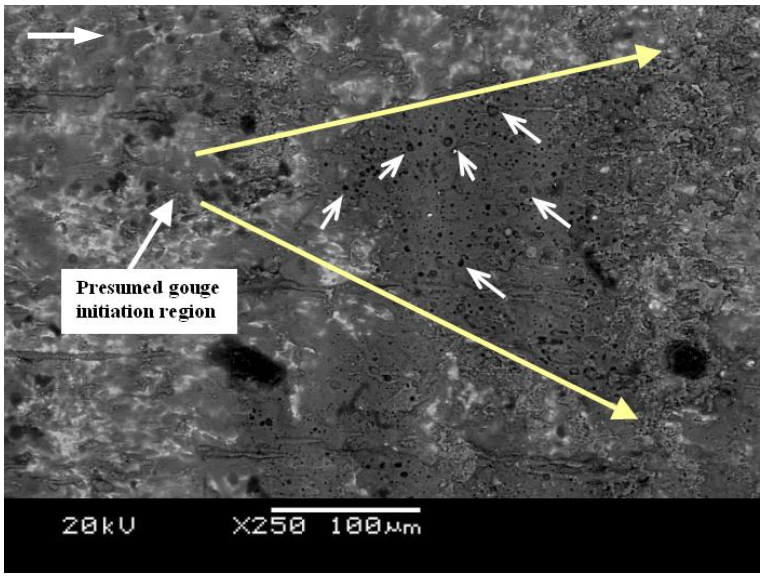

Figure 4.63. Back-scatter electron SEM image of AA7075-T6/C11000 gouge onset at 1,400 m/s

Figure 4.64 shows two SEM images of a gouge created by an AISI 4140 slider against C11000 rails (MCL 623). The left image is the secondary electron image (SEI) while the right is the back-scatter electron images (BEI). The two SEM images show that the slider is transferring material to the rail surface for several mm prior to gouge formation. This is a potentially significant aspect as it relates to the impact theory of gouging.

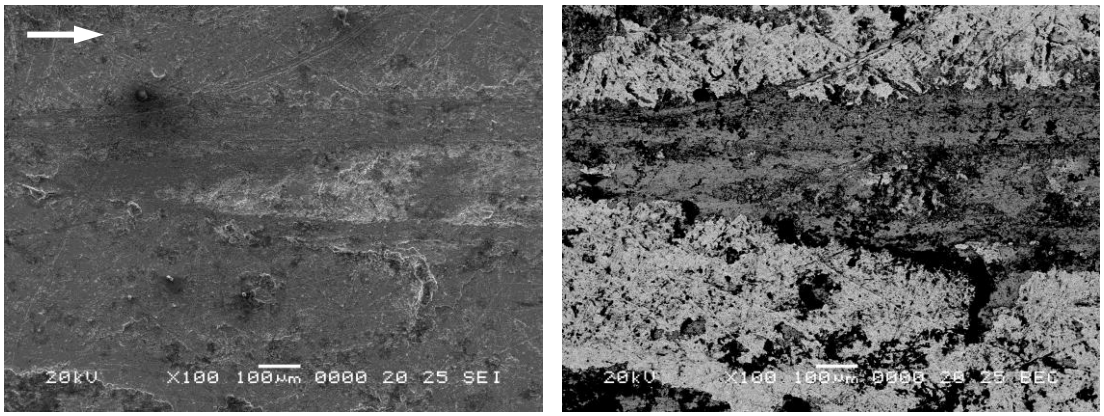

Figure 4.64. SEI (left) and BEI (right) images of gouge initiation for AISI 4140 slider on C11000 rails

The gouge crater is shown again as a false-color image in Figure 4.65. This image was created by mapping the BEI grayscale value associated with copper to orange, the BEI iron grayscale value to gray, and applying the colors to the grayscale SEI. The atomic element / grayscale correlation was confirmed with energy dispersive spectroscopy (EDS).

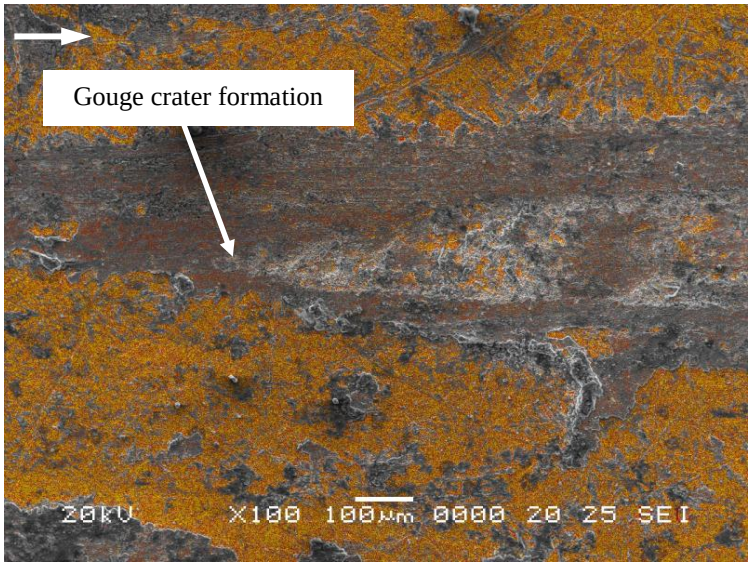

Figure 4.65. False–color SEM image of AISI 4140 gouge on C11000 (1,300 m/s)

Cross-sections were taken of several slider/rail gouges, and examined using optical and SEM microscopy. In this approach the sample was cut several millimeters from the visually determined gouge onset location. The surface was then analyzed using a low-power optical microscope to calculate a distance from the cut surface to the location of gouge onset. The sample was then mounted in Bakelite and ground down by the previously measured amount, which was checked with a micrometer. The error of the observed plane relative to the gouge initiation point is approximately 20 µm.

A gouge for the 4140 slider on C11000 at 1,500 m/s is shown in Figure 4.66. Small ripples are seen on the rail surface at the onset of gouging. Once the gouge crater begins the ripples become larger in both amplitude and wavelength. The surface of the

rail shows evidence of plastic deformation, indicated by the deformed grains and altered texture as a result of etching. This extends to a depth of 20-30 μm.

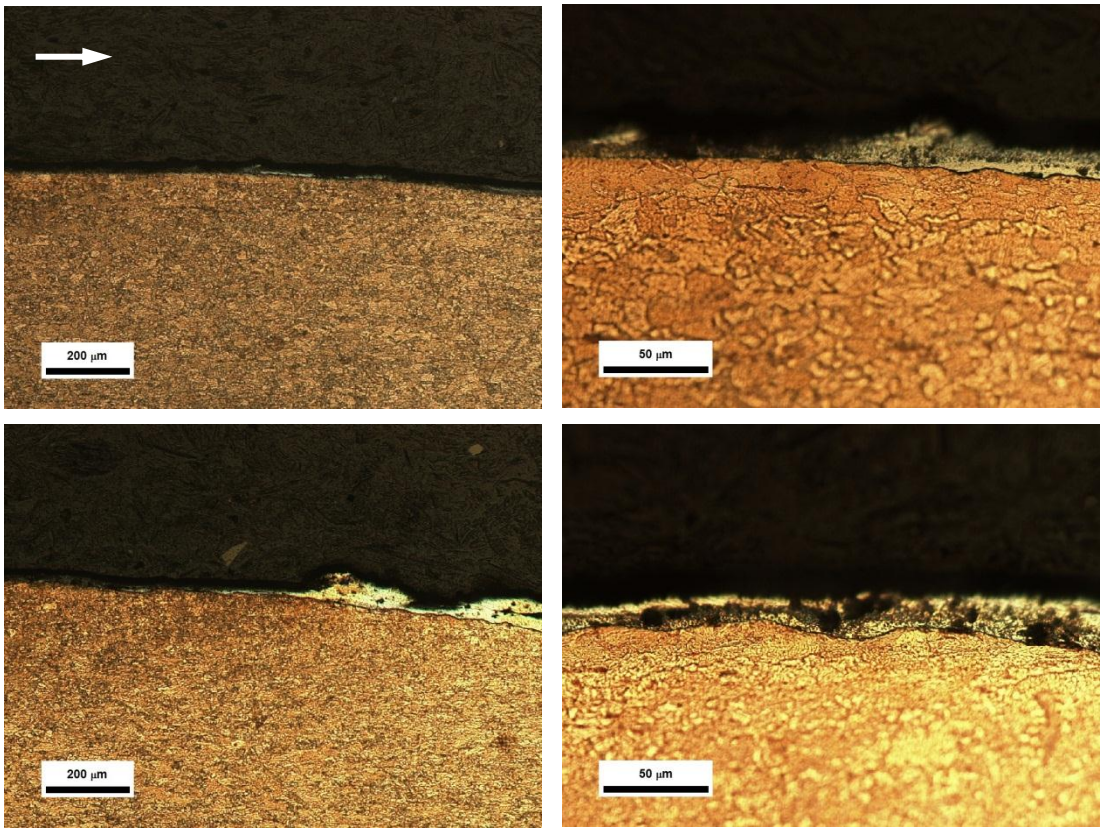

Figure 4.66. AISI 4140 slider on C11000, MCL 623 (1,550 m/s)
top: gouge initiation, bottom: start of gouge crater

As velocity increases the surfaces of the gouge craters become more deformed, showing greater wave character as indicated in Figure 4.67. The depth of significant plastic deformation extends to around 50 μm, with significant deformation of the surface layers including the creation of wave crests and folds.

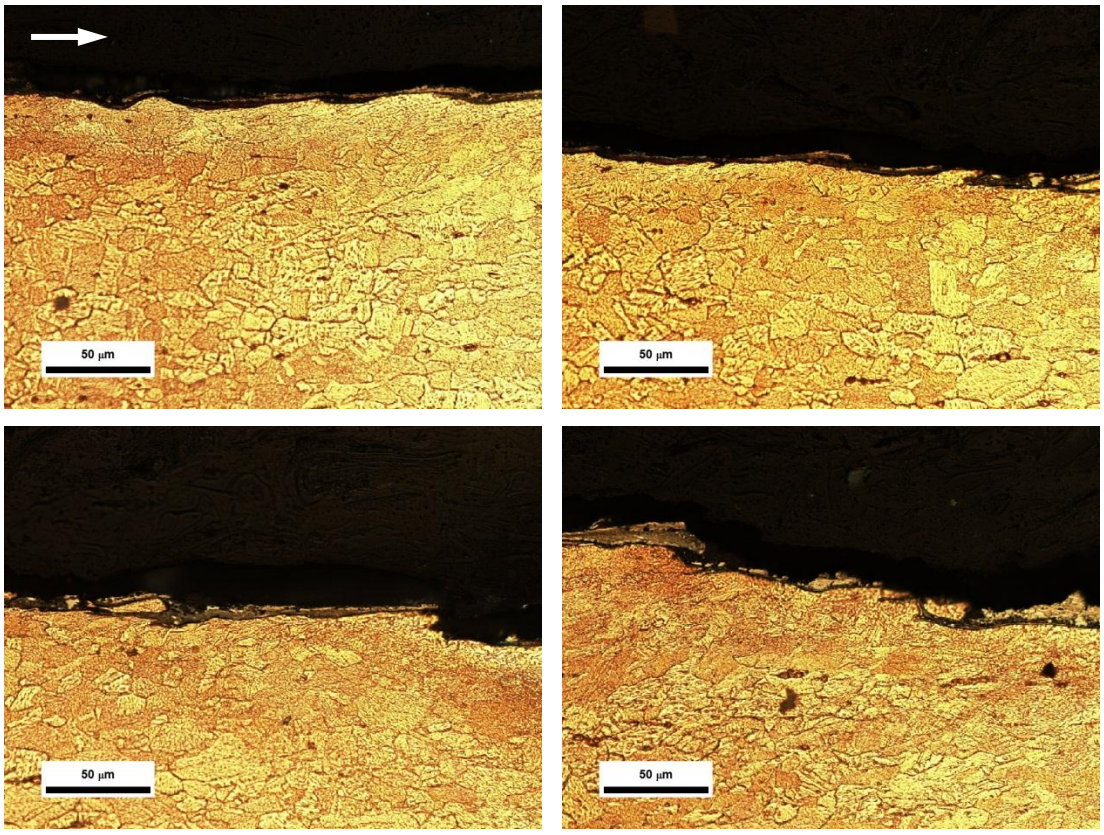

Figure 4.67. AISI 4140 slider on C11000, MCL 623 (1,570 m/s)

The general trend observed with AISI 4140 on C11000 does not change significantly with other slider materials. Cross-section images for Ta/C11000 gouges are shown in Figure 4.68. Again there are small ripples in the rail surface prior to gouge onset, with large ripples and "cresting" waves developing after the gouge forms. A cross-section image of a Zr/C11000 gouge crater is shown in Figure 4.69. In this case, severe plastic deformation that is likely the result of shear band formation results in a platelet of rail material that has become smeared over the original rail surface.

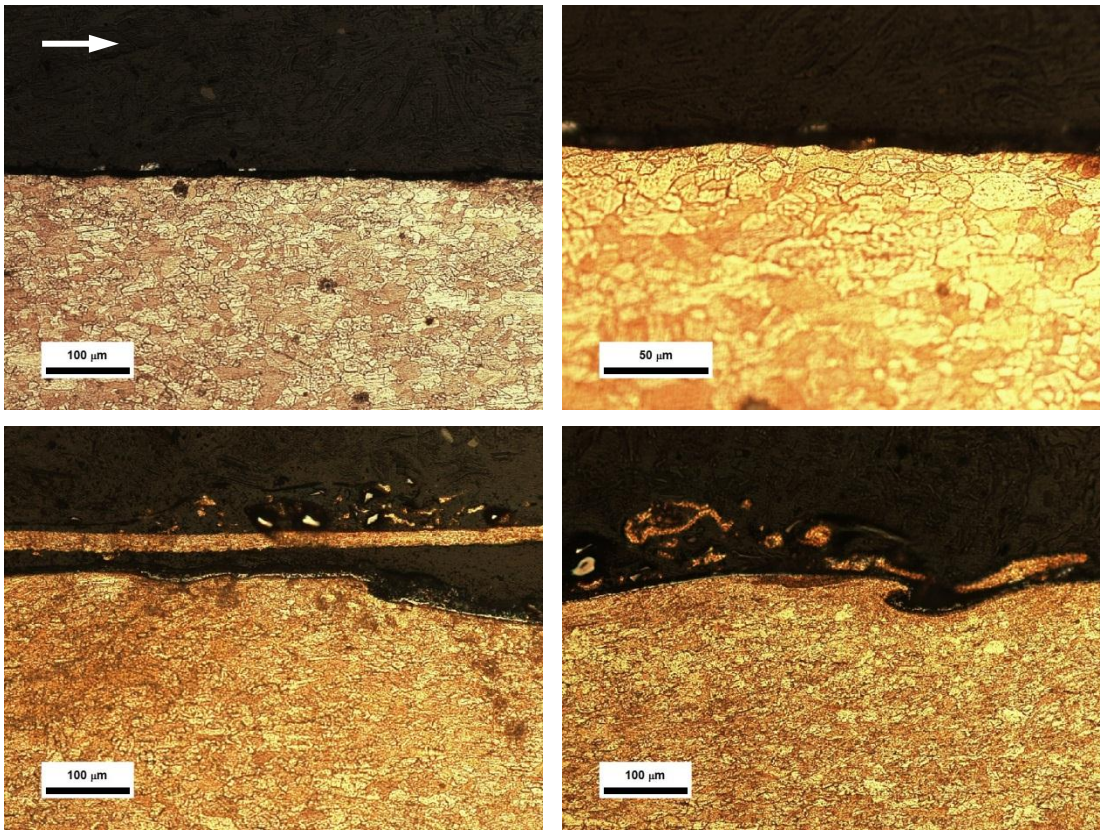

Figure 4.68. Ta slider on C11000, MCL 677 (1,340 m/s)

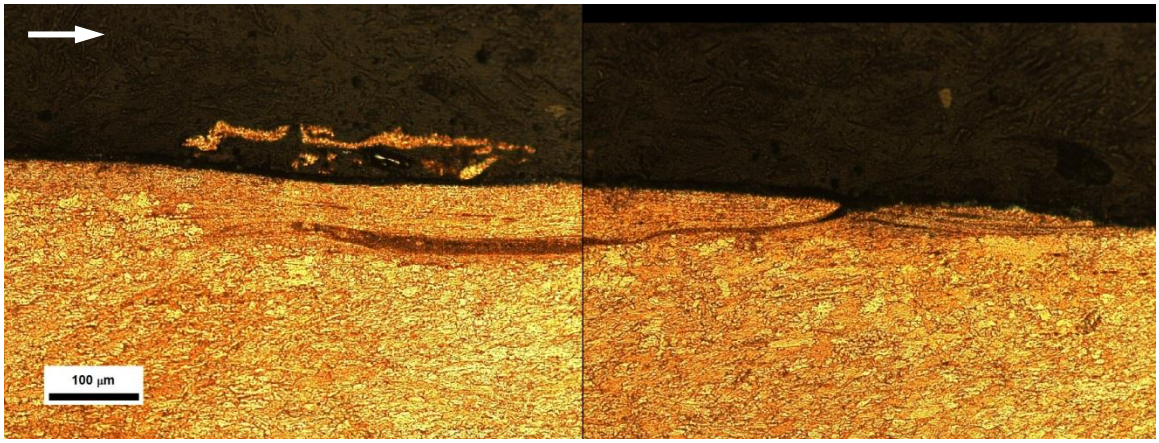

Figure 4.69. Zr Slider on C11000, MCL 679 (1,440 m/s)

4.3 Series 3, Coated Rail Experiments

4.3.1 Series 3 Experimental Overview and Waveforms

The third test series was designed to explore the effects of thin surface coatings on gouging. A total of six tests were conducted using both uncoated and Al-electroplated C15725 rails. The 140-gram launch packages used AA7075-T6 armatures and polycarbonate fore-bodies launched to velocities up to 2,450 m/s on the test claddings. A photograph of a launch package prior to testing is shown in Figure 4.70.

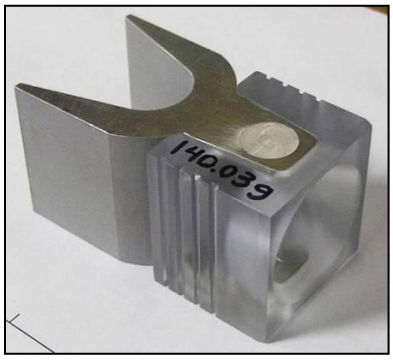

Figure 4.70. Lightweight launch package

A summary of the tests is provided in Table 4.7. Four coatings were tested with an average thickness of 2, 5, 25, and 50 micrometers. Several tests were conducted on 5-micrometer Al to establish repeatability, and verify consistency across two different electroplating batches. High exit currents precluded the use of X-rays since high exit currents damage the muzzle sensor hardware used to trigger the X-rays.

Table 4.7. Series 3 (coated rail) experimental results

MCL #	Slider	Rail	I_{pk} *kA*	I_{exit} *kA*	V_{exit} *m/s*	X_{trans} *m*	V_{trans} *m/s*
628	AA7075-T651	C15725 + 25 μm Al	1,222	239	3,423	1.64	2,463
629	AA7075-T651	C15725 + 50 μm Al	1,209	247	3,415	1.62	2,456
630	AA7075-T651	C15725 + 5 μm Al	1,208	244	3,472	1.57	2,434
650	AA7075-T651	Un-coated C15725		Data unavailable			
651	AA7075-T651	C15725 + 5 μm Al	1,209	201	3,323	1.32	2,189
652	AA7075-T651	C15725 + 5 μm Al	1,220	237	3,452	1.62	2,480
653	AA7075-T651	C15725 + 2 μm Al	1,212	216	3,364	1.57	2,402

The gouging threshold for bare C15725 was observed to be 1,960 m/s. No gouging occurred on any of the coated rails, suggesting that thin (2+ μm) coatings can delay the onset of gouging. A summary of the results is provided in Table 4.8.

Table 4.8. Coated rail gouging results (AA7075-T6 Armature, HV 176 ± 2)

MCL #	Rail	Rail *HV*	Coating *HV*	V_{edge} *m/s*	V_{gouge} *m/s*
628	C15725 + 25 μm Al	169 ± 5	47 ± 2	1,850 ± 11	~
629	C15725 + 50 μm Al	"	"	1,880 ± 175	~
630	C15725 + 5 μm Al	"	"	1,930 ± 179	~
650	Bare C15725	"	~	N/A	1,960 ± 100
651	C15725 + 5 μm Al	"	"	1,900 ± 131	~
652	C15725 + 5 μm Al	"	"	1,910 ± 15	~
653	C15725 + 2 μm Al	"	"	1,920 ± 24	~

Experimental waveforms from the experiments are shown in Figure 4.71 through Figure 4.76. For the coated rails, the first part of the launcher used AA7075-T6 rail claddings, with the 72"-long coated C15725 test claddings beginning around 1 m (39.4"). The transition from AA7075-T6 to C15725 resulted in a reduction in muzzle voltage, which is easily seen in the first two experiments.

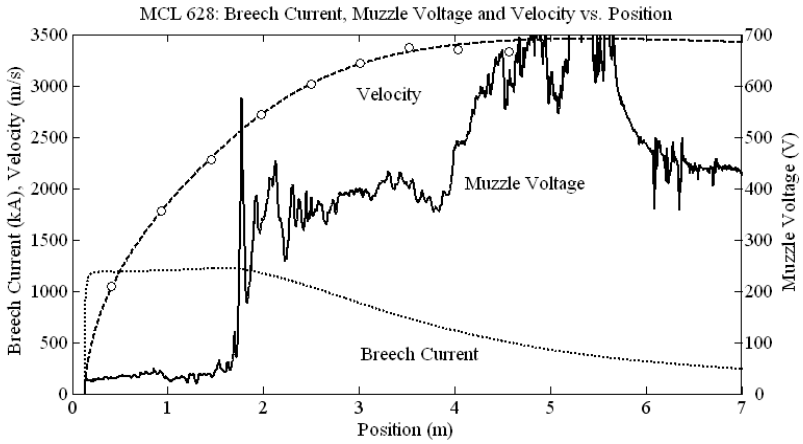

Figure 4.71. MCL 628 breech current, muzzle voltage, and velocity

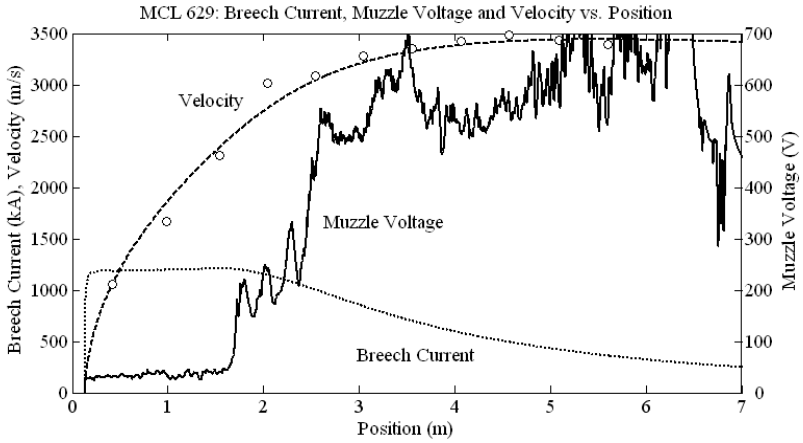

Figure 4.72. MCL 629 breech current, muzzle voltage, and velocity

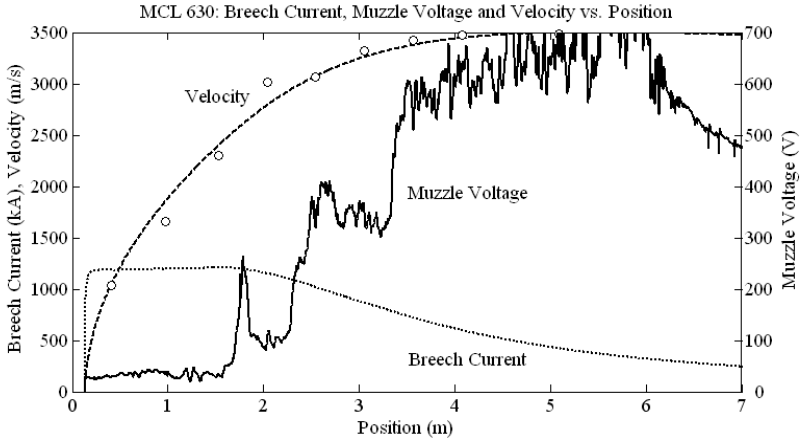

Figure 4.73. MCL 630 breech current, muzzle voltage, and velocity

In MCL 651 and 652 the transition between rail claddings at 1 m resulted in a voltage spike (see Figure 4.74 and Figure 4.75). This is presumed to be due to a small gap or difference in cladding thickness. In the case of a small gap, current flowing into the armature at the leading edge must suddenly move back along the contact face as the leading edge moves into the gap. When the armature leading edge makes contact with the downstream cladding, the current then rapidly changes to where the armature leading edge now makes contact. This rapid change in current flow results in an inductive voltage spike which can be seen in the muzzle voltage trace.

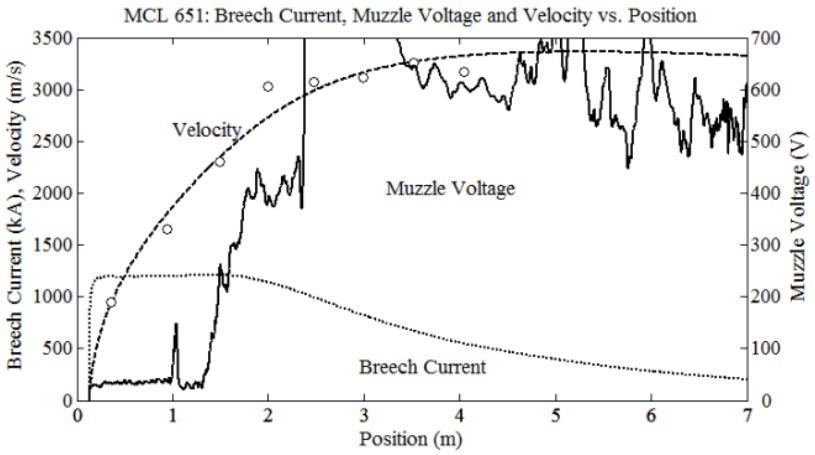

Figure 4.74. MCL 651 breech current, muzzle voltage, and velocity

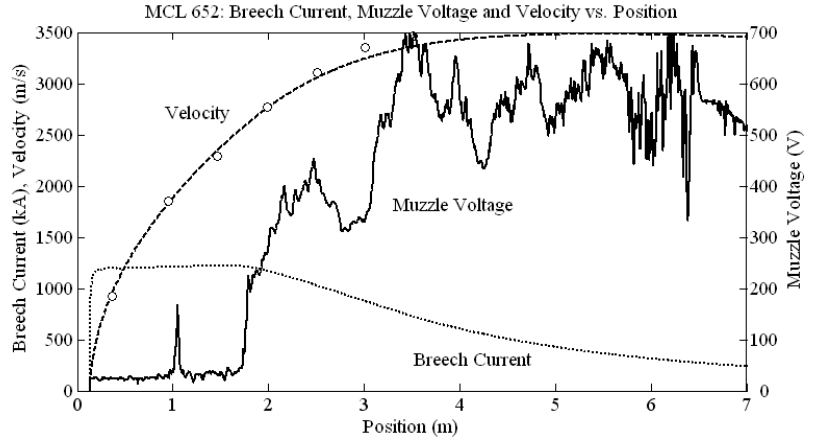

Figure 4.75. MCL 652 breech current, muzzle voltage, and velocity

The muzzle voltage trace in Figure 4.76 shows a sudden drop at around 1.8 meters (70.9", 1.4 ms). After this the muzzle voltage never recovers to the expected behavior as seen in the previous figures. It is not clear what causes this behavior. The transition performance of the armatures was largely unaffected by coating thicknesses. The muzzle voltage was similarly unaffected. This is more easily observed by calculating the effective resistance of the armature/rail voltage drop (muzzle voltage divided by the breech current), shown for three of the coating thicknesses in Figure 4.77.

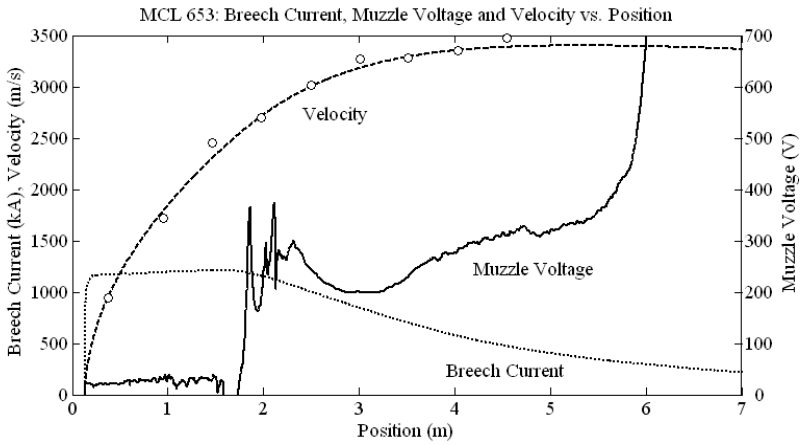

Figure 4.76. MCL 653 breech current, muzzle voltage, and velocity

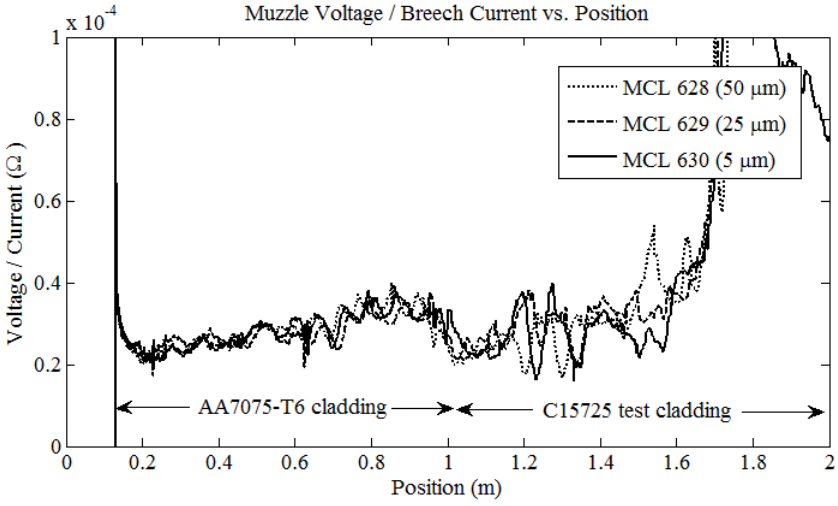

Figure 4.77. Effective resistance of armature/rail for different coatings

4.3.2 SERIES 3 RAIL PHOTOGRAPHS AND GOUGE LOCATIONS

Photographs of the as-shot rails are shown in Figure 4.78 through Figure 4.85. For the coated rails, gouging only occurs at the leading edge of the cladding. There was no gouging on the flat portion of any of the coated rails. The uncoated rail (MCL 650) shows gouge craters starting at 0.99 m (39.0"), or 1,960 m/s.

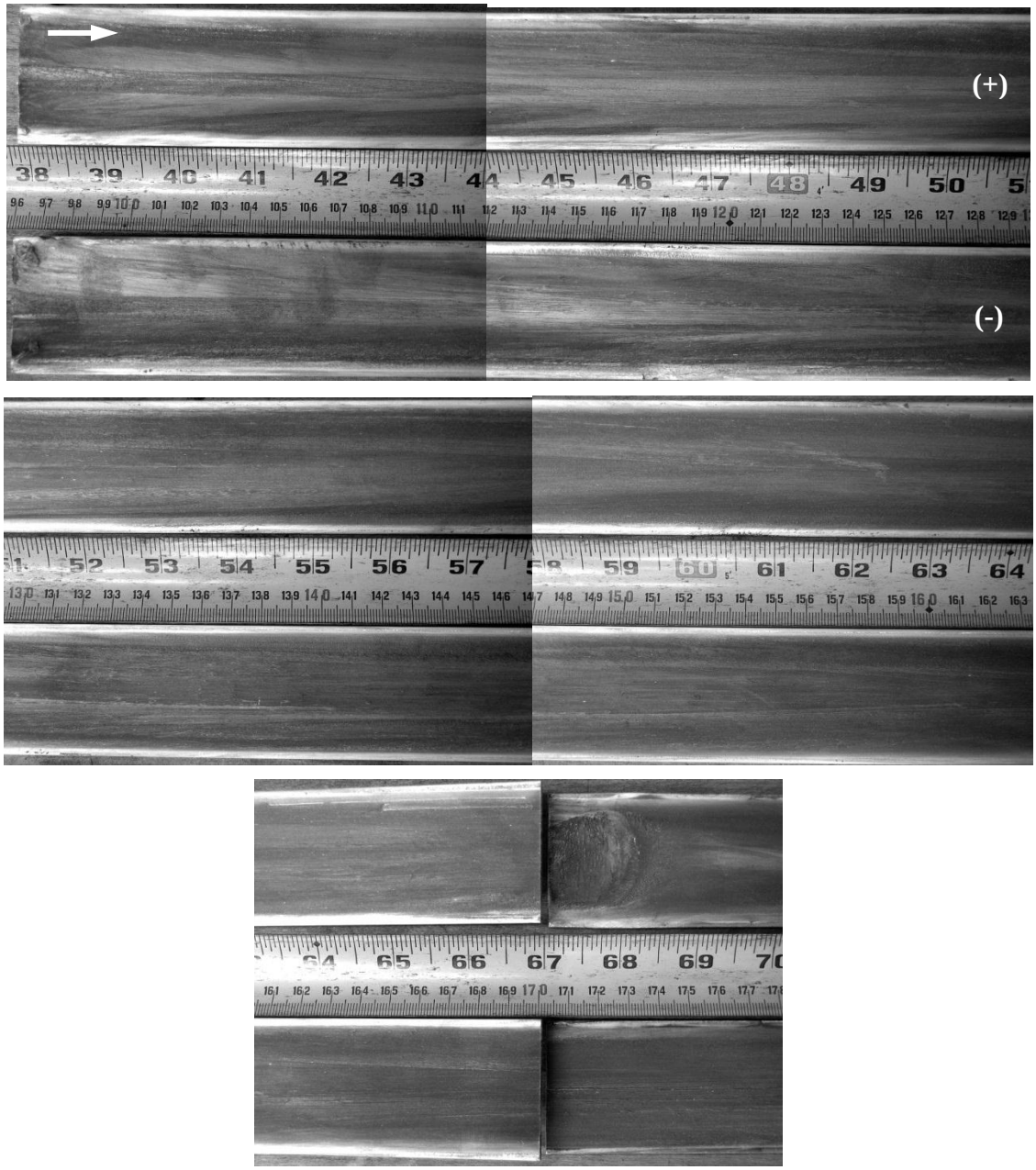

Figure 4.78. MCL 628, 25 µm coated rail photographs

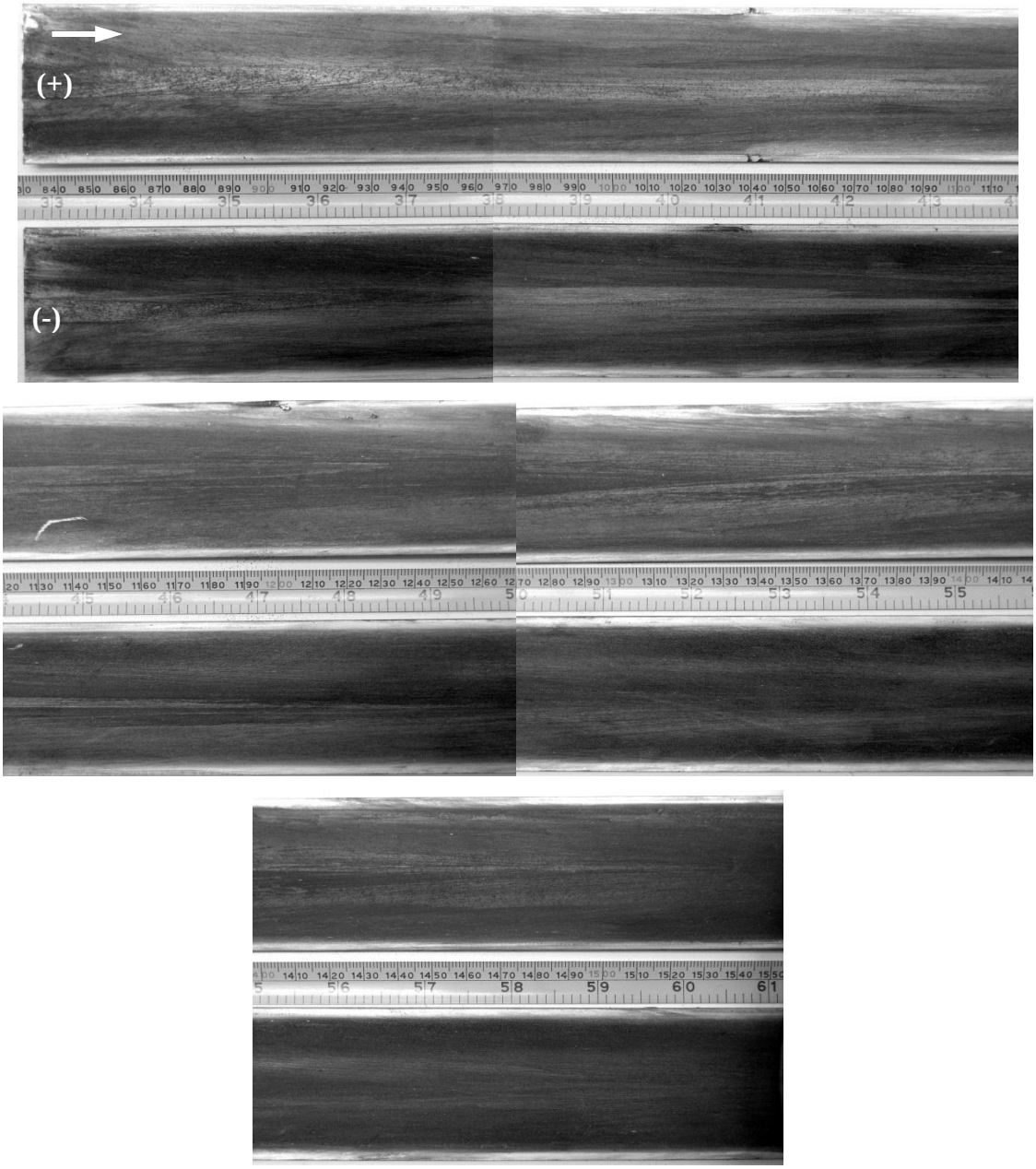

Figure 4.79. MCL 629, 50 µm coated rail photographs

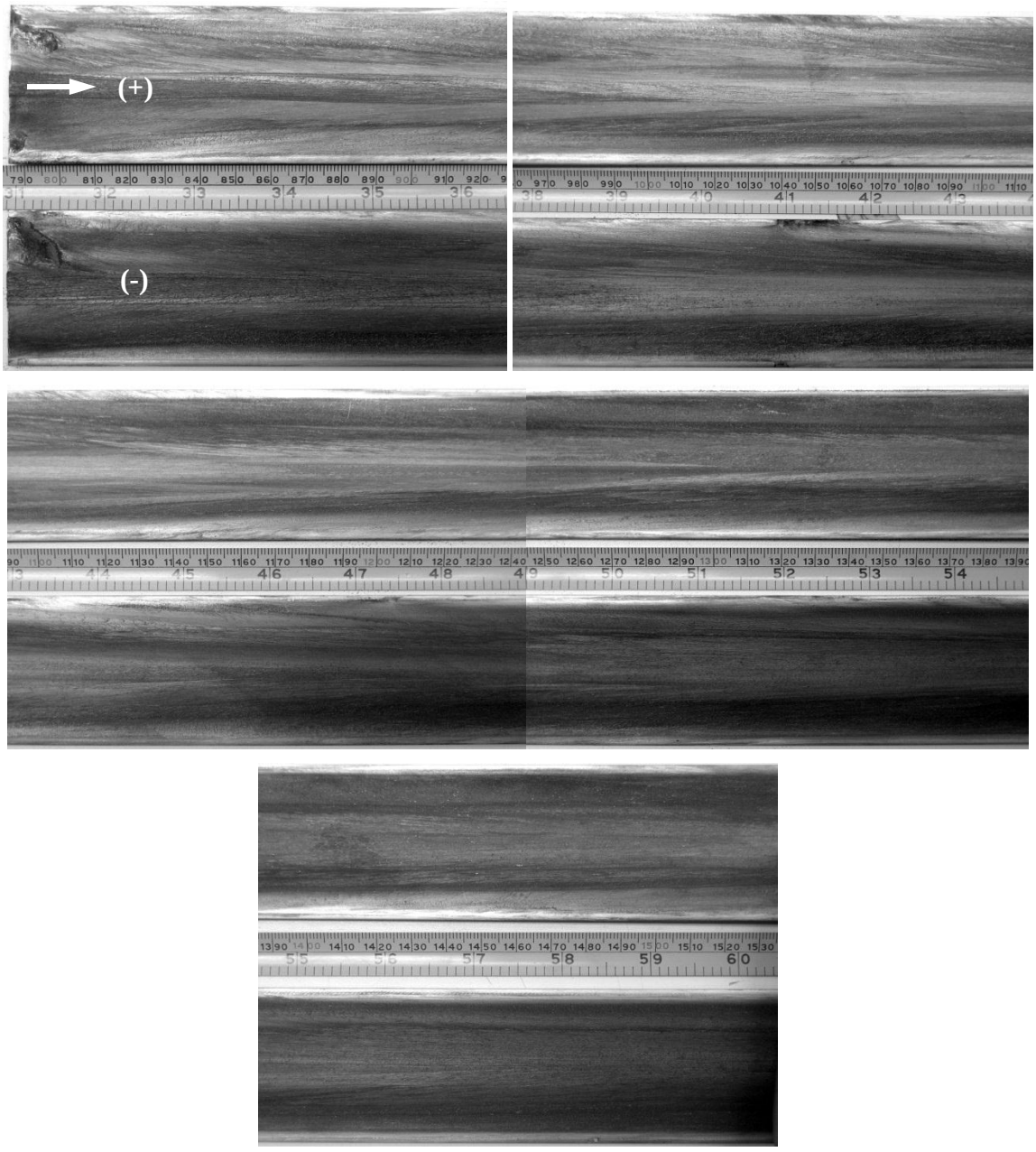

Figure 4.80. MCL 630, 5 µm coated rail photographs

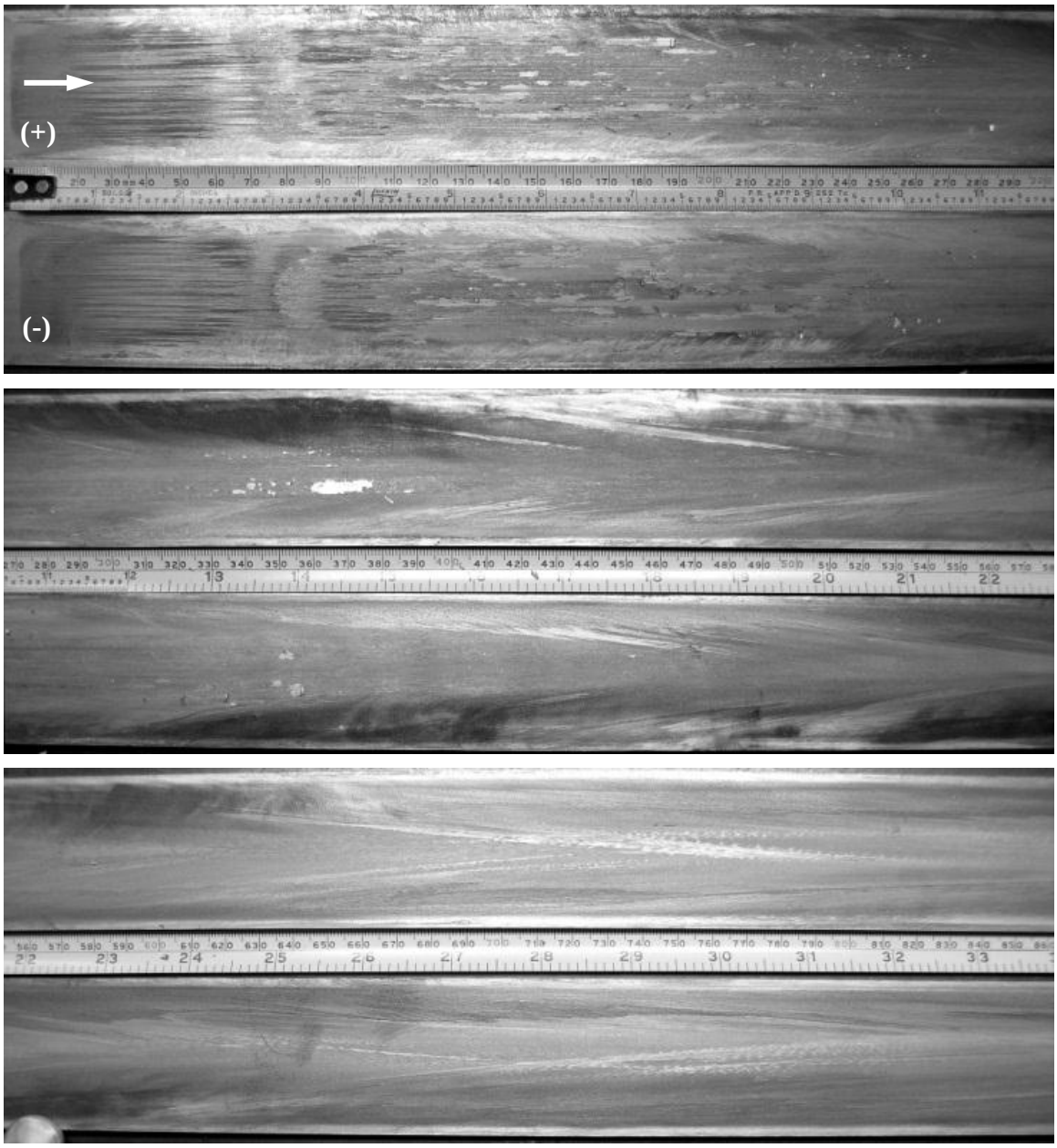

Figure 4.81. MCL 650 un-coated rail photographs (0-0.86 m, 0-33.9")

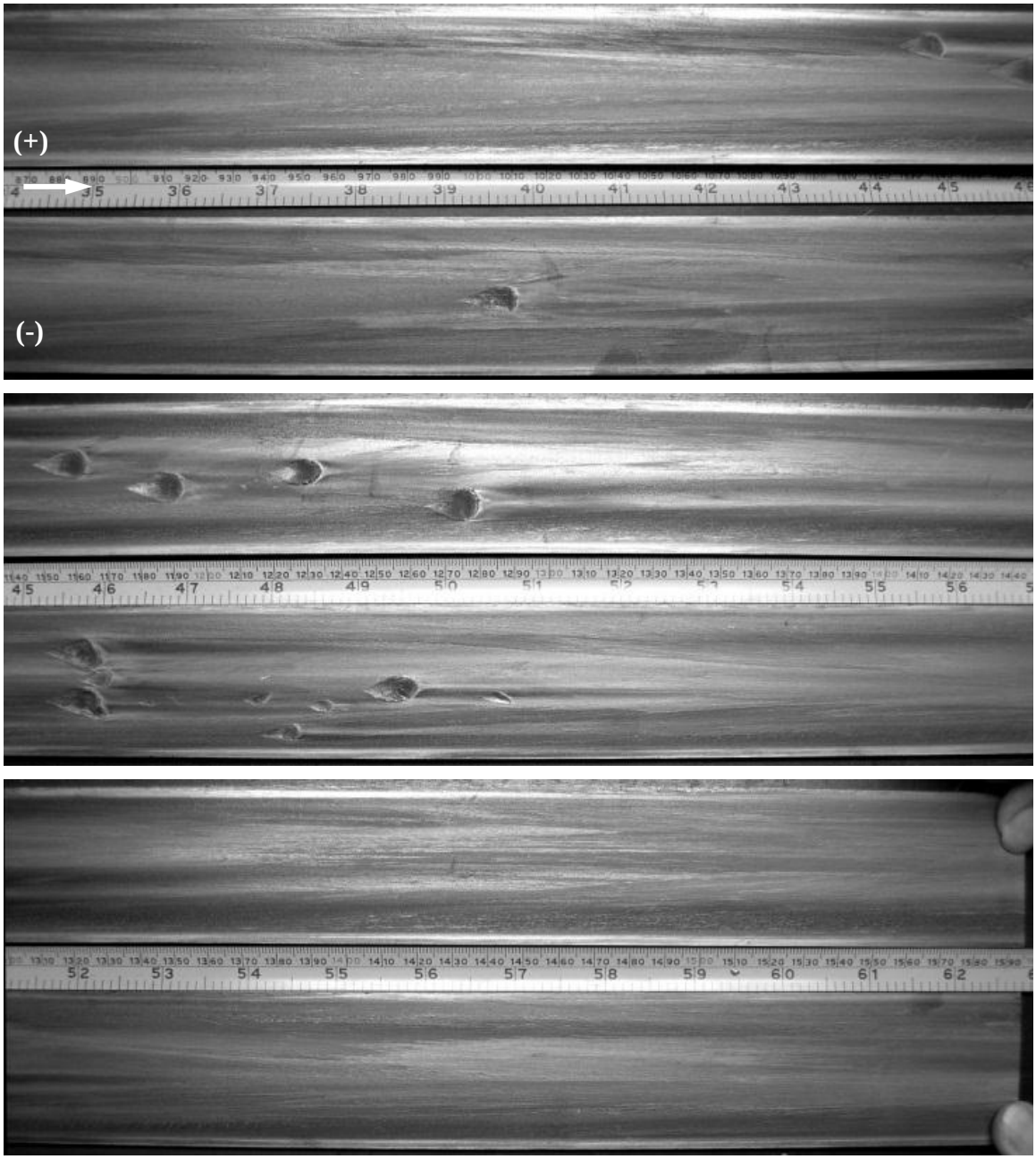

Figure 4.82. MCL 650 un-coated rail photographs (0.87-1.59 m, 34.3-62.6")

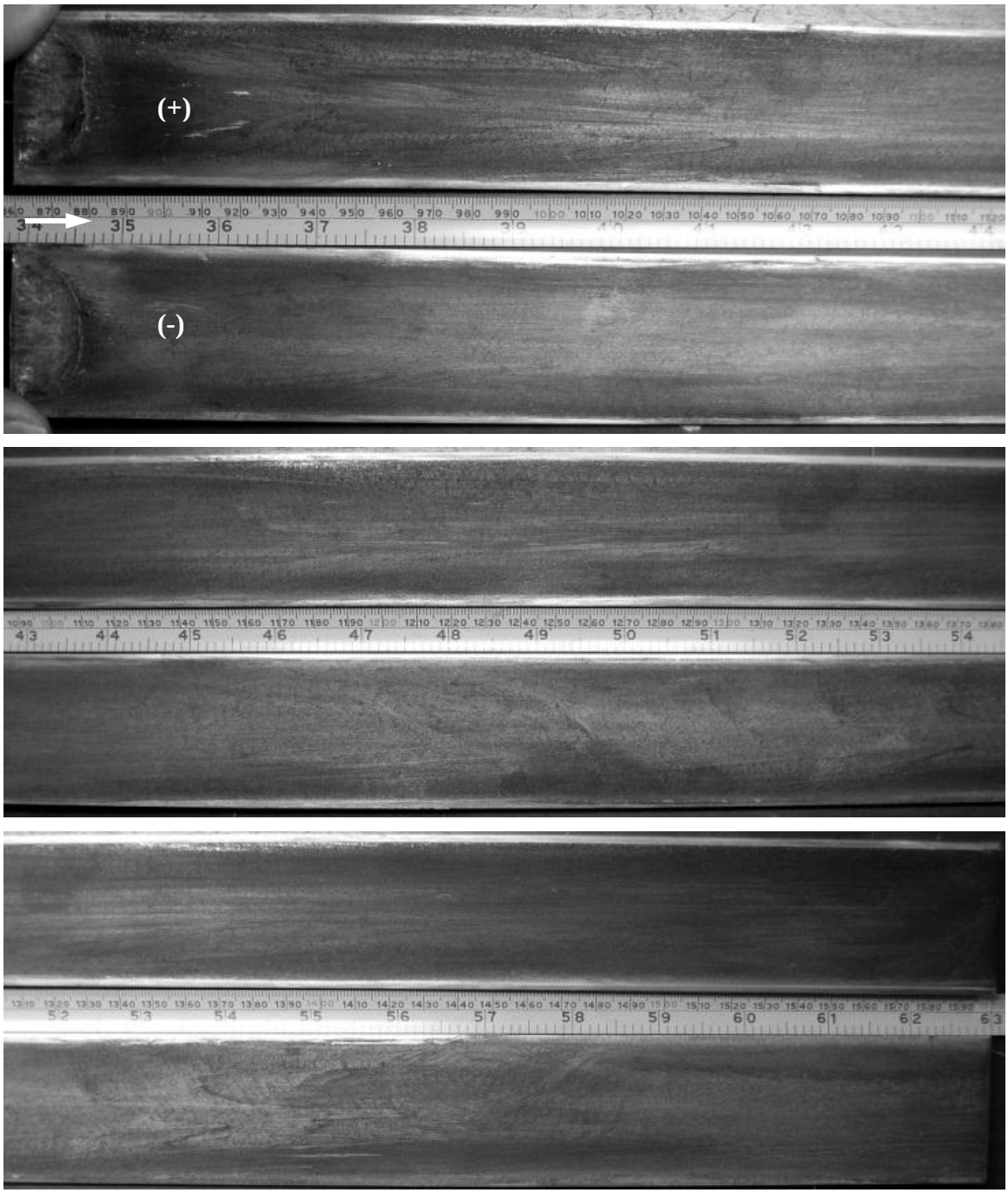

Figure 4.83. MCL 651, 5 µm coated rail photographs

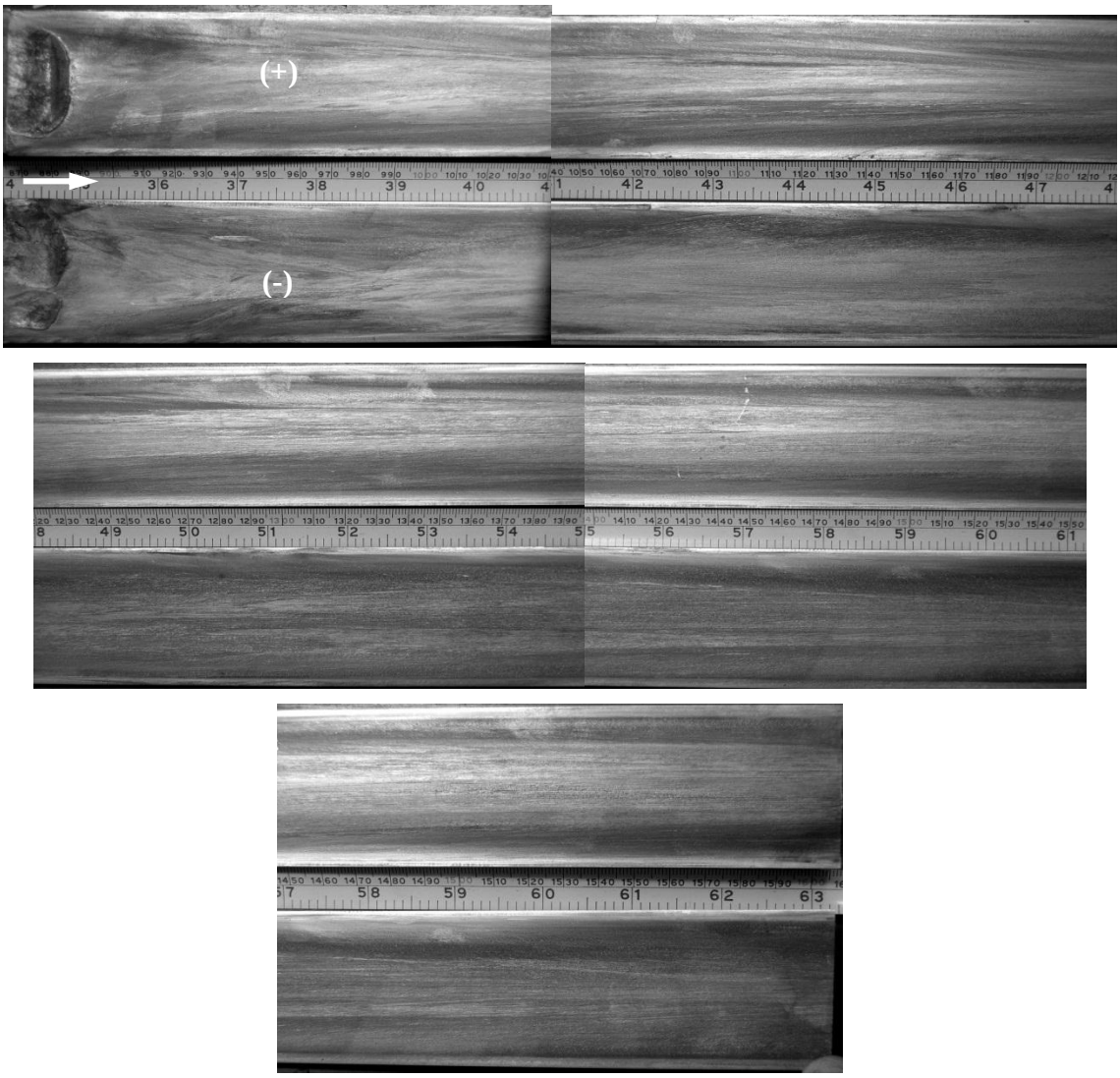

Figure 4.84. MCL 652, 5 µm coated rail photographs

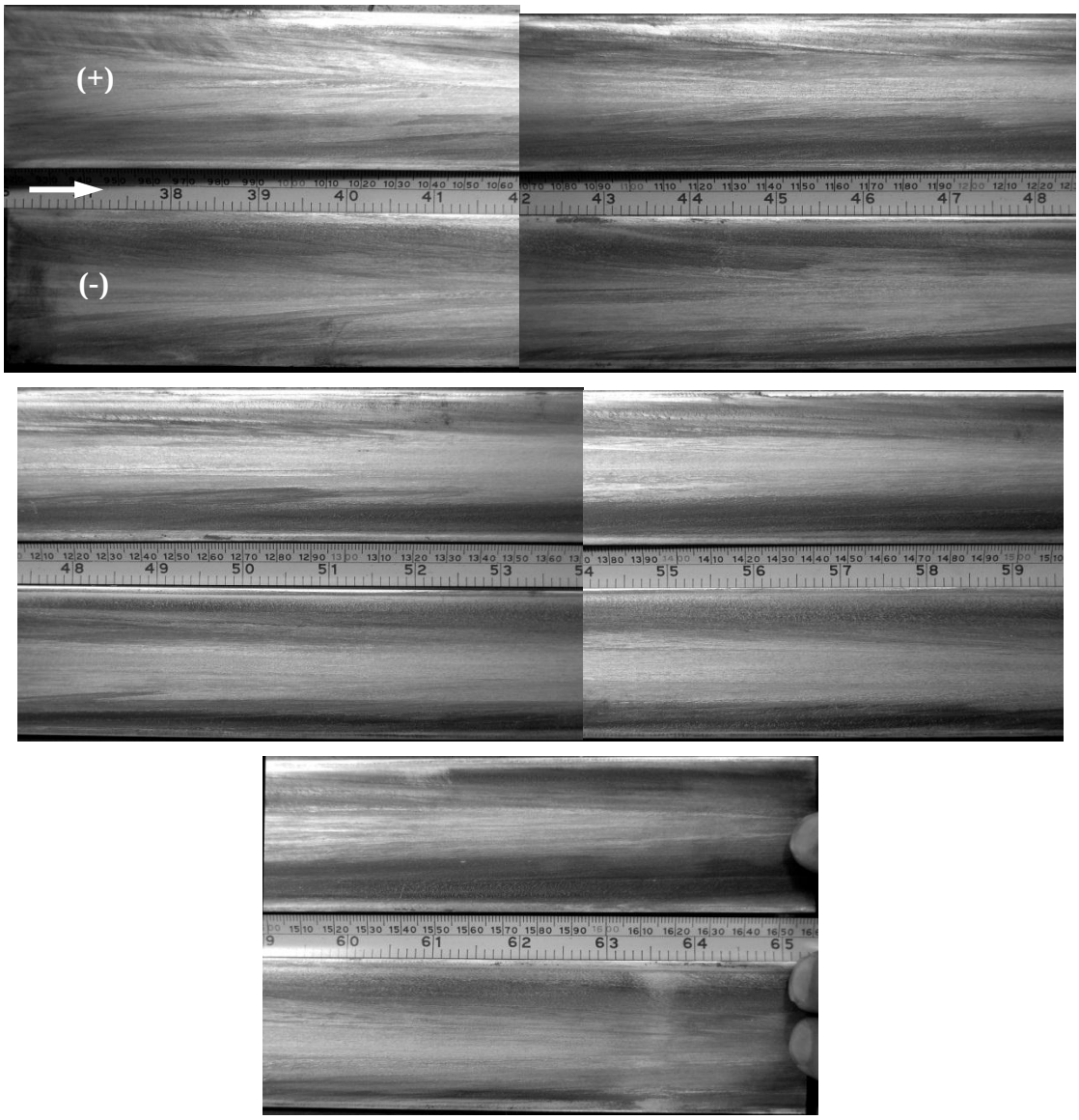

Figure 4.85. MCL 653, 2 μm coated rail photographs

Figure 4.86 shows a close-up photograph of gouges on the un-coated experiment (MCL 650). Teardrop-shaped gouges begin at 1,960 m/s and continue until transition. Figure 4.87 shows the leading-edge gouges for MCL 628, 630, 651 and 652. For MCL 628 (25 μm) and 630 (5 μm) multiple gouges initiate at the leading edge of the cladding. For MCL 651 and 652 (both 5 μm), a singular gouge initiates across the entire armature contact width.

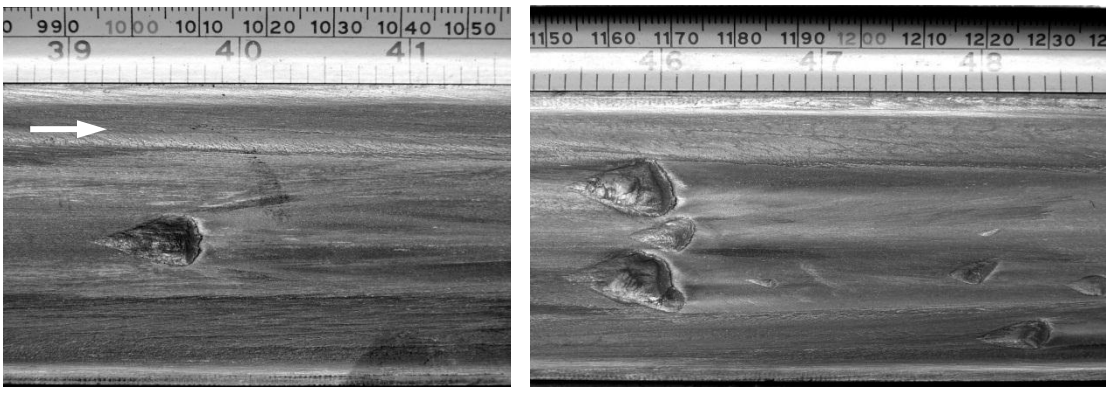

Figure 4.86. Example of gouging seen on bare C15725 (MCL 650)

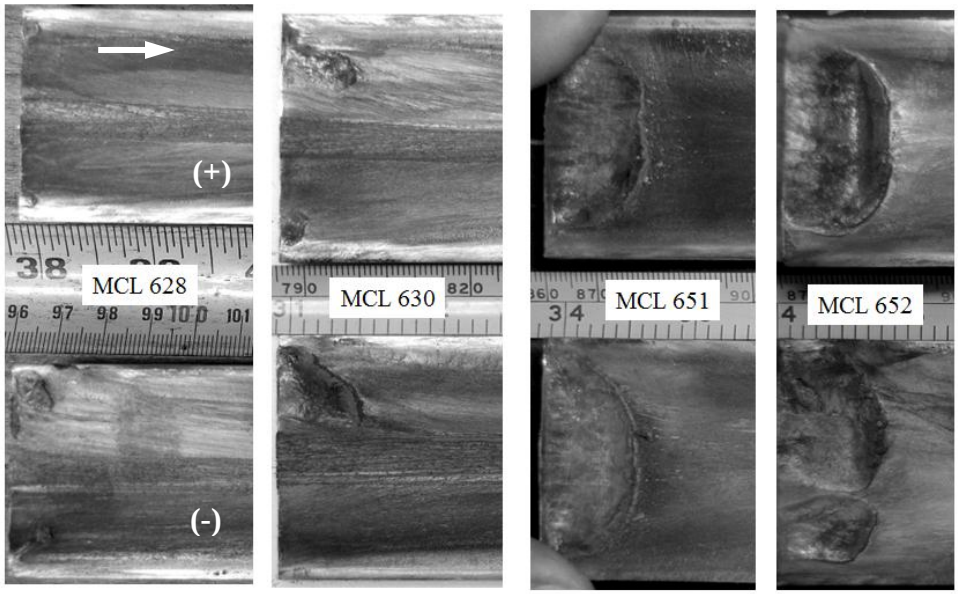

Figure 4.87. Gouging at leading edge of coated rail claddings

4.3.3 SERIES 3 MICROSCOPY

Post-test inspection of all the conductors indicated that none of the Al-electroplated coatings delaminated, and that the typical deposition of armature material had occurred on top of the electroplated coating. Samples were cut from the rail, mounted in Bakelite, polished, and etched with dilute aqueous Keller's reagent (2.5% HNO_3, 1.5% HCl, 1% HF) to reveal the Al grain structure [198]. Figure 4.88 shows optical microscope images of the "50 μm" coated rail after testing. The three images show three locations on

the rail: (a) center, (b) inside the armature contact edge, and (c) outside the contact zone. The edges of the rails have a greater coating thickness than the center, as discussed in the previous Chapter.

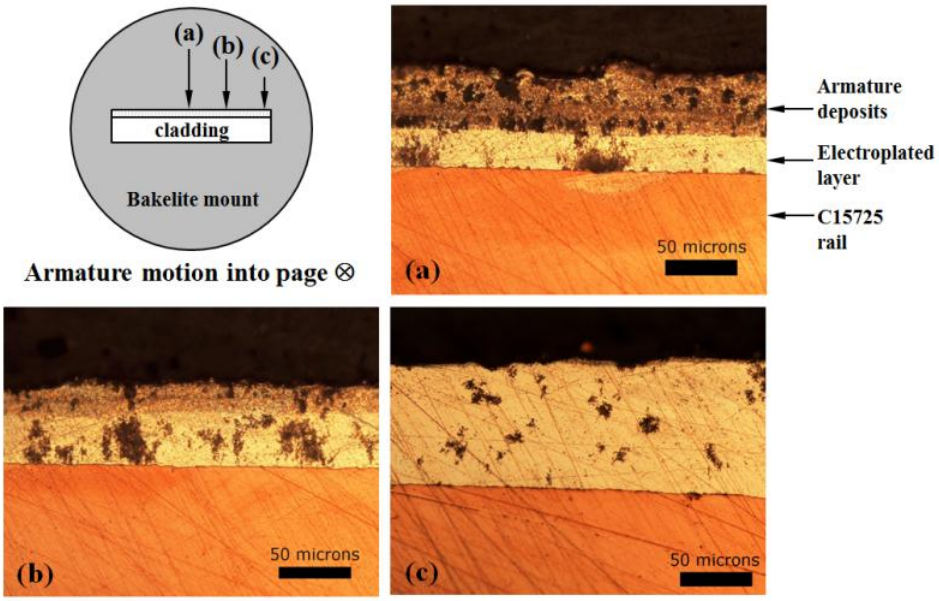

Figure 4.88. Optical microscope images of 50 µm coating cross-section after testing (© 2011 IEEE)

The images in Figure 4.88 show that the electroplated Al layer survived the launch without significant delamination or other failure. A layer of fine-grained deposited aluminum from the armature is bonded to the electroplated layer, seen in Figure 4.88a-b. A scanning electron microscope (SEM) was used to examine the conductor surfaces in the middle portion of the coated surface in an as-coated 5 µm sample (Figure 4.89) and a tested 5 µm sample (MCL 630, Figure 4.90). The armature deposits were typical for aluminum armatures tested at high currents and velocities, with significant porosity and numerous "mud cracks" across the surface (Figure 4.90a-b). Figure 4.90d shows a section of deposits with a fine cellular grain structure. The grain sizes in this region measure around 1-2 micrometers, suggesting a solidification rate on the order of 10^5 K/s [33]. While this is high, it is not as high nor are the grains as small as observed with aluminum armatures on bare copper rails.

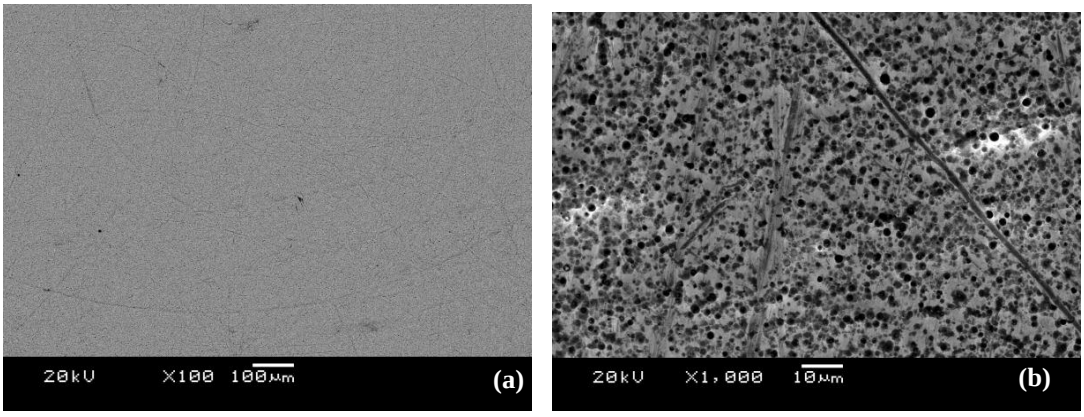

Figure 4.89. SEM images of coated rail prior to testing: (a) BSE image of coating at 100X, (b) SEI of coating at 1000X (© 2011 IEEE) [195]

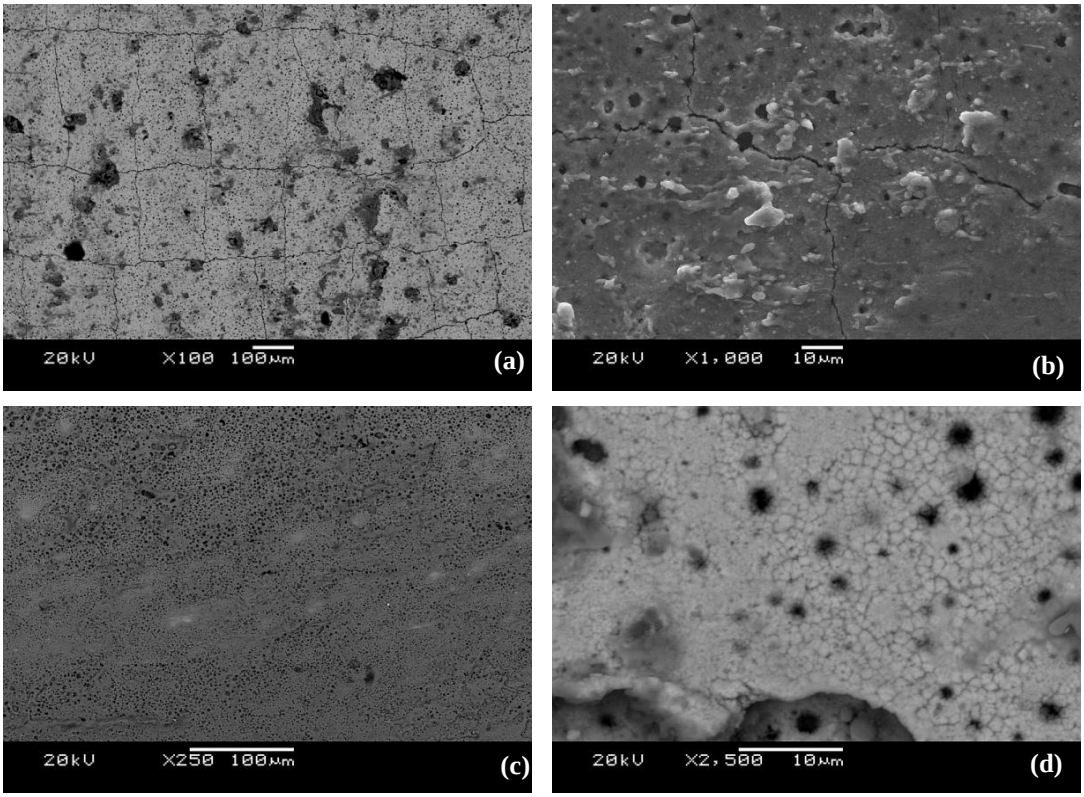

Figure 4.90. SEM images of coated rail after testing: (a) BSE image showing mud cracks, (b) SE image crack features with porosity, (c) BSE image showing reduced coating thickness, (d) BSE image showing fine grain sizes indicating rapid solidification rates (© 2011 IEEE) [195].

4.4 Series 4, Surface Indentation Experiments

4.4.1 Series 4 Experimental Overview and Waveforms

The final test series was intended to explore the behavior of gouging in the presence of macroscopic surface indentations. For this series the HEMCL railgun was used, as the MCL was unavailable. A photograph of the launch package is shown in Figure 4.91. The launch package was a "mono-body" design made from AA7075-T6 and polycarbonate bore riders. The rails were made from C11000-H02. This material combination has been tested numerous times and has a well-documented gouging threshold of 1,300 m/s on the MCL [25].

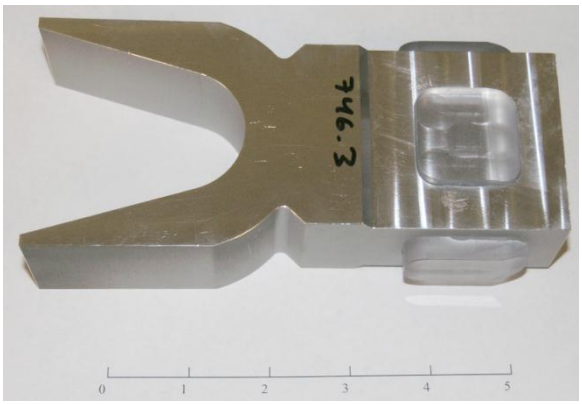

Figure 4.91. HEMCL launch package photograph

Results of the surface indentation experiments are summarized in Table 4.9. Table 4.10 provides the calculated velocities at the location of first observed galling damage and gouging. Both damage mechanisms, while qualitatively different, occur at around the same velocity. It should be noted that the gouging threshold is reduced compared to results obtained in previous MCL experiments.

Table 4.9. Series 4 (surface indentation) experimental results

HEMCL #	Slider	Rail	I_{pk} *kA*	I_{exit} *kA*	V_{exit} *m/s*	X_{trans} *m*	V_{trans} *m/s*
1341	AA7075-T6	C11000-H02 indented	1,457	693	2,057	1.44	1,370
1342	"	C11000-H02 flat	1,457	706	2,052	1.54	1,413

Table 4.10. Series 4 gouging results (AA7075-T6 slider)

HEMCL #	Rail	Slider *HV*	Rail *HV*	V_{gall} *m/s*	V_{gouge} *m/s*
1341	C11000-H02 indented	176 ± 2	89 ± 2	688 ± 17	1,109 ± 14
1342	C11000-H02 flat	"	"	719 ± 20	1,138 ± 17

The experimental waveforms for HEMCL 1341 (indented) and 1342 (flat) are provided in Figure 4.92 and Figure 4.93. Both muzzle voltages traces undergo a jump from 40 to 80 V at 1 m. This corresponds roughly to the onset of gouging as shown in Figure 4.94 and Figure 4.98.

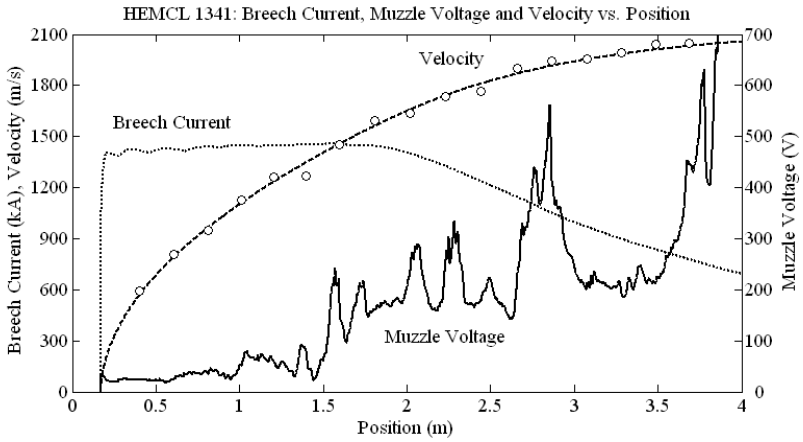

Figure 4.92. HEMCL 1341 (indented rail) breech current, muzzle voltage and velocity

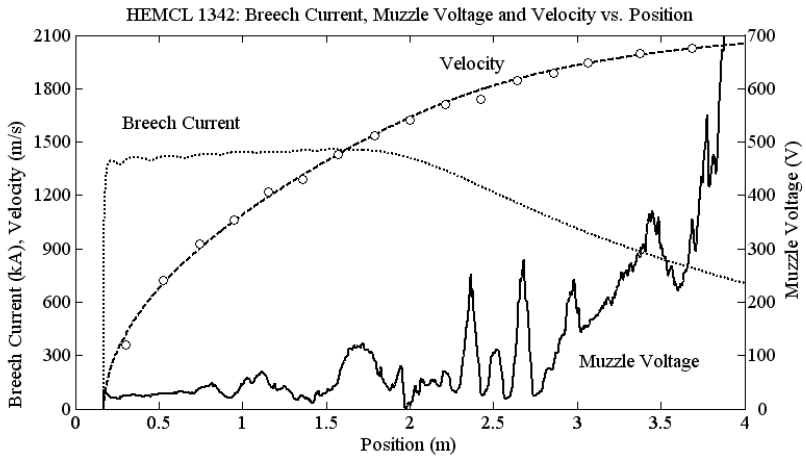

Figure 4.93. HEMCL 1342 (flat rail) breech current, muzzle voltage and velocity

4.4.2 SERIES 4 RAIL PHOTOGRAPHS AND GOUGE LOCATIONS

Photographs of the as-shot rail surfaces for the first test are shown in Figure 4.94. The (-) rail was subsequently etched to remove the aluminum deposits, with the results shown in Figure 4.95. Starting at 0.6 m (23.6"), thin galling tracks are observed on the downstream side of the indentations. After 1 m gouges are observed on the (-) rail. Gouges then initiate on each subsequent indentation until the end of the rail cladding. In some cases the indentations produce multiple simultaneous gouges, while other indentations produce a large gouge crater with an initiation width that spans most of armature contact height.

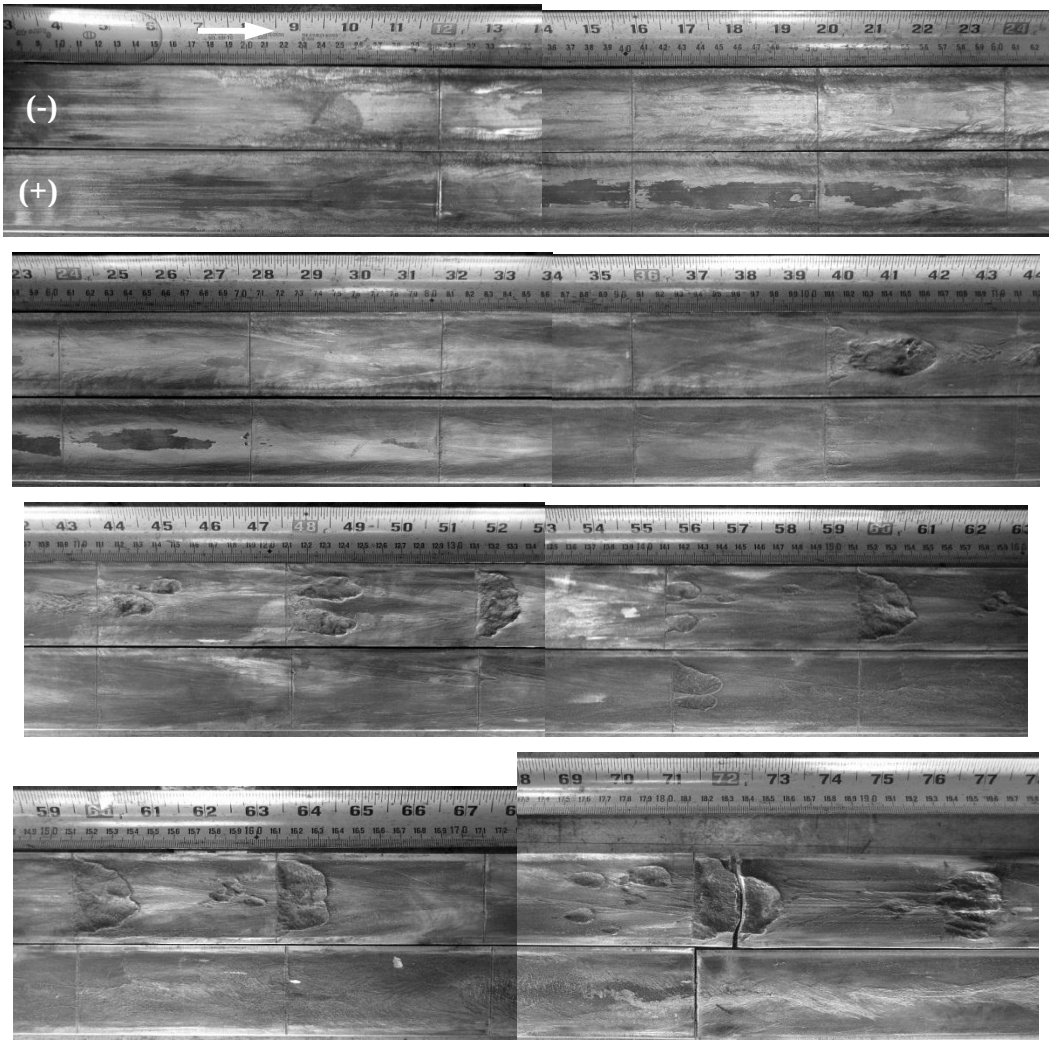

Figure 4.94. HEMCL 1341 rail photographs

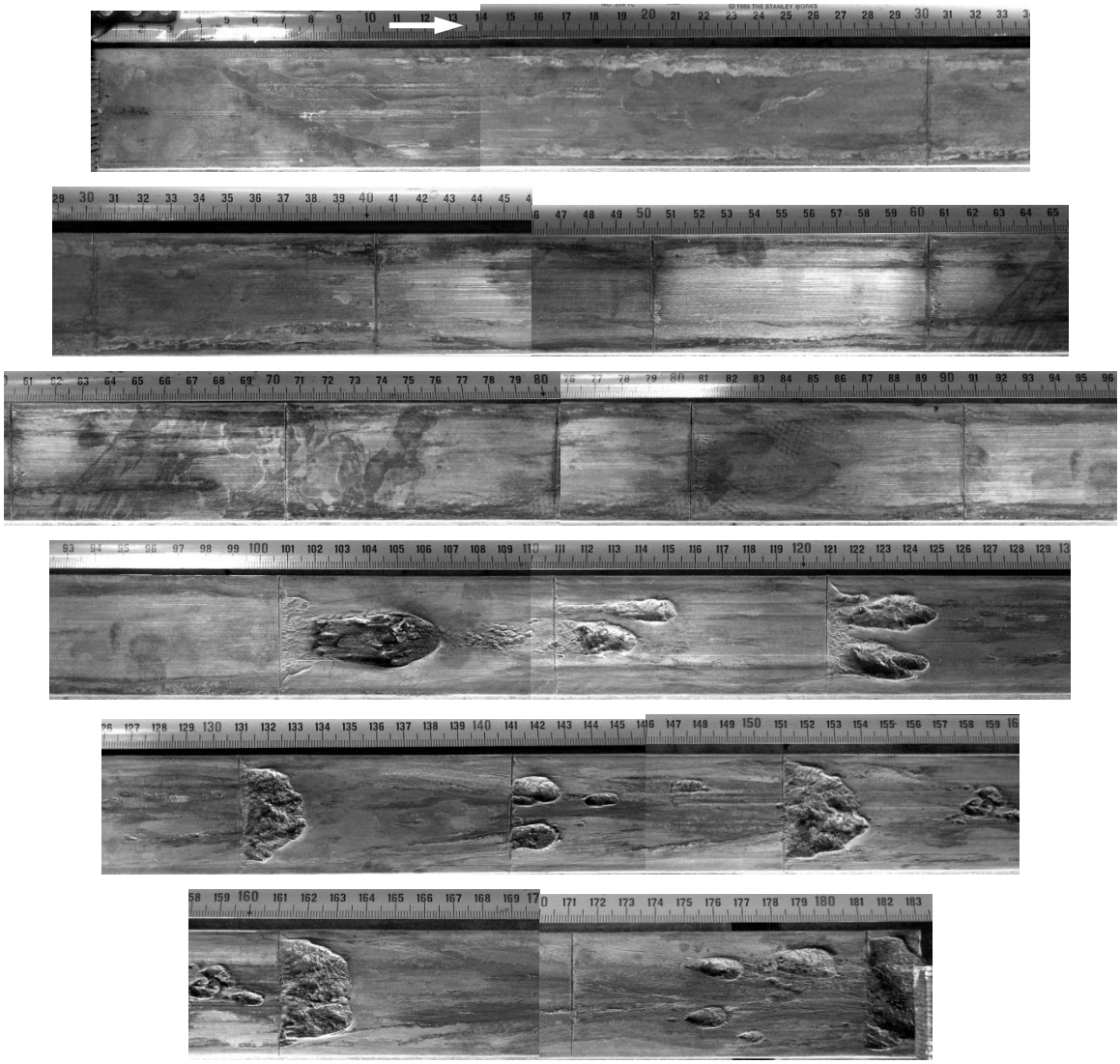

Figure 4.95. HEMCL 1341 etched (-) rail photographs

The galling tracks downstream of the (-) rail indentations initially have a short length (~2 mm) and grow progressively (7-8 mm) until they result in a gouge crater (Figure 4.96). The next few gouge craters are also initiated in this manner, with a region of shallow galling followed by gouging (Figure 4.97). The gouge on the top-left of Figure 4.97 shows a relatively long length (~20 mm) of galling prior to the formation of a gouge crater.

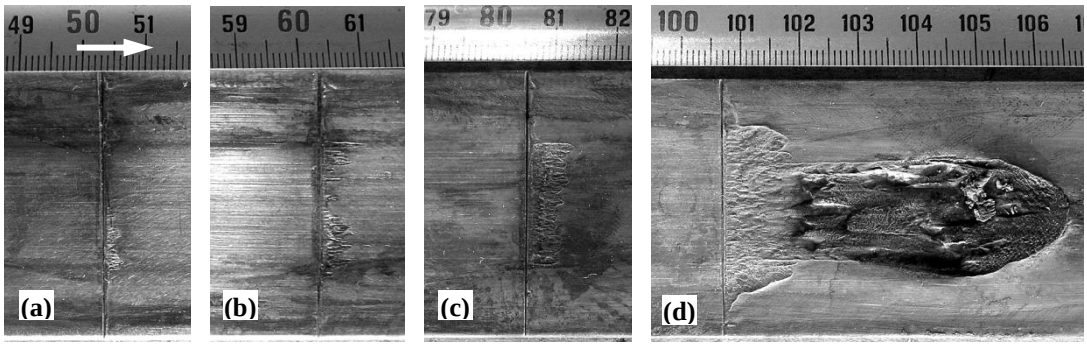

Figure 4.96. Examples of galling sheets prior to gouging

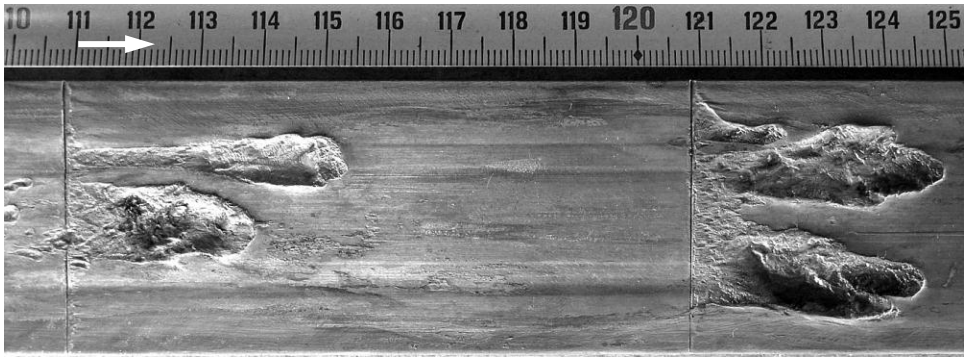

Figure 4.97. Gouges triggered by rail indentations

Photographs from the flat rail experiments (HEMCL 1342) are shown in Figure 4.98. As before, the (-) rail was etched to remove aluminum deposits, shown in Figure 4.99. The gouges observed here have the "classical" shape with a small initiation point and a teardrop-shaped crater. However, there is also galling damage on the rails prior to gouging. The galling is observed starting around 0.6 m (23.6"), while the first gouge crater is observed at 1.0 m (39.4"). These locations are about the same as the galling and gouging seen in the indented rails.

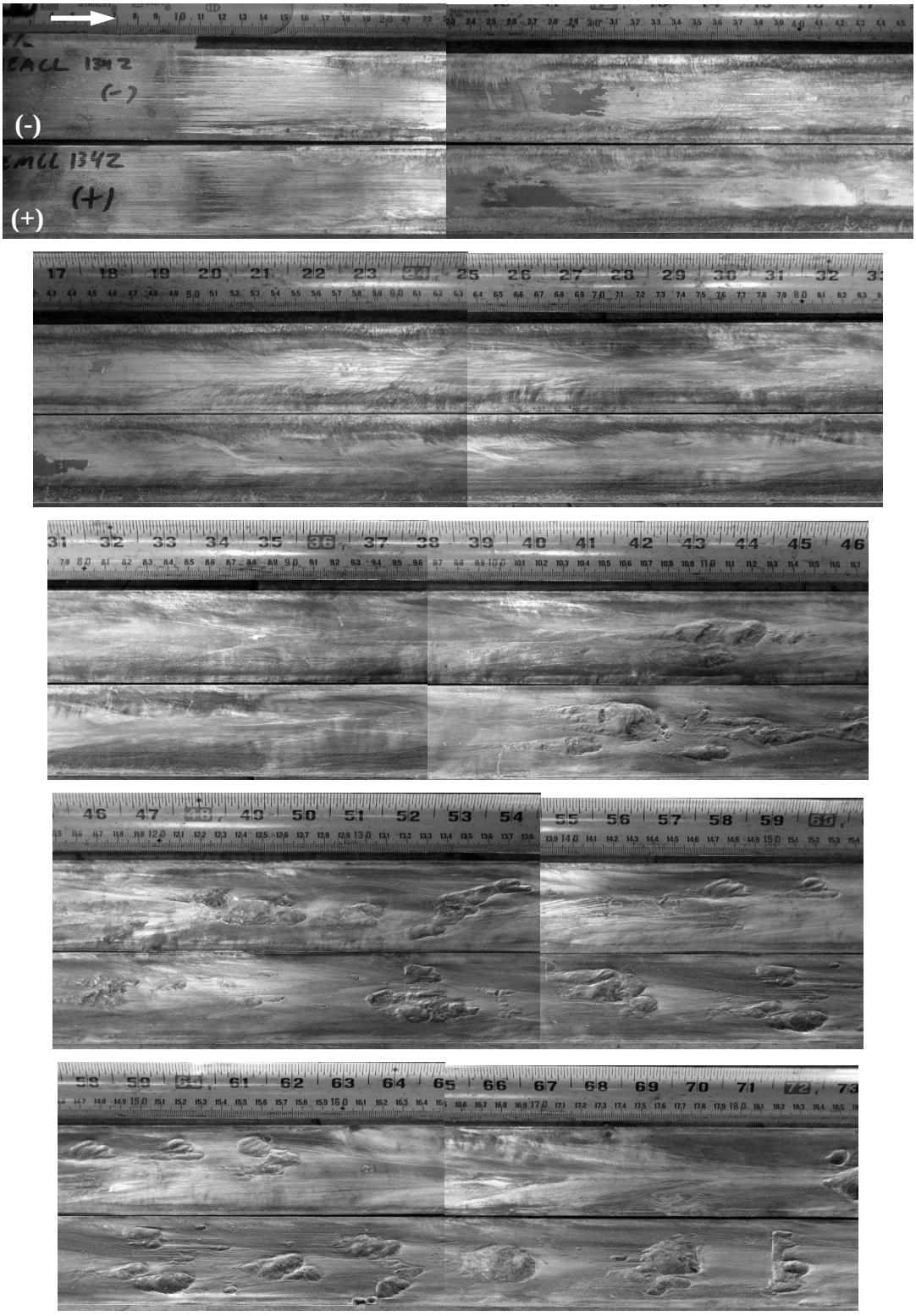

Figure 4.98. HEMCL 1342 rail photographs

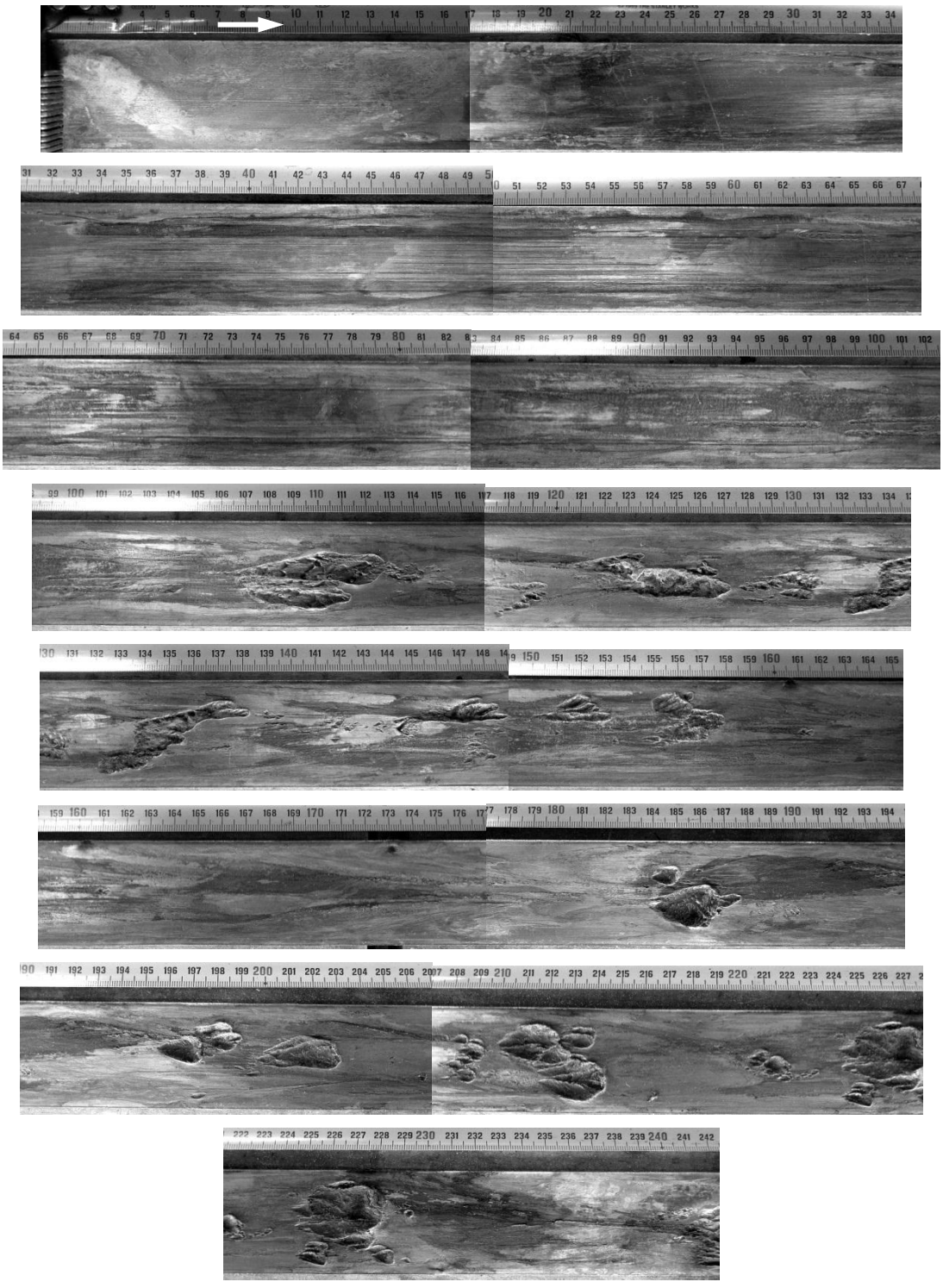

Figure 4.99. HEMCL 1342 etched (-) rail photographs

Examples of the galling damage are shown in Figure 4.100. The damage takes the form of shallow channels, similar to what was seen in the Cu/Cu experiments (MCL 609-610). Figure 4.100 shows that the gouges initiate at the same vertical location as the preceding galling marks. A comparison of the galling damage seen on the two rail configurations is shown in Figure 4.101. Galling shows up in both configurations at around the same location and velocity.

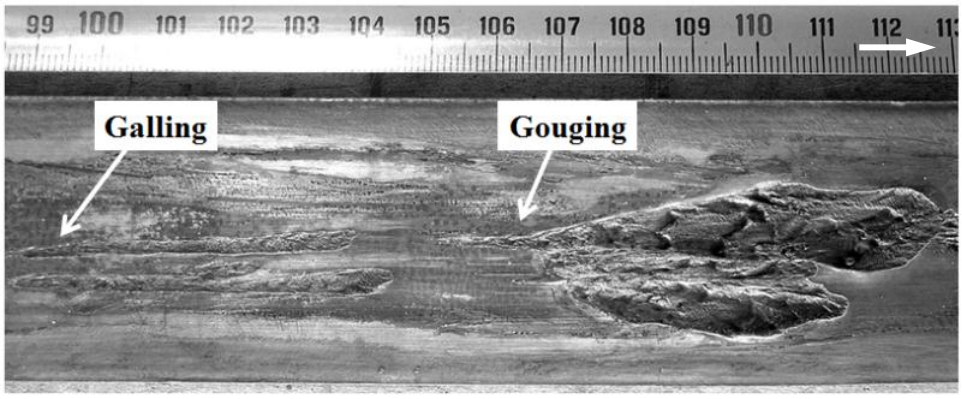

Figure 4.100. Galling prior to gouging

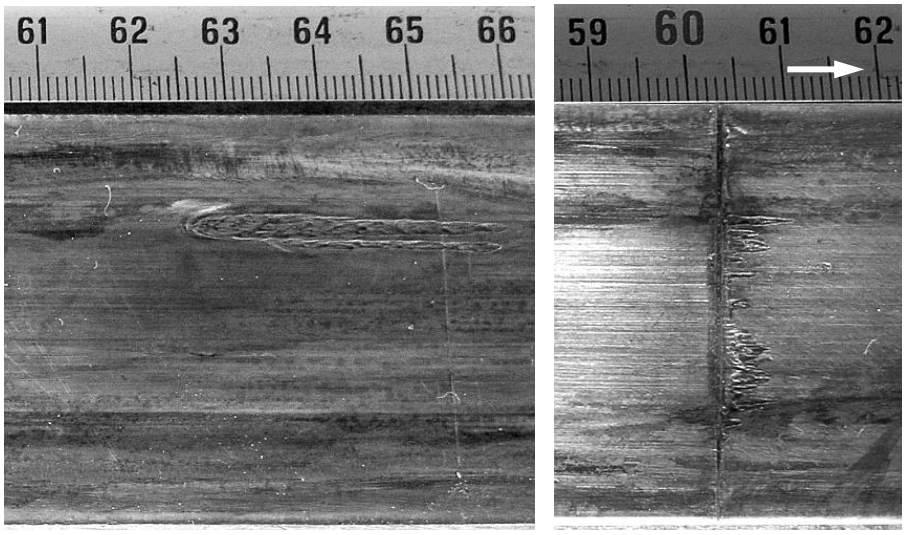

Figure 4.101. Comparison of galling on flat (left) and perturbed (right) rail surfaces (~780 m/s)

Based on these results, the threshold velocity for gouging appears largely unaffected by the presence of macroscopic surface indentations. However, the shape of the gouges is significantly affected by the indentations, which often result in gouge craters that initiate across the entire armature contact width. The first gouges seen on both configurations are compared in Figure 4.102.

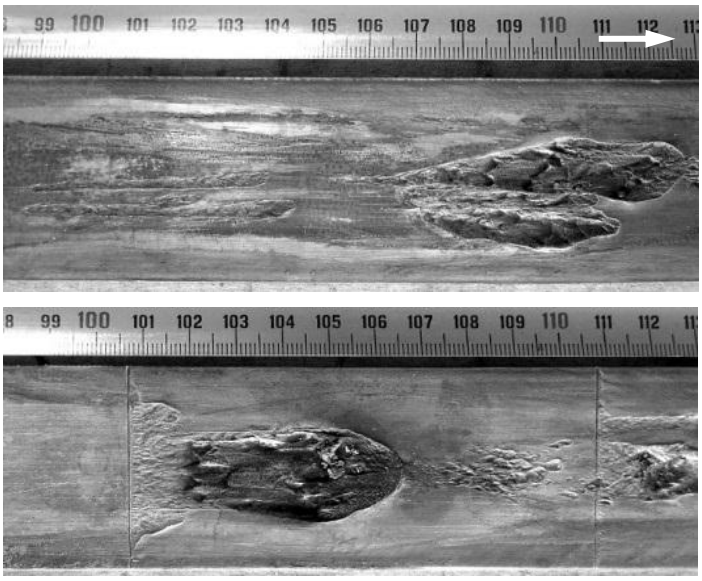

Figure 4.102. Comparison of gouging on flat (top) and indented (bottom) rail surfaces (~1,100 m/s)

4.4.3 SERIES 4 MICROSCOPY

SEM images of the etched (-) indented rail from HEMCL 1341 are shown at increasing velocities in Figure 4.103 through Figure 4.118. Three locations were analyzed: 0.6 m (23.6", 790 m/s), 0.8 m (31.5", 960 m/s), and 1.3 m (51.2", 1,300 m/s). Refer to Figure 4.95 and Figure 4.96 for photographs of these locations. All SEM images were taken in secondary electron image (SEI) mode. Figure 4.103 shows the upper part of the rail indentation shown in Figure 4.96b. In this case there is negligible downstream damage to the rail surface, as evidenced by the original machining marks.

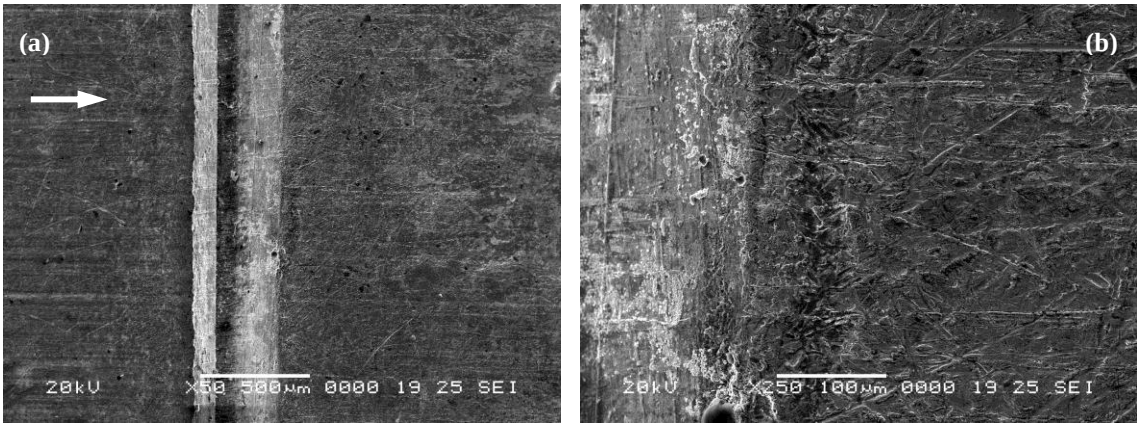

Figure 4.103. SEM images of indented rail at 0.6 m (23.6", 790 m/s, HEMCL 1341)

Figure 4.104 shows the bottom portion of the indentation with downstream damage. There is a 30-50 µm region of smooth rail material, followed by 40-60 µm of small (~1 µm) bumps, and finally a smeared-out region of material 50-100 µm long (see Figure 4.105). This could be the raised-edge of the indent that has been sheared off by the armature and deposited back onto the rail surface.

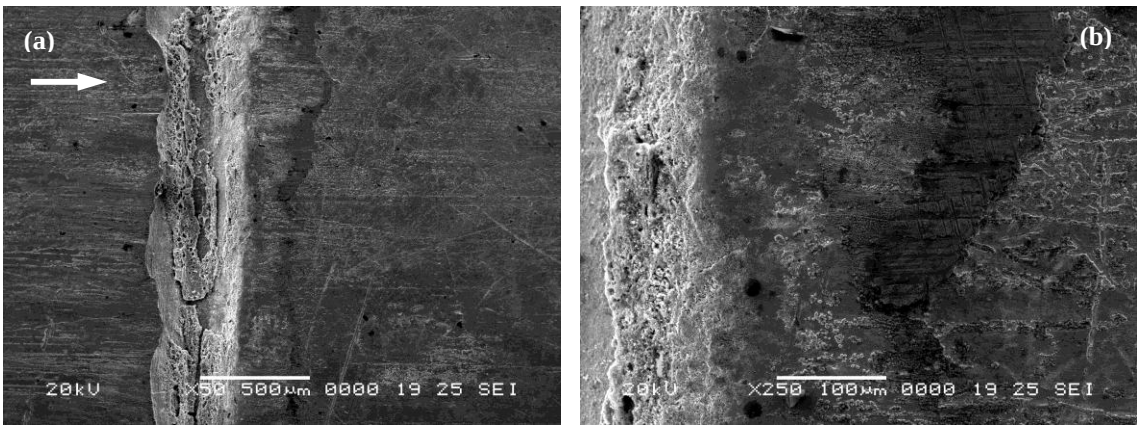

Figure 4.104. SEM images of indented rail at 0.6 m (23.6", 790 m/s, HEMCL 1341)

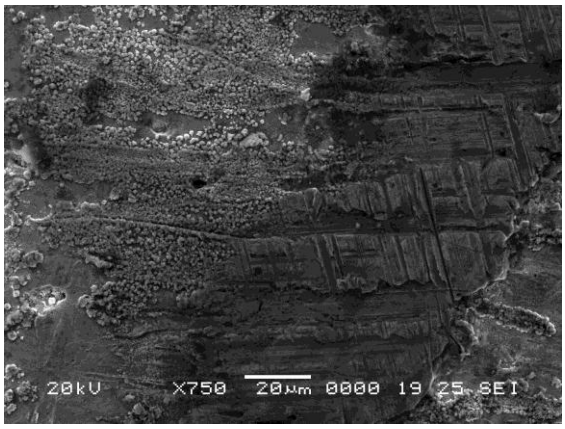

Figure 4.105 SEM image of indented rail at 0.6 m (23.6", 790 m/s, HEMCL 1341)

Figure 4.106 shows the region just below the central portion of the rail. Here a ~2 mm long galling crater is observed downstream of the indent. Figure 4.106b-d shows the upper-left part of the crater at progressively higher magnifications. The surface is largely composed of rough bands of material with an average "wavelength" of around 1 μm. The structure is reminiscent of that shown in Figure 4.22 and Figure 4.23 for Cu/Cu gouges (Series 1).

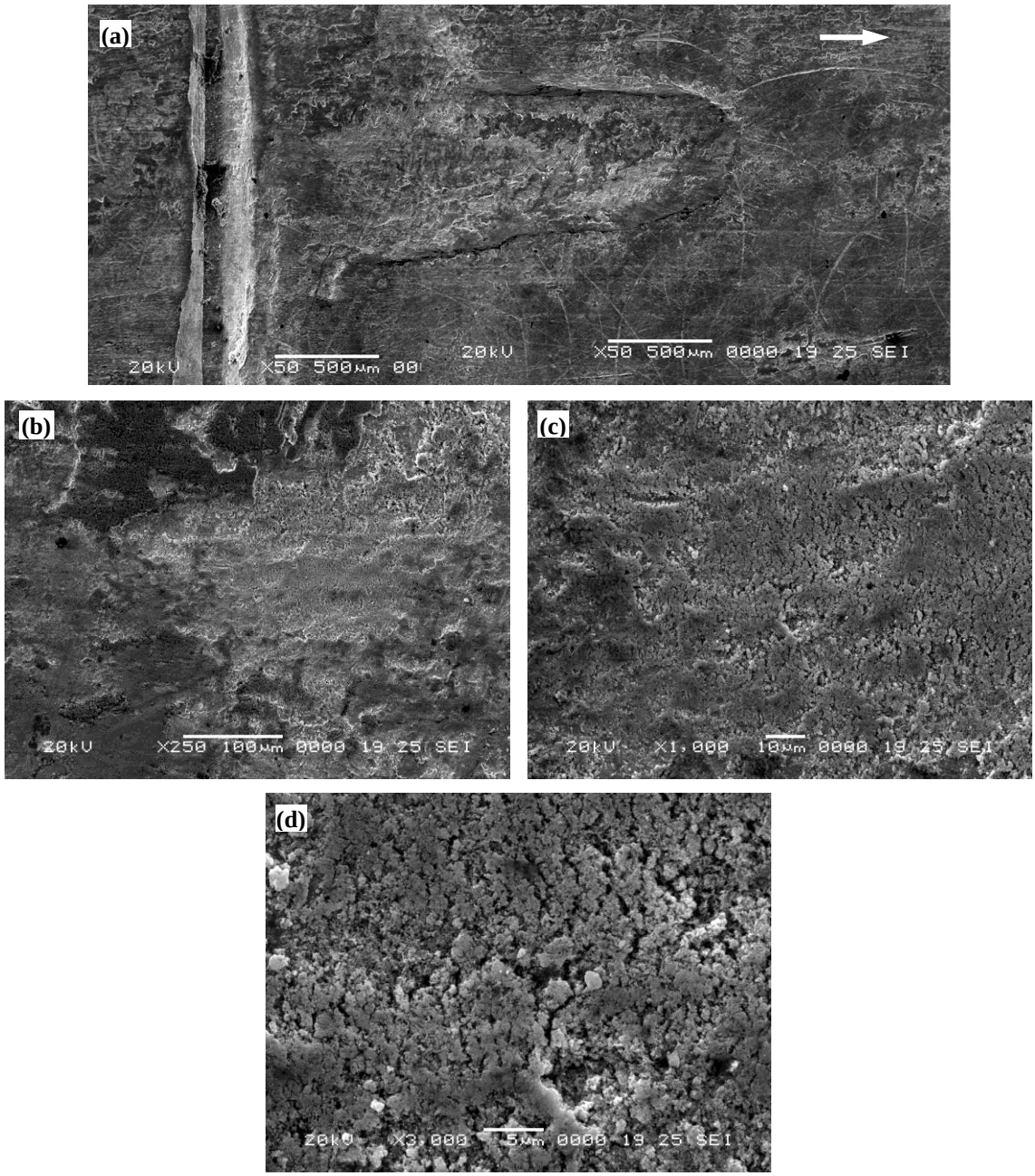

Figure 4.106. SEM images of indented rail damage at 0.6 m (790 m/s, HEMCL 1341)

At the approximate center of the rail there are numerous galling craters that emanate from a wide region downstream of the indent. This is shown in Figure 4.107 (orthogonal view) and Figure 4.108 (angled view). Immediately following the indent

there is a 100-200 μm region of smooth rail surface followed by a region of surface ripples which eventually become shallow craters.

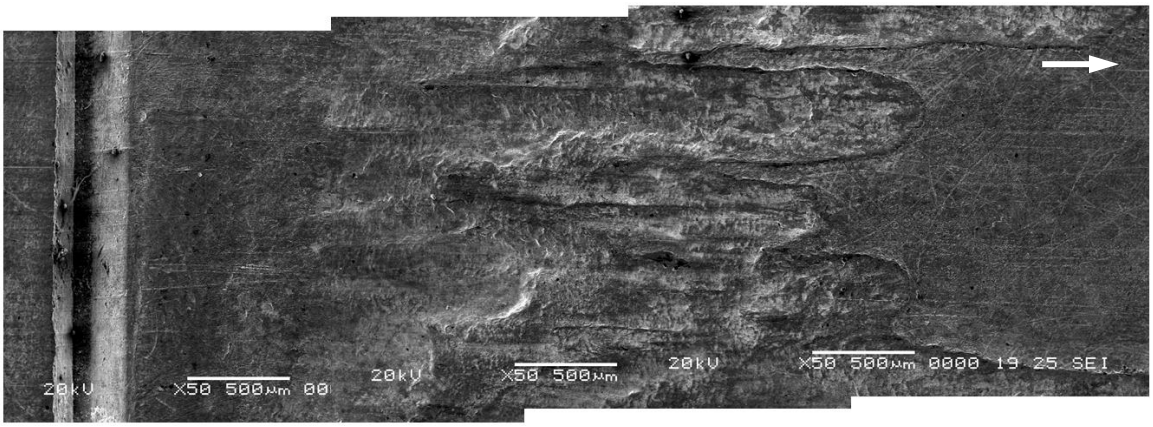

Figure 4.107. SEM images of indented rail damage at 0.6 m (23.6", 790 m/s, HEMCL 1341)

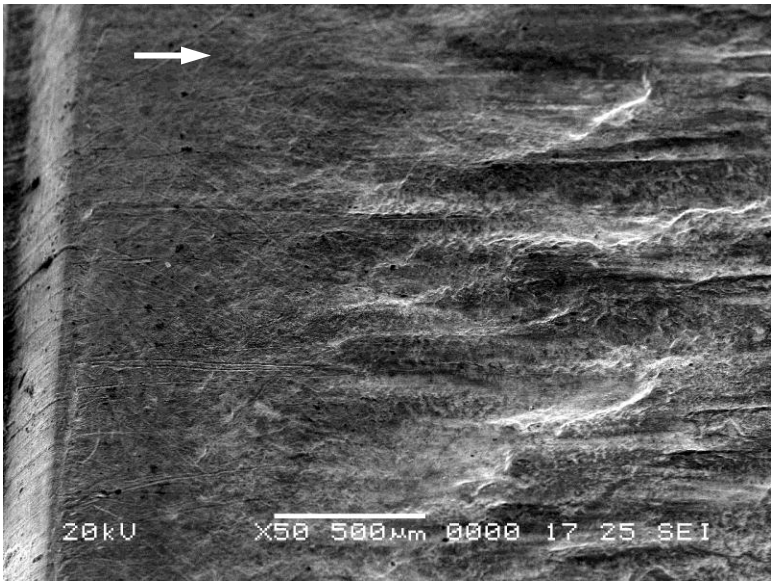

Figure 4.108. SEM image of indented rail damage at 0.6 m (23.6", 790 m/s, HEMCL 1341)

Cross-section images of the above regions are shown in Figure 4.34. Like the cross-section images of the previous flat-rail gouges, the surface ripples are evident just downstream of the indent. There is also a region of deformed below the rail surface, to a depth of around 20 μm.

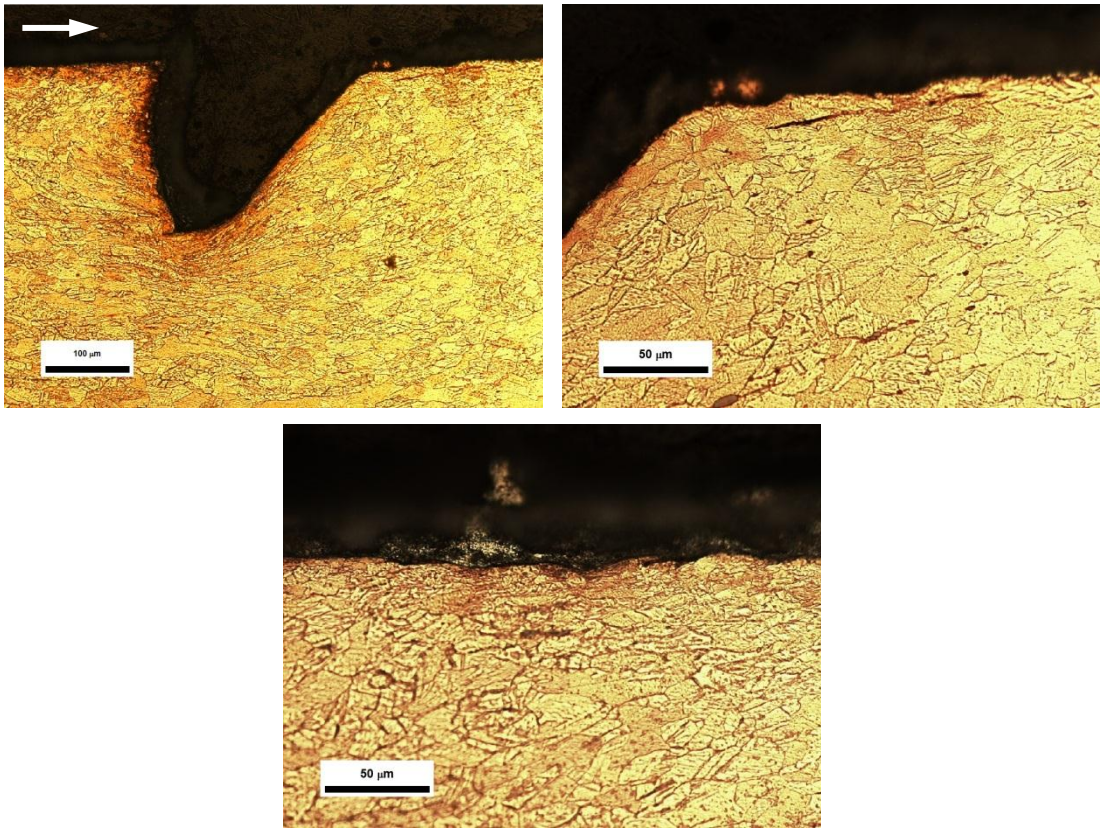

Figure 4.109. Cross-section microscope images of indented rail at 0.6 m (790 m/s, HEMCL 1341)

Figure 4.110 shows the progression of damage at 250X magnification, form the indent edge to crater formation. There is a faint wavy character to the surface as early as 200 µm after the indent. As the damage progresses the ripples have shorter and shorter wavelengths, and become readily apparent after ~1 mm.

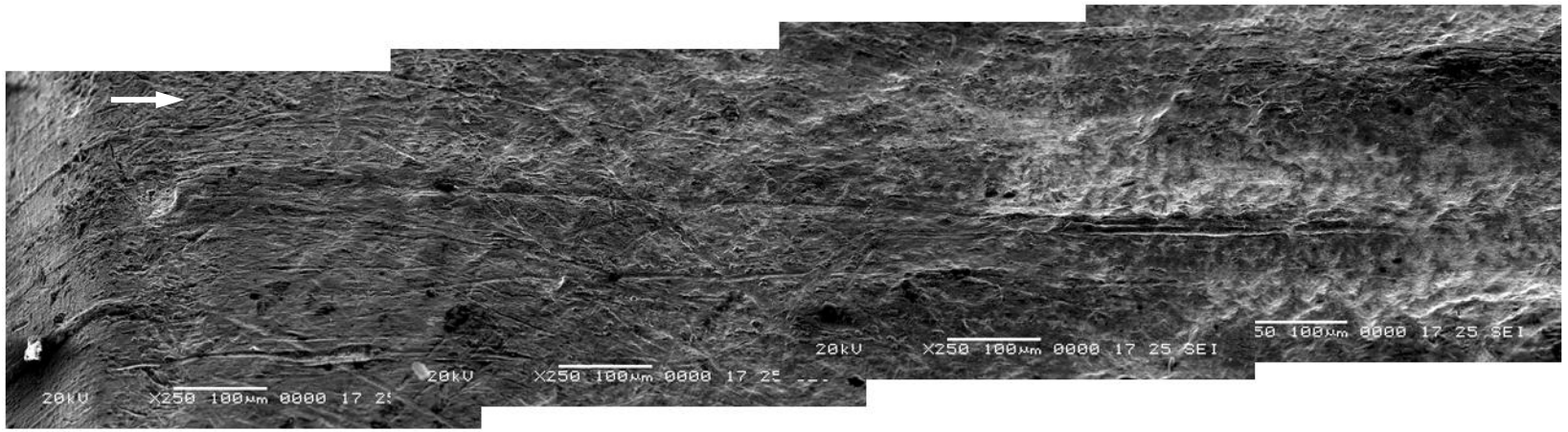

Figure 4.110. SEM images of indented rail at 0.6 m (23.6", 790 m/s, HEMCL 1341)

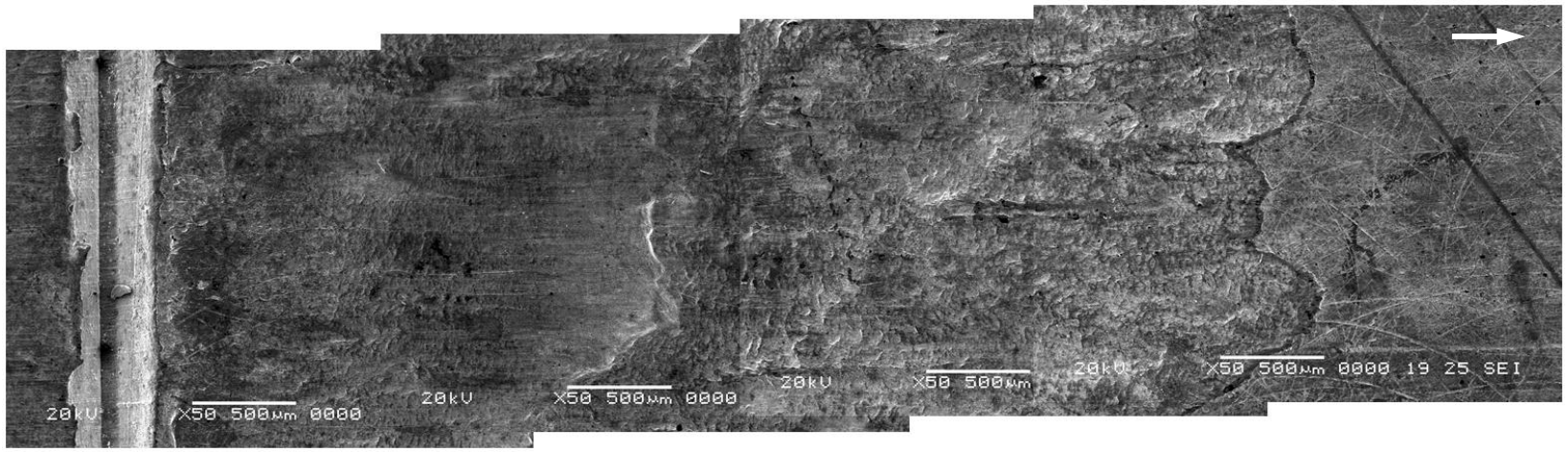

Figure 4.111. SEM images of indented rail damage at 0.8 m (31.5", 960 m/s, HEMCL 1341)

Figure 4.111 and Figure 4.112 show damage from the 0.8 m (31.5", 960 m/s) location. In the center portion of the rails the same general morphology is present as the 0.6 m (23.6") location, though the smaller ripples begin earlier (350 μm vs. 600 μm).

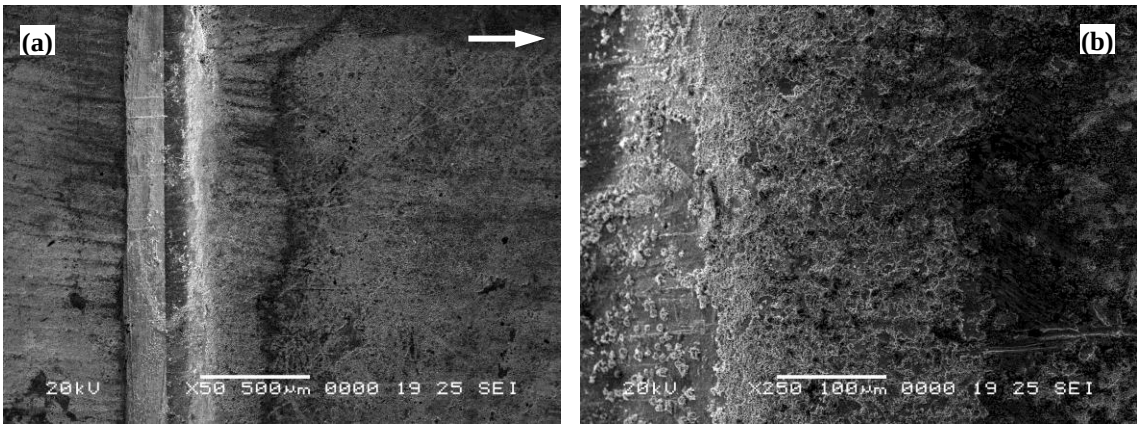

Figure 4.112. SEM images of indented rail damage at 0.8 m (31.5", 960 m/s, HEMCL 1341)

Cross-section examination of the indent at 0.8 m (Figure 4.35) shows significant plastic deformation downstream of the indent, extending several hundred micrometers into the rail. As the gouge progresses the depth of significant deformation reduces to around 30 μm, similar to gouges on flat rails. Wave-like character of the surface is immediately evident downstream of the indent.

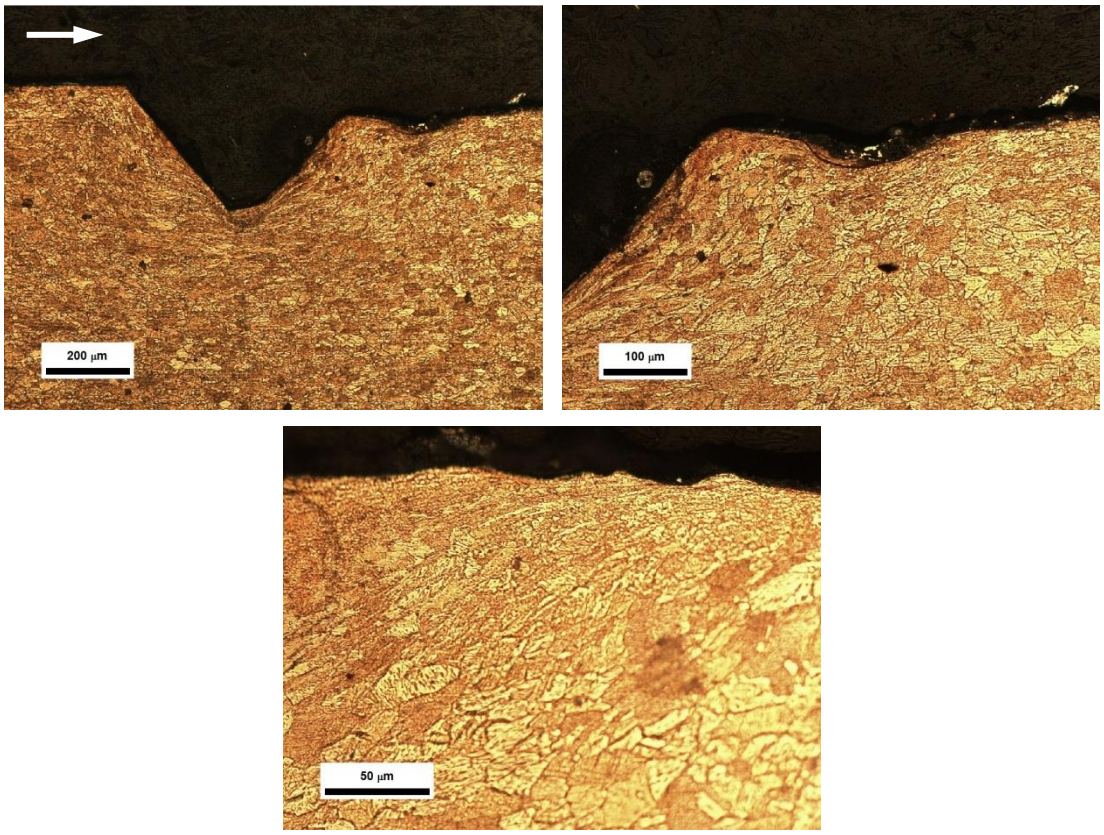

Figure 4.113. Cross-section microscope images of indented rail at 0.8 m (960 m/s, HEMCL 1341)

The indent damage at 0.6 m (790 m/s) and 0.8 m (960 m/s) are compared side-by-side in Figure 4.114. At both locations there are regions of moderate damage which "smears out" the downstream edge of the indentation but does not result in crater formation (see Figure 4.104, Figure 4.112). This is not the case at high speeds, as is shown in Figure 4.115 for the 1.3 m (51.2", 1,300 m/s) location.

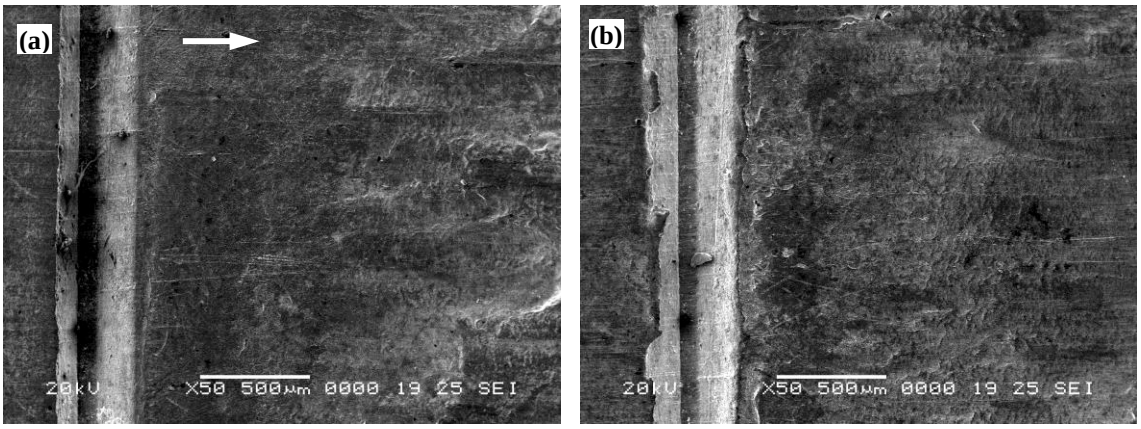

Figure 4.114. SEM images of indented rail at 0.6 m (790 m/s, left) and 0.8 m (31.5", 960 m/s, right) Both indentations result in the formation of galling craters

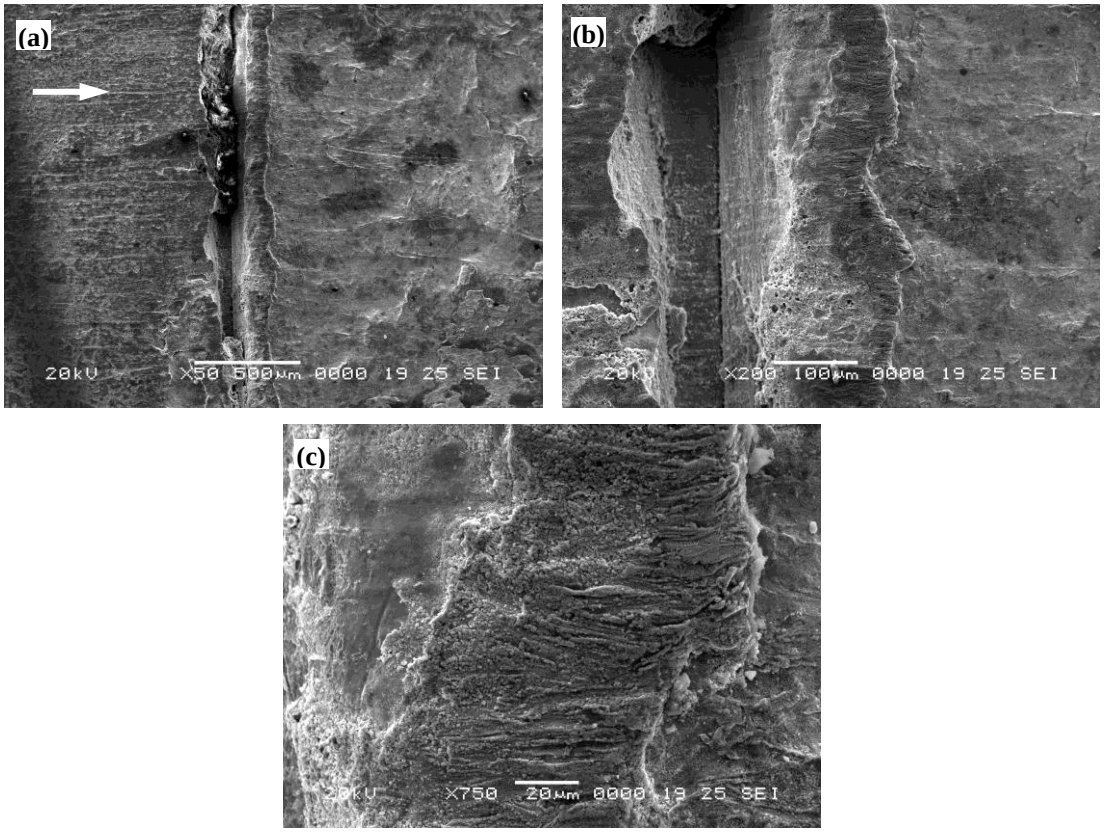

Figure 4.115. SEM images of indented rail at 1.3 m (51.2", 1,300 m/s)

Figure 4.116 shows the region in Figure 4.115 at an angled view. There is a lip of highly deformed material at the downstream indentation edge, which is immediately

followed by a large region of resolidified material. This is more easily seen at higher magnifications, shown in Figure 4.117. The surface is covered by small droplets of material, on the order of 200-400 nm in size.

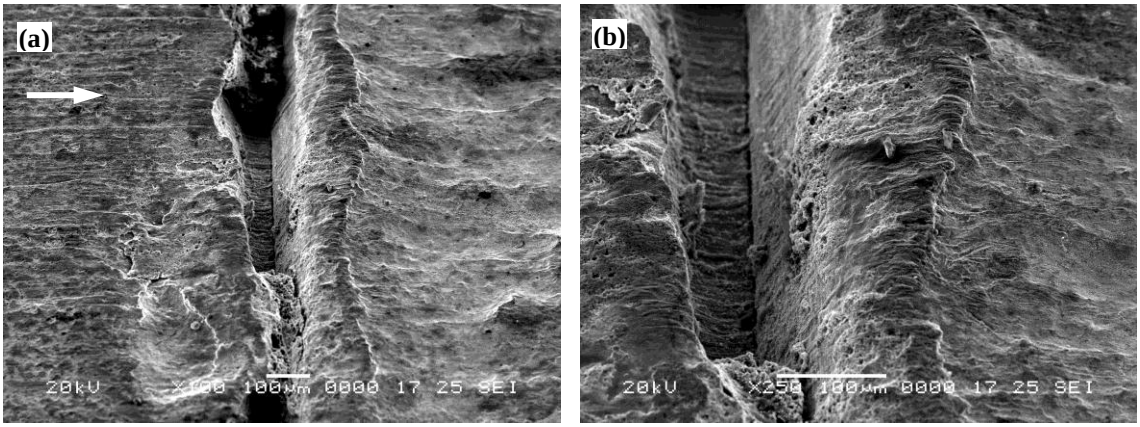

Figure 4.116. SEM images of indented rail at 1.3 m (51.2", 1,300 m/s)

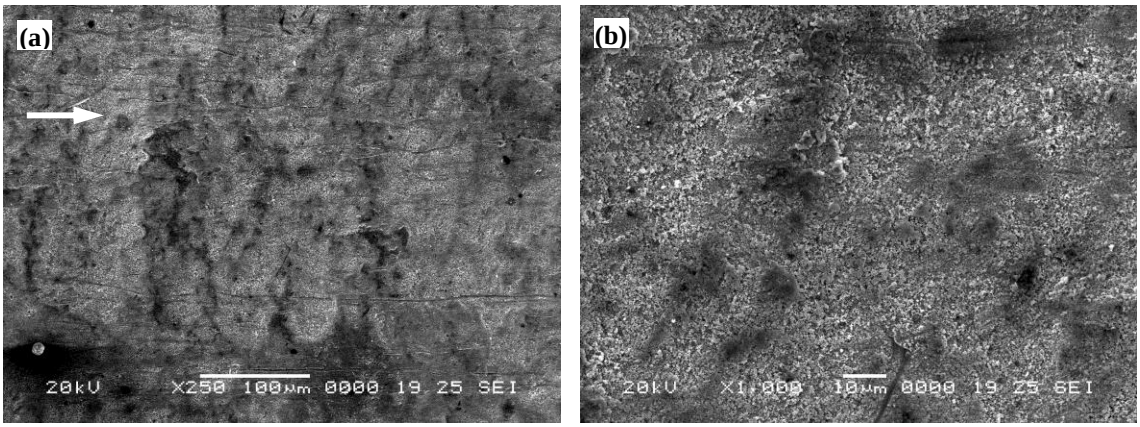

Figure 4.117. SEM images of indented rail at 1.3 m (51.2", 1,300 m/s)

Figure 4.118 shows a composite image of the large gouge crater's lower edge at 1.3 m. The initial deformed lip is followed by a region of small ripples for several mm, which then turns into large-amplitude surface waves which persist for the remainder of the crater.

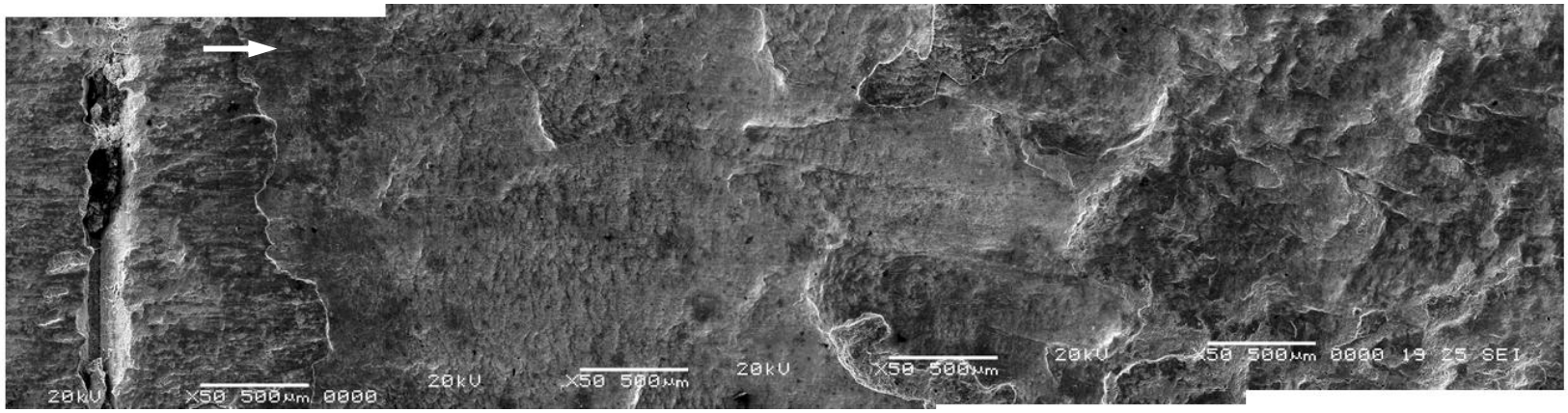

continued below:

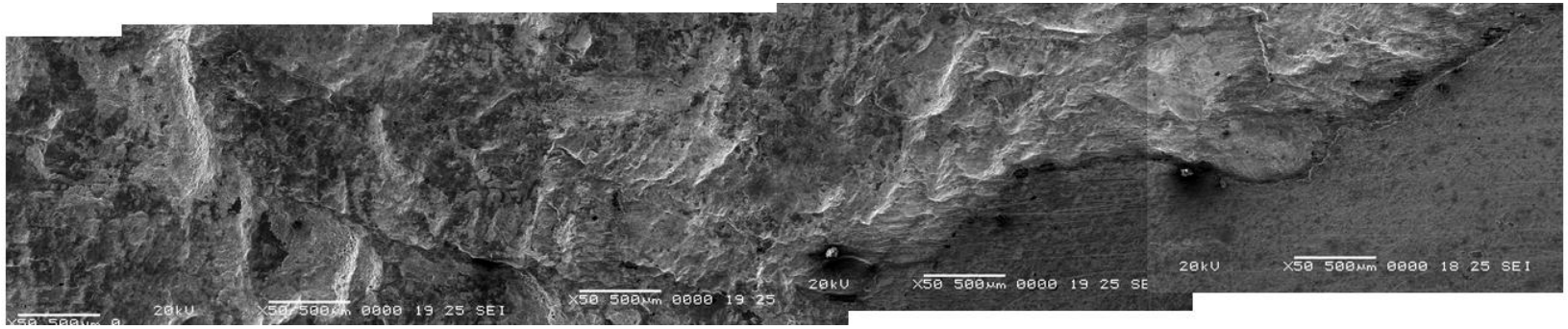

Figure 4.118. SEM images of indented rail gouge crater at 1.3 m (51.2", 1,300 m/s)

SEM images of the (-) etched (flat) rail from HEMCL 1342 are shown at increasing velocities in Figure 4.119 through Figure 4.124. Figure 4.119 shows the long galling trench shown previously in Figure 4.101. There are many fine ripples again observed on the surface of the galling mark, though these appear to be regions of resolidified material and do not show the shear bands observed in previous images.

Figure 4.120 shows gouges which originate from a microscopic surface defect at 0.99 m (39.0", 1,080 m/s). There are multiple craters which are triggered, two of which progress for many centimeters. Figure 4.121 shows the same craters in Figure 4.120 at an angled view.

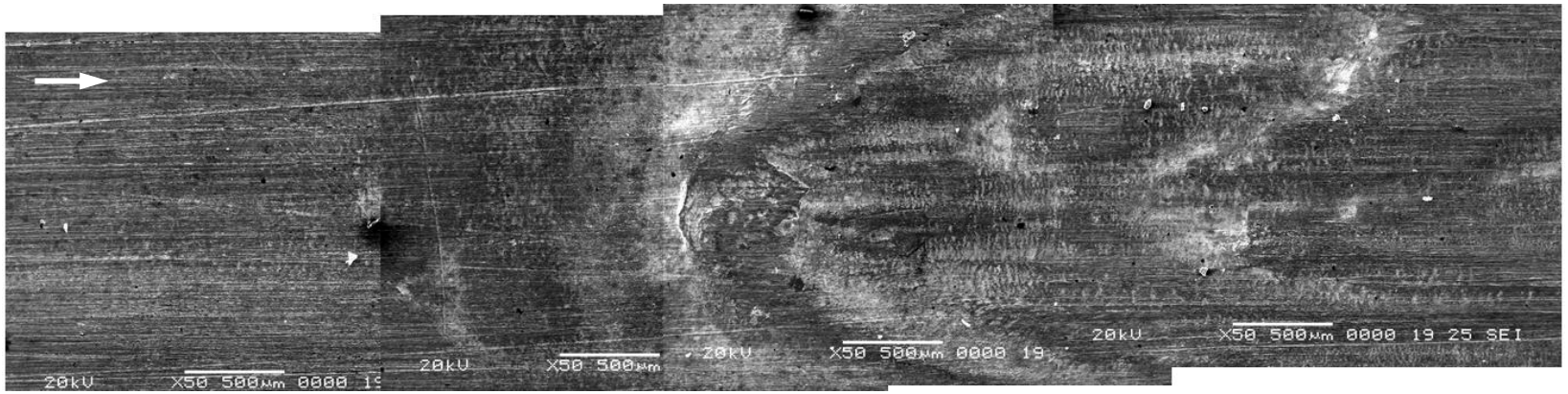

Figure 4.119. SEM images of flat rail galling at 0.63 m (24.8", 805 m/s, HEMCL 1342)

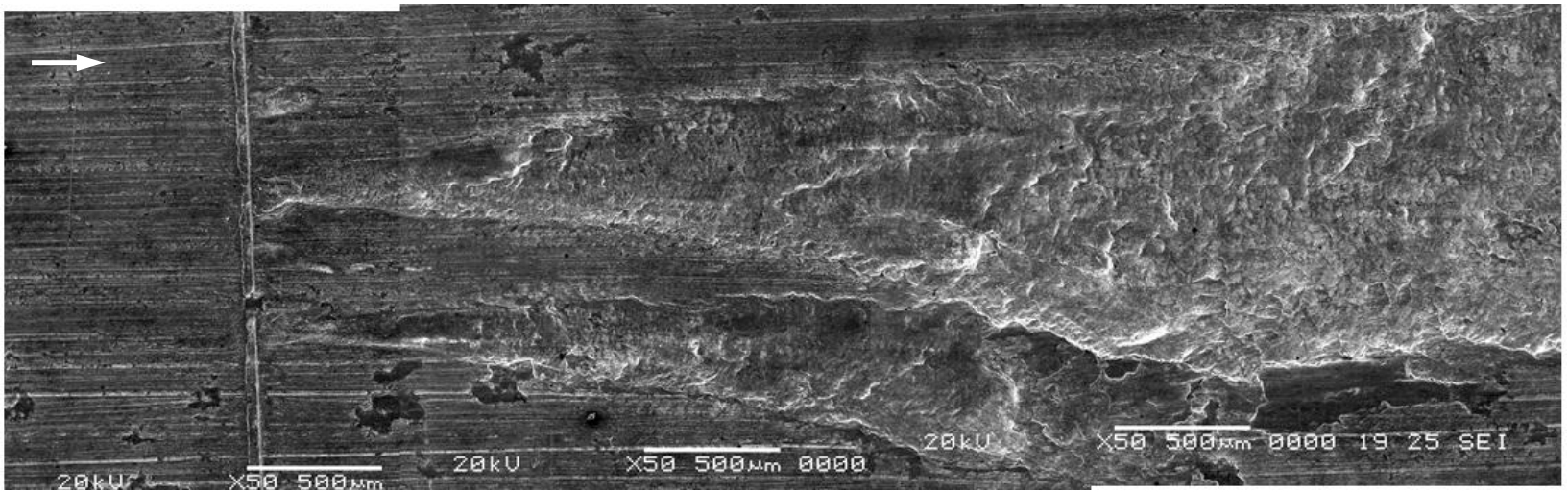

Figure 4.120. SEM images of flat-rail gouging at 0.99 m (39.0", 1080 m/s, HEMCL 1342)

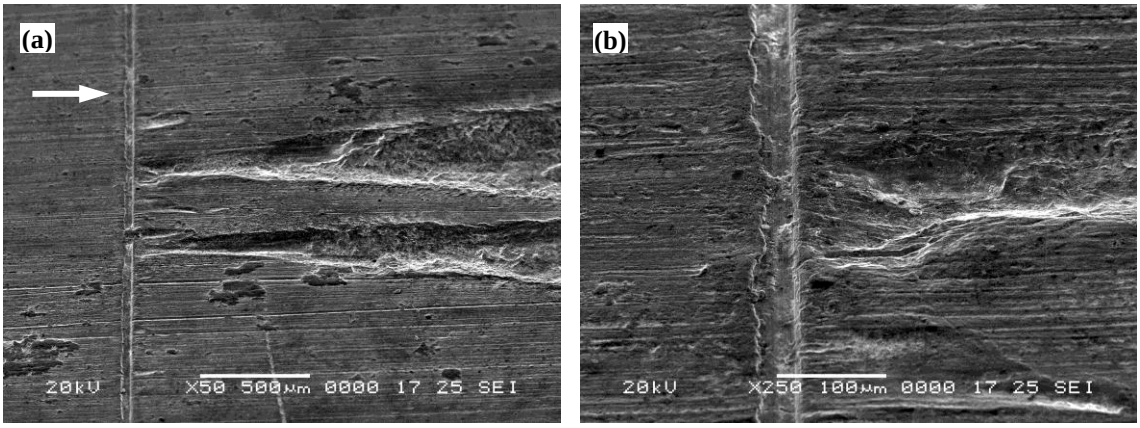

Figure 4.121. SEM images of gouge initiation at existing scratches 0.99 m (39.0", 1,080 m/s, HEMCL 1342)

Figure 4.122 shows the beginning of a gouge crater at 1.06 m (41.7", 1,130 m/s). The initiation region is shown at progressively higher magnifications in Figure 4.123 and Figure 4.124. There is a definite spot where the gouge is started, about 10 μm wide, and resembles a hemisphere. It is possible that an embedded particle in the rail triggered the gouge.

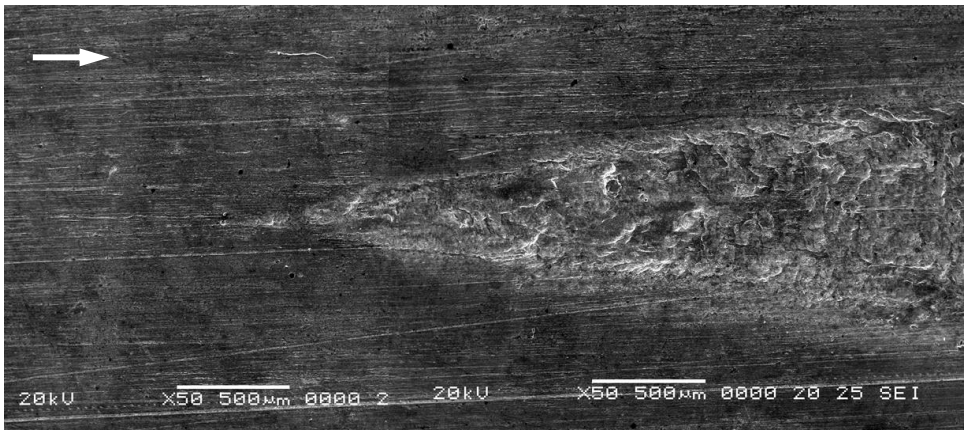

Figure 4.122. SEM images of flat-rail gouge initiation at 1.06 m (41.7", 1,130 m/s, HEMCL 1342)

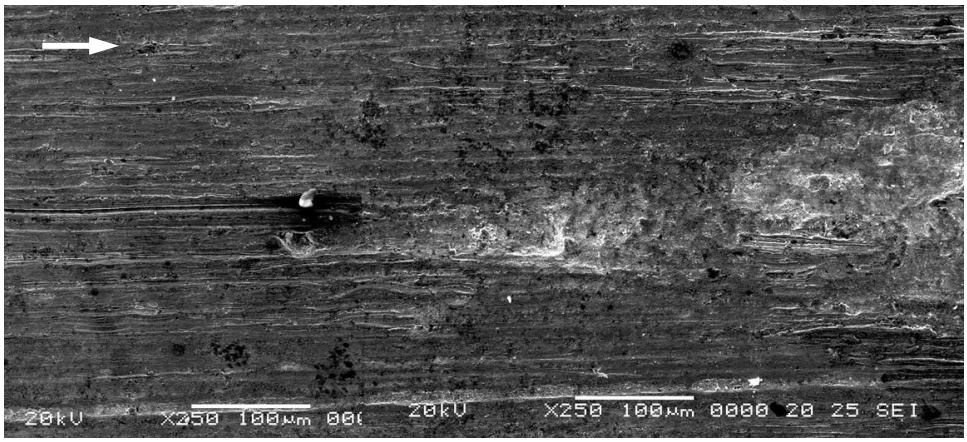

Figure 4.123. SEM image of gouge initiation at defect at 1.06 m (41.7", 1,130 m/s, HEMCL 1342)

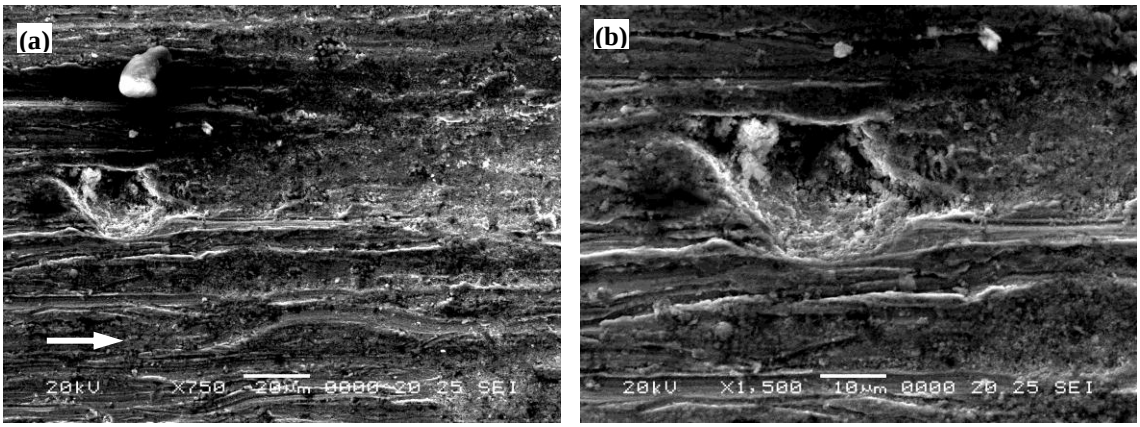

Figure 4.124. SEM images of gouge initiation at defect at 1.06 m (41.7", 1,130 m/s, HEMCL 1342)

Cross-section optical microscope images of the first gouge on the (+) rail are shown in Figure 4.125. As in the previous examples, there is a region of surface ripples just at gouge onset. Inside the gouge crater there are large waves with severely deformed regions of "cresting" waves that suggests the formation of a shear band.

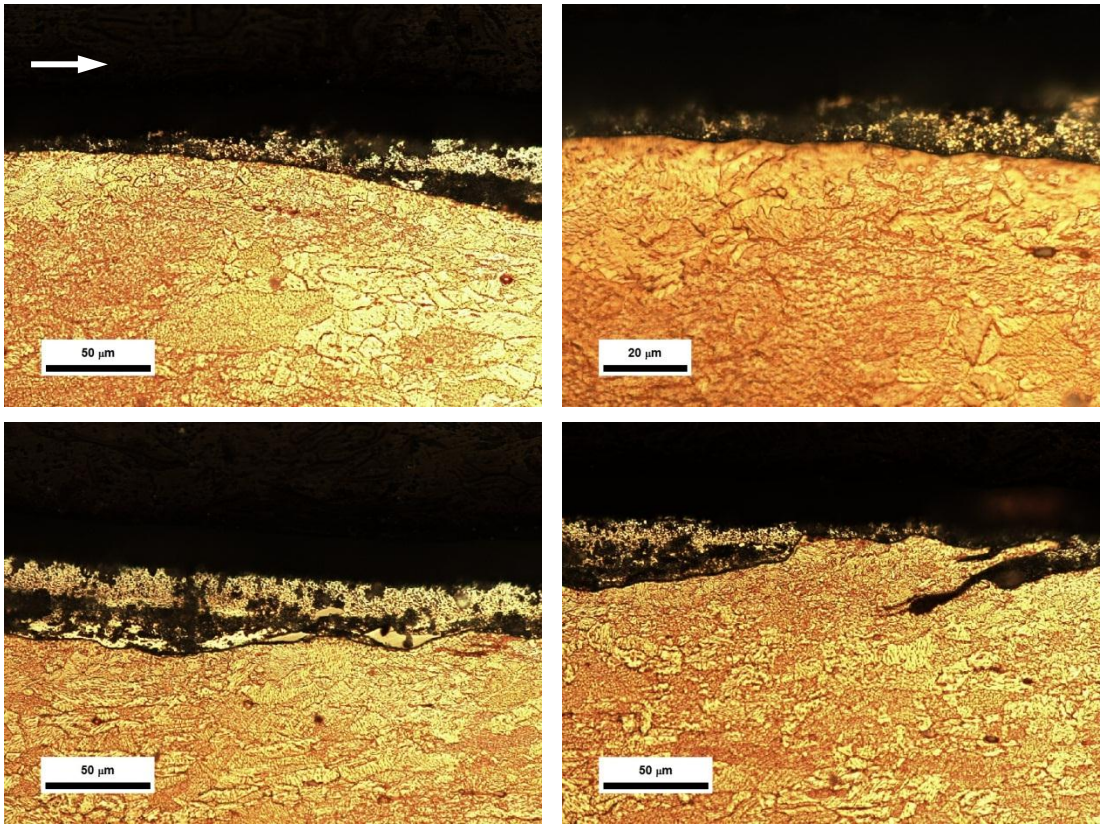

Figure 4.125. Cross-section microscope images of flat rail at 1.0 m (1,130 m/s, HEMCL 1342)

CHAPTER 5. DISCUSSION

5.1 General Experimental Observations

5.1.1 ARMATURES ON FLAT RAILS

Results for the baseline experiments, the uncoated test from Series 3, and the flat rails from Series 4 are shown in Table 5.1. V_{est} is the estimated gouging velocity based on the Stefani-Parker impact model and the effective Reynolds number model developed in Chapter Two. In each of these tests gouging was observed for a C-shaped armature sliding against a flat rail. The slightly increased rail hardness from MCL 609-610 resulted in delayed galling by the C11000 armatures, but did not have an appreciable effect on gouging onset. The increased hardness between C11000, C26000, and C15725 resulted in a significant increase in gouging velocity.

Table 5.1. Gouging results for basic armature experiments

Test #	Slider	Rail	Slider *HV*	Rail *HV*	V_{gall} *m/s*	V_{gouge} *m/s*	V_{est} *m/s*
MCL 609	C11000	C11000	139 ± 4	83 ± 1	683 ± 16	820 ± 12	800
MCL 610	C11000	C11000	139 ± 4	88 ± 4	731 ± 4	820 ± 3	800
HEMCL 1342	AA7075	C11000	176 ± 2	89 ± 2	719 ± 20	1,138 ± 17	1,300
MCL 687	AA7075	C26000	176 ± 2	137 ± 5	~	1,731 ± 26	1,600-1,900
MCL 650	AA7075	C15725	176 ± 2	169 ± 5	~	1,960 ± 100	1,570-2,000

Unlike C11000, the C26000 and C15725 rails did not show any galling prior to gouging. Instead these materials formed the classical tear-drop craters without any obvious precursor damage. The C11000 rails showed galling for both C11000 and AA7075 armatures. The galling damage was worse for the Cu/Cu pair, which was expected, and began well before the gouging craters start to develop (Figure 4.9). The galling for Al/Cu was not as widespread as Cu/Cu, with a few galling marks immediately preceding the gouge craters (Figure 5.2). This latter behavior implies persistent high-spots on the armature contact surface that are responsible for both phenomena.

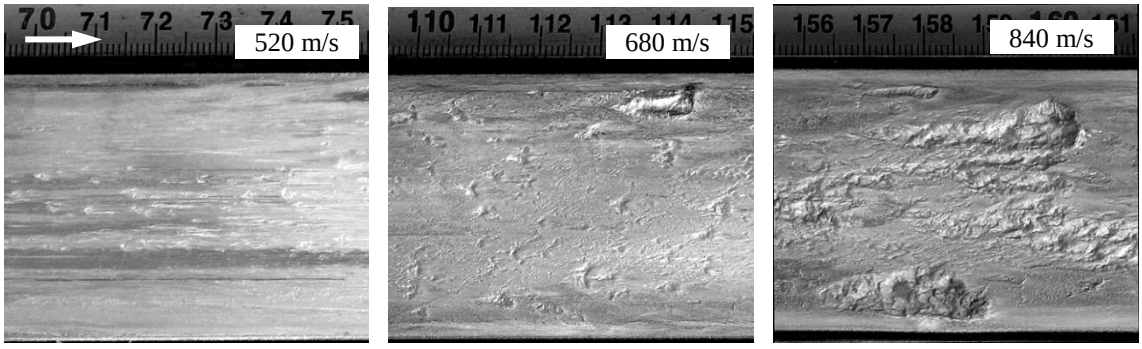

Figure 5.1. Sliding damage from C11000 on C11000 at increasing velocity (MCL 609)

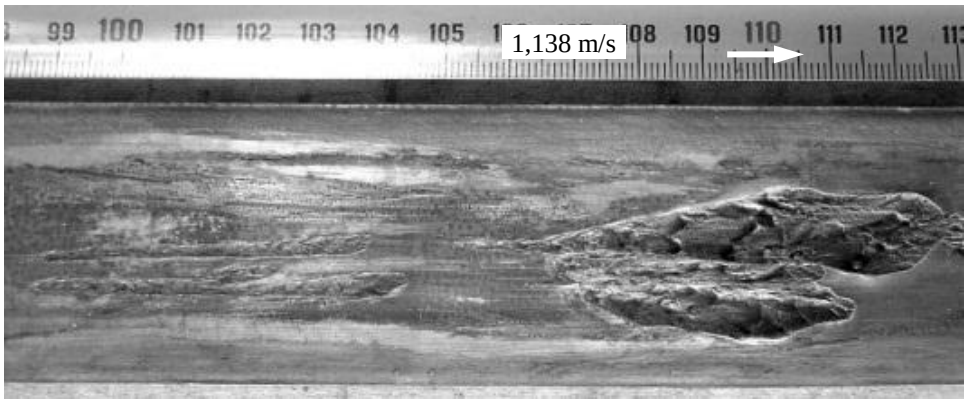

Figure 5.2. Sliding damage from AA7075 on C11000 (HEMCL 1342)

An unexpected deviation from previous results is the gouging velocity for AA7075 on C11000 (HEMCL 1342), which was observed at 1,138 m/s. Gouging of AA7075 on C11000 has been observed numerous times in the MCL to be closer to 1,300 m/s. This amounts to a 20% reduction in gouging velocity. The difference could be due to the increased apparent contact pressure between the MCL and HEMCL experiments. HEMCL uses a different bore and a higher current, and the bore pressure (Lorentz force divided by bore area) is increased by 30% relative to the MCL.

5.1.2 SLIDER EXPERIMENTS:

Results for the slider experiments are summarized in Table 5.2, in order of increasing slider hardness. Grey numbers indicate damage at the leading of the cladding,

which serves as an upper bound for the threshold velocity. The galling tracks seen for the harder slider materials are often several times longer than the sliders. This indicates that the sliders remain largely intact during the galling process. This is supported by muzzle X-rays which do not show appreciable net removal of slider material. Galling damage is observed for all materials *except* AA1100 and MACOR®. It is likely that this absence of rail galling is because the hardness values are less than the rails'. A plausible scenario is that galling is occurring on the slider material while the rail remains intact, the opposite of what occurs for the harder slider materials.

Table 5.2. Gouging results for slider experiments (C11000 rail, HV 83 ± 4)

Test #	Slider	Slider HV	V_{edge} *m/s*	V_{gall} *m/s*	V_{gouge} *m/s*	V_{est} *m/s*
MCL 678	AA1100 H14	42 ± 2	563 ± 26	~	1,341 ± 23	900-1,200
MCL 680	MACOR®	80 ± 20	1,082 ± 88	~	1,267 ± 23	1,300
MCL 677	Tantalum	129 ± 6	563 ± 44	756 ± 44	1,495 ± 63	600-800
MCL 679	Zirconium	210 ± 12	562 ± 161	770 ± 161	1,495 ± 49	1,100
MCL 682	4340 HRC 27	276 ± 9	1,087 ± 36	1,130 ± 37	1,447 ± 46	1,100-1,300
MCL 623	4140 HRC 35	318 ± 6	0	997 ± 11	1,285 ± 11	1,300-1,400
MCL 681	4340 HRC 35	348 ± 16	1,073 ± 95	1,073 ± 95	1,743 ± 65	1,300-1,400
MCL 684	4340 HRC 41	420 ± 18	1,122 ± 71	1,478 ± 10	~	1,600-1,700
MCL 685	4340 HRC 51	597 ± 16	1,425 ± 22	1,440 ± 19	1,879 ± 68	1,700-2,100
MCL 686	4340 HRC 59	724 ± 28	1,415 ± 29	1,435 ± 26	~	2,000-2,700

The gouging behavior follows the expected trend of increasing threshold velocity with increasing slider hardness. In most of the steel slider tests, galling begins immediately after the rail cladding starts, so a threshold cannot be determined. Galling damage is generally reduced for harder steel sliders, which is in basic agreement with adhesive wear theory as discussed in Chapter One.

Based on previously-developed gouging models (Stefani-Parker impact model and the effective Reynolds number model) the predicted onset of gouging occasionally corresponds to galling instead of gouging. This occurs for the tantalum and AISI 4340 HRC 27/41 sliders.

5.1.3 ALUMINUM COATINGS:

Thin aluminum coatings appear to be an effective mechanism at preventing gouging in a railgun. It is believed that the low acoustic impedance of the coating layer acts as a shield for the substrate material. Pure aluminum layers proved just as effective as preventing gouging as the aluminum deposits laid down by armatures which contain hard oxides and Al-Cu inter-metallic compounds.

While the simple armatures did not produce any gouges on electroplated rails, the coatings failed in the slider experiments (Table 5.3). V_{edge} is the velocity at the leading edge of the rail cladding. The likely reason for this is that the contact pressure after chamfering the inner contact edge of the armature was high enough to significantly plastically deform both the rail substrate and the aluminum layer. The average contact pressure for the chamfered armatures was calculated to be around 50 ksi (350 MPa). The basic armatures, in contrast, had average contact pressures around 25 ksi (175 MPa).

Table 5.3. Galling and gouging damage on stripe-electroplated rails (AA7075-T6 HV-176 armature)

MCL #	Rail Material	Hardness *HV*	V_{edge} *m/s*	V_{gall} *m/s*	V_{gouge} *m/s*	V_{est} *m/s*
623	C11000-H02 plain	83 ± 4	0	975 ± 11	1,285 ± 11	~1,300
677	C11000-H02 plated	41 ± 1	563 ± 44	899 ± 37	1,312 ± 32	"
678	"	"	563 ± 26	975 ± 18	1,370 ± 23	"
679	"	"	562 ± 161	894 ± 161	1,347 ± 11	"
680	"	"	1,082 ± 88	1,095 ± 84	1,543 ± 54	"
681	"	"	1,073 ± 95	1,289 ± 20	1,392 ± 15	"
682	"	"	1,087 ± 36	~	1,574 ± 55	"
684	"	"	1,122 ± 71	1,478 ± 10	1,807 ± 57	"
685	"	"	1,425 ± 22	~	1,425 ± 22	"
686	"	"	1,415 ± 29	~	1,415 ± 29	"

Coating failures occurred via both galling and gouging damage. Galling damage occurred between 900-980 m/s, or at the leading edge of the rail cladding when the starting velocity was above that. Gouging occurred in four of the experiments just above the uncoated predicted gouging velocity of 1,300 m/s. In three of the experiments gouging was delayed. It is not clear why. For rail claddings whose velocities at the

leading edge were above 1,300 m/s (MCL 685-686), gouges were observed on the leading edges of the claddings.

The initiation of gouges at the leading edge of the coated claddings occurred for both the stripe-electroplated rails as well as the fully-electroplated rails (Figure 4.87). However, for the fully electroplated rails no downstream gouges were observed. These leading edge gouges (shown in Figure 5.3) could be the result of exposed substrate material, a different stress state in the cladding caused by the free surface, or a raised edge acting as a perturbation. One common feature for leading edge gouging is that it only occurs if the slider/rail material pair normally gouges at that velocity. The velocities at the leading edges are listed in Table 5.4.

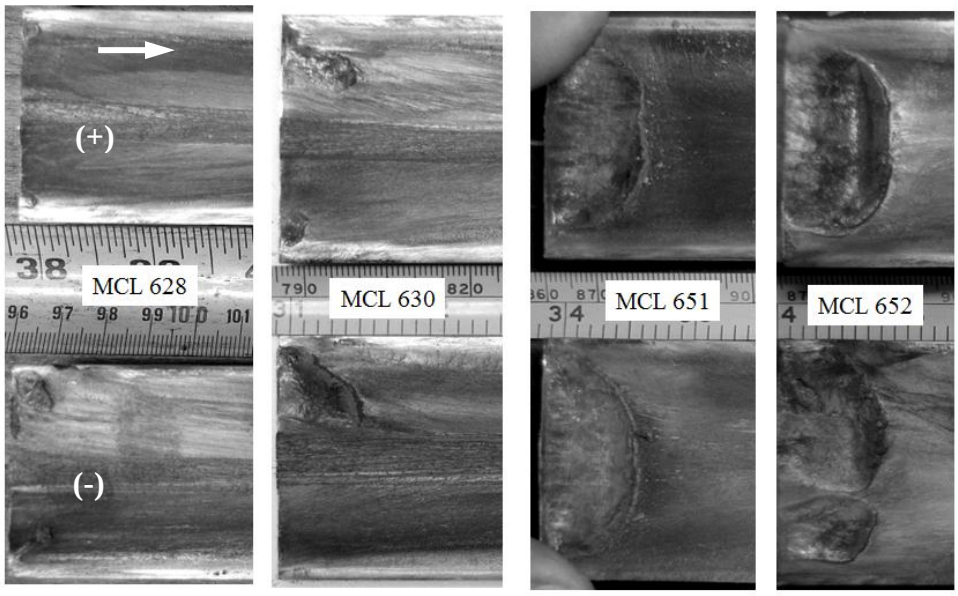

Figure 5.3. Gouging at leading edge of fully-coated rail claddings

Table 5.4. Leading-edge gouging observations (AA7075-T6 armature, HV 176 ± 2)

MCL #	Rail	Rail *HV*	Coating *HV*	V_{edge} *m/s*	V_{est} *m/s*	Result
628	C15725 + 25 μm Al	169 ± 5	47 ± 2	1,850 ± 11	1,570-2,000	Gouge
629	C15725 + 50 μm Al	"	"	1,880 ± 175	"	Gouge
630	C15725 + 5 μm Al	"	"	1,930 ± 179	"	Gouge
651	C15725 + 5 μm Al	"	"	1,900 ± 131	"	Gouge
652	C15725 + 5 μm Al	"	"	1,910 ± 15	"	Gouge
653	C15725 + 2 μm Al	"	"	1,920 ± 24	"	Gouge
677	C11000	83 ± 4	41 ± 1	563 ± 44	~1,300	No gouge
678	"	"	"	563 ± 26	"	No gouge
679	"	"	"	562 ± 161	"	No gouge
680	"	"	"	1,082 ± 88	"	No gouge
681	"	"	"	1,073 ± 95	"	No gouge
682	"	"	"	1,087 ± 36	"	No gouge
684	"	"	"	1,122 ± 71	"	No gouge
685	"	"	"	1,425 ± 22	"	Gouge
686	"	"	"	1,415 ± 29	"	Gouge

5.1.4 RAIL INDENTATION TESTS:

A central question from nonlinear instability theory is what size of disturbance is required for unstable flow. Typical rail preparation involves sanding with 600-grit paper to remove scale, followed by cleaning with ethanol and a Scotch-Brite™ 3M No. 7447 aluminum oxide pad. The resulting average surface roughness is on the order of 1 μm. In the previous series, the leading edge of rails consistently initiated gouging. The effective size of the leading-edge surface perturbation should possess an amplitude less than 0.002" (50 μm) based on machining tolerances.

Both the unmodified and indented surfaces suffered galling (~700 m/s) and gouging (~1,100 m/s) at about the same velocities. Gouging on both rails also generated craters which were more elongated than the typical tear-drop gouge shape, although they did not exceed the armature contact length (see Figure 4.102). For both galling and gouging the nature of the damage is significantly affected by indentations. For flat rails, both galling and gouging start at a point and then propagate outward. The distinguishing feature between the two is that galling forms a track which does not significantly change

its width or depth for its duration. Gouging, on the other hand, starts at a small point and increases in both width and depth until it nears the free edge of the slider.

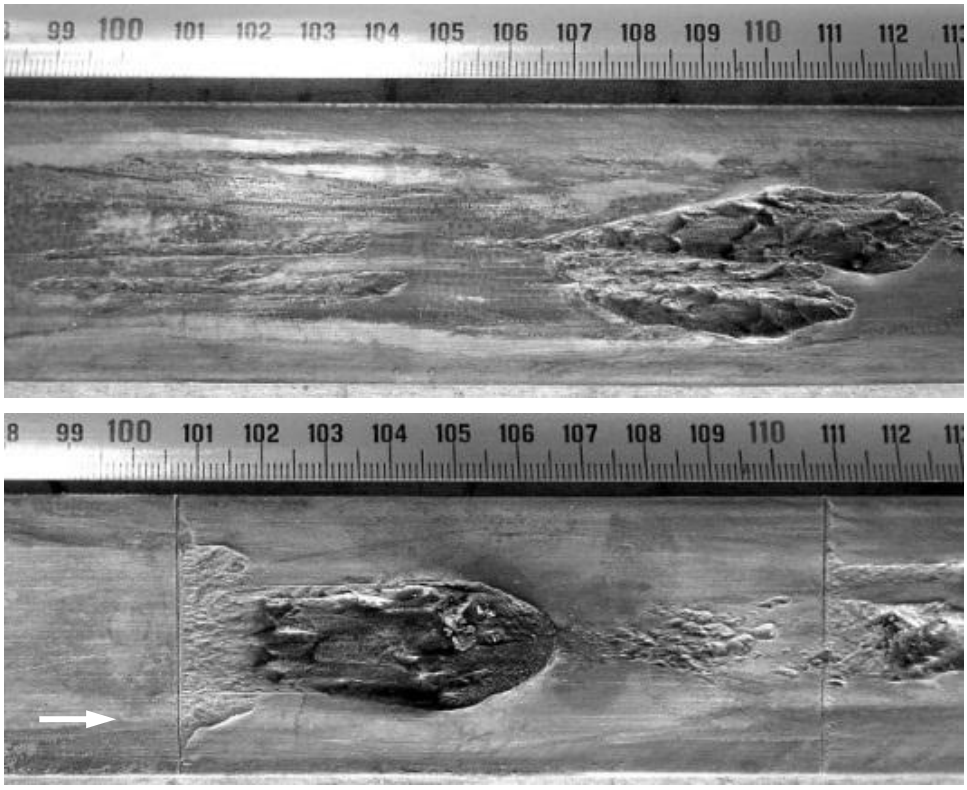

Figure 5.4. Gouging on flat (top) and indented (bottom) rail surfaces (~1,100 m/s)

For the indented rails, both galling and gouging are initiated over a span of tens of millimeters. The galling tracks increase in duration as velocity increases. At 1,100 m/s the galling tracks extend from the indent for ~12 mm, then result in a gouge crater. As velocity increases, the span between galling and gouging decreases until a gouge crater forms immediately downstream of the indentation. The velocity at which gouge craters form without a preceding region of galling corresponds to the gouging velocity of 1,300 m/s for AA7075/C11000 in previous MCL experiments.

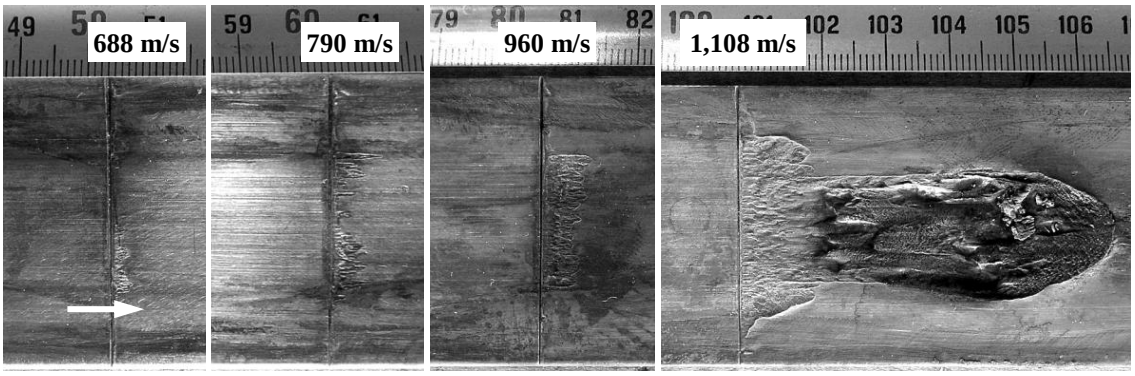

Figure 5.5. Galling sheets prior to gouging (part 1)

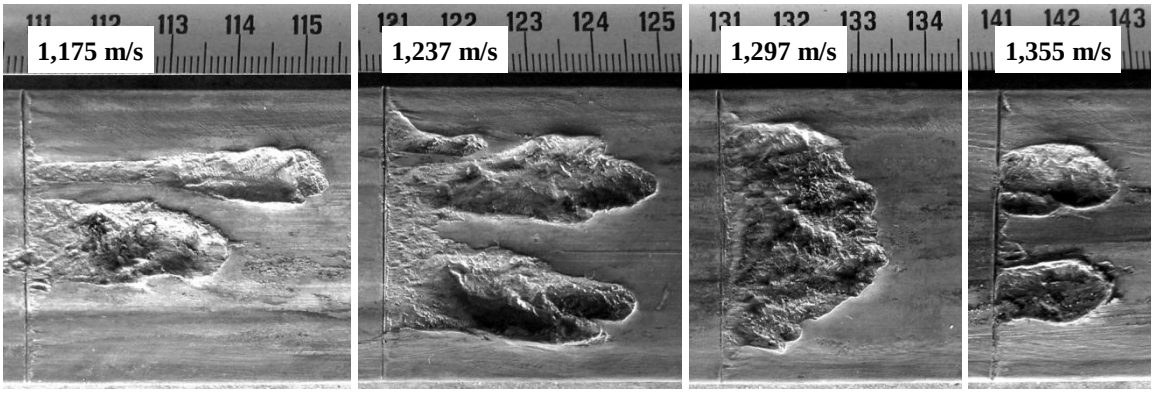

Figure 5.6. Galling sheets prior to gouging (part 2)

Based on the relative behavior of gouging on flat and indented rails under the same launch conditions, it seems reasonable to declare that indentations do not have a first-order effect on the gouging threshold velocity, but do affect the geometry of the resulting gouges.

5.1.5 SUMMARY OF GOUGING OBSERVATIONS:

Perhaps the most striking result in the experiments is the persistent lack of a well-defined gouging threshold for the observed material combinations. Historically gouging has been presented as a sudden change from mild wear to catastrophic crater formation. It is not clear why such a departure from this model is being observed. A summary of the galling and gouging damage observed in the experiments is provided in Table 5.5.

Table 5.5. Galling and Gouging Results

Test #	Slider	Rail	Bore Pressure *MPa*	V_{gall} *m/s*	V_{gouge} *m/s*
MCL 623	AISI 4140 HV-318	C11000 HV-83	45.3	997 ± 103	1,285 ± 82
MCL 682	AISI 4340 HV-276	C11000 HV-83	58.9	1,130 ± 37	1,447 ± 46
MCL 681	AISI 4340 HV-343	C11000 HV-83	57.2	1,073 ± 95	1,743 ± 65
MCL 684	AISI 4340 HV-420	C11000 HV-83	58.4	1,478 ± 10	~
MCL 685	AISI 4340 HV-597	C11000 HV-83	59.9	1,440 ± 19	1,879 ± 68
MCL 686	AISI 4340 HV-724	C11000 HV-83	59.1	1,435 ± 26	~
MCL 680	MACOR® HV-80	C11000 HV-83	44.9	~	1,267 ± 23
MCL 677	Tantalum HV-129	C11000 HV-83	79.5	756 ± 44	1,495 ± 63
MCL 679	Zirconium HV-210	C11000 HV-83	54.7	770 ± 161	1,495 ± 49
MCL 609	C11000 HV-139	C11000 HV-83	132	683 ± 16	820 ± 12
MCL 610	C11000 HV-139	C11000 HV-88	134	731 ± 4	820 ± 3
MCL 678	AA1100 HV-42	C11000 HV-83	45.5	~	1,341 ± 23
MCL 623	AA7075 HV-176	C11000 HV-83	330	975 ± 11	1,285 ± 11
HEMCL 1342	AA7075 HV-176	C11000 HV-89	199	719 ± 20	1,138 ± 17
HEMCL 1341	AA7075 HV-176	C11000 HV-89 (I)	201	688 ± 17	1,109 ± 14
MCL 650	AA7075 HV-176	C15725 HV-169	186	~	1,960 ± 100
MCL 687	AA7075 HV-176	C26000 HV-137	167	~	1,731 ± 26

The only material combinations that did not suffer any galling damage prior to gouging were the C26000 and C15725 rails, and the AA1100 and MACOR® sliders on C11000. It is likely that the hardness of the AA1100 and MACOR® sliders was less than the rails and therefore failure occurred preferentially in the slider material. While the sliders on the C15725 and C26000 rails did not generate galling damage, they were only harder than the rails by 4% and 25%, respectively. It is possible that frictional heating resulted in sufficient thermal softening to bring the slider hardness below that of the rail.

It is interesting that galling damage on C11000 rails occurred around 700 m/s for C11000, AA7075, Ta, and Zr sliders. Only the steel sliders appear to have an increased galling velocity. This is somewhat expected because galling is initiated by the formation of metallic junctions, and the above materials have a greater chemical compatibility with copper than does iron, according the Rabinowicz's theory of adhesion [6]. To see if galling follows a similar trend as gouging, the acoustic stresses were calculated at the galling velocities and plotted vs. the maximum and average hardness values, as was done

for the gouging velocities. The results are shown in Figure 5.7 and Figure 5.8, together with the previous gouging data.

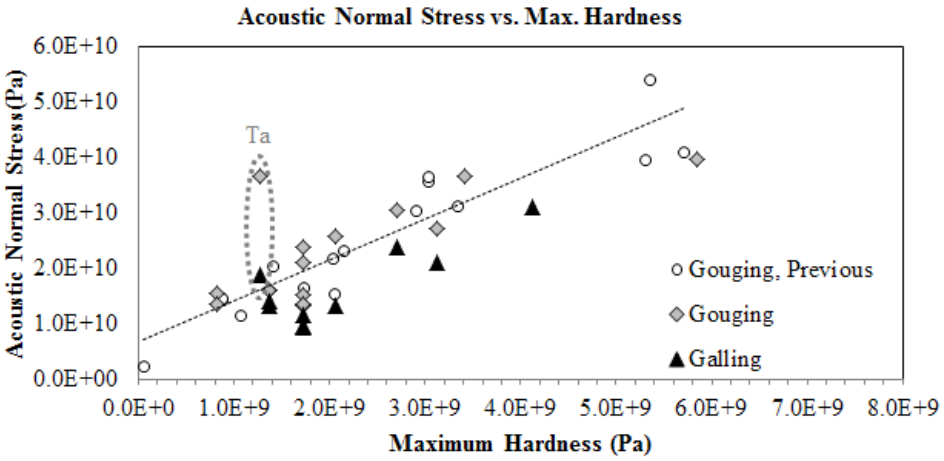

Figure 5.7. Galling and gouging acoustic normal stress vs. max hardness

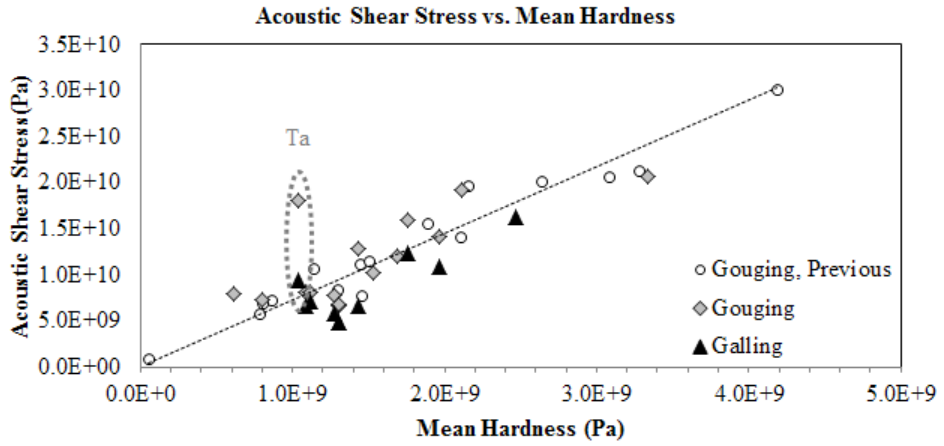

Figure 5.8. Galling and gouging acoustic shear stress vs. mean hardness

In general, the gouging behavior of the current series matches the published data. A notable exception is the data for Tantalum, indicated by the dotted ellipse. In this case the Ta/Cu galling velocity matches the expected trend much better than the gouging velocity. This could be due to the complex strain- and strain-rate hardening behavior of

pure Tantalum [199]. In general, the galling pressures follow the same trend as gouging, with increased hardness resulting in an increased galling threshold.

An earlier observation called into question the effect of contact pressure on gouging. The relevant data concerning this is provided in Table 5.6. Gouging observed in previous MCL experiments for AA7075/C11000 occurred around 1,300 m/s. In the HEMCL experiments gouging occurred around 1,100 m/s. The contact pressure was calculated for the MCL slider armature on plain C11000 rails and was found to be even higher than the HEMCL tests, yet the gouging velocity for that experiment was about the same as previous MCL experiments despite a four-fold increase in contact pressure. This behavior can partly be explained through the concept of real vs. apparent contact area: As the load is increased, the surface accommodates it by forcing more asperities into contact, not necessarily by significantly increasing the pressure at a given asperity.

Table 5.6. Contact pressure effects on galling and gouging

Test #	**Slider**	**Rail**	**Bore Pressure** *MPa*	$\mathbf{V_{gall}}$ *m/s*	$\mathbf{V_{gouge}}$ *m/s*
Stefani *et al.* [25]	AA7075 HV-175	C11000 HV-88	80	~	1,300 ± 65
HEMCL 1342	AA7075 HV-176	C11000 HV-89	199	719 ± 20	1,138 ± 17
MCL 623	AA7075 HV-176	C11000 HV-83	330	975 ± 11	1,285 ± 11

A plot of the gouging pressures is plotted vs. the average hardness again in Figure 5.9. Except for the tantalum slider, the results agree quite well with the previously reported data.

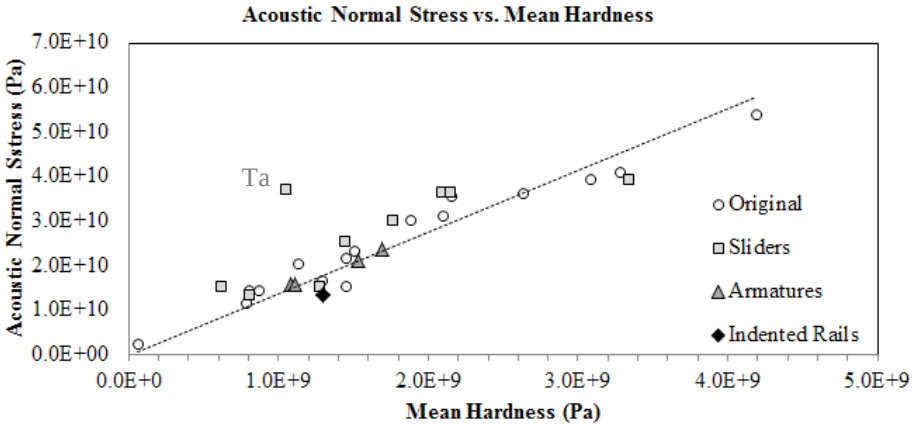

Figure 5.9. Existing and new gouging data: acoustic stress vs. mean hardness

Thin rail coatings can prevent gouging in low pressure contacts, but contact pressures that well exceed the strength of the coating and substrate can result in gouging. This also applies to galling damage. The same principle holds true for macroscopic surface perturbations, as in the case of exposed rail edges perpendicular to the direction of launch. However, there is likely some critical perturbation size relative to the coating thickness for this to be the case. Future tests would prove useful in determining this critical size.

5.2 Microstructural Observations

5.2.1 ARMATURES ON FLAT RAILS:

Both galling and gouging damage initiate at existing defects. In most cases these are machining marks as shown in Figure 5.10 for AA7075/C11000, and Figure 5.11 for C11000/C11000 contacts. Many of the triggering perturbations are very small, on the order of a few micrometers. In some cases a void is seen at the onset of gouging as shown in Figure 5.12. This is likely the result of an embedded third-body particle that gets torn out as the slider encounters it.

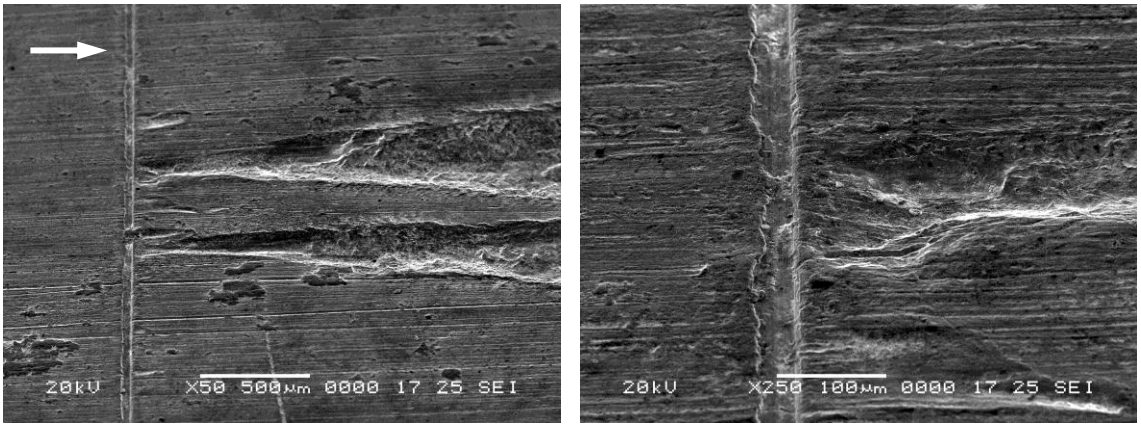

Figure 5.10. SEM images of gouge initiation for AA7075/C11000 at 1,080 m/s (HEMCL 1342)

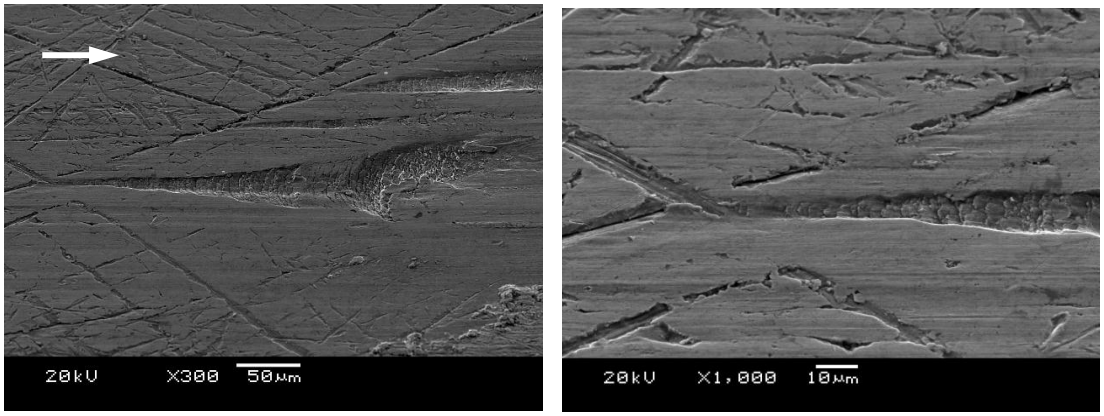

Figure 5.11. SEM images for Cu/Cu galling at 510 m/s (MCL 609)

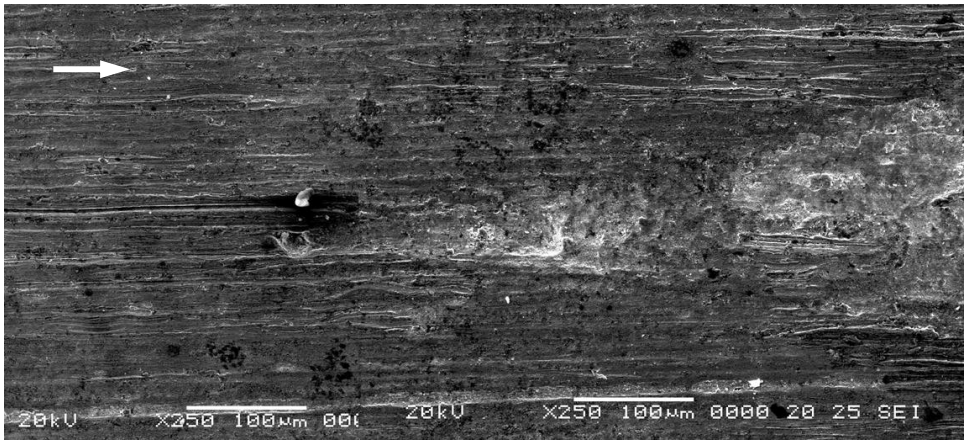

Figure 5.12. SEM image of Al/Cu gouge initiation at point defect at 1,130 m/s (HEMCL 1342)

A prominent feature appearing at the onset of both galling and gouging of the Cu/Cu material pair is the presence of deformation bands, though their character changes with distance and velocity. An example of this is shown in Figure 4.22 which shows a high-speed galling mark. Early on, the deformed bands are angled to the surface with a pitch of 1-2 micrometers. These could be shear bands, although the band spacing is extremely small [55]. The deformation bands bear a striking resemblance to persistent slip bands (PSBs), which are typically found in high-cycle loading conditions (Figure 5.14) [200]. However, PSBs have a preferred crystallographic preference, so one would expect to see intermittent variations in band angle relative to the surface. The region in the middle of the gall in Figure 4.22 could be an example of this.

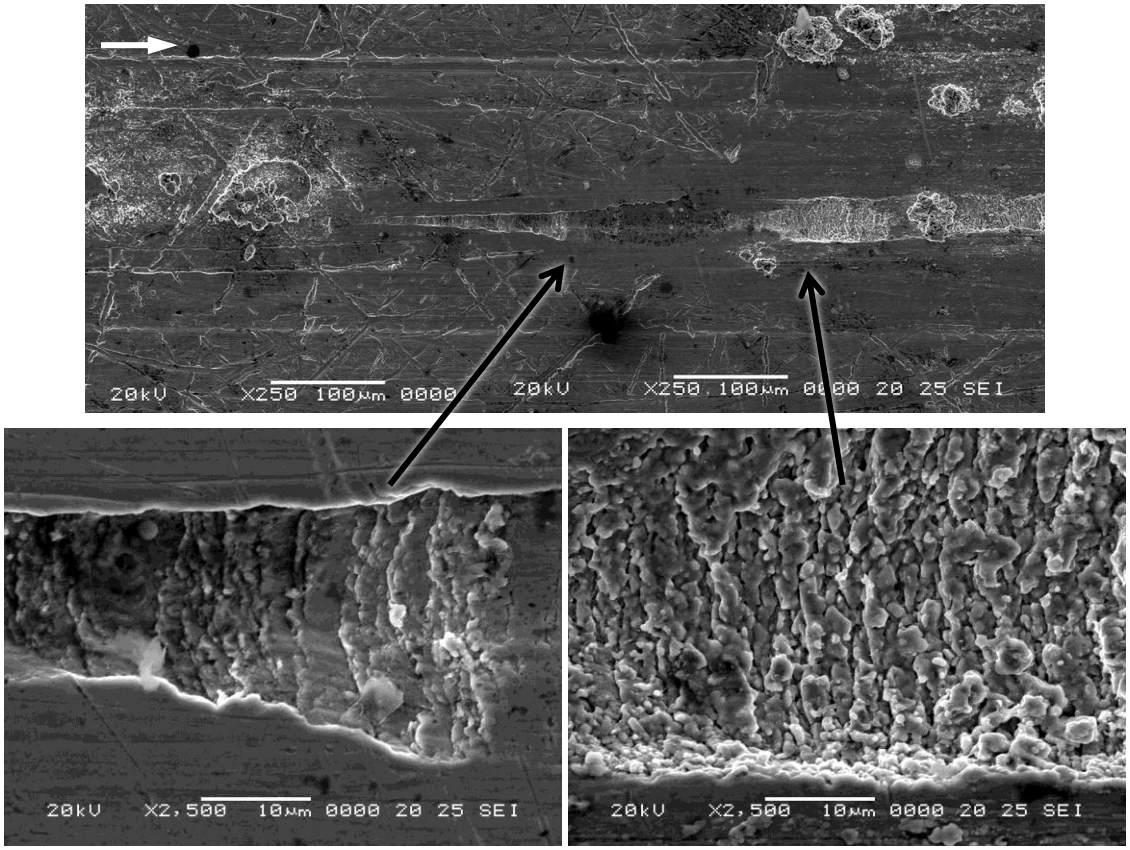

Figure 5.13. SEM images of Cu/Cu galling damage evolution at 580 m/s (MCL 610)

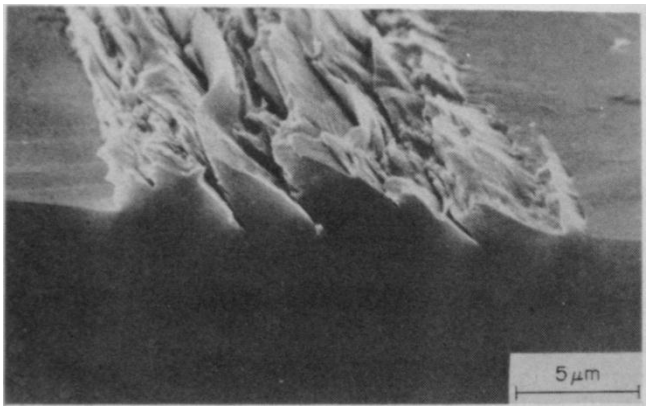

Figure 5.14. Persistent slip bands in copper subjected to 0.2% plastic strain for 60,000 cycles[20]

[20] Reprinted from A. Hunsche, P. Neumann, "Quantitative measurement of persistent slip band profiles and crack initiation," Acta metall., Vol. 34, No. 2, pp. 207-217, Copyright 1986, with permission from Elsevier

Prior to gouging, there is a region of surface damage similar to the bands shown previously. However, at these higher speeds the bands are 100-300 nm wide, about two orders of magnitude smaller than those that occur at lower speeds (Figure 5.15). Within 20-50 μm, the bands are replaced by re-solidified material, though there is still an "imprint" of a banded structure (Figure 5.16). This suggests that the microstructural process responsible for damage at slower speeds is also responsible for initiating a gouge. Once inside the gouge crater there is significant melting, as shown in Figure 5.17.

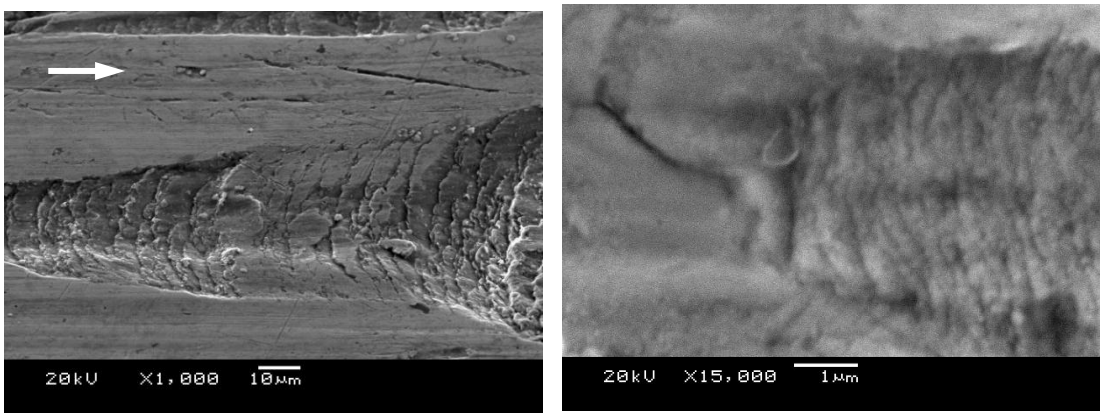

Figure 5.15. SEM images of galling and gouging deformation bands
Left: 510 m/s, right: 960 m/s (MCL 609)

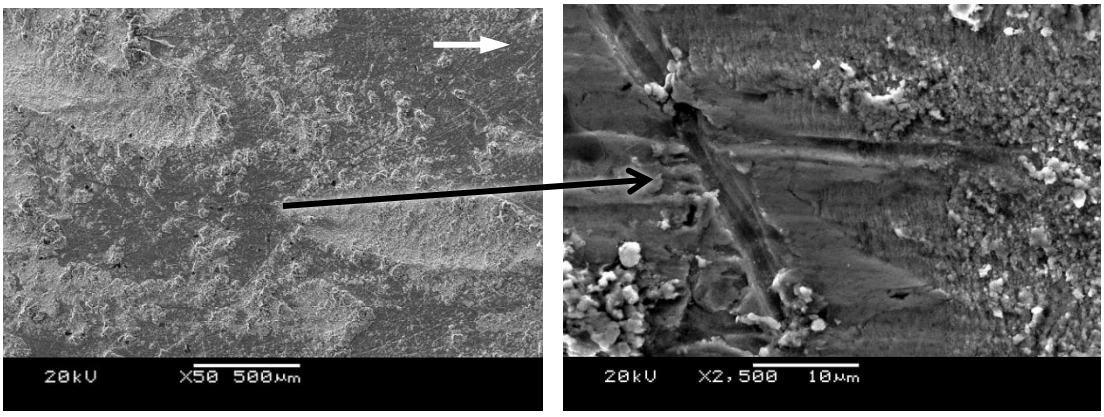

Figure 5.16. SEM images of Cu/Cu gouge initiation at 960 m/s (MCL 609)

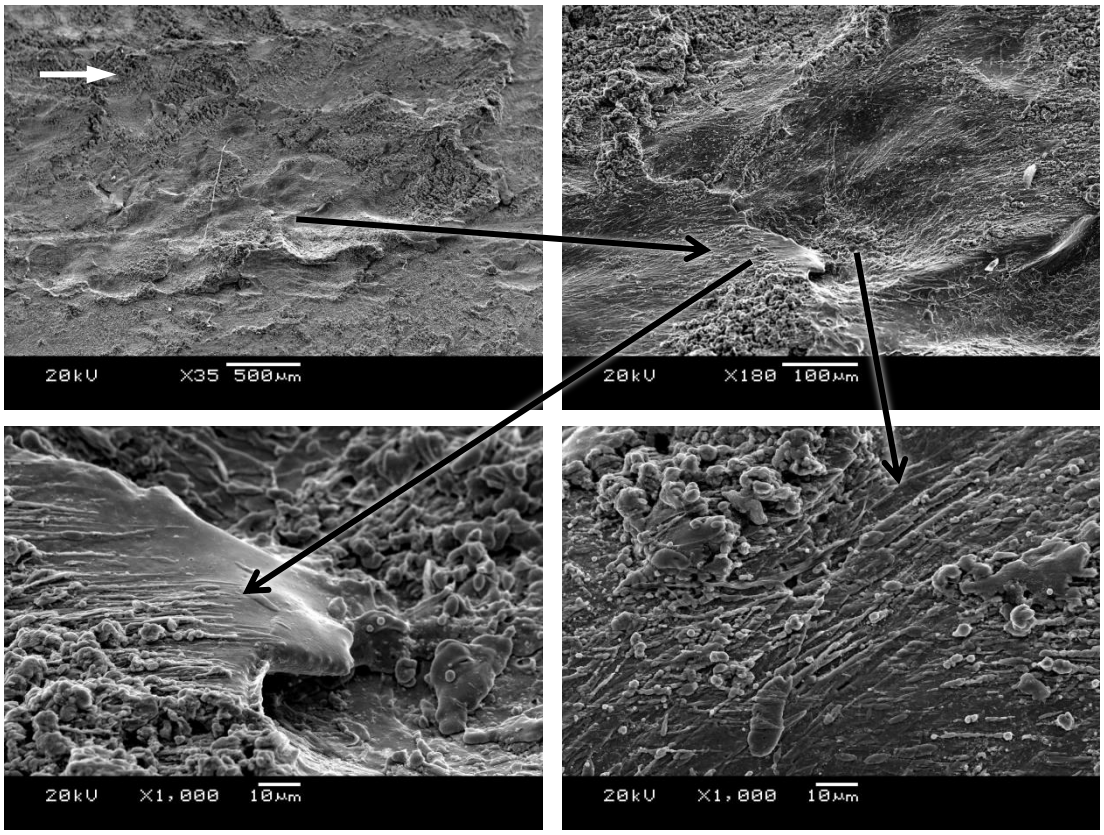

Figure 5.17. SEM images of melting in gouge crater at 944 m/s (MCL 609)

At the downstream end of the gouge crater there is a lip of raised material (Figure 5.18). Beyond the lip is a region of severely deformed material, not unlike what occurs during plowing wear at lower speeds (Figure 5.19). The gouge crater surface is resolidified up to the edge of the lip, indicating highly localized heating.

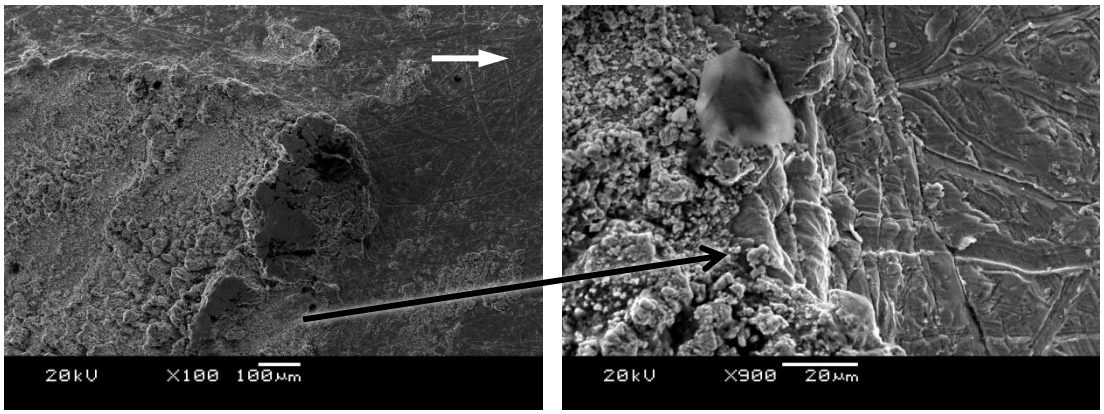

Figure 5.18. Downstream crater lip of Cu/Cu gouge at 960 m/s (MCL 609)

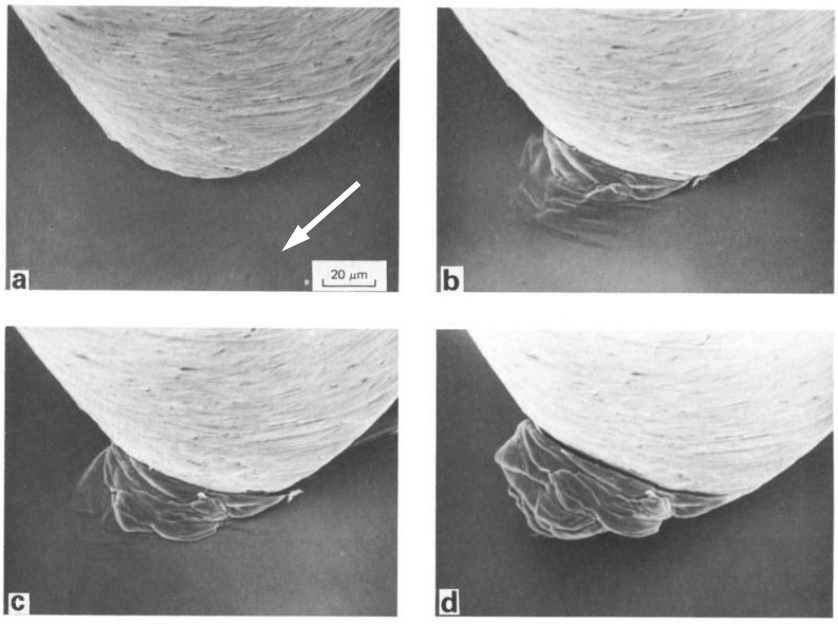

Figure 5.19. SEM image of a steel pin plowing a stainless steel rail at increasing times[21]

In the case of railgun armatures an additional source of heat comes from Ohmic losses. The majority of Ohmic heating takes place near the armature contact edge, as magnetic diffusion restricts current to the outer edges [201]. This usually melts the edges

[21] Reprinted from K. Hokkirigawa, K. Kato, "An experimental and theoretical investigation of ploughing, cutting and wedge formation during abrasive wear," Tribology International, Vol. 21, No. 1, pp. 51-57, Copyright 1988, with permission from Elsevier

of the armature, and in the case of Cu armatures on Cu rails, it also results in melting of the rail. This is shown at armature startup in Figure 5.20 through Figure 5.22.

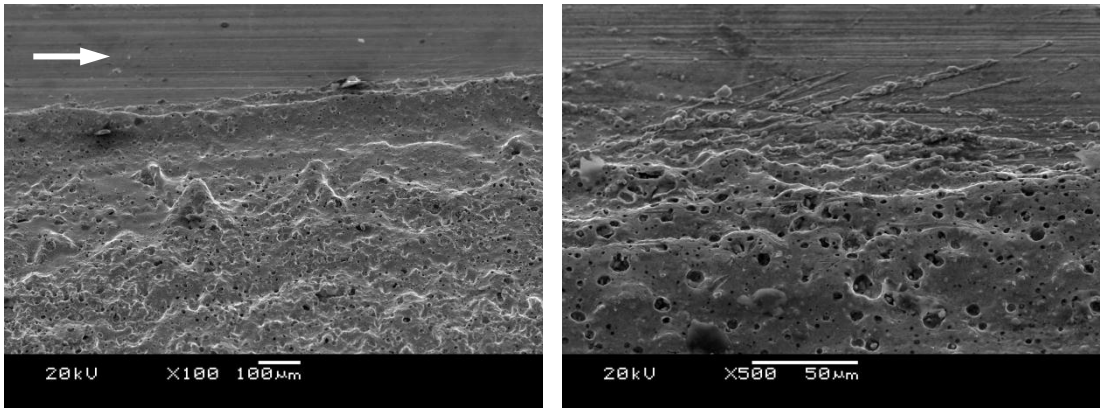

Figure 5.20. Ohmic melting deposits on rail at inside of armature contact (MCL 609)

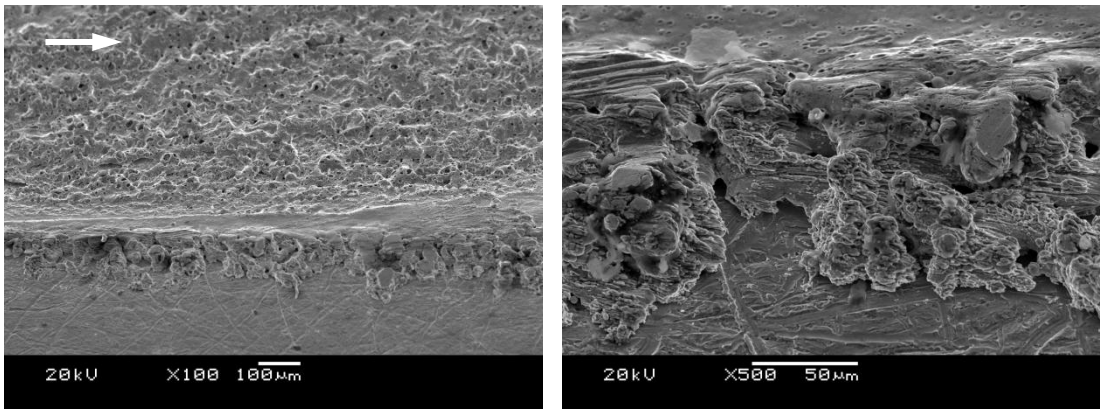

Figure 5.21. Ohmic melting deposits on rail at outer edge of armature contact (MCL 609)

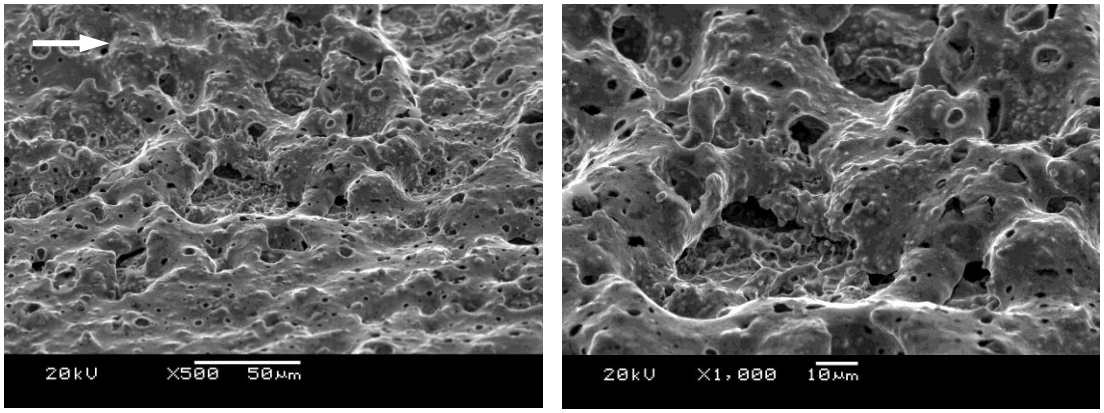

Figure 5.22. Ohmic melting deposits on rail inside armature contact zone (MCL 609)

Unlike the resolidified deposits in the gouge crater, the deposits at the edges show considerable porosity and very few “droplets”. The edge deposits resemble a continuous fluid that has flown over and solidified to the rail surface. In contrast, the gouge crater resembles the solidification of a thin, turbulent liquid (Figure 5.23).

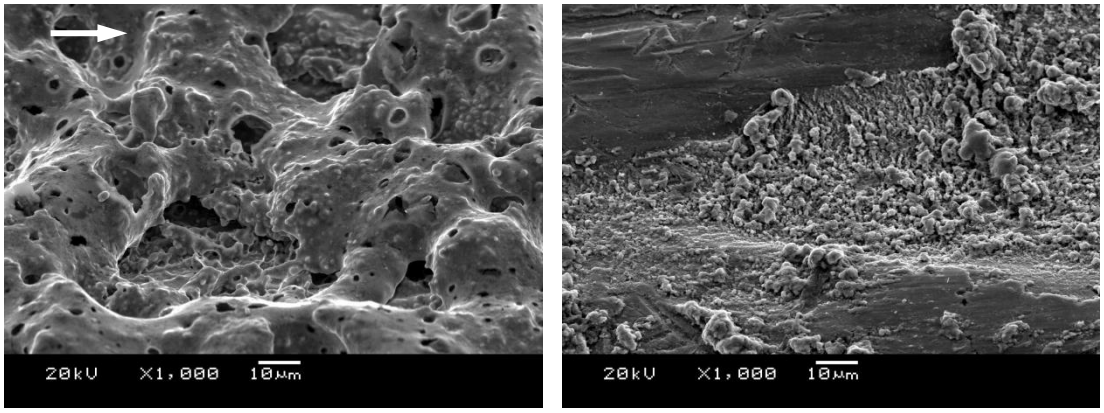

Figure 5.23. Melting on rail at armature edge (left), and gouge crater (right, MCL 609)

A cross-section view of the AA7075/C15725 material pair at the onset of gouging is shown using optical microscopy in Figure 5.24. Waves are observed in the rail surface both during gouge onset as well as inside the gouge crater. The waves increase in amplitude and wavelength inside the crater. At onset, the wavelength is around 10 micrometers, which is followed by a smooth region as the crater increases in depth. As the depth of the crater increases, the wavelength increases to around 50 micrometers.

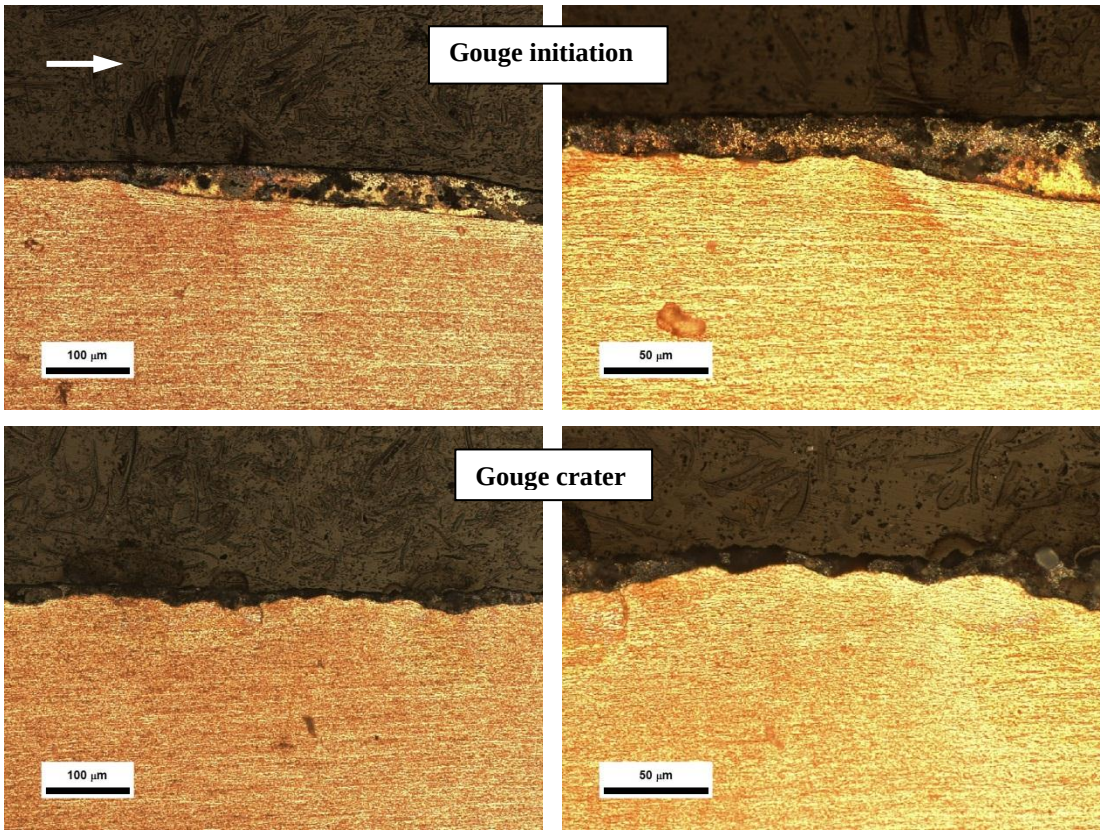

Figure 5.24. Cross-section microscope images of AA7075/C15725 gouging at 1,980 m/s (MCL 650)

5.2.2 SLIDER EXPERIMENTS:

Figure 5.25 and Figure 5.26 show SEM images of Zr/Cu galling damage. Images on the left are secondary electron images (SEI) indicating topographic contrast, while images on the right are back-scattered electron composition (BEC) images indicating atomic number contrast. The lighter regions in the BEC images are zirconium, while the darker potions are copper. In all cases of galling damage (and later gouging) there is significant material transfer from the slider to the rail.

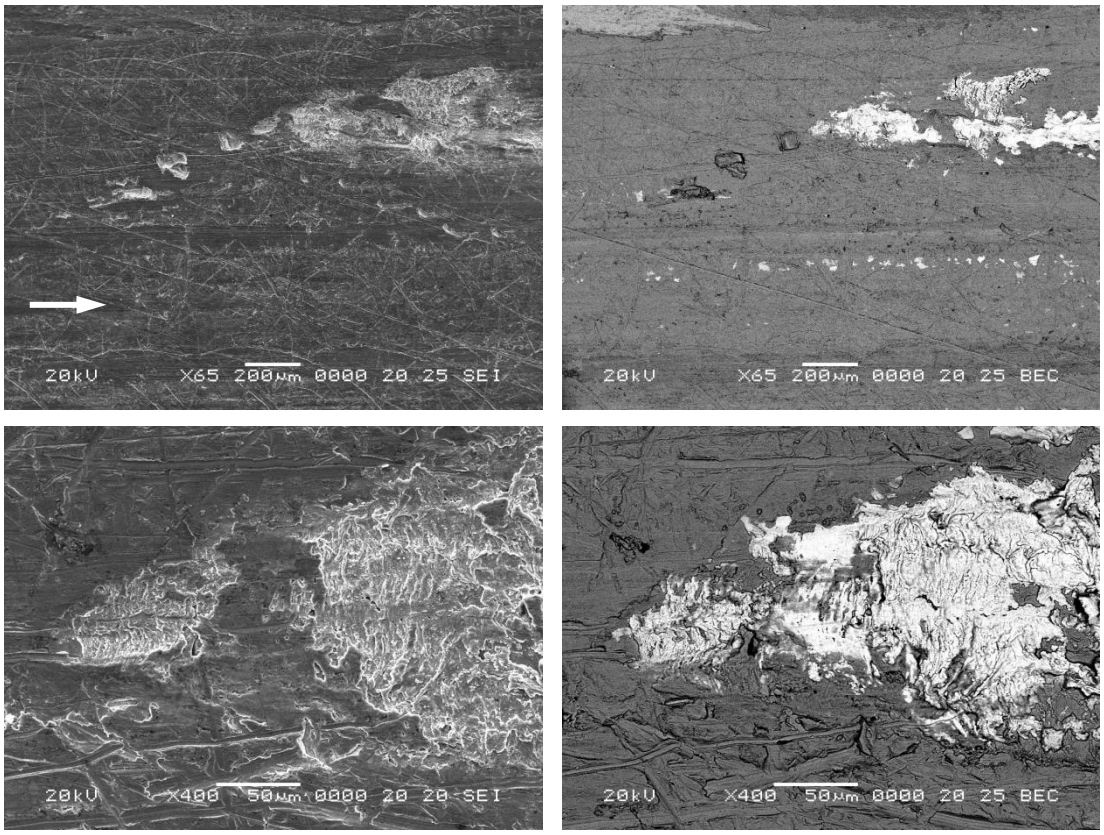

Figure 5.25. Galling damage for Zr slider on C11000 at 780 m/s (MCL 679)

The ripples observed in the Cu/Cu system prior to galling are observed for other slider materials as well. This is shown at higher magnification in Figure 5.26, with each deformation band in the copper containing a "coating" of zirconium. This finding is in agreement with the correlation between galling and adhesive wear, and suggests that metallic bonding is occurring between the slider and rail material prior to high-speed galling. This was seen as well for AISI 4140/C11000 gouging, as shown in the previous chapter.

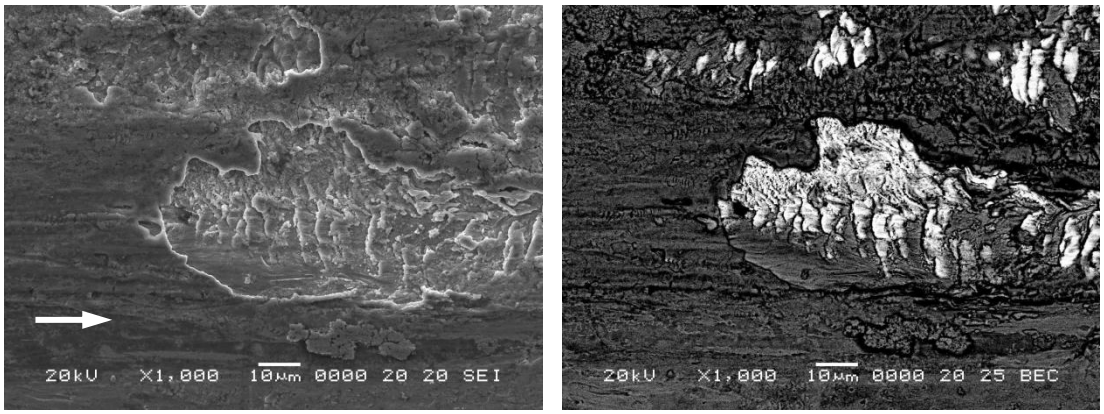

Figure 5.26. Zr/Cu galling damage at 780 m/s (MCL 679)

Cross-section optical microscope images of gouge crater for AISI 4140/C11000 and Ta/C11000 are shown in Figure 5.27 and Figure 5.28. As in the case of AA7075/C15725 (Figure 5.24), there is a region of surface waves that immediately precedes crater formation. Beneath these waves is a layer of deformed grains, down to a depth of around 10 μm.

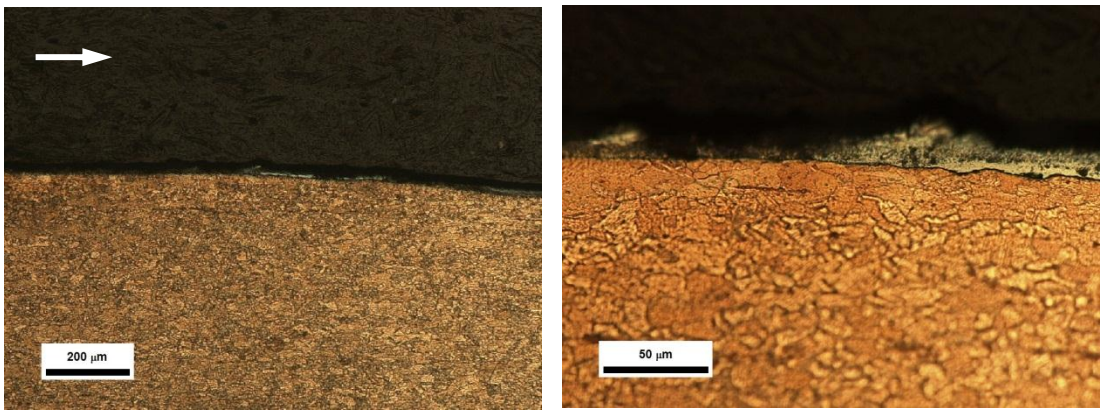

Figure 5.27. Cross-section microscope images of AISI 4140 on C11000 at 1,550 m/s (MCL 623)

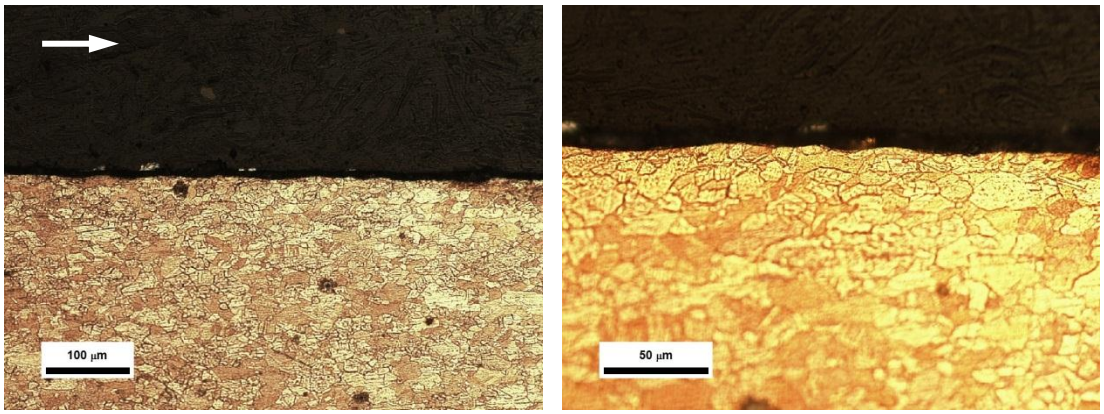

Figure 5.28. Cross-section microscope images of Ta on C11000 at 1,340 m/s (MCL 677)

The above images show significant plastic deformation of the surface, but not to the extent expected of shear bands. For copper, shear bands can occur once a gouge is formed but do not appear to be present during onset.

5.2.3 ALUMINUM COATINGS:

In the case of the fully electroplated rails, the lack of gouging is attributed to the acoustic properties of the thin aluminum layer. Microscope images of the rail cross-section indicate typical armature deposits on top of the electroplated aluminum coating, which survives the launch process without delamination (Figure 5.29).

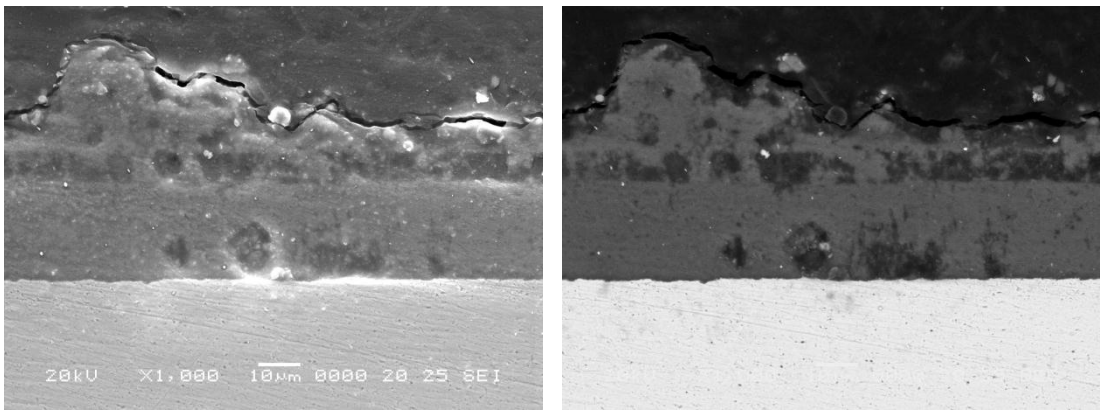

Figure 5.29. Cross-section SEM images of post-shot electroplated rail: SEI (left), and BEI (right)

Figure 5.30 shows the onset of gouging at the leading edge of an electroplated rail. The C15725 rail material is significantly work hardened prior to testing (CW 75%). Since the alloy is dispersion strengthened via aluminum oxide particles, it retains much of its strength at high temperatures, as well as its grain structure. The combination of prior work hardening and grain boundary stability results in a striking visual of the strain accumulated during the gouging event. The grains at the leading edge show a stagnation point with surface grains sheared by over 90°. Surface waves are present on the crater surface, becoming larger as the crater deepens.

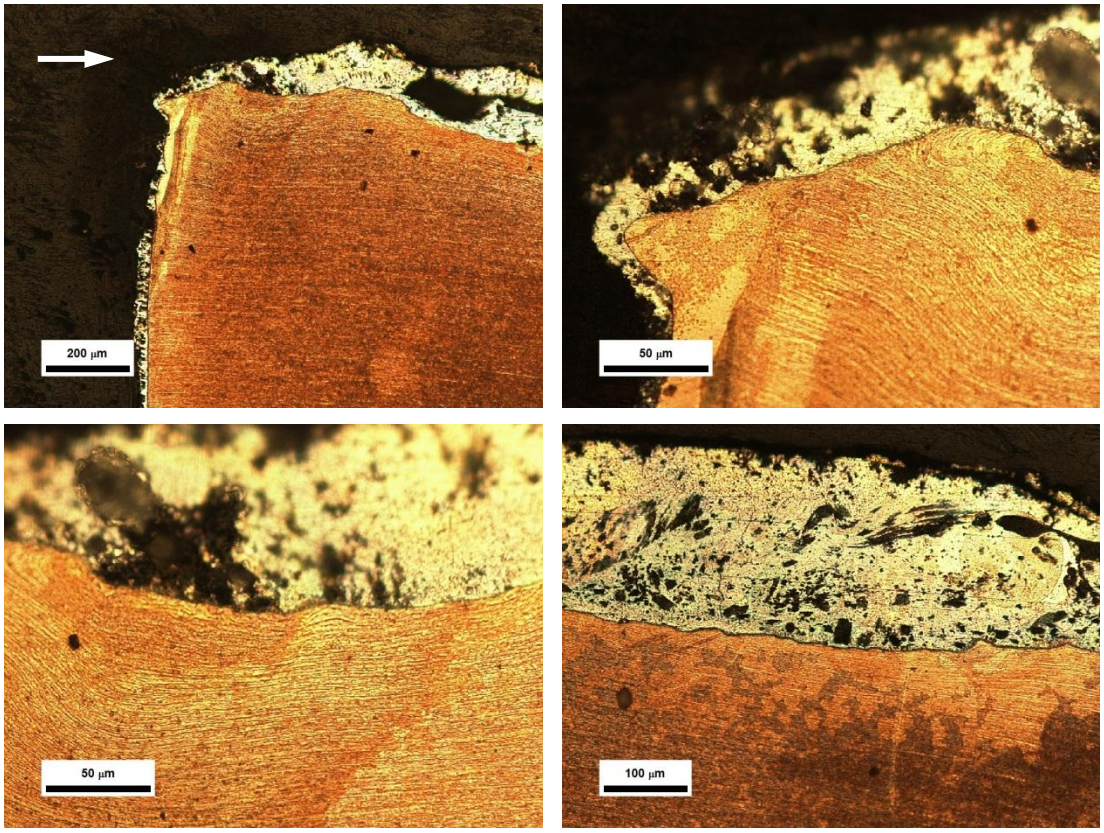

Figure 5.30. Cross-section microscope images of AA7075 on Al-plated C15725 at 1,900 m/s (MCL 651)

Figure 5.31 shows the downstream "lip" of the above gouge crater. It is not clear how this shape formed, but it is clearly the result of significant plastic deformation. There is no evidence of melting, as the original grain boundaries have largely been left intact, if

severely deformed. The dark region at the interface indicates a shear band. Shear bands in pure copper require a minimum shear strain of 6.0, though this critical strain is likely reduced for C15725 [36].

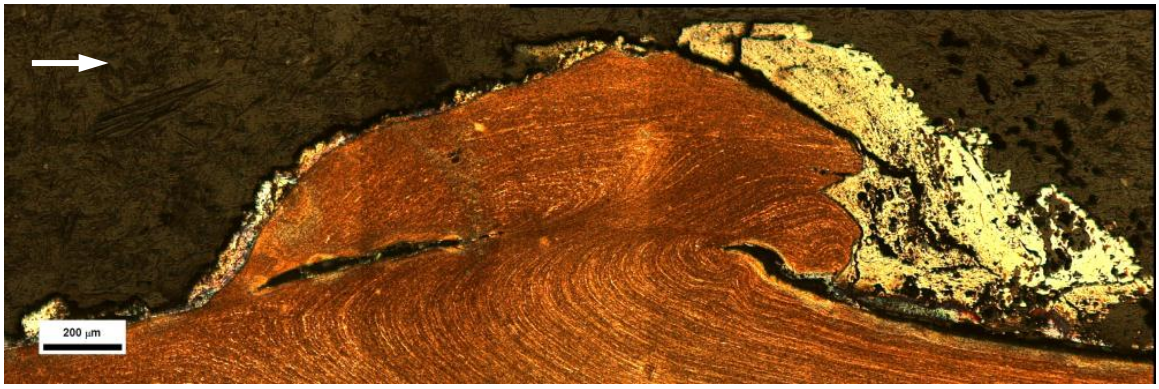

Figure 5.31. Composite microscope image of AA7075/C15725 gouge crater lip at 1,900 m/s (MCL 651)

5.2.4 RAIL INDENTATION TESTS:

Galling damage for AA7075 on the indented C11000 rail is shown in Figure 5.32. In this and the following images, the aluminum armature deposits have been etched from the rail. The rail surface is smooth just after the indentation, but ripples in the rail become evident after ~500 µm of travel. As damage progresses, these waves become more pronounced until the galling craters terminate.

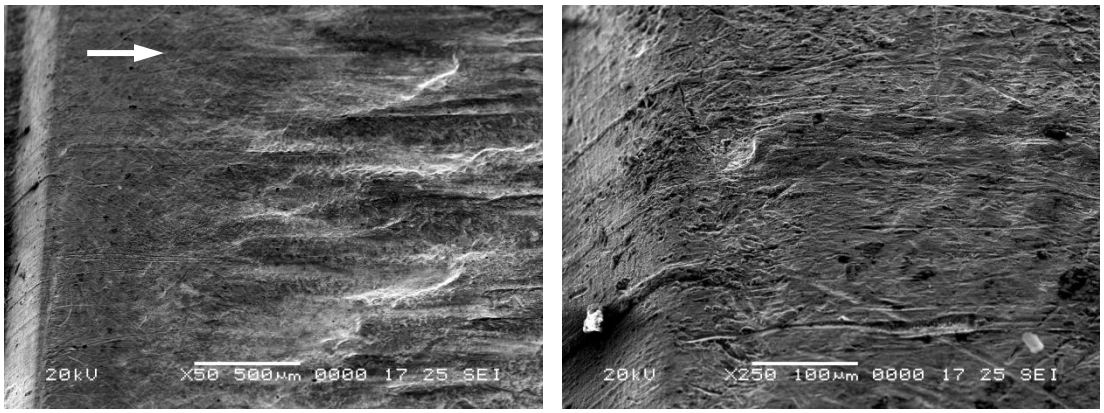

Figure 5.32. Galling of AA7075/C11000 on indented rail at 790 m/s (HEMCL 1341)

Figure 5.33 shows indent-generated gouging downstream of the previous image. At higher speeds, the downstream indent edge is sheared over and covers the initial region of the gouge. The gouge surface from onset contains resolidified rail material and a wavy surface.

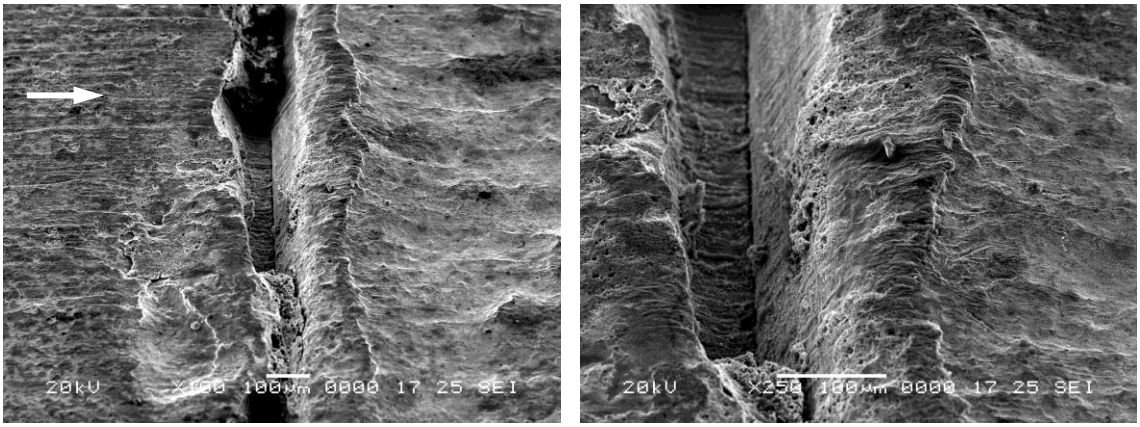

Figure 5.33. Gouging of AA7075/C11000 on indented rail at 1,300 m/s (HEMCL 1341)

A comparison of the surfaces of the galling and gouging craters in Figure 5.33 is shown in Figure 5.34. The galling damage at 790 m/s contains regions of loosely-formed bands, reminiscent of the semi-solid deformation bands in Cu/Cu at 600 m/s (Figure 4.22). The surface of the Al/Cu gouge at 1,300 m/s has a similar collection of particles or "droplets" as the Cu/Cu interface at 960 m/s (Figure 5.18). The texture of the two crater surfaces is overall very similar, with the salient difference being the absence of band structure at higher velocity.

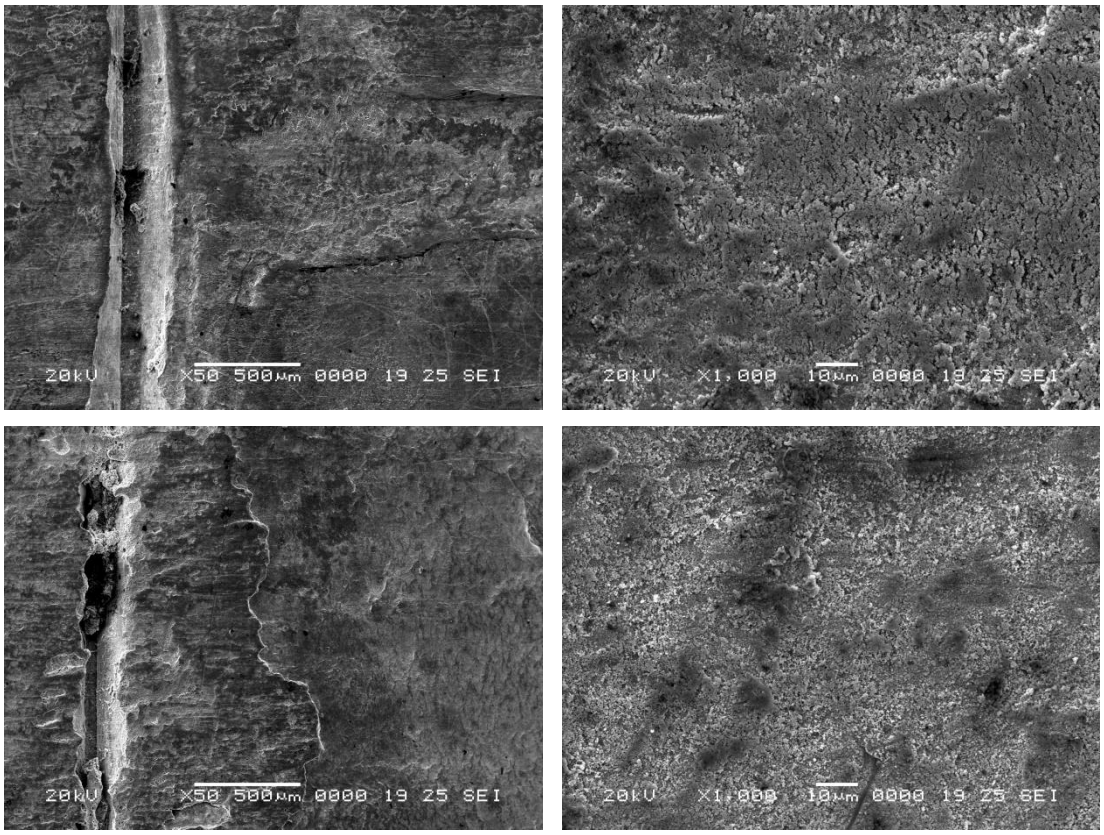

Figure 5.34. Galling and gouging of AA7075/C11000 on indented rail
Top: 790 m/s, Bottom: 1,300 m/s (HEMCL 1341)

Figure 5.35 shows cross-section optical microscope images from the indented rail at 787, 955, and 1,102 m/s. The most prominent difference between the three velocities is the shape of the downstream indentation lip, which becomes more wave-like as velocity increases. Smaller surface waves are present at all three velocities downstream of the lip. Plastic deformation under the crater surface is evident down to a depth of ~50 μm in all cases, which increases closer to the indentation.

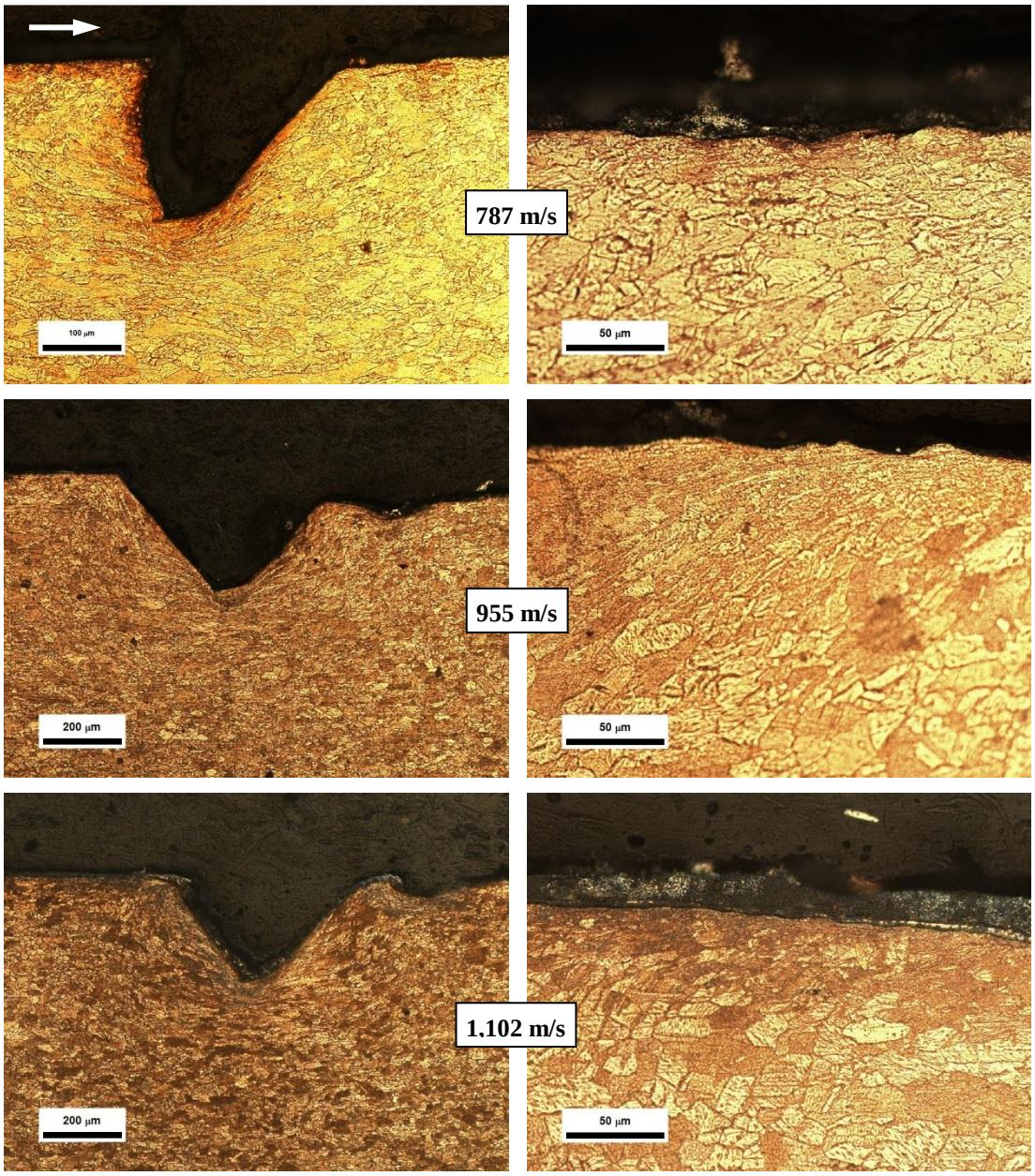

Figure 5.35. Cross-section microscope images of AA7075-T6 on indented C11000 (HEMCL 1341) Top: 0.6 m (787 m/s), Middle: 0.8 m (955 m/s), Bottom: 1.0 m (1,102 m/s)

5.2.5 SUMMARY OF MICROSCOPIC OBSERVATIONS:

Both galling and gouging are triggered at existing surface defects. This is obvious for macroscopic surface perturbations like the rail indentations in HEMCL 1341. In most experiments these were machining or polishing marks, often on the order of a few micrometers across. In a few cases gouges were traced back to a 10-20 μm hole in the rail surface, presumably the result of a third-body particle. A wide defect can trigger multiple simultaneous gouges. This can occur for both microscopic scratches as well as macroscopic indents. The primary difference between microscopic and macroscopic defects is that macroscopic defects can create gouge craters that initiate over a very large width (tens of millimeters). In contrast, microscopic defects seldom result in a gouge initiation region wider than a few micrometers.

In experiments with dissimilar material pairs, SEM analysis shows transfer of slider material to the rail prior to both galling and gouging. For galling this takes the form of patches of slider material bonded to deformed bands in the rail. For gouging this is usually seen as a layer of slider material "smeared" onto the rail prior to onset. Both galling and gouging require a strong bond to form between the slider and rail material.

An additional similarity between galling and gouging is deformation bands that precede their onset. At low velocities, these bands are present throughout the entire galling crater, with a band-spacing around 1-2 μm. As velocity increases, the bands begin as before, then become semi-solid, indicating increased viscoplastic heating of the deformed rail. As velocities approach the gouging threshold velocity, the preceding bands become very small, with a pitch on the order of 100 nm. These bands then are then replaced by resolidified rail material in the gouge crater. While melting is often observed in gouge craters, it is limited to the surface, and does not extend into the rail. Similarly, the presence of shear bands in gouge craters only occurs in a few instances for copper rails.

The transition from galling to gouging appears closely tied with the behavior of the deformation bands that become smaller and more closely-spaced as slider velocity approaches the gouging threshold. These features bear a close resemblance to persistent

slip bands, which implies something of a “slip cascade” prior to gouge onset. There is perhaps a critical band-width, on the order of a few hundred nanometers, at which gouging is initiated.

There is little morphological evidence to support a generalized normal impact model for gouging. In only a few cases do gouges initiate at a third-body particle, which supports a planar impact argument. However, in the bulk of observed gouge craters the onset begins a few micrometers downstream of microscopic defects, and contains severely sheared rail material. This suggests that shear instability is a more likely cause, and that the shear impedance model may be more appropriate for future model development.

5.3 Review of Gouging Models

5.3.1 Semi-Empirical Models

The semi-empirical models developed in Chapter Two were applied for the new gouging data discussed in Chapter Four. The results are shown in Figure 5.36 and Figure 5.37. The trend observed with the original set of gouging data is continued, with the average hardness methods yielding a slightly better correlation compared to the maximum hardness methods.

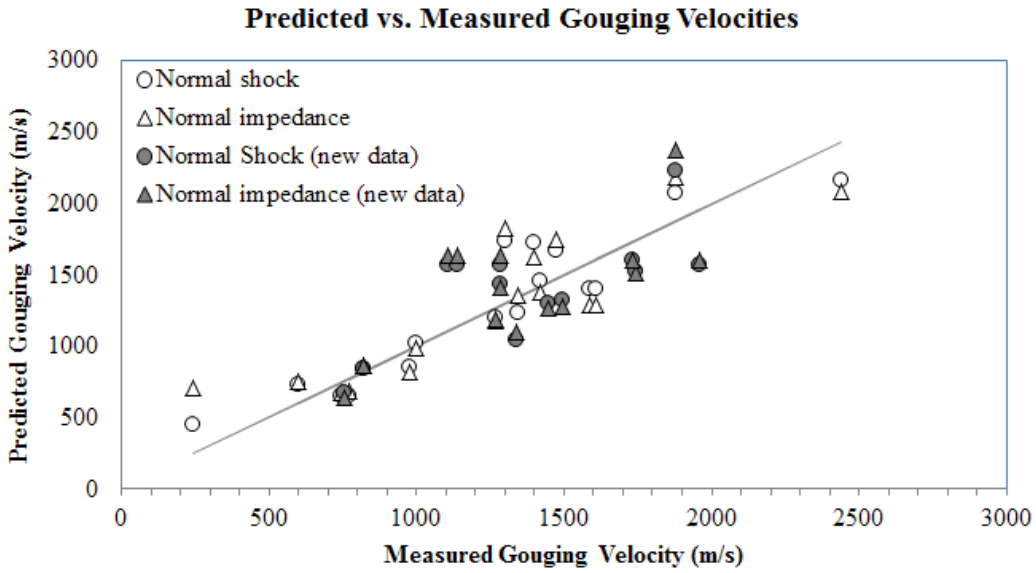

Figure 5.36. Predicted gouging velocities for normal shock and normal acoustic impedance methods

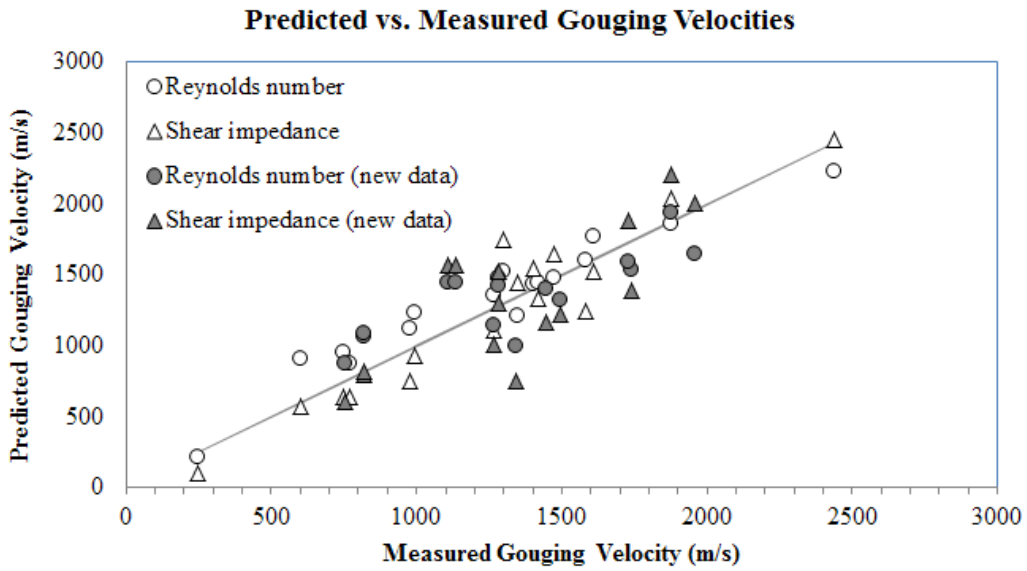

Figure 5.37. Predicted gouging velocities for Reynolds number and shear impedance methods

Table 5.7 lists the measured and predicted gouging velocities using the above models. The tantalum slider gouging velocity was changed to the galling velocity as discussed previously.

Table 5.7. Gouge velocities and model estimates

Slider	Rail	V_{gouge}	V_{Shock}	V_{Normal}	$V_{Reynolds}$	V_{Shear}	Source
		m/s	*m/s*	*m/s*	*m/s*	*m/s*	
AISI 304	AISI 1080	1,585 ± 79	1,404	1,293	1,602	1,250	Tarcza [28]
AISI 4340	AISI 1080	1,610 ± 81	1,401	1,286	1,776	1,525	"
Vascomax 300	AISI 1080	2,438 ± 122	2,161	2,081	2,231	2,460	"
Pb	Pb	245 ± 12	453	713	212	106	"
C11000-H02	C11000-H00	600 ± 30	734	754	908	578	"
AA7075-T6	C11000-H02	1,400 ± 70	1,723	1,627	1,439	1,554	"
C11000	C11000	746 ± 50	656	676	955	639	Stefani [25]
AA7075-T6	C11000	1,300 ± 65	1,734	1,827	1,527	1,749	"
Au80-Cu20	C11000	1,346 ± 75	1,233	1,353	1,217	1,444	"
AISI 1015	C11000	977 ± 110	850	818	1,127	753	"
Ag	C11000	770 ± 90	656	688	881	636	"
Mo	C11000	1,268 ± 30	1,198	1,178	1,361	1,115	"
Ni	C11000	996 ± 70	1,025	992	1,237	933	"
W	C11000	1,474 ± 45	1,676	1,751	1,482	1,650	"
Ti	C11000	1,420 ± 55	1,456	1,377	1,451	1,336	"
AISI 4340	C11000	1,878 ± 90	2,077	2,184	1,861	2,039	"
AISI 4140 HRC35	C11000-H02	1,285 ± 11	1,510	1,503	1,532	1,381	MCL 623
AISI 4340 HRC27	C11000-H02	1,447 ± 46	1,300	1,272	1,406	1,164	MCL 682
AISI 4340 HRC35	C11000-H02	1,743 ± 65	1,540	1,537	1,549	1,413	MCL 681
AISI 4340 HRC41	C11000-H02	~	1,739	1,768	1,664	1,631	MCL 684
AISI 4340 HRC51	C11000-H02	1,879 ± 68	2,227	2,377	1,935	2,205	MCL 685
AISI 4340 HRC59	C11000-H02	~	2,550	2,814	2,108	2,616	MCL 686
AA1100-H14	C11000-H02	1,341 ± 23	1,043	1,098	997	758	MCL 678
AA7075-T651	C11000-H02	1,285 ± 11	1,565	1,633	1,428	1,530	MCL 623
MACOR®	C11000-H02	1,267 ± 23	~	1,189	1,148	1,014	MCL 680
Tantalum	C11000-H02	*756 ± 44*	672	644	876	608	MCL 677
Zirconum	C11000-H02	1,495 ± 49	1,325	1,279	1,323	1,220	MCL 679
C11000-H04	C11000-H00	820 ± 12	844	866	1,070	803	MCL 609
C11000-H04	C11000-H04	820 ± 4	844	866	1,085	825	MCL 610
AA7075-T651	C26000-H02	1,731 ± 26	1,605	1,604	1,595	1,884	MCL 687
AA7075-T651	C15725	1,960 ± 98	1,567	1,604	1,651	2,002	MCL 650
AA7075-T651	C11000i	1,109 ± 14	1,565	1,633	1,445	1,565	HEMCL 1341
AA7075-T651	C11000	1,138 ± 17	1,565	1,633	1,445	1,565	HEMCL 1342

The four models were subsequently tested to see the effect of slider and rail hardness on the predicted gouging velocity. This was done by independently varying the slider and rail hardness for an AA7075 slider on C11000 rails. The normal shock and impedance models were run using the maximum hardness, while the Reynolds number

and shear impedance models were run using the average hardness. The result of varying the AA7075 slider hardness is shown in Figure 5.38. The lower value of 0.4 GPa corresponds to a Vickers hardness of 40, which is well below the room-temperature value of HV176 (1.72 GPa), but is about the same as the hardness of AA1100. In all models the estimated gouging velocity decreases linearly with decreasing hardness until the rail hardness is reached at 0.87 GPa. At this point the maximum-hardness models result in a constant gouging threshold estimate.

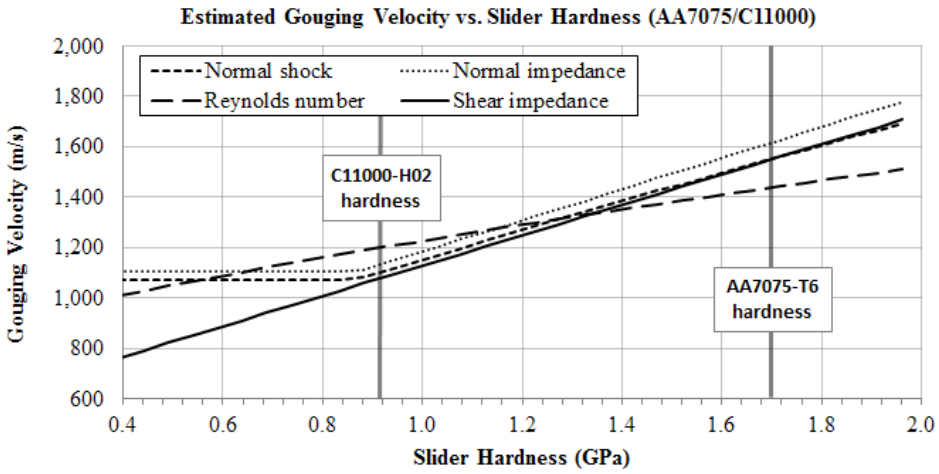

Figure 5.38. Effect of slider hardness on predicted gouging velocities for AA7075/C11000 system

The effect of varying the rail hardness is shown in Figure 5.39. The resulting difference is more pronounced compared to changing the slider hardness. The models that use the maximum hardness do not vary over a wide range, while the mean hardness models vary linearly with hardness. Recall that the C15725 rails have twice the hardness of C11000 with a minimal change in composition, and a significantly higher gouging threshold velocity. This behavior is only predicted by the shear impedance (average hardness) model. It therefore seems that the average hardness models may be more appropriate. An appropriate series of tests would be to use the same rail alloy with a wide range of hardness values, and a slider material with a hardness value lying in the middle

of that range. If an inflection point is observed in the gouging velocity with increasing rail hardness, then the average hardness model is justified.

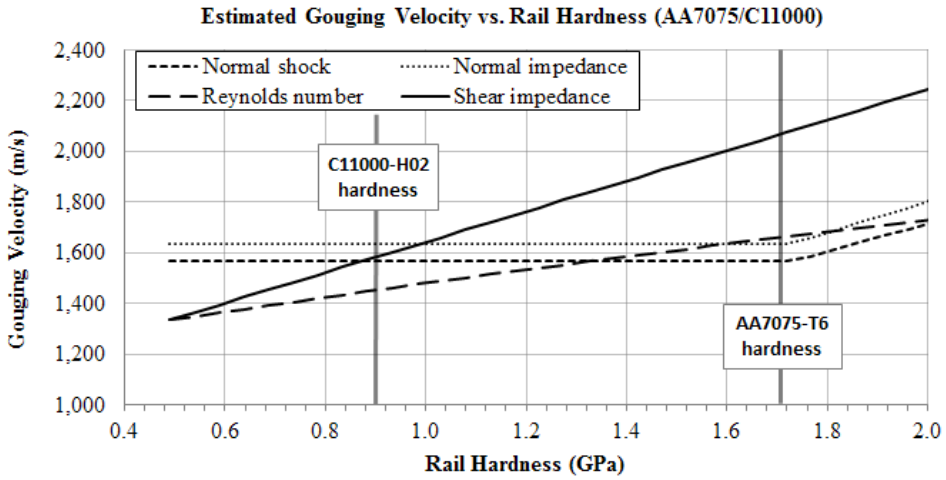

Figure 5.39. Effect of rail hardness on predicted gouging velocities or AA7075/C11000 system

5.3.2 LINEAR INSTABILITY MODELS

It has been stated several times in previous papers that there is a possible link between gouging, explosive welding, and the Kelvin-Helmholtz instability. This link was attempted here by employing the Reynolds number approach developed for welding waves to gouging, with good results.

Unfortunately, the linear instability approach for fluids did not prove to be useful for predicting gouging. There are numerous reasons for this. First, there is an implicit assumption regarding the flow field height. This ranges from a few micrometers for liquids, or tens of micrometers for plastically deforming solids. Viscosities for liquid metals can be used, but the wave perturbation growth rates are several orders of magnitude too long for gouging. Another problem is the jump conditions used between the two flows. There is not a fully agreed-upon set of jump conditions, and a single change in assumptions can have a significant impact on eigenvalue spectra for perturbation wave velocities. Lastly, there are numerical difficulties associated with

calculating the eigenvalues for very small flow fields or large wavenumbers. This can be alleviated by normalizing the equations, or by employing a fully non-dimensionalized equation, but numerical instabilities can still be encountered unless higher precision arithmetic is used.

There are several other considerations worth noting. First, while Squire's theorem justifies the use of 2D flow fields to model both 2D and 3D flow perturbations, it has been shown experimentally that Poiseuille flow is unstable for 3D flow perturbation while it is stable for 2D perturbations [148]. This may be the result of coupling between fluid and thermal perturbations and temperature-dependent material properties that are typically treated as constant. The role of temperature in linear instability has been ignored here, but could be incorporated into incompressible or compressible flow models. The related continuity equations would need to be modified for variable properties, and an additional row would be added to the flow matrix for the conservation of energy equation. A principal concern for such a method is that all equations of state and constitutive equations must be linearized, which could severely limit accuracy.

An alternative to fluid mechanics is to use a solid mechanics formulation for instability. This has been done in the literature for elastic slip waves, with the general result being that elastic sliding is either always stable or never stable depending on the assumptions for friction, separation, and heat transfer. What is convenient about the solid mechanics approach is that there is no implicit length-scale as there is in the fluid instability approach. It would be possible to modify the Chebyshev collocation procedure in Chapter Two for solid mechanics, though such is beyond the scope of this work.

CHAPTER 6. CONCLUSIONS

6.1.1 NEW EXPERIMENTAL RESULTS

A total of 22 experiments were performed over a span of two years to explore different aspects of gouging. These experiments investigated the effects of new materials, thin coatings, and rail indentations on gouging velocity threshold and morphology.

Existing gouging models estimate that increasing the hardness of either the slider or rail should increase the threshold velocity for gouging, though until now this has only been tested by increasing the slider hardness. In these experiments, three copper alloys were tested as rail materials. Gouging velocity was shown to increase for AA7075 armatures from 1,300 m/s for C11000 rails, to 1,960 m/s for C15725 rails. It is expected that harder copper alloys should be able to further delay the onset of gouging.

A new projectile was developed for testing arbitrary slider materials on conductive rails. This projectile isolates the slider sample material using an electrically-isolated and inertially-driven wedge, permitting gouging research without Ohmic heating from the drive current pulse. Four new slider materials were tested: pure aluminum, tantalum, zirconium, and MACOR® ceramic – all of which resulted in gouging. Six steel alloys ranging from HV 276-724 were also tested. While all of these materials are new additions to the gouging database, this was the first known occurrence of gouging using a ceramic slider.

In many cases, the galling damage to the rail was just as severe as the gouging damage. This is in stark contrast to previous gouging publications which depict minor adhesive/abrasive wear tracks that are suddenly replaced by gouge craters. The velocity threshold predicted by the gouging models was often between the onset of galling and gouging damage. In the case of C11000 rails, the onset of gouging is much more nuanced and involves a gradual transition from galling to gouging damage. A distinct threshold velocity for gouging may not be appropriate in this case.

An alternative to using harder rail materials is to use rail coatings to mitigate gouging. Results here have shown that gouging can be prevented with electroplated aluminum coatings as thin as 2 μm, and that the delay of gouging is likely due to the low acoustic impedance of the coating. However, additional tests are needed to confirm this.

For segmented rails, exposed leading edges consistently resulted in gouges, even though the surface was electroplated and no gouges occurred downstream of the exposed edge. Thin rail coatings can also be compromised in high-pressure contacts. For sliding systems that contain either high steady contact pressures, or significant lateral balloting, the use of thin rail coatings is not recommended.

Macroscopic indentations that spanned the width of the rails were found to have no effect on the threshold velocity for either galling or gouging damage. However, while gouge craters on flat rails start at a point and fan outward, gouge crater initiation on indented rails can span the width of the slider, resulting in greater overall damage.

6.1.2 MICROSTRUCTURAL ONSET OF GOUGING

Many authors have examined the cross-section of gouge craters, but until now there has been little published on the rail surface morphology during gouge onset. Both galling and gouging craters start at existing defects. This is true for both macroscopic and microscopic defects. Galling and gouging craters invariably form just downstream of microscopic scratches, and occasionally at surface inclusions. The features responsible often have length-scales on the order of a few micrometers.

A consistent microscopic feature observed prior to galling and gouging are deformation bands that lie angled to the rail surface. These resemble persistent slip bands (PSBs) observed in high-cycle loading of single crystals, or adiabatic shear bands (ASBs) in high strain-rate experiments. However, neither of these comparisons is particularly satisfying since PSBs are typically due to cyclical loading and have a strong crystallographic preference, and materials that form ASBs are less likely to gouge. The bands consistently decrease in spacing as velocity increases from a few micrometers for

galling damage, to a few hundred nanometers for gouging. This is an interesting finding, and opens a new avenue for future gouging research.

Another consistent feature observed using SEM analysis is the transfer of slider material to the rail during galling and gouging. Intimate contact and material transfer between the slider and rail proceeds for several hundred micrometers to several millimeters prior to the formation of a gouge crater. There does not appear to be a distinctive impact event, as has been proposed in the literature. Instead, the onset of gouging seems related to the simultaneous shearing of both slider and rail surfaces.

6.1.3 PREDICTIVE MODELS FOR GOUGING

There are a few semi-empirical models that work very well for predicting the onset of gouging, while other previously proposed models can be ruled out. Bending waves do not appear to play a dominant role in gouging, as they do not depend on slider properties, and predict critical velocities well below observed gouging velocities. Other waves such as dilatational, shear, and Rayleigh waves all predict velocities well in excess of observed gouging velocities. In the case of generalized Rayleigh waves (slip waves), the critical sliding velocities are again too high to correspond to observed gouging velocities.

The models that work well are the Stefani-Parker impact model, and the Effective Reynolds number adapted from work on explosive welding waves. The correlation between gouging and explosive welding has been made numerous times, but this is the first attempt at drawing a distinct behavioral link between the two. Acoustic normal and shear impedance models were also developed, which work about as well at predicting gouging onset and do not require the advanced material properties required by the impact model. Based on microstructural observations, the shear impedance model seems the best candidate for further development.

The use of the average material hardness instead of the maximum material hardness provides a better fit to the experimental data. However, this is probably not physical and is likely masking the complex dependence of strength on strain, strain-rate

and temperature. Advanced constitutive models can be used to estimate the actual dynamic slider and rail strengths relevant to gouging, though this requires significant assumptions.

There have been similarities drawn between gouging, explosive welding, and Kelvin-Helmholtz waves in fluids. The threshold nature of gouging also supports the notion that it can be treated as an instability. In practice, this does not appear to be justified – at least in the case of simple linear instability analysis. For fluids, the timescales required for instability growth are far too long to be applicable to gouging. For solids, previous analyses by others have shown that sliding surfaces are either unconditionally stable or unstable depending on the chosen jump conditions and adiabatic or diffusive heat transfer conditions. Indeed, the instability of both fluid and solid interfaces is highly dependent on the presumed jump conditions, which are an ongoing subject of research.

6.1.4 PATH FORWARD

There have been numerous findings in the course of this work that merit future attention. Additional rail materials could be examined to determine how far the gouging threshold can be extended for aluminum armatures. The gouging of ceramics and polymers is another area that is largely unexplored.

The robustness of thin rail coatings also has lingering questions. While evidence supports the role of the coating's acoustic properties as mitigating gouging, there could be some intrinsic geometric property of thin coatings that prevents or mitigates gouging. A possible test for this would be to use a copper armature on an aluminum-plated copper rail at a velocity above 1,300 m/s. If gouging is prevented even at this velocity, it is likely the geometric property of the coating is responsible for delaying gouging.

Another question is what ratio of coating thickness to perturbation size can prevent gouging. It is expected that a very thin coating on a large perturbation would result in gouging. This could readily be tested by electroplating an indented rail and independently varying the indentation size and coating thickness. Similarly, hard third-

body particles could be bonded to the electroplated rail surface to see if gouging can be triggered through the coating. This could be tested using silicon carbide particles, and independently varying particle size and coating thickness.

The evolution of the deformation bands preceding galling and gouging also warrants further analysis. The main difficulty is getting an accurate cross-sectional view of the bands. One way to accomplish this would be to place a galling/gouging onset region in a SEM equipped with a focused ion beam. This could allow for accurate location of the bands, and subsequent ion milling through the cross-section at that location. Once the cross-sectional surface has been obtained, it can be analyzed using a conventional SEM, though electron backscatter diffraction analysis would also be desirable to reveal grain orientations.

There are modeling avenues that can also be pursued. One is using the existing semi-empirical models to estimate the dynamic strength of the materials during gouging onset. This was briefly discussed in Chapter Two, and could readily be applied to arbitrary strength models to determine approximate strain, strain-rate, and temperature of the materials at the onset of gouging. Another avenue of research is the extension of the instability analysis developed for fluids. The Chebyshev collocation technique can be adapted to include multiple effects such as compressibility, heat transfer, and variable materials properties for fluids and/or solids. However, care must be taken in establishing the appropriate jump conditions, as well as analyzing both eigenvalue wave speeds and stress/energy growth of multiple eigenvalues over time. Unstable eigenvalues may develop too slowly to be a plausible representation of gouging.

Hypervelocity gouges serve as a rich source of interesting and complex material behavior. Many microstructural features are common in gouge craters. However, it is perilous to assign a causal role to them as the processes responsible for gouge initiation may not be the same as those that govern crater growth. Similarly, the semi-empirical models work very well for predicting gouging, and are easy to use, but do not necessarily describe the underlying physics.

Appendices

Appendix A. Coordinate Transformation Procedure

A (-1,1) grid is required for the Chebyshev collocation method. However, the general fluid flows are prescribed in the regions ($-d_1<y_1<0$) and ($0<y_2<d_2$). We wish to convert each flow to a ($-1<z<1$) grid with the original interface ($y=0$) specified at $z=-1$, similar to Dongarra *et al.* [148]. This results in the following equations for z:

$$(-d_1 \le y_1 \le 0) \rightarrow (-1 \le z \le 1): z = -\frac{2y_1}{d_1} - 1$$

$$(0 \le y_2 \le d_2) \rightarrow (-1 \le z \le 1): z = \frac{2y_2}{d_2} - 1$$

These equations can also be written as:

$$y_1 = \frac{-d_1}{2}(z+1)$$

$$y_2 = \frac{d_2}{2}(z+1)$$

The general form of the decomposition and perturbation equations do not change, but for ∂/∂y operations the following modification must be made. First, the derivatives of z with respect to the two y-coordinates are determined:

$$\frac{\partial z}{\partial y_1} = -\frac{2}{d_1}$$

$$\frac{\partial z}{\partial y_2} = \frac{2}{d_2}$$

For an arbitrary function $\xi(y)$, the derivative of ξ with respect to y can be written as:

$$\frac{\partial \xi}{\partial y} = \frac{\partial \xi}{\partial z}\frac{\partial z}{\partial y}$$

Therefore, the ∂/∂y operator can be re-written as:

$$\frac{\partial}{\partial y} = \left(\frac{\partial z}{\partial y}\right)\frac{\partial}{\partial z}$$

For higher-order differentiation, this is written as:

$$\frac{\partial^n}{\partial y^n} = \left(\frac{\partial z}{\partial y}\right)^n \frac{\partial^n}{\partial z^n}$$

Therefore, for arbitrary orders of differentiation:

$$\frac{\partial^n}{\partial y_1^n} = c_{y1}^n \frac{\partial^n}{\partial z^n}, \qquad c_{y1} = -\frac{2}{d_1}$$
$$\frac{\partial^n}{\partial y_2^n} = c_{y2}^n \frac{\partial^n}{\partial z^n}, \qquad c_{y2} = \frac{2}{d_2}$$

Appendix B. Matlab Script For Calculating Dongarra *et al.* Eigenvalues

```
% based on 1996 Dongarra paper
clear all;

% Test Cases
R = 10^4; a = 1; m = 2; n = 1.2; Un = 0; % Dongarra Figure 7
%R = 10^4; a = 1; m = 2; n = 2; Un = 0; % Dongarra Figure 8
%R = 25; a = 1; m = 2; n = 10; Un = 3; % Dongarra Figure 9
%R = 125; a = 1; m = 2; n = 10; Un = 3; % Dongarra Figure 10
%R = 100; a = 0.3; m = 2; n = 10; Un = 2; % Dongarra Figure 11
%R = 100; a = 2.3; m = 2; n = 10; Un = 2; % Dongarra Figure 12
%R = 200; a = 2; m = 2; n = 10; Un = 0; % Dongarra Figure 13

removeNaNs = 1;
removeLarge = 10;

% Velocity profile parameters
A1 = (-(m+n)+m*Un)/(n^2+n);
A2 = A1/m;
a1 = (n^2-m+m*Un)/(n^2+n);
a2 = a1/m;

k = 2:N-1;
I = eye(N,N);
Z = zeros(N,N);

% Differentation Matrices: size(N,N)
[X,DM] = chebdif(N,2);
D1 = DM(:,:,1); % 1st order differentiation matrix
D2 = DM(:,:,2); % 2nd order differentiation matrix
z = X'; % Chebyshev points [-1,1] size(1,N)

% Chebyshev velocity profiles: size(1,N)
y1 = -(1+z)/2; % -1 < y1 < 0
y2 = n/2*(z+1); % 0 < y2 < n
u = A1*y1.^2+a1*y1+1; % = u(z)
v = A2*y2.^2+a2*y2+1; % = v(z)
u = diag(u); % create diagonal matrices
v = diag(v);

% Flow equations: A matrix coefficients
A11f = 4*D2(k,:)-a^2*I(k,:);
A12f = -I(k,:);
A21f = 1i*2*a*A1*R*I(k,:);
A22f = 4*D2(k,:)-a^2*I(k,:)-1i*a*R*u(k,:);
A33f = 4/n^2*D2(k,:)-a^2*I(k,:);
```

```
A34f = -I(k,:); % corrected from Dongarra paper
A43f = 2i*A2*a*R/m*I(k,:);
A44f = 4/n^2*D2(k,:)-a^2*I(k,:)-1i*a*R/m*v(k,:);
% Null values:
A13f = zeros(N-2,N); A14f = zeros(N-2,N); A23f = zeros(N-2,N);
A24f = zeros(N-2,N); A31f = zeros(N-2,N); A32f = zeros(N-2,N);
A41f = zeros(N-2,N); A42f = zeros(N-2,N);

% Flow equations: B matrix coefficients
B22f = -1i*a*R*I(k,:);
B44f = -1i*a*R/m*I(k,:);
% Null values:
B11f = zeros(N-2,N); B12f = zeros(N-2,N); B13f = zeros(N-2,N);
B14f = zeros(N-2,N); B21f = zeros(N-2,N); B23f = zeros(N-2,N);
B24f = zeros(N-2,N); B31f = zeros(N-2,N); B32f = zeros(N-2,N);
B33f = zeros(N-2,N); B34f = zeros(N-2,N); B41f = zeros(N-2,N);
B42f = zeros(N-2,N); B43f = zeros(N-2,N);

% Boundary Conditions: A matrix coefficients
A11b = I(1,:);
A21b = D1(1,:);
A33b = I(1,:);
A43b = D1(1,:);
% Null values:
A12b = zeros(1,N); A13b = zeros(1,N); A14b = zeros(1,N);
A22b = zeros(1,N); A23b = zeros(1,N); A24b = zeros(1,N);
A31b = zeros(1,N); A32b = zeros(1,N); A34b = zeros(1,N);
A41b = zeros(1,N); A42b = zeros(1,N); A44b = zeros(1,N);

% Boundary Conditions: B matrix coefficients
% Null values:
B11b = zeros(1,N); B12b = zeros(1,N); B13b = zeros(1,N);
B14b = zeros(1,N); B21b = zeros(1,N); B22b = zeros(1,N);
B23b = zeros(1,N); B24b = zeros(1,N); B31b = zeros(1,N);
B32b = zeros(1,N); B33b = zeros(1,N); B34b = zeros(1,N);
B41b = zeros(1,N); B42b = zeros(1,N); B43b = zeros(1,N);
B44b = zeros(1,N);

% Jump Conditions: A matrix coefficients
A11j = I(N,:);
A13j = -I(N,:);
A21j = 2*a^2*I(N,:);
A22j = I(N,:);
A23j = -2*a^2*m*I(N,:);
A24j = -m*I(N,:);
A31j = -2*a^2*D1(N,:);
A32j = D1(N,:);
A33j = -2*m/n*a^2*D1(N,:);
A34j = m/n*D1(N,:);
A41j = D1(N,:) - a1/2*(1-m)/m*I(N,:);
A43j = 1/n*D1(N,:);
% Null values:
```

```
A12j = zeros(1,N); A14j = zeros(1,N);
A42j = zeros(1,N); A44j = zeros(1,N);

% Jump Conditions: B matrix coefficients
B41j = D1(N,:);
B43j = 1/n*D1(N,:);
% Null values:
B11j = zeros(1,N); B12j = zeros(1,N); B13j = zeros(1,N);
B14j = zeros(1,N); B21j = zeros(1,N); B22j = zeros(1,N);
B23j = zeros(1,N); B24j = zeros(1,N); B31j = zeros(1,N);
B32j = zeros(1,N); B33j = zeros(1,N); B34j = zeros(1,N);
B42j = zeros(1,N); B44j = zeros(1,N);

% Assemble matrices and solve
A= [[A11b;A11f;A11j] [A12b;A12f;A12j] [A13b;A13f;A13j] ...
[A14b;A14f;A14j]; ...
    [A21b;A21f;A21j] [A22b;A22f;A22j] [A23b;A23f;A23j] ...
[A24b;A24f;A24j]; ...
    [A31b;A31f;A31j] [A32b;A32f;A32j] [A33b;A33f;A33j] ...
[A34b;A34f;A34j]; ...
    [A41b;A41f;A41j] [A42b;A42f;A42j] [A43b;A43f;A43j] ...
[A44b;A44f;A44j]];
B= [[B11b;B11f;B11j] [B12b;B12f;B12j] [B13b;B13f;B13j] ...
[B14b;B14f;B14j]; ...
    [B21b;B21f;B21j] [B22b;B22f;B22j] [B23b;B23f;B23j] ...
[B24b;B24f;B24j]; ...
    [B31b;B31f;B31j] [B32b;B32f;B32j] [B33b;B33f;B33j] ...
[B34b;B34f;B34j]; ...
    [B41b;B41f;B41j] [B42b;B42f;B42j] [B43b;B43f;B43j] ...
[B44b;B44f;B44j]];
cn = eig(A,B,'qz');
c0 = cn;

% remove infinite/NaN eigenvalues
if removeNaNs
    remid = [];
    for index = 1:length(cn)
        if isnan(cn(index)) || isinf(cn(index))
            remid = [remid,index];
        end;
    end;
    cn(remid) = [];
end;
% remove spurious eigenvalues
if removeLarge
    remid = [];
    for index = 1:length(cn)
        if abs(real(cn(index))) > removeLarge || ...
            abs(imag(cn(index))) > removeLarge
            remid = [remid,index];
        end;
    end;
```

```
    cn(remid) = [];
end;
% remove BC-determined eigenvalue (c = 1.0 +0i)
remid = find(abs(imag(cn))<1e-10 & abs(real(cn)-1.0)<1e-10);
cn(remid) = [];

figure;
plot(real(cn),imag(cn),'ko');
xlabel('c_r');
ylabel('c_i');
title(['Reduced Results, N = ',num2str(N)]);
grid;

% find eigenvalue with maximum imaginary component
[maxval,maxind] = max(imag(cn));
fprintf('R = %5.5f : %8.8f + %8.8f i\n',[R, ...
      real(cn(maxind)),imag(cn(maxind))]);
```

Appendix C. Eigenvalue Calculation Benchmarks

The Matlab® script for solving viscous incompressible stratified flow is compared to the results obtained by Dongarra *et al.* [148]. The results from Dongarra's paper are on the left, with the Matlab® results on the right.

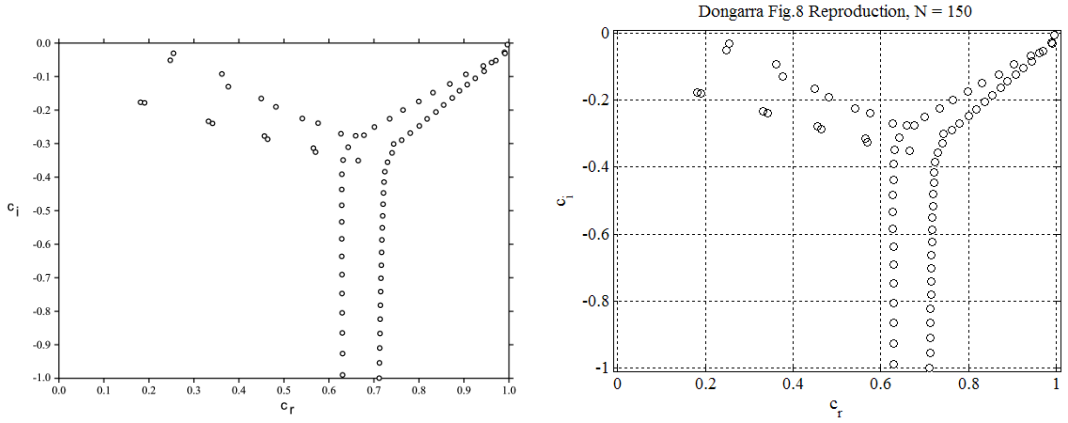

Figure C.1. Dongarra *et al.* Fig. 8 eigenvalues (left)[22], and re-created using Matlab® script R = 10^4, a = 1, m = 2, n = 2, V = 0

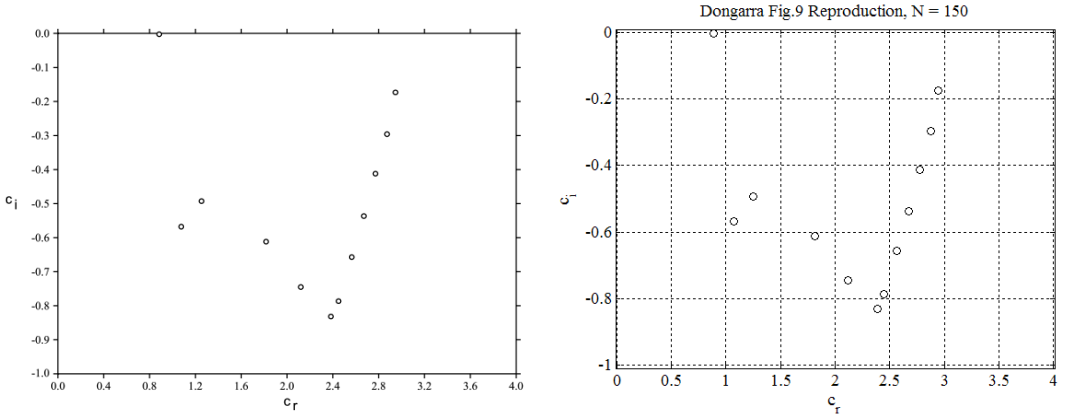

Figure C.2. Dongarra *et al.* Fig. 9 eigenvalues (left)[22], and re-created using Matlab® script R = 25, a = 1, m = 2, n = 10, V = 3

[22] Reprinted from J.J. Dongarra, B. Straughan, D.W. Walker, "Chebyshev tau – QZ Algorithm Methods for Calculating Spectra of Hydrodynamic Stability Problems," Applied Numerical Mathematics, Vol. 22, No. 4, pp. 399-434, Copyright 1996, with permission from Elsevier

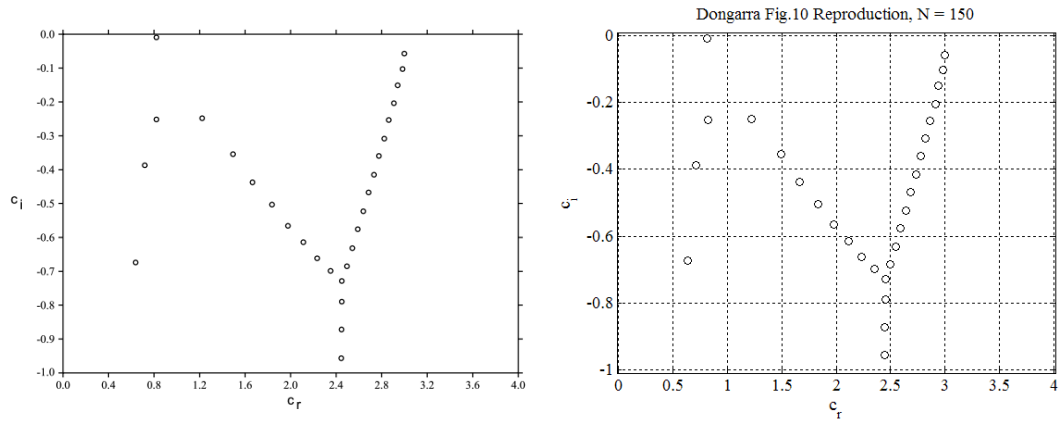

Figure C.3. Dongarra *et al.* Fig. 10 eigenvalues (left)[22], and re-created using Matlab® script R = 125, a = 1, m = 2, n = 10, V = 3

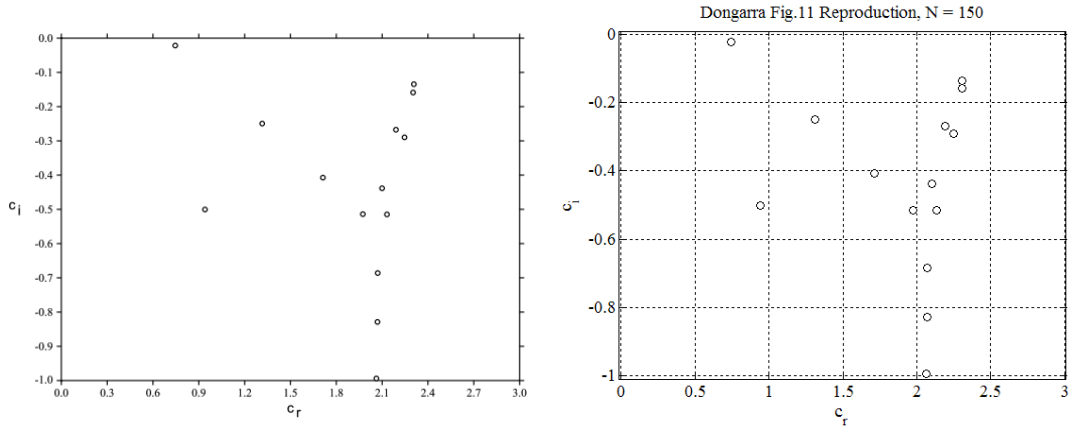

Figure C.4. Dongarra *et al.* Fig. 11 eigenvalues (left) [22], and re-created using Matlab® script R = 100, a = 0.3, m = 2, n = 10, V = 2

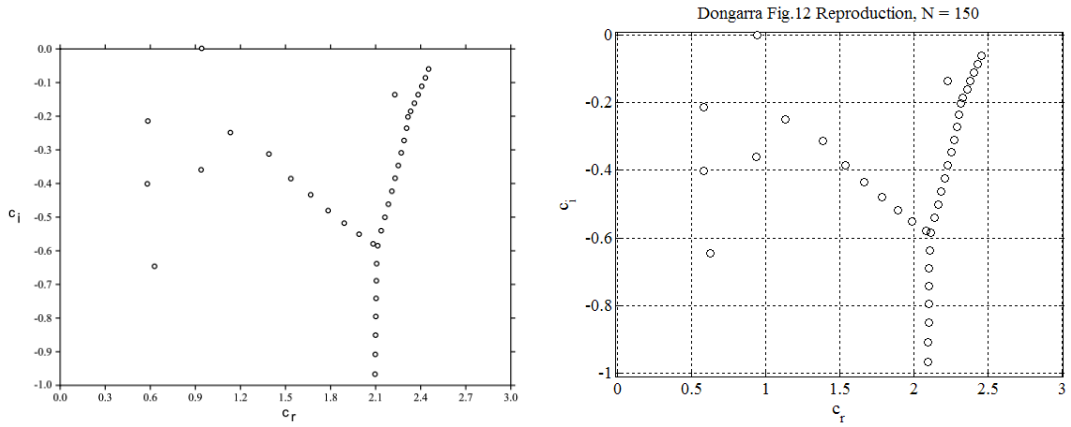

Figure C.5. Dongarra *et al.* Fig. 12 eigenvalues (left) [22], and re-created using Matlab® script R = 100, a = 2.3, m = 2, n = 10, V = 2

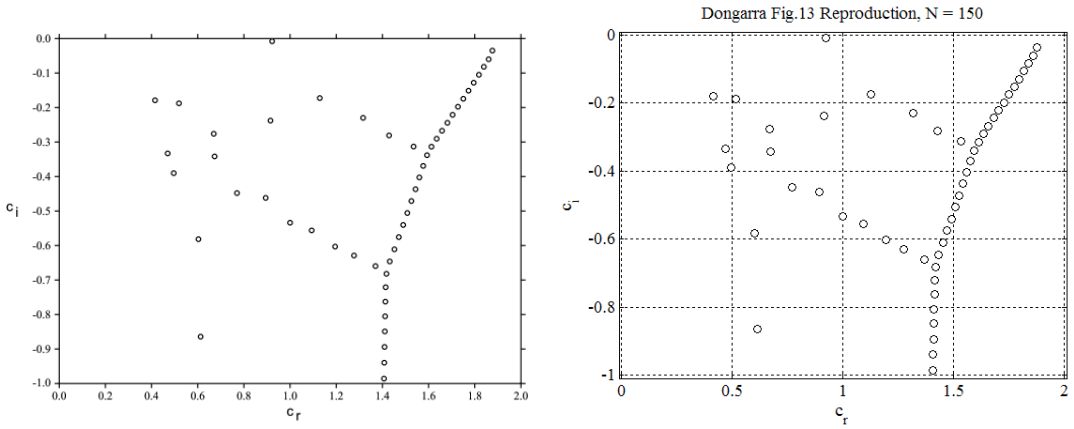

Figure C.6. Dongarra *et al.* Fig. 13 eigenvalues (left)[22], and re-created using Matlab® script R = 200, a = 2, m = 2, n = 10, V = 0

Appendix D. Matlab Scripts For Calculating Stratified Flow Eigenvalues

```
% calculate_eigenvalues.m
% Viscosities at Melting Temperature [Battezzati 1989]
% rho (kg/m^3), mu (mPa-s)
matl = 'Cu'; T = 1356; rho = 8020; mu = 4.00;
rho1 = rho; mu1 = mu*1e-3;
%matl = 'Ti'; T = 1958; rho = 4110; mu = 2.20;
%matl = 'Fe'; T = 1809; rho = 6999; mu = 5.50;
%matl = 'Ni'; T = 1728; rho = 7810; mu = 4.90;
matl = 'Al'; T = 933; rho = 2372; mu = 1.30;
%matl = 'Pb'; T = 600; rho = 10660; mu = 2.65;
rho2 = rho; mu2 = mu*1e-3;

N = 100; % total rows (including 2 boundaries)
a = 0.01; % manual
Vspec = 2000; % manual
d1 = 0.01;
d2 = d1;
shear_JC = 1; % 1: Yih 1967, 2: Boomkamp 1996

sfac = 1; % geometric scale factor (1000 = mm)
a = a/sfac;
Vspec = Vspec*sfac;
d1 = d1*sfac;
d2 = d2*sfac;
rho1 = rho1/sfac^3;
rho2 = rho2/sfac^3;
mu1 = mu1/sfac;
mu2 = mu2/sfac;

nu1 = mu1/rho1;
nu2 = mu2/rho2;
m = mu2/mu1; % viscosity ratio
n = d2/d1; % depth ratio
r = rho2/rho1;

ploteigs = 1; % plot eigenvalues
plotflow = 0; % plot cumulative flow velocities
plot_pert = 0; % plot perturbation velocities
calc_energy = 1; % calculate perturbation kinetic energy
removeNaNs = 1; % remove NaN eigenvalues
removeLarge = Vspec; % remove spurious eigenvalues

k = 2:N-1;
```

```
I = eye(N,N);
Z = zeros(N-2,N);
Z1 = zeros(1,N);

% Differentation Matrices: size(N,N)
[X,DM] = chebdif(N,2);
D1 = DM(:,:,1); % 1st order differentiation matrix
D2 = DM(:,:,2); % 2nd order differentiation matrix
z = X'; % Chebyshev points [-1,1] size(1,N)

% Chebyshev velocity profiles: size(1,N)
kf = (n/m+1)^-1;
cy1 = -2/d1;
cy2 = 2/d2;
% Fluid 1
y1 = -d1/2*(z+1); % -d1 < y1 < 0
u = kf*Vspec*(1+y1/d1); % = u(z)
u1 = -Vspec/2*kf*I; % = du/dz
U = diag(u); % create diagonal matrices
% Fluid 2
y2 = d2/2*(z+1); % 0 < y2 < d2
v = Vspec*( (1-kf)*y2/d2 + kf ); % = v(z)
v1 = Vspec/2*(1-kf)*I; % = dv/dz
V = diag(v);
% Reynolds numbers using interface velocity
Vint = kf*Vspec;
R = Vint*d1/nu1;
R2 = Vint*d2/nu2;

% Flow equations: A matrix coefficients
A11f = cy1^2*D2(k,:) - a^2*I(k,:);
A12f = -I(k,:);
A13f = Z; A14f = Z; A21f = Z;
A22f = 1i*nu1/a*( cy1^2*D2(k,:) - a^2*I(k,:) ) + U(k,:);
A23f = Z; A24f = Z; A31f = Z; A32f = Z;
A33f = cy2^2*D2(k,:) - a^2*I(k,:);
A34f = -I(k,:);
A41f = Z; A42f = Z; A43f = Z;
A44f = 1i*nu2/a*( cy2^2*D2(k,:) - a^2*I(k,:) ) + V(k,:);

% Flow equations: B matrix coefficients
B11f = Z; B12f = Z; B13f = Z; B14f = Z; B21f = Z;
B22f = I(k,:);
B23f = Z; B24f = Z; B31f = Z; B32f = Z; B33f = Z;
B34f = Z; B41f = Z; B42f = Z; B43f = Z;
B44f = I(k,:);

% Boundary Conditions: A matrix coefficients
A11b = I(1,:);
A12b = Z1; A13b = Z1; A14b = Z1;
A21b = D1(1,:);
A22b = Z1; A23b = Z1; A24b = Z1; A31b = Z1; A32b = Z1;
```

```
A33b = I(1,:);
A34b = Z1; A41b = Z1; A42b = Z1;
A43b = D1(1,:);
A44b = Z1;

% Boundary Conditions: B matrix coefficients
B11b = Z1; B12b = Z1; B13b = Z1; B14b = Z1;
B21b = Z1; B22b = Z1; B23b = Z1; B24b = Z1;
B31b = Z1; B32b = Z1; B33b = Z1; B34b = Z1;
B41b = Z1; B42b = Z1; B43b = Z1; B44b = Z1;

% Jump Conditions: A matrix coefficients
A11j = I(N,:);
A12j = Z1;
A13j = -I(N,:);
A14j = Z1;
if shear_JC == 1
    % Yih 1967 JC (A21-A24):
    A21j = 2*a^2*I(N,:);
    A22j = I(N,:);
    A23j = -2*m*a^2*I(N,:);
    A24j = -m*I(N,:);
elseif shear_JC == 2
    % Boomkamp 1996 JC Modification (A21-A24):
    A21j = 2*a^2*U(N,:);
    A22j = U(N,:);
    A23j = 2*m*a^2*U(N,:);
    A24j = m*U(N,:);
else
    fprintf('shear_JC incorrect');
    return;
end;
A31j = 2*cy1/(rho1*d1)*a^2*U(N,:).*D1(N,:);
A32j = -cy1*D1(N,:);
A33j = -m*2*cy2/(rho1*d2)*a^2*V(N,:).*D1(N,:);
A34j = r*m*cy2*D1(N,:);
A41j = cy1*U(N,:).*D1(N,:) - m*v1(N,:);
A42j = Z1;
A43j = -( r*cy2*V(N,:).*D1(N,:) - r*v1(N,:) );
A44j = Z1;

% Jump Conditions: B matrix coefficients
B11j = Z1; B12j = Z1; B13j = Z1; B14j = Z1;
if shear_JC == 1
    % Yih 1967 JC (B21-B24):
    B21j = Z1; B22j = Z1; B23j = Z1; B24j = Z1;
elseif shear_JC == 2
    % Boomkamp 1996 JC Modification (B21-B24):
    B21j = -2*a^2*I(N,:);
    B22j = -I(N,:);
    B23j = 2*m*a^2*I(N,:);
    B24j = m*I(N,:);
```

```
else
    fprintf('shear_JC incorrect');
    return;
end;
B31j = Z1; B32j = Z1; B33j = Z1; B34j = Z1;
B41j = cy1*D1(N,:);
B42j = Z1;
B43j = -r*cy2*D1(N,:);
B44j = Z1;

% Assemble matrices and solve
A= [[A11b;A11f;A11j] [A12b;A12f;A12j] ...
    [A13b;A13f;A13j] [A14b;A14f;A14j]; ...
    [A21b;A21f;A21j] [A22b;A22f;A22j] ...
    [A23b;A23f;A23j] [A24b;A24f;A24j]; ...
    [A31b;A31f;A31j] [A32b;A32f;A32j] ...
    [A33b;A33f;A33j] [A34b;A34f;A34j]; ...
    [A41b;A41f;A41j] [A42b;A42f;A42j] ...
    [A43b;A43f;A43j] [A44b;A44f;A44j]];
B= [[B11b;B11f;B11j] [B12b;B12f;B12j] ...
    [B13b;B13f;B13j] [B14b;B14f;B14j]; ...
    [B21b;B21f;B21j] [B22b;B22f;B22j] ...
    [B23b;B23f;B23j] [B24b;B24f;B24j]; ...
    [B31b;B31f;B31j] [B32b;B32f;B32j] ...
    [B33b;B33f;B33j] [B34b;B34f;B34j]; ...
    [B41b;B41f;B41j] [B42b;B42f;B42j] ...
    [B43b;B43f;B43j] [B44b;B44f;B44j]];
[c_vec,c_val] = eig(A,B);
% save all eigenvalues
c_val = diag(c_val);
c0 = c_val;
cv0 = c_vec;

% remove infinite/NaN eigenvalues
if removeNaNs
    remid = [];
    for index = 1:length(c_val)
        if isnan(c_val(index)) || isinf(c_val(index))
            remid = [remid,index]; %#ok<*AGROW>
        end;
    end;
    c_val(remid) = [];
    c_vec(:,remid) = [];
end;

% remove spurious eigenvalues
if removeLarge
    remid = [];
    for index = 1:length(c_val)
        if abs(real(c_val(index))) > removeLarge || ...
                abs(imag(c_val(index))) > removeLarge
            remid = [remid,index];
```

```
        end;
    end;
    c_val(remid) = [];
    c_vec(:,remid) = [];
end;

% sort eigenvalues
[Y,index_list] = sort(imag(c_val),'descend');
[maxval,maxind] = max(imag(c_val));

% Plot eigenvalues
if ploteigs
    figure;
    plot(real(c_val)/sfac,imag(c_val)/sfac,'.');
    xlabel('c_r');
    ylabel('c_i');
    title(['Reduced Results, N = ',num2str(N)]);
    grid;
end;
% output eigenvalues to screen
fprintf('R_1 = %5.3g : %5.3f %5.3fi\n',...
    [R,
real(c_val(index_list(1)))/sfac,imag(c_val(index_list(1)))/sfac]);

% largest eigenvalue wave speed
cspec = c_val(index_list(1));
c_vspec = c_vec(:,index_list(1));
x = 0;
t = 1e-6;
plot_incomp; % plot flow data

if calc_energy
    plot_energy;
    plot_fix;
end
```

```
% plot_incomp.m
titlestr = ['Eigenvalue ',num2str(cspec),' at ',num2str(t),' s'];

% extract velocity u(z) profiles from matrix
u_p = c_vspec(1:N);
us_p = c_vspec((N+1):(2*N));
v_p = c_vspec((2*N+1):(3*N));
vs_p = c_vspec((3*N+1):(4*N));

% calculate velocity u(y) profiles
uf_x = cy1*D1*u_p*exp(1i*a*(x-cspec*t))/sfac;
uf_y = -1i*a*u_p*exp(1i*a*(x-cspec*t))/sfac;
vf_x = cy2*D1*v_p*exp(1i*a*(x-cspec*t))/sfac;
```

```
vf_y = -1i*a*v_p*exp(1i*a*(x-cspec*t))/sfac;

% calculate fluid stress (assumed perturbation form)
f1 = -1i*mu1*cy1/a*D1*us_p + (cspec - diag(u))*rho1*cy1*D1*u_p + ...
    rho1*u1*u_p;
f2 = -1i*mu2*cy2/a*D1*vs_p + (cspec - diag(v))*rho2*cy2*D1*v_p + ...
    rho2*v1*v_p;
p1 = f1*exp(1i*a*(x-cspec*t))/sfac;
p2 = f2*exp(1i*a*(x-cspec*t))/sfac;

if plotflow
    figure;
    plot([real(u),real(v)]/sfac,[y1,y2]/sfac,'b','Marker','none');
    hold on;
    plot([real(u'+uf_x);real(v'+vf_x)]'/sfac,[y1,y2]/sfac,'r');
    ylabel('Y');
    xlabel('Flow Velocity');
end;

if plot_pert
    figure;
    plot(real(uf_x)/sfac,y1/sfac,'b','LineStyle','-'); hold on;
    plot(real(vf_x)/sfac,y2/sfac,'b','LineStyle','-');
    ylabel('Y');
    xlabel('X Perturbation Velocity');
    title(titlestr);
    figure;
    plot(real(uf_y)/sfac,y1/sfac,'r','LineStyle','-'); hold on;
    plot(real(vf_y)/sfac,y2/sfac,'r','LineStyle','-');
    ylabel('Y');
    xlabel('Y Perturbation Velocity');
    title(titlestr);
end;
```

```
% plot_energy.m
for index = 1:length(c_val)
    cspec = c_val(index_list(index));
    c_vspec = c_vec(:,index_list(index));
    % extract velocity u(z) profiles from matrix
    u_p = c_vspec(1:N);
    v_p = c_vspec((2*N+1):(3*N));
    timeid = 0;
    timevec = [];
    for tindex = -6:0.1:3
        t = 10^tindex;
        timeid = timeid + 1;
        timevec = [timevec t];
        % calculate velocity u(y) profiles
        uf_x = cy1*D1*u_p*exp(1i*a*(x-cspec*t))/sfac;
        uf_y = -1i*a*u_p*exp(1i*a*(x-cspec*t))/sfac;
```

```
        vf_x = cy2*D1*v_p*exp(1i*a*(x-cspec*t))/sfac;
        vf_y = -1i*a*v_p*exp(1i*a*(x-cspec*t))/sfac;
        if calc_energy
            % calculate fluid kinetic energy
            KE_u = rho1*(real(uf_x).^2 + real(uf_y).^2)*sfac^3;
            KE_v = rho2*(real(vf_x).^2 + real(vf_y).^2)*sfac^3;
            KE_maxf(index,timeid) = max([KE_u;KE_v]);
            KE_JCf(index,timeid) = max([KE_u(N);KE_v(N)]);
            KE_sumf(index,timeid) = mean(integrate(KE_u,y1)) + ...
                mean(integrate(KE_v,y2));
        end;
    end;
    if calc_energy
        KE_max(index) = max(KE_maxf(index,:));
        KE_JC(index) = max(KE_JCf(index,:));
        KE_sum(index) = max(KE_sumf(index,:));
    end;
end;
if calc_energy && ~a_auto
    figure;
    scatter(real(c_val(index_list))/sfac,...
        imag(c_val(index_list))/sfac,...
        KE_max./max(KE_max)*500);
    title('Maximum Perturbation Kinetic Energy');
    hold on;
    plot(real(c_val(index_list))/sfac,...
        imag(c_val(index_list))/sfac,'k.');
    xlabel('c_r');
    ylabel('c_i');
end;
figure;
plot(timevec,KE_maxf(1,:));
set(gca,'XScale','log');
xlabel('Time (s)');
ylabel('Energy');
title(['Perturbation Kinetic Energy vs. Time for ',...
    num2str(c_val(index_list(1)),'%5.4g')]);
```

Appendix E. B-dot waveforms

BASELINE EXPERIMENTS

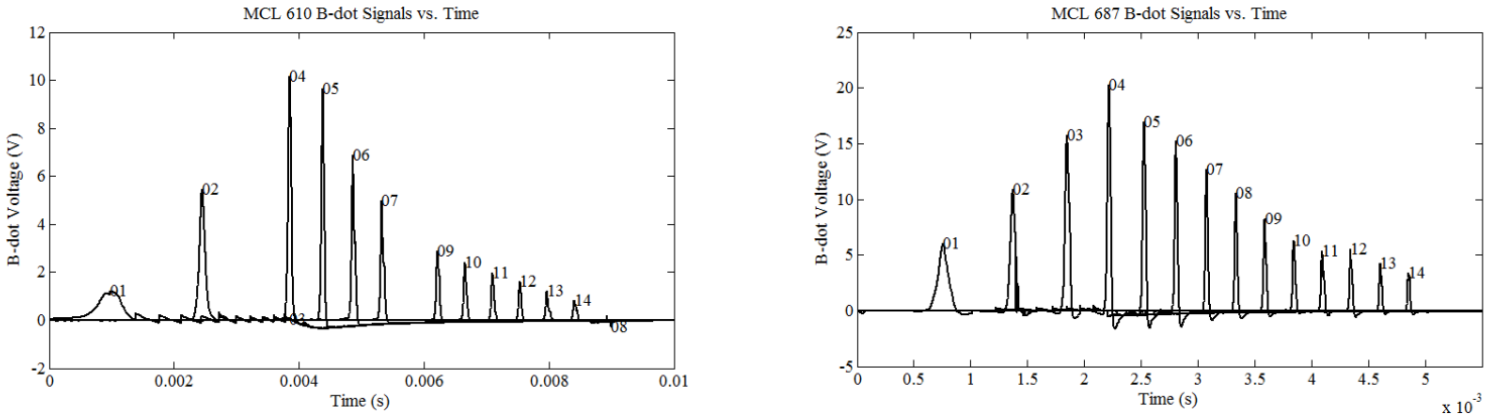

Figure E.1. MCL 610 (left), 687 (right) B-dot waveforms

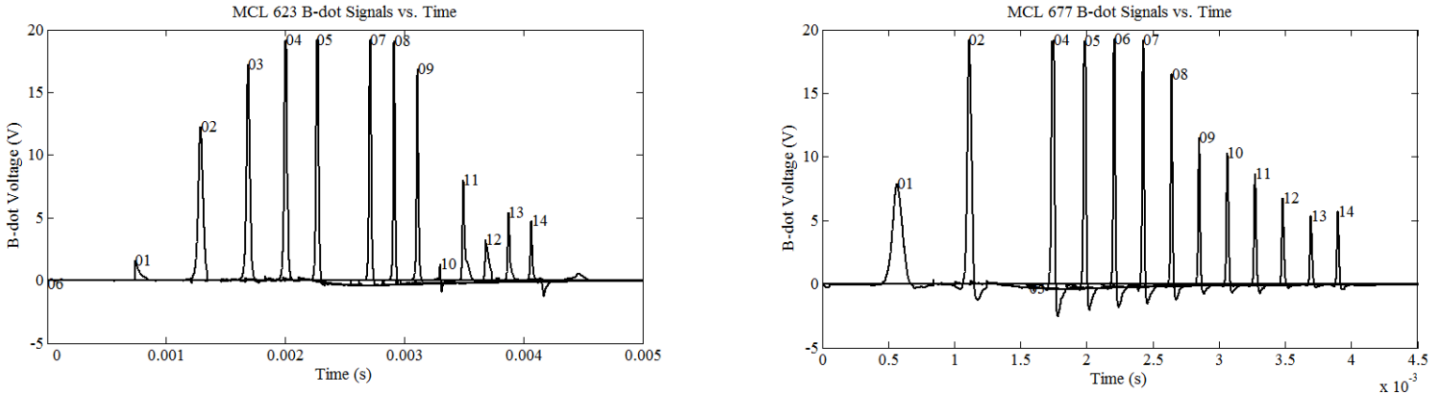

Figure E.2. MCL 623 (left), 677 (right) B-dot waveforms

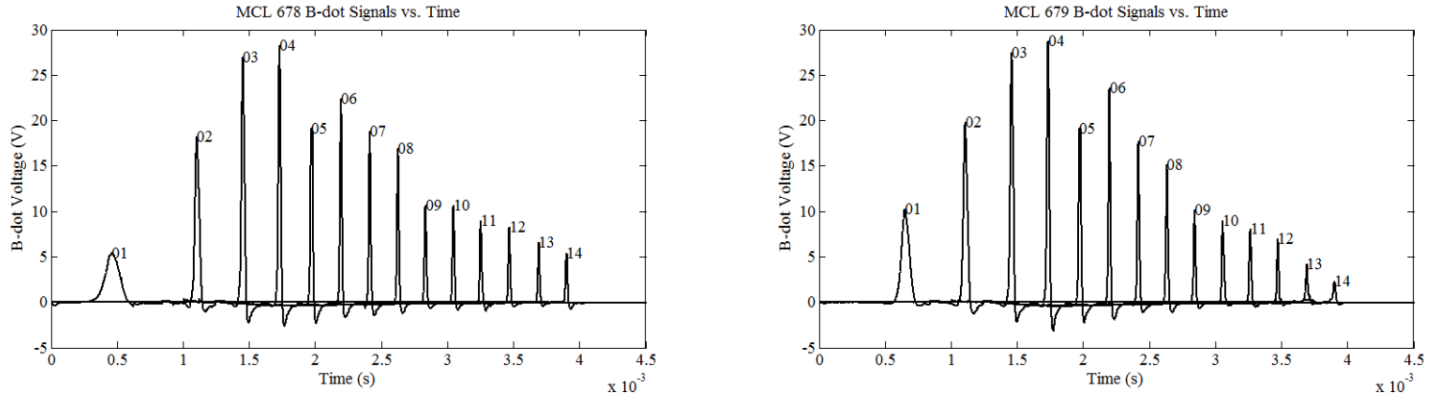

Figure E.3. MCL 678 (left), 679 (right) B-dot waveforms

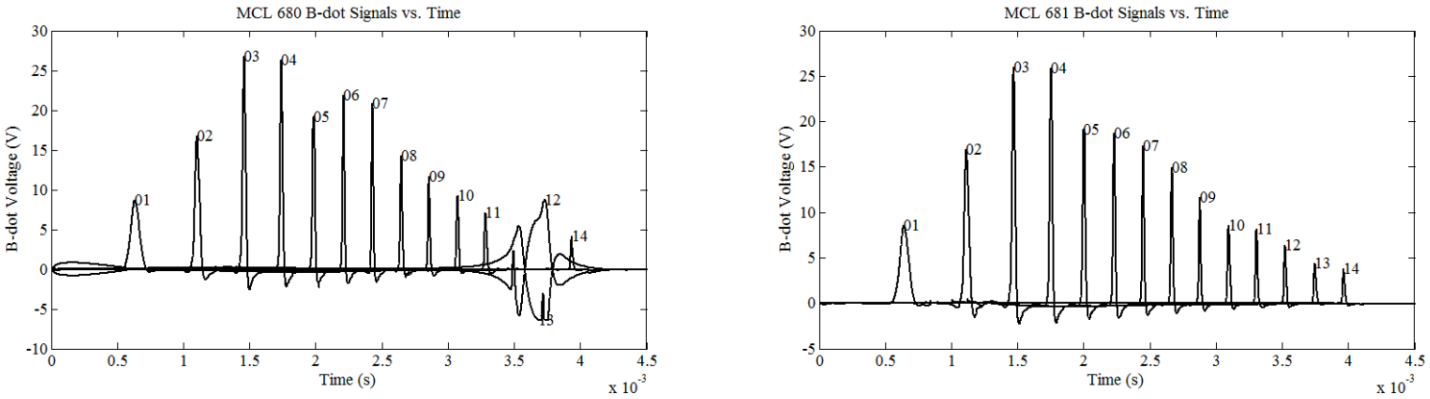

Figure E.4. MCL 680 (left), 681 (right) B-dot waveforms

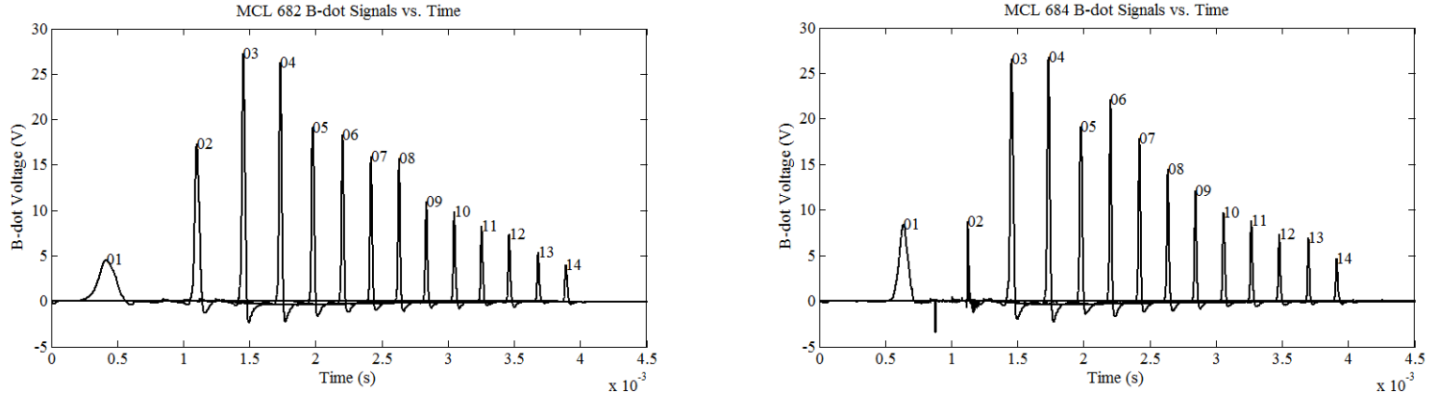

Figure E.5. MCL 682 (left), 684 (right) B-dot waveforms

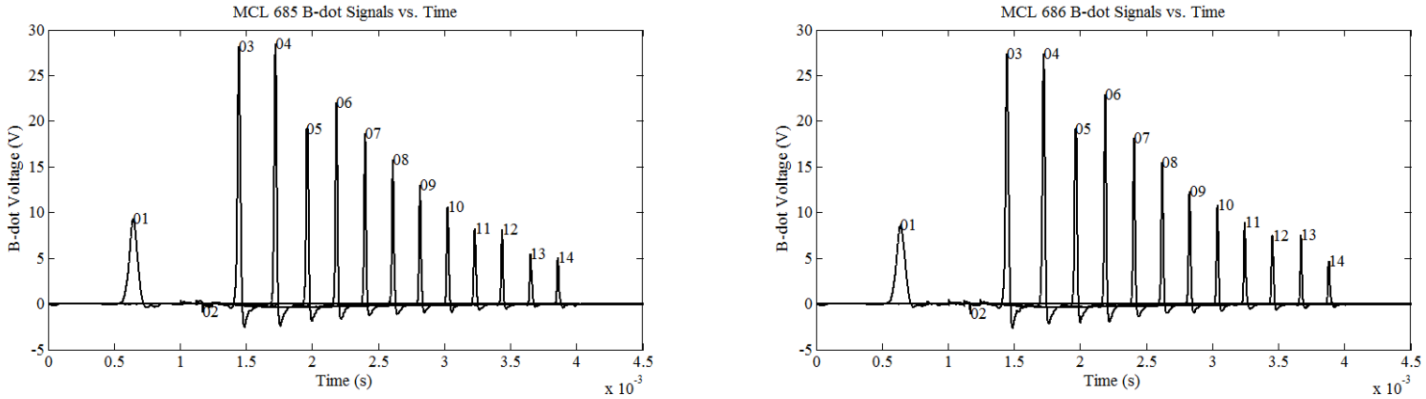

Figure E.6. MCL 685 (left), 686 (right) B-dot waveforms

COATED RAIL EXPERIMENTS

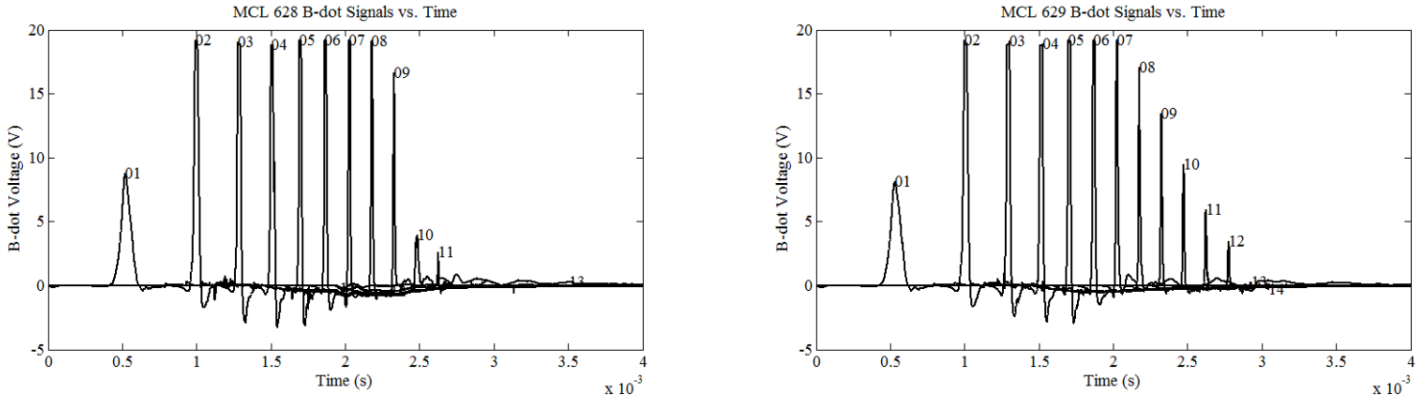

Figure E.7. MCL 628 (left), 629 (right) B-dot waveforms

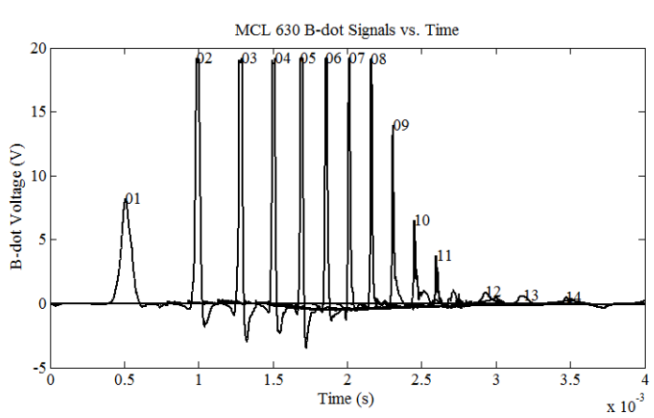

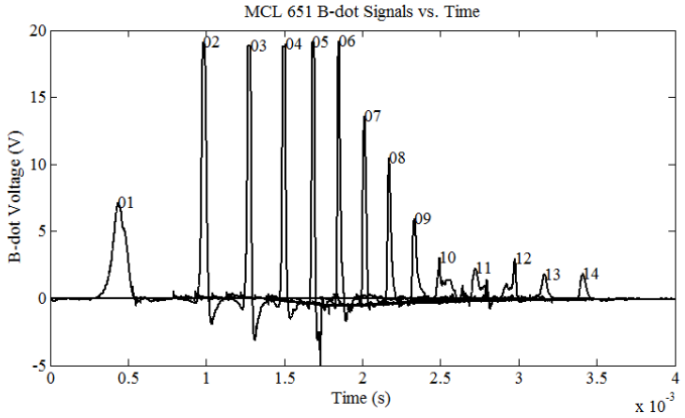

Figure E.8. MCL 630 (left), 651 (right) B-dot waveforms

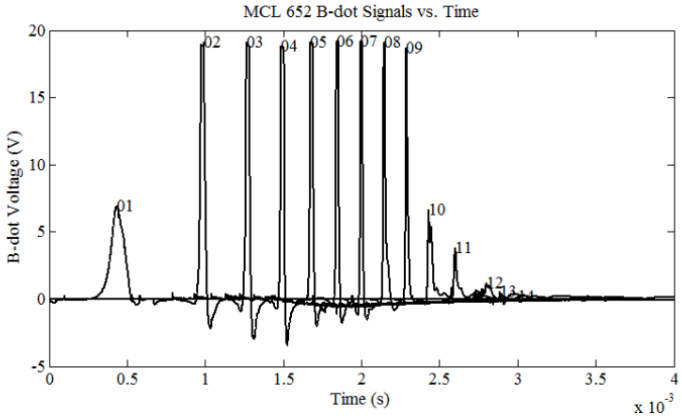

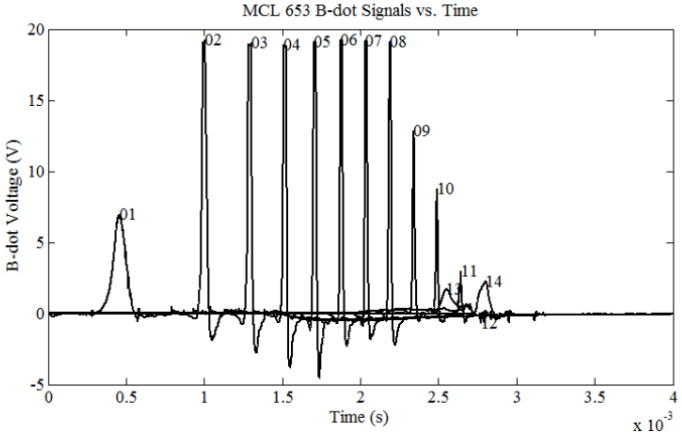

Figure E.9. MCL 652 (left), 653 (right) B-dot waveforms

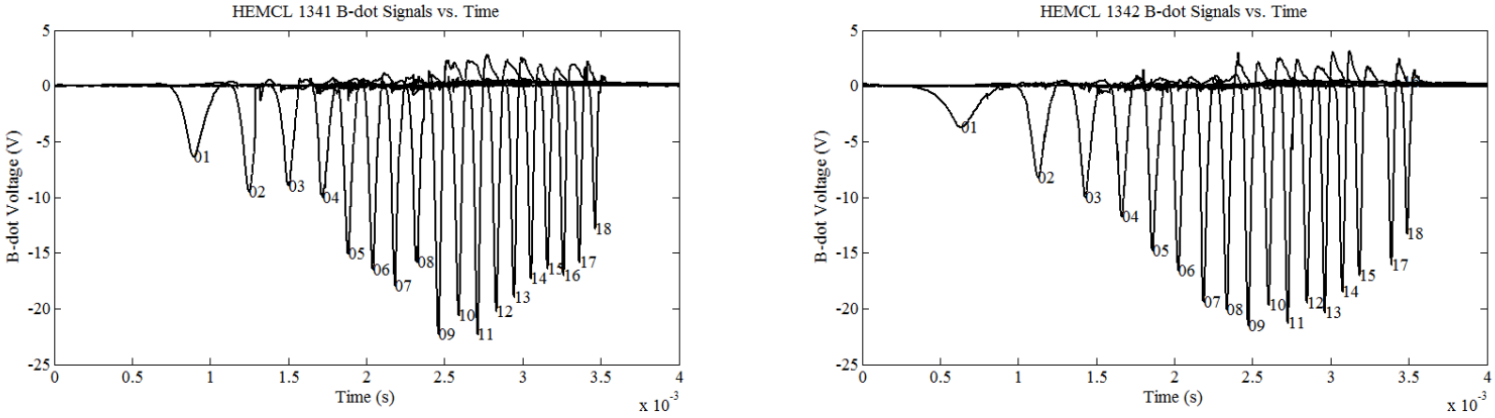

Figure E.10. HEMCL 1341 (left), 1342 (right) B-dot waveforms

NOMENCLATURE

Symbol	
A	Area
a	Acceleration
B	*R*ail width
c	Perturbation complex wave velocity
c_0	Hugoniot curve fitting parameter ($U_S = c_0 + su_p$)
C_D	Dilatational wave speed
C_R	Rayleigh wave speed
C_S	Shear wave speed
c_{yi}	Coordinate transformation scale factor for differentiation
D	Differentiation matrix $D^{(n)} = \partial^{(n)}/\partial y^{(n)}$
E	Young's modulus
E	Energy
e_{ij}	Strain tensor
Eu	Euler number
F	Force
g	Gravity
H	Hardness
h	Height
H_{max}	Maximum hardness
HV	Vickers microhardness
I	Identity matrix
I_A	Armature Current
I_{pk}	Peak current
$\hat{\imath}, \hat{\jmath}$	Unit normal vectors
J	Cross-sectional moment of inertia
K	Bulk viscosity
k_0	Foundation stiffness
KE	Kinetic energy
K_W	Dimensionless wear coefficient
L	Length
L'	Inductance gradient
m	Mass
m_μ	Ratio of fluid viscosities ($m_\mu = \mu_2/\mu_1$)
N	Number of collocation nodes
P	Pressure
$\acute{p}$	Fluid perturbation pressure

Symbol	
R'	*R*esistance gradient
Re	Reynolds number
Re_{cr}	Critical Reynolds number
R_{eff}	Effective Reynolds number
Ri	Richardson number
s	Hugoniot curve fitting parameter ($U_S = c_0 + su_p$)
t	Time
$\mathbf{T}$	Deviatoric stress tensor
T	Surface tension
T^*	Homologous temperature $T^* = (T-T_{ref})/(Tm-T_{ref})$
T_k	Chebyshev polynomial of the first kind
T_m	Melt temperature
T_{ref}	Reference temperature
U_S	Shock velocity
u_p	Particle velocity
u	Flow velocity in x-direction
$\boldsymbol{u}$	Particle velocity vector
U	Steady state flow velocity in *x*-direction
$\acute{u}$	Perturbed horizontal velocity
V	Volume
V_{arm}	Armature voltage drop
V_{charge}	Capacitor bank charge voltage
V_{crit}	Minimum phase speed for an un-attenuated wave on a beam on an elastic foundation
V_{est}	Estimated gouging velocity
V_{exit}	Exit (muzzle) velocity
V_{gall}	Galling onset velocity
V_{gouge}	Gouging onset velocity
V_{edge}	Velocity at leading edge of rail cladding
V_{range}	Velocity range on test sample
V_{trans}	Transition velocity
v	Flow velocity in y-direction
$\acute{v}$	Perturbed vertical velocity
W	Applied load
w	Fluid perturbation vorticity
x,y	Rectilinear coordinates
x_k	Collocation node
X_{trans}	Transition position
Z	Acoustic impedance $Z = \rho u_p$
z	Coordinate on domain (-1,+1)
α	Fluid perturbation wave number

Symbol	
G	2nd elastic Lamé constant (shear modulus)
μ	Dynamic viscosity
ν	Poisson's ratio
σ	Stress tensor
σ_{HEL}	Stress at Hugoniot elastic limit
σ_Y	Yield strength
ρ	Mass density
λ	1st elastic Lamé constant
θ	Angle
γ	Grüneisen parameter
Ψ	Fluid perturbation stream function potential
ϕ	Fluid perturbation stream function potential, y-component
δ_{ij}	Dirac delta function
$\dot{\varepsilon}$	Strain rate tensor
ε	Strain tensor
A,B,C,m,n	Johnson-Cook curve fitting parameters
A,c_1,c_2,c_3,c_4,c_5,n	Zerilli-Armstrong curve fitting parameters

Acronym	
ABAQUS	Finite element analysis software (SIMULIA, Dassault Systèmes)
AISI	American Iron and Steel Institute
ASB	Adiabatic shear band
BC	Boundary Condition
BCC	Body-Centered Cubic (crystal structure)
BEI	Backscattered Electron Image
CAD	Computer Aided Design
CHART-D	Computational Hydrodynamics and Radiative Thermal Diffusion (software, Sandia National Laboratories)
CTH	CHART-D squared to the Three Halves (software, Sandia National Laboratories)
DAQ	Data Acquisition
EDS	Energy Dispersive Spectroscopy
ELF	Electric Launch Facility
EPIC	Elastic-Plastic Impact Calculations (software, Wright Laboratory)
EW	Explosive Welding
FCC	Face-Centered Cubic (crystal structure)
FEA	Finite Element Analysis
HCP	Hexagonal Close-Packed (crystal structure)
HEL	Hugoniot Elastic Limit
HEMCL	High Energy Medium Caliber Launcher
HHSTT	Holloman High-Speed Test Track

Acronym	
HRC	Rockwell Hardness, C-scale
IAT	Institute for Advanced Technology
JC	Jump Condition
J-C	Johnson-Cook (material model)
K-H	Kelvin-Helmholtz (waves)
LS-DYNA	Livermore Software - Dynamic Analysis (software, Livermore Software Technology Corporation)
MCL	Medium Caliber Launcher
ODE	Ordinary Differential Equation
PFN	Pulse Forming Network
PPS	Pulsed Power Supply
PSB	Persistent Slip Band
RHA	Rolled Homogeneous Armor
SEI	Secondary Electron Image
SEM	Scanning Electron Microscope
S-P	Stefani-Parker (gouging model)
UNS	Unified Numbering System
VK	von Karman (waves)
Z-A	Zerilli-Armstrong (material model)

REFERENCES

1 C. Persad, G. Prabhu, G. White, A. Yeoh, Z. Eliezer, "Characterization of Hypervelocity Gouge Craters in Rail Conductors," *IEEE Trans. Mag.*, Vol. 33, No. 1, January 1997.

2 D. Godfrey, "Diagnosis of Wear Mechanisms," *Wear Control Handbook*, ASME, pp. 283-311, 1980.

3 K.-H. Z. Gahr, "Microstructure and Wear of Materials," *Tribology Series 10*, Elsevier Science Publishers B.V., 1987.

4 M.B. Peterson, "Classification of Wear Processes," *Wear Control Handbook*, ASME, pp. 9-15, 1980.

5 T. Akagaki, D.A. Rigney, "Sliding friction and wear of metals in vacuum," *Wear*, Vol. 149, pp. 353-374, 1991.

6 E. Rabinowicz, "The Determination of the Compatibility of Metals through Static Friction Tests," *ASLE Transactions*, Vol. 14, pp. 198-205, 1971.

7 K. Hokkirigawa, K. Kato, "An experimental and theoretical investigation of ploughing, cutting and wedge formation during abrasive wear," *Tribology International*, Vol. 21, No. 1, pp. 51-57, 1988.

8 K.J. Bhansali, A.E. Miller, "The Role of Stacking Fault Energy on Galling and Wear Behavior," *Wear*, Vol. 75, pp. 241-252, 1982.

9 S.C. Lim, M.F. Ashby, "Wear-Mechanism Maps," *Acta metall.*, Vol. 35, No. 1, pp. 1-24, 1987.

10 J.F. Archard, "Wear Theory and Mechanisms," *Wear Control Handbook*, ASME, pp. 35-80, 1980.

11 E. Rabinowicz, "Wear Coefficients – Metals," *Wear Control Handbook*, ASME, pp. 475-506, 1980.

12 M.D. Bryant, J.-P. Wang, J.-W. Lin, "Thermal mounding in high speed dry sliders: experiment, theory and comparison," *Wear* 181-183, pp. 668-677, 1995.

13 M. Okada, N.-S. Liou, V. Prakash, K. Miyoshi, "Tribology of High-Speed Metal-on-Metal Interfacial Temperatures," *Wear*, Vol. 249, pp. 672-686, 2001.

14 F. Stefani, J.V. Parker, "Experiments to Measure Armature Wear, Part 1: Wear Measurements on the KJ202 Armature," Technical Report, IAT.R 0180, IAT-UT, 1998.

15 K.F. Graff and B.B. Dettloff, "The gouging phenomenon between metal surfaces at very high sliding speeds," *Wear,* Vol. 14, pp. 87-97, 1969.

16 J.D. Cinnamon, A.N. Palazotto, "Metallographic Examination and Validation of Thermal Effects in Hypervelocity Gouging," *Journal of Pressure Vessel Technology*, Vol. 129, pp. 133-141, 2007.

17 C.S. Hale, A.N. Palazotto, G.J. Cameron, A.J. Chmiel, "Consideration of Wear at High Velocities," *49th AIAA/ASME/ASCE/AHS/ASC Structures, Structural Dynamics, and Materials Conference*, Schaumburg, IL, AIAA 2008-1747, April 2008.

18 A.G. Szmerekovsky, A.N. Palazotto, W.P. Baker, "Scaling numerical models for hypervelocity test sled slipper-rail impacts," *International Journal of Impact Engineering*, Vol. 32, pp. 928–946, 2006.

19 D.J. Laird, A.N. Palazotto, "Gouge development during hypervelocity sliding impact," *Int. J. Impact Eng.*, Vol. 30, pp. 205–223, 2004.

20 D.J. Laird, A.N. Palazotto, "Effect of Temperature on the Process of Hypervelocity Gouging," *AIAA Journal*, Vol. 41, No. 11, pp. 2251-2260, November 2003.

21 J.D. Cinnamon, "Hypervelocity Gouging Impacts," *Progress in Astronautics and Aeronautics*, Vol. 228, American Institute of Aeronautics and Astronautics, Inc., Reston, Virginia, 2009.

22 J.P. Barber and K.P. Bauer, "Contact Phenomena at Hypervelocities," *Wear*, Vol. 78, pp 163-169, 1982.

23 L.M. Barker, T.G. Trucano, "Railgun Rail Gouging by Hypervelocity Sliding Contact," *IEEE Trans. Mag.*, Vol. 25, No. 1, pp. 83-87, January 1989.

24 M. Schneider, R. Schneider, "Advanced Rail-Sabot Configurations for Brush Armatures," *IEEE Trans. Mag.*, Vol. 43, No. 1, pp. 186-189, January 2007.

25 F. Stefani, J.V. Parker, "Experiments to Measure Gouging Threshold Velocity for Various Metals Against Copper," *IEEE Trans. Mag.*, Vol. 35, No. 1, January 1999.

26 J.D. Cinnamon, A.N. Palazotto, A.G. Szmerekovsky, R.J. Pendleton, "Investigation of Scaled Hypervelocity Gouging Model and Validation of Material Constitutive Models," *AIAA JOURNAL* Vol. 45, No. 5, pp. 1104-1112, May 2007.

27 J.D. Cinnamon, A.N. Palazotto, A.G. Szmerekovsky, and R.J. Pendleton, "Further Investigation of a Scaled Hypervelocity Gouging Model and Validation of Material Constitutive Models," *47th AIAA/ASME/ASCE/AHS/ASC Structures,*

Structural Dynamics, and Materials Conference, Newport, Rhode Island, AIAA, pp. 2006-2087, May 2006.

28 K.R. Tarcza, W.F. Weldon, "Metal gouging at low relative sliding velocities," *Wear*, Vol. 209, pp. 21-30, 1997.

29 K.R. Tarcza, "The Gouging Phenomenon at Low Relative Sliding Velocities," Thesis, The University of Texas at Austin, 1995.

30 S. Satapathy, C. Persad, R. Monfredo Gee, S. Bless, "Gouging Induced Fractures in Tungsten Long Rods," *Int. J. Impact Eng.*, Vol. 29, pp. 621–630, 2003.

31 A.G. Szmerekovsky, "The Physical Understanding of the Use of Coatings to Mitigate Hypervelocity Gouging Considering Real Test Sled Dimensions," Dissertation, Air Force Institute of Technology, Air University, September 2004.

32 A.G. Szmerekovsky, A.N. Palazotto, "Structural Dynamic Considerations for a Hydrocode Analysis of Hypervelocity Test Sled Impacts," *AIAA JOURNAL*, Vol. 44, No. 6, pp. 1350-1359, June 2006.

33 C. Persad, A. Yeoh, G. Prabhu, G. White, Z. Eliezer, "On the Nature of the Armature-Rail Interface: Liquid Metal Effects," *IEEE Transactions on Magnetics*, Vol. 33, No. 1, pp. 140-145, Jan. 1997.

34 R.E. Kothmann, F. Stefani, "A Thermal Hydraulic Model of Melt-Lubrication in Railgun Armatures," *IEEE Transactions on Magnetics*, Vol. 37, No. 1, pp. 86-91, Jan. 2001.

35 K.P. Cooper, H.N. Jones, R.A. Meger, "Analysis of Railgun Barrel Material," *IEEE Transactions on Magnetics*, Vol. 43, No. 1, pp. 120-125, Jan. 2007.

36 M.A. Meyers, "Dynamic Behavior of Materials," John Wiley & Sons, Inc., New York, NY, 1994.

37 I.A. Viktorov, "Rayleigh and Lamb Waves: physical theory and applications", Plenum Press, New York, 1967.

38 K. Ranjith, "Destabilization of long-wavelength Love and Stoneley Waves in slow sliding," *International Journal of Solids and Structures*, Vol. 46, pp. 3086-3092, 2009.

39 D.M. Barnett, S.D. Gavazza, J. Lothe, "Slip waves along the interface between two anisotropic elastic half-spaces in sliding contact," *Proc. R. Soc. Lond.* A, Vol. 415, pp. 389-419, 1988.

40 K. Ranjith, J.R. Rice, "Slip dynamics at an interface between dissimilar materials," *Journal of the Mechanics and Physics of Solids*, Vol. 29, 341-361, 2001.

41 Y.-S. Wang, N. Li, G.-L. Yu, "Subsonic slip waves and steady sliding at the interface between two anisotropic elastic half-spaces in frictional contact with stick-slip," *Wave Motion*, Vol. 44, pp. 439-457, 2007.

42 Y.-S. Wang, G.-L. Yu, J. Qu, "Subsonic slip waves along the interface between two anisotropic elastic half-spaces in sliding contact with separation," *International Journal of Engineering Science*, Vol. 41, pp. 1785-1798, 2003.

43 E.M. Dunham, "Dissipative interface waves and the transient response of a three-dimensional sliding interface with Coulomb friction," *Journal of Mechanics and Physics of Solids*, Vol. 53, pp. 327-357, 2005.

44 L. Afferrante, M. Ciavarella, J.R. Barber, "Sliding thermoelastodynamic instability," *Proc. R. Soc. A*, Vol. 462, pp. 2161-2176, 2006.

45 T.J. Watt and S. Fish, "Examination of High Frequency Contact Chatter in Trailing Arm Armatures," *IEEE Transactions on Magnetics*, Vol. 37, No. 1, pp. 106-110, 2001.

46 J.T. Tzeng, "Dynamic Response of Electromagnetic Railgun Due to Projectile Movement," *IEEE Transactions on Magnetics*, Vol. 39, No. 1, pp. 471-475, 2003.

47 A.J. Johnson, F.C. Moon, "Elastic Waves and Solid Armature Contact Pressure in Electromagnetic Launchers," *IEEE Transactions on Magnetics*, Vol. 42, No. 3, pp. 422-429, 2006.

48 A.J. Johnson, T. Haran, F.C. Moon, W. Robinson, "Stress Wave Measurements in an Electromagnetic Launcher," *14th Symposium on Electromagnetic Launch Technology*, pp. 1-6, 2008.

49 N.V. Nechitailo, K.B. Lewis, "Critical velocity for rails in hypervelocity launchers," *International Journal of Impact Engineering*, Vol. 33, pp. 485-495, 2006.

50 K. Daneshjoo, M. Rahimzadeh, R. Ahmadi, M. Ghassemi, "Dynamic Response and Armature Critical Velocity Studies in an Electromagnetic Railgun," *IEEE Transactions on Magnetics*, Vol. 43, No. 1, pp. 126-131, 2007.

51 A.J. Johnson, F.C. Moon, "Elastic Waves in Electromagnetic Launchers," *IEEE Transactions on Magnetics*, Vol. 43, No. 1, pp. 141-144, 2007.

52 K.B. Lewis, N.V. Nechitailo, "Transient Resonance in Hypervelocity Launchers at Critical Velocities," *IEEE Transactions on Magnetics*, Vol. 43, No. 1, pp. 157-162, 2007.

53 F.P. Gerstle, Jr., P.S. Follansbee, G.W. Pearsall, M. L. Shepard, "Thermoplastic Shear and Fracture of Steel During High-Velocity Sliding," *Wear*, Vol. 24, pp. pp 97-106, 1973.

54 W. Wang, S. To, C.Y. Chan, C.F. Cheung, W.B. Lee, "Elastic strain induced shear bands in the microcutting process," *International Journal of Machine Tools & Manufacture,* Vol. 50, pp. 9-18, 2010.

55 Y. Bai, B. Dodd, "Adiabatic Shear Localization: Occurrence, Theories and Applications," Permagon Press, Oxford, England, 1992.

56 T.W. Wright, "The Physics and Mathematics of Adiabatic Shear Bands," Cambridge University Press, Cambridge, UK, 2002.

57 A.G. Szmerekovsky, A.N. Palazotto, "Numerical Analysis for a study of the Mitigation of Hypervelocity Gouging," *45th AIAA/ASME/ASCE/AHS/ASC Structures, Structural Dynamics & Materials Conference*, Palm Springs, California, AIAA 2004-1922, April 2004.

58 D.L. Bourell, C. Persad, "Simulation of Railgun Gouging," *IEEE Trans. Mag.*, Vol. 35, No. 1, January 1999.

59 J.D. Cinnamon, A.N. Palazotto, Z. Kennan, "Material characterization and development of a constitutive relationship for hypervelocity impact of 1080 Steel and VascoMax 300," *International Journal of Impact Engineering*, Vol. 33, pp. 180–189, 2006.

60 G.S. Rickerd, A.N. Palazotto, J.D. Cinnamon, "Investigation of a Simplified Hypervelocity Gouging Model," *46th AIAA/ASME/ASCE/AHS/ASC Structures, Structural Dynamics & Materials Conference*, Austin, Texas, AIAA 2005-2355, April 2005.

61 J.M. McGlaun, S.L. Thompson, M.G. Elrick, "CTH: A three-dimensional shock wave physics code," *International Journal of Impact Engineering*, Vol. 10, No. 1-4, pp. 351-360, 1990.

62 R.D.M. Tachau, C.H. Yew, T.G. Trucano, "Gouge Initiation in High-Velocity Rocket Sled Testing," *Int. J. Impact Eng.*, Vol. 17, pp. 825-836, 1995.

63 R.D.M. Tachau, "An Investigation of Gouge Intiation in High-Velocity Sliding Contact," Dissertation, The University of Texas at Austin, 1991.

64 F.J. Zerilli, "Dislocation Mechanics-Based Constitutive Equations," *Metallurgical and Materials Transactions*, Vol. 35A, pp. 2547-2555, September 2004.

65 J.D. Cinnamon, A.N. Palazotto, "Analysis and simulation of hypervelocity gouging impacts for a high speed sled test," *Int. J. Impact Eng*, Vol. 36, No. 2, pp. 254-262, 2009.

66 D.J. Laird, A.N. Palazotto, "Temperature Effects on the Gouging and Mixing of Solid Metals During Hypervelocity Sliding Impact," *43rd AIAA/ASME/ASCE/*

AHS/ASC Structures, Structural Dynamics, and Materials Conference, Denver Colorado, AIAA 2002-1691, April 2002.

67 J.M. Walsh and R.H. Christian, "Equation of State of Metals from Shock Wave Measurements," *Phys. Rev.*, Vol 97, p 1544–1556, 1955.

68 O.E. Petel, F.X. Jette, "Comparison of methods for calculating the shock hugoniot of mixtures," *Shock Waves*, Vol. 20, No. 1, pp. 73-83, February 2010.

69 G. Subhash, "Dynamic Indentation Testing," ASM International, 2003.

70 G. Subhash, "Dynamic Indentation of Brittle Materials," ASM International, 2003.

71 S.K. Ghosh, "Experimental Tests of Buckling Folds un Relation to Strain Ellipsoid in Simple Shear Deformations," *Tectonophysics*, Vol. 3, pp. 169-185, 1966.

72 H. Ramberg, K.E. Strömgård, "Experimental Tests of Modern Buckling Theory Applied on Multilayered Media," *Tectonophysics*, Vol. 11, pp. 461-472, 1971.

73 H. Ramberg, "Selective Buckling of Composite Layers with Contrasted Rheological Properties, A Theory for Simultaneous Formation of Several Orders of Folds," *Tectonophysics*, Vol. 1, No. 4, pp. 307-341, 1964.

74 D. Berthe, J.P. Brun, "Evolution of folds during progressive shear in the South Armorican Shear Zone, France," *Journal of Structural Geology*, Vol. 2, pp. 127-133, 1980.

75 J. Carreras, E. Druguet, A. Griera, "Shear zone-related folds," *Journal of Structural Geology*, Vol. 27, pp. 1229-1251, 2005.

76 B. Goscombe, "Intense non-coaxial shear and the development of mega-scale sheath folds in the Arunta Block, Central Australia," *Journal of Structural Geology*, Vol. 13, No. 3, pp. 299-318, 1991.

77 M.A. Biot, "Folding Instability of a Layered Viscoelastic Medium under Compression," *Proceedings of the Royal Society of London. Series A, Mathematical and Physical Sciences*, Vol. 242, No. 1231, pp. 444-454, 1957.

78 M.A. Biot, "Rheological Stability with Couple Stresses and Its Application to Geological Folding," *Proceedings of the Royal Society of London. Series A, Mathematical and Physical Sciences*, Vol. 298, No. 1455, pp. 402-423, 1967.

79 H. Ramberg, "Folding of Laterally Compressed Multilayers in the Field of Gravity, I," *Phys. Earth Planet. Interiors*, Vol. 2, pp. 203-232, 1970.

80 H. Ramberg, "Folding of a Single Viscous Layer: Exact Infinitesimal-Amplitude Solution – Discussion," *Tectonophysics*, Vol. 56, pp. 321-326, 1979.

81 F.O. Marques, S.M. Guerreiro, A.R. Fernandes, “Sheath fold development with viscosity contrast: Analogue experiments in bulk simple shear,” *Journal of Structural Geology,* Vol. 30, pp. 1348-1353, 2008.

82 P.R. Cobbold, H. Quinquis, “Development of sheath folds in shear regimes,” *Journal of Structural Geology,* Vol. 2, pp. 119-126, 1980.

83 L. Skjernaa, “Tubular folds and sheath folds: definitions and conceptual models for their development, with examples from the Grapesvare area, northern Sweden,” *Journal of Structural Geology,* Vol. 11, No. 6, pp. 689-703, 1989.

84 D.J. Wollkind, J.I.D. Alexander, “Kelvin-Helmholtz Instability in a Layered Newtonian Fluid Model of the Geological Phenomenon of Rock Folding” *SIAM Journal on Applied Mathematics,* Vol. 42, No. 6, pp. 1276-1295, 1982.

85 F. Rosas, F.O. Marques, A. Luz, S. Coelho, “Sheath folds formed by drag induced by rotation of rigid inclusions in viscous simple shear flow: nature and experiment,” *Journal of Structural Geology,* Vol. 24, pp. 45-55, 2002.

86 U. Exner, N.S. Mancktelow, B. Grasemann, “Progressive development of s-type flanking folds in simple shear,” *Journal of Structural Geology,* Vol. 26, pp. 2191-2201, 2004.

87 J.W. Mies, “Planar dispersion of folds in ductile shear zones and kinematic interpretation of fold-hinge girdles,” *Journal of Structural Geology,* Vol. 13, No. 3, pp. 281-297, 1991.

88 A. Yassaghi, P.R. James, T. Flottmann, “Geometric and kinematic evolution of asymmetric ductile shear zones in thrust sheets, southern Adelaide Fold-Thrust Belt, South Australia,” *Journal of Structural Geology,* Vol. 22, pp. 889-912, 2000.

89 O. Lexa, J. Cosgrove, K. Schulmann, “Apparent shear-band geometry resulting from oblique fold sections,” *Journal of Structural Geology,* Vol. 26, pp. 155-161, 2004.

90 A.A. Deribas, I.D. Zakharenko, “Determination of Limiting Collision Conditions Ensuring the Welding of Metals by Explosion,” Novosibirsk, UDC 621.791.1, 1974.

91 I.D. Zakharenko, B.S. Zlobin, “Effect of the Hardness of Welded Materials on the Position of the Lower Limit of Explosive Welding,” Novosibirsk, UDC 621.7.044, Plenum Publishing Corporation, 1984.

92 B.C. Zlobin, “Explosion Welding of Steel with Aluminum,” *Combustion, Explosionm and Shock Waves,* Vol. 38, No. 3, pp. 374-377, 2002.

93 O.B. Drennov, A.I. Davydov, A.L. Mikhailov, V.A. Raevskii, “Shear instability at the “explosion product-metal” interface for sliding detonation of an explosive charge,” *International Journal of Impact Engineering*, Vol. 32, pp. 155–160, 2005.

94 V.V. Demchenko, M.A. Sergeev, “Instability of a Collision Surface During High-Velocity Impact,” *Fluid Dynamics*, Vol. 38, No. 6, pp. 923–932, 2003.

95 O.B. Drennov, A.L. Mikhailov, P.N. Nizovtsev, V.A. Raevskii, “Instability of an interface between steel layers acted upon by an oblique shock wave,” *International Journal of Impact Engineering*, Vol. 32, 161–172, 2005.

96 A.S.Bahrani, T.J.Black and B.Crossland, “The mechanics of wave formation in explosive welding,” *Proc. Roy. Soc. A*, Vol. 296, pp. 123-136 (1966).

97 A.A. Akbari Mousavi, S.T.S. Al-Hassani, “Numerical and experimental studies of the mechanism of the wavy interface formations in explosive/impact welding,” *Journal of the Mechanics and Physics of Solids*, Vol. 53, pp. 2501–2528, 2005.

98 M.P. Bondar, “Localization of Plastic Deformation on Contacts, Determing the Formation fo a Strong Joint,” *Combustion, Explosion, and Shock Waves*, Vol. 31, No. 5, pp. 612-616, 1995.

99 V.G. Petushkov, “Physical Intepretation of Explosion Welding near Its Lower Boundary,” *Combustion, Explosionm and Shock Waves*, Vol. 36, No. 6, pp. 771-776, 2000.

100 M.P. Bondar, “Localization of Plastic Deformation on Contacts, Determining the Formation of a Strong Joint,” *Combustion, Explosion, and Shock Waves*, Vol. 31, No. 5, pp. 612-616, 1995.

101 M.P. Bondar, “Evolution of the Mcuirostructre of Dynamically Loaded Materials,” *Combustion, Explosionm and Shock Waves*, Vol. 38, No. 2, pp. 239-247, 2002.

102 E.P. Carton, “Wave Forming Mechanisms in Explosive Welding,” *Materials Science Forum*, Vol. 465-466, pp. 219-224, 2004.

103 G.R.Cowan and A.H.Holtzman, “Flow configurations in colliding plates: explosive bonding,” *J. Appl. Phys.*, Vol. 34, No. 4, pp. 928-939, 1963.

104 R.A. Gerwin, “Stability of the Interface between Two Fluids in Relative Motion,” *Reviews of Modern Physics*, Vol. 40, No. 3, pp. 652-658, July 1968.

105 G.R. Cowan, O.R. Bergnrann and A.H. Holtzman, “Mechanism of bond zone wave formation in explosive – clad metals,” *Metallurgical Transactions*, Vol. 2, No. 11, pp. 3145 -3155, 1971.

106 V.V. Pai, Ya.L. Luk'yanov, G.E. Kuz'min, I.V. Yakovlev, "Wave Formation in a High-Velocity Symmetric Impact of Metal Plates," *Combustion, Explosion, and Shock Waves*, Vol. 42, No. 5, pp. 611-616, 2006.

107 C. Chemin, T. Qingming, "Mechanism of Wave Formation at the Interface in Explosive Welding," *Acta Mechanica Sinica*, Vol. 5, No. 2, pp. 97-108, 1989.

108 O.B. Drennov, "Development of Perturbations at an Aluminum-Copper Contact Boundary in a Nonsteady Regime of Oblique Collision," Moscow, Plenum Publishing Corp., UDC 534.222.2, 1989.

109 O.B. Drennov, "About the State of Two-Metal Contact Boundary at a High-Velocity Oblique Impact," *International Journal of Impact Engineering*, Vol. 23, pp. 205-213, 1999.

110 O.B. Drennov, A.L. Miklhailov, R.S. Osipov, L.D. Rodigina, "Stabilization of Wave Formation at the Contact Boundary of Metal Layers in an Explosive Welding Regime," Moscow, UDC 534.222.2, Plenum Publishing Corporation, 1990.

111 D.B. Hayes, "Introduction to Stress Wave Phenomena," Technical Report, SLA-73-0801, Sandia National Laboratories, Albuquerque, NM, August 1973.

112 G.E. Duvall, R.A. Graham, "Phase transitions under shock-wave loading," *Review of Modern Physics*, Vol. 49, No. 3, pp. 523-579, July 1977.

113 H. Kolsky, "Stress Waves in Solids," Dover Publications, Inc., New York, NY, 1963.

114 S.-H. Sheen, H.-T. Chien, A.C. Raptis, "Measurement of Shear Impedances of Viscoelastic Fluids," *IEEE International Ultrasonics Symposium*, San Antonio TX, November 3-6, 1996.

115 GRAHAMUK at the English language Wikipedia [GFDL (www.gnu.org/copyleft/fdl.html)], via Wikimedia Commons

116 H.L. Swinney, J.P. Gollub, "Hydrodynamic Instabilities and the Transition to Turbulence," *Topics in Applied Physics*, Vol. 45, Springer-Verlag, Berlin, 1981.

117 J.H. Gerrard, "The Wakes of Cylindrical Bluff Bodies at Low Reynolds Number," *Philosophical Transactions of the Royal Society of London, Series A, Mathematical and Physical Sciences*, Vol. 288, No. 1354, pp. 351-382, 1978.

118 L.D. Landau, E.M. Lifshitz, "Fluid Mechanics, 2nd Ed.," Pergamon Press, New York, NY, 2004.

119 J.P. Albert, J.L. Bona, J.-C. Saut, "Model Equations for Waves in Stratified Fluids," *Proc. Mathematical, Physical and Engineering Sciences*, Vol. 453, No. 1961, June 1997.

120 R.F. Davey, A. Roshko, "The effect of a density difference on shear-layer instability," *J. Fluid Mech,* Vol. 53, part 3, pp. 523-543, 1972.

121 H.B. Squire, "On the Stability for Three-Dimensional Disturbances of Viscous Fluid Flow between Parallel Walls," *Proc. R. Soc. Lond. A,* Vol. 142, pp. 621-628, 1933

122 X.Y. You, "Squire Theorem with Variable Physical Properties," *Int. Comm. Heat Mass Transfer,* Vol. 29, No. 1, pp. 141-144, 2002.

123 C.-S. Yih, "Wave velocity in parallel flows of a viscous fluid," *J. Fluid Mech.*, vol. 58, part 4, 703-708, 1973.

124 F.K. Browand, C.D. Winant, "Laboratory Observations of Shear-Layer Instability in a Stratified Fluid," *Boundary-Layer Meteorology,* Vol. 5, pp. 67-77, 1973.

125 P.I. Kolykhalov, "Dissipative Instability of Fluid Flows with Piecewise Linear Velocity Profiles," *Izvestiya Akademii Nauk SSSR, Mekhanika Zhidkosti I Gaza*, No. 6, pp. 14-19, 1986.

126 A.P. Hooper, W.G.C. Boyd, "Shear-flow instability at the interface between two viscous fluids," *J. Fluid Mech.*, Vol. 128, pp. 507-528, 1983.

127 A.D.D. Craik, F.I.P. Smith, "The stability of free-surface flows with viscosity stratification," *J. Fluid Mech.*, Vol. 34, part 2, pp. 393-406, 1968.

128 C.-S. Yih, "Instability due to viscosity stratification," *J. Fluid Mech.*, Vol. 27, No. 2, pp. 337-352, 1967.

129 V. Lee, C.P. Caulfield, "Nonlinear evolution of a layered stratified shear flow," *Dynamics of Atmospheres and Oceans*, Vol. 34, pp. 103-124, 2001.

130 F. Treyssède, M.B. Tahar, "Jump conditions for unsteady small perturbations at fluid-solid interfaces in the presence of initial flow and prestress," *Wave Motion*, Vol. 46, pp. 155-167, pp. 2009.

131 R.E. Esch, "The instability of a shear layer between two parallel streams," *Journal of Fluids Mechanics,* Vol. 3, pp. 289-303, 1957.

132 S. Chandrasekhar, "Hydrodynamic and Hydromagnetic Stability," Dover Publications, Inc., New York, NY, 1981.

133 H.P. Greenspan, D.J. Benney, "On shear-layer instability, breakdown and transition," *Journal of Fluid Mechanics,* Vol. 15, pp. 133-153, 1963.

134 M.C. Potter, "Stability of plane Couette-Poiseuille flow," *J. Fluid Mech.*, Vol. 24, part 3, pp. 609-619, 1966.

135 C.-S. Yih, "Stability of Liquid Flow down and Inclined Plane," *The Physics of Fluids*, Vol. 6, No. 3, pp. 321-334, March 1963.

136 C. Canuto, M.Y. Hussaini, A. Quarteroni, T.A. Zang, "Spectral Methods," Springer-Verlag Berlin Heidelberg, 2007.

137 S.A. Orszag, "Accurate solution of the Orr-Sommerfeld stability equation," *J. Fluid Mech.*, Vol. 50, part 4, pp. 689-703, 1971.

138 S.A. Orszag, L.C. Kells, "Transition to turbulence in plane Poiseuille and plane Couette flow," *J. Fluid Mech.*, Vol. 96, part 1, pp. 159-205, 1980.

139 P.A.M. Boomkamp, M.J. Boersma, R.H.M. Miesen, G.V. Beijnon, "A Chebyshev Collocation Method for Solving Two-Phase Flow Stability Problems," *Journal of Computational Physics*, Vol. 132, pp. 191-200, 1997.

140 S.M. Cox, "Rotating Convection in a Shear Flow," *Proceedings: Mathematical, Physical and Engineering Sciences*, Vol. 454, No. 1974, pp. 1699-1717, 1998.

141 R. Piché, "Solving BVPs using differentiation matrices," Tampere University of Technology, March 2007.

142 J.A.C. Weideman, S.C. Reddy, "A MATLAB Differentiation Matrix Suite," *ACM Transactions on Mathematical Software*, Vol. 26, No. 4, pp. 465-519, 2000.

143 "A Matlab Differentiation Matrix Suite," Last updated: August 29, 2003, http://dip.sun.ac.za/~weideman/research/differ.html.

144 C.B. Moler, G.W. Stewart, "An Algorithm for Generalized Matrix Eigenvalue Problems," *SIAM Journal on Numerical Analysis*, Vol. 10, No. 2, pp. 241-256, April 1973.

145 R. Miesen, B.J. Boersma, "Hydrodynamic stability of a sheared liquid film," *J. Fluid Mech.*, Vol. 301, pp. 175-202, 1995.

146 C.-S. Yih, "Wave formation on a liquid layer for de-icing airplane wings," *J. Fluid Mech.*, Vol. 212, pp. 41-53, 1990.

147 P.A.M. Boomkamp, R.H.M. Miesen, "Classification of Instabilities in Parallel Two-Phase Flow," *Int. J. Multiphase Flow*, Vol. 22, Suppl., pp. 67-88, 1996.

148 J.J. Dongarra, B. Straughan, D.W. Walker, "Chebyshev tau – QZ Algorithm Methods for Calculating Spectra of Hydrodynamic Stability Problems," *Applied Numerical Mathematics*, Vol. 22, No. 4, pp. 399-434, 1996.

149 J.H. Hildebrand, R.H. Lamoreaux, "Viscosity of liquid metals: An interpretation," *Proc. Nat. Acad. Sci. USA*, Vol. 73, No. 4, pp. 988-989, April 1976.

150 L. Battezzati, A.L. Greer, "The viscosity of liquid metals and alloys," Acta metall. Vol. 37, No. 7, pp. 1791-1802, 1989.

151 M.J. Assael, K. KAkosimos, R.M. Banish, J. Brillo, I. Egry, R. Brooks, P.N. Quested, K.C. Mills, A. Nagashima, Y. Sato, W.A. Wakeham, "Reference Data

for the Density and Viscosity of Liquid Aluminum and Liquid Iron," *J. Phys. Chem. Ref. Data*, Vol. 35, No. 1, 2006.

152 W.M. Haynes, CRC Handbook of Chemistry and Physics, 91st Edition, Section 4: Properties of the Elements and Inorganic Compounds, CRC Press, 2010.

153 M.C. Flemings, "Behavior of Metal Alloys in the Semisolid State," *Metallurgical Transactions B*, Vol. 22B, pp. 269-293, 1991.

154 G.K. Sigworth, "Rheological Properties of Metal Alloys in The Semi-Solid State," *Canadian Metallurgical Quarterly*, Vol. 35, No. 2, pp. 101-122, 1996.

155 G.G. Savenkov, Yu.I. Meshcheryakov, "Structural Viscosity of Solids," *Combustion, Explosionm and Shock Waves*, Vol. 38, No. 3, pp. 352-357, 2002.

156 W. Blumen, "Shear layer instability of an inviscid compressible fluid," *J. Fluid Mech.*, vol. 40, part 4, pp. 769-781, 1970.

157 W. Blumen, P.G. Drazin, D.F. Billings, "Shear layer instability of an inviscid compressible fluid, Part 2," *J. Fluid Mech.*, vol. 71, part 2, pp. 305-316, 1975.

158 P.G. Drazin, A. Davey, "Shear layer instability of an inviscid compressible fluid, Part 3," *J. Fluid Mech.*, Vol. 82, part 2, pp. 255-260, 1977.

159 P.A. Davis, W.R. Peltier, "Resonant Parallel Shear Instability in the Stably Stratified Planetary Boundary Layer," *Journal of Atmospheric Sciences*, Vol. 33, pp. 1287-1330, July 1976.

160 H.D.I. Abarbanel, D.D. Holm, J.E. Marsden, T. Ratiu, "Richardson Number Criterion for the Nonlinear Stability of Three-Dimensional Stratified Flow," *Physical Review Letters*, Vol. 52, No. 26, pp. 2352-2355, June 1984.

161 N.R. Sibgatullin, A.N. Sibgatullina, "Two-Dimensional Instability of a Tangential Discontinuity in Dispersive Media," *Fluid Dynamics*, Vol. 31, No. 1, 1997, pp. 11-17.

162 M. Malik, J. Dey, "Linear stability, transient energy growth and the role of viscosity stratification in compressible plane Couette flow," *Physical Review E*, Vol. 77, 2008.

163 G.V. Stepanov, "Strength of Metals at High Strain Rates," *Strength of Materials*, Vol. 34, No. 3, pp. 214-218, 2002.

164 J.C. Swearengen, J. Lipkin, C.M. Percival, "Influence of microstructure on the dynamic high-temperature elastic moduli of aluminum," *Journal of Applied Physics*, Vol. 44, No. 12, pp. 5209-5212, 1973.

165 W.S. Lee, W.C. Sue, C.F. Lin, C.J. Wu, "The train rate and temperature dependence of the dynamics impact properties of 7075 aluminum alloy," *Journal of Materials Processing Technology*, Vol. 100, pp. 116-122, 2000.

166 R.W. Balluffi, et. al., “Kinetics of Materials,” John Wiley & Sons, Inc., Hoboken, NJ, 2005.

167 F.J. Zerilli, R.W. Armstrong, “Dislocation-mechanics-based constituve relations for material dynamics calculations,” *J. Appl. Phys.*, Vol. 61, No. 5, pp. 1816-1825, 1987.

168 F.J. Zerilli, R.W. Armstrong, “Description of tantalum deformation behavior by dislocation mechanics based constitutive relations,” *J. Appl. Phys.*, Vol. 68, No. 4, pp. 1580-1591, August 1990.

169 J.D. Cinnamon, A.N. Palazotto, N.S. Brar, Z. Kennan, D. Bajaj, “Johnson-Cook Strength Model Constants for Vascomax 300 and 1080 Steels,” *SHOCK COMPRESSION OF CONDENSED MATTER - 2005: Proceedings of the Conference of the American Physical Society Topical Group on Shock Compression of Condensed Matter. AIP Conference Proceedings*, Vol. 845, pp. 709-712, 2006.

170 G.R. Johnson, W.H. Cook, “A Constitutive Model and Data for Metals Subjected to Large Strains, High Strain Rates and High Temperatures,” *Proceedings of the Seventh International Symposium on Ballistics*, The Hague, The Netherlands, p. 541-547, 1983.

171 G.T. Gray III, S.R. Chen, W. Wright, M.F. Lopez, “Constitutive Equations for Annealed Metals Under compression at High Strain Rates and High Temperatures,” Los Alamos National Laboratory, LA-12669-MS, 1994.

172 R.D. Dick, R.W. Armstrong, J.D. Williams, “Split-Hopkinson pressure bar tests on pure tantalum,” *AIP Conf. Proc.*, Vol. 429, pp. 471-474, 1998.

173 J.D. Cinnamon, A.N. Palazotto, N.S. Brar, “Further Refinement of Material Models for Hypervelocity Gouging Impacts,” *47th AIAA/ASME/ASCE/AHS/ASC Structures, Structural Dynamics, and Materials Conference*, Newport, Rhode Island, AIAA 2006-2086, May 2006.

174 R.W. Armstrong, F.J. Zerilli, W.H. Hole, W. Mock Jr., “Dislocation Mechanics Based Constitutive Relations for Plastic Flow and Strength of HY Steels,” *American Institute of Physics Conference Proceedings*, Vol. 309, pp. 1001-1004, 1994.

175 F.J. Zerilli, R.W. Armstrong, “Constitutive Relations for the Plastic Deformation of Metals,” *American Institute of Physics Conference Proceedings*, Vol. 309, pp. 989-992, 1994.

176 W.H. Holt, W. Mock Jr., J.B. Clark,. F.J. Zerilli, R.W. Armstrong, “Gas-Gun Reverse-Ballistic Impact Deformation and Fracture of Armco Iron Taylor

Specimens of Differing Grain Sizes," *American Institute of Physics Conference Proceedings*, Vol. 309, pp. 1193-1196, 1994.

177 F.J. Zerilli, R.W. Armstrong, "Constitutive relations for titanium and Ti-6Al-4V," *AIP Conf. Proc.*, Vol. 370, pp. 315-318, 1996.

178 F.J. Zerilli, R.W. Armstrong, "Dislocation mechanics based constitutive equation incorporating dynamic recovery and applied to thermomechanical shear instability," *AIP Conf. Proc.*, Vol. 429, pp. 215-218, 1998.

179 R.W. Armstrong, W. Arnold, F.J. Zerilli, "Dislocation Mechanics Under Extreme Pressures," *Shock Compression of Condensed Matter*, Vol. 955, pp. 623-626, 2007.

180 R.W. Armstrong, W. Arnold, F.J. Zerilli, "Dislocation mechanics of copper and iron in high rate deformation tests," *Journal of Applied Physics*, Vol. 105, 2009.

181 J.V. Parker, D.T. Berry, P.T. Snowden, "The IAT Electromagnetic Launch Research Facility," *IEEE Trans. Mag.*, Vol. 33, No. 1, pp. 129-133, 1997.

182 D.A. Ward; J.La.T. Exon, "Using Rogowski coils for transient current measurements," *Engineering Science and Education Journal*, Volume 2, Issue 3, pp. 105–113, 1993.

183 K.M. Chakravarthy, T.J. Watt, D.L. Bourell, "The Use of High-Speed Video as an In-Bore Diagnostic for Electromagnetic Launchers," *IEEE Transactions on Plasma Science*, Vol. 39, No. 2, 2011.

184 F. Stefani and R. Merrill, "Experiments to measure melt-wave erosion in railgun armatures," *IEEE Trans. Magn.*, Vol. 39, no. 1, pp. 188–192, 2003.

185 T. Watt and F. Stefani, "The Effect of Current and Speed on Perimeter Erosion in Recovered Armatures," *IEEE Transactions on Magnetics*, Vol. 41, pp. 448-452, 2005.

186 D.P. Bauer, J.P. Barber, "Direct Measurement of Rail Resistance," *IEEE Transactions on Magnetics*, Vol. 25, No. 1, pp. 88-91, 1999.

187 B.K. Sen, R.L. Wheeler, "Skin Effects Models for Transmission Line Structures Using Generic SPICE Circuit Simulators", *IEEE 7th Topical Meeting on Electrical Performance of Electronic Packaging*, pp. 128-131, 1998

188 J.P. Barber, D.P. Bauer, K. Jamison, J.V. Parker, F. Stefani, A. Zielinski, "A survey of armature transition mechanisms," *IEEE Transactions on Magnetics*, Vol. 39, No. 1, pp. 47-51, 2003.

189 F. Stefani and J. V. Parker, "Experiments to measure wear in aluminum armatures," *IEEE Trans. Magn.*, Vol. 35, no. 1, pp. 100–106, 1999.

190 T.J. Watt, M.D. Bryant, "Modeling Assumptions for Railguns," *IEEE Transactions on Magnetics*, Vol. 43, No. 1, pp. 380-383, January 2007.

191 T.J. Watt, M.D. Bryant, "Cracking and Dominant Stresses in the Throat Region of C-Shaped Solid Armatures," *IEEE Transactions on Magnetics*, Vol. 43, No. 1, pp. 418-421, 2007.

192 T. Watt, F. Stefani, "Experimental and Computational Investigation of Root Radius Melting in C-shaped Solid Armatures," *IEEE Transactions on Magnetics*, Vol. 41, pp. 442-447, 2005.

193 D.A. Hopkins, F. Stefani, K.T. Hsieh, B.K. Kim, "Analysis of startup behavior in a "C-shaped" armature using linked EMAP3D/DYNA3D finite element codes," *IEEE Transactions on Magnetics*, Vol. 35, No. 1, 1999, pp. 59-64.

194 H.D. Yun and J.H. Price, "Electromagnetic and Structural Analyses of Electric Gun and Integrated Launch Package Systems," *IEEE Transactions on Magnetics*, Vol. 31, No. 1, 1995, pp. 253-258.

195 T.J. Watt, D.T. Motes, "The Effects of Surface Coatings on the Onset of Rail Gouging," *IEEE Transactions on Plasma Science*, Vol. 39, No. 1, pp. 168-173, 2011.

196 Juergen K.S. Fischer, Alumiplate Incorporated (2007) *Aluminium electroplating formulations*, U.S. Patent 7,250,102.

197 T.J. Watt, D.L. Bourell, "Sliding Instabilities and Hypervelocity Gouging," *IEEE Transactions on Plasma Science*, Vol. 39, No. 1, pp. 162-167, 2011.

198 G. Petzow, "Metallographic Etching", ASM International, 1976.

199 S.R. Chen, G.T. Gray III, "Constitutive Behavior of Tantalum and Tantalum-Tungsten Alloys," Metallurgical and Materials Transactions A, Vol. 27A, pp. 2994-3006, October 1996.

200 A. Hunsche, P. Neumann, "Quantitative measurement of persistent slip band profiles and crack initiation," *Acta metall.*, Vol. 34, No. 2, pp. 207-217, 1986.

201 T. Watt and F. Stefani, "The Effect of Current and Speed on Perimeter Erosion in Recovered Armatures," *IEEE Transactions on Magnetics*, Vol. 41, pp. 448-452, 2005.